



UNIVERSITY OF
BIRMINGHAM

NUMERICAL INVESTIGATIONS OF TURBULENT
FLOW THROUGH FORESTS AND URBAN
CANOPIES

by

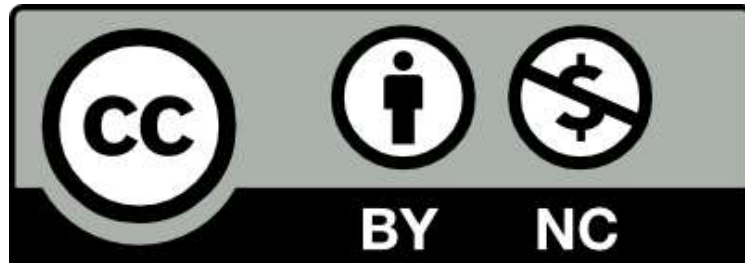
EDWARD JAMES BANNISTER

A thesis submitted to the University of Birmingham
for the degree of DOCTOR OF PHILOSOPHY

School of Geography, Earth, and Environmental Sciences
College of Life & Environmental Sciences
University of Birmingham

September 2022

University of Birmingham Research Archive e-theses repository



This unpublished thesis/dissertation is under a Creative Commons Attribution-NonCommercial 4.0 International (CC BY-NC 4.0) licence.

You are free to:

Share — copy and redistribute the material in any medium or format

Adapt — remix, transform, and build upon the material

The licensor cannot revoke these freedoms as long as you follow the license terms.

Under the following terms:



Attribution — You must give appropriate credit, provide a link to the license, and indicate if changes were made. You may do so in any reasonable manner, but not in any way that suggests the licensor endorses you or your use.



NonCommercial — You may not use the material for commercial purposes.

No additional restrictions — You may not apply legal terms or technological measures that legally restrict others from doing anything the license permits.

Notices:

You do not have to comply with the license for elements of the material in the public domain or where your use is permitted by an applicable exception or limitation.

No warranties are given. The license may not give you all of the permissions necessary for your intended use. For example, other rights such as publicity, privacy, or moral rights may limit how you use the material.

Unless otherwise stated, any material in this thesis/dissertation that is cited to a third-party source is not included in the terms of this licence. Please refer to the original source(s) for licencing conditions of any quotes, images or other material cited to a third party.

Abstract

Most of the terrestrial living world, humanity included, spends nearly all of its time in the atmospheric boundary layer (the ABL). This thesis addresses some of the limitations in our knowledge of turbulent exchange in the ABL. It is relevant to anyone wishing to understand the details of the weather, climate, and air quality around cities, forests, and crops. The work pays particular attention to the transport of scalar quantities—e.g., pollutants, CO₂, or bioaerosols—in patchy, inhomogeneous landscapes, especially those comprising canopies of large obstacles, such as forests and cities. This thesis comprises three main research sections. The work is presented in order of ‘increasing realism’, with the studies becoming less idealised and more realistic and one moves through the thesis.

The first section investigates pollution in an idealised model of a patchy urban area. It uses conceptual arguments and large-eddy simulation to identify and diagnose two urban flow regimes based on the size of patches of different density. This work: (i) identifies possible locations of pollution hot spots; (ii) quantifies what is loosely referred to as the ‘urban background’ in an air-pollution context; and (iii) provides a conceptual basis for further research into neighbourhood-scale air-pollution problems and the transport of fluid constituents in other porous media.

The second section reviews, synthesises, and discusses current understanding of forest-atmosphere exchange around patchy real-world forests. The overarching goal of this broad chapter is to improve numerical models of forest-atmosphere exchange by making the model forests less idealised, and more like the real world. For example, the transport equations can be modified efficiently to account for patchy forests and moving plant elements. The chapter provides rules-of-thumb for forest areas in which edge effects dominate, a minimum size constituting a gap from an aerodynamic perspective, and recommendations for using computing resources effectively when faced with the dilemma of improving a model’s scale versus its resolution.

The third section investigates air-parcel residence times in a mature forest, calculated from observations at a free-air carbon dioxide enrichment facility. It shows that median daytime residence times in the tree crowns are twice as long when the trees are in leaf versus when they are not. Residence times increase with greater atmospheric stability, as does the variability around their central values. Robust parametrisations of air-parcel residence times can be obtained using gamma-like distributions, with the parameters estimated from widely measured flow variables. Large volumes of pooled air are sometimes sporadically and unpredictably vented during calm evenings. Under certain circumstances, simple models can be used to model the passage of passive scalar quantities on the mean flow.

This thesis is dedicated to the loving memory of

my dear friend

Anna-Maria Rauf

27 November 1955 – 2 April 2019

my grandmother

Mollie Tinker

4 January 1928 – 27 April 2020

and my father-in-law

黃先意

Kenny Ooi Sian Ee

23 September 1957 – 7 March 2022

May I be the things I miss most about them.

Acknowledgments

It takes a village. I thank Prof Rob MacKenzie, Dr Xiaoming Cai, and Dr Mike Jesson for their excellent supervision. Having one good supervisor is not a given, and having two is rare. Having three is like finding a hen's gold filling. I am also very grateful to my proto-supervisor Dr Jian Zhong. I spent many hours looking over his shoulder while he explained programming details that were intricate to me, but no doubt trivial to him. Learning from and working with you all has been the highlight of my professional life so far.

I extend my thanks to the wider BIFoR FACE team, in particular, to Nick Harper, Dr Kris Hart, Peter Miles, and Tom Downes for doing most of the heavy lifting (figuratively and literally) of the wind equipment. I want to acknowledge their suffering through long and tedious email chains about logger output, data stability, and baud rates. I hope one day to be able to return all that those measurements have taken from them. Thank you to Dr Eric Casella at Forest Research UK for his laser scans of BIFoR FACE, and many interesting conversations about forests. Thanks to Prof Gregor Leckebusch for his advice on the wider applications of meteorological research. I am eternally grateful to all the invisible workers who keep home lives running, maintain equipment and databases, provide mentorship and counsel, write open-source code, review manuscripts, and the millions of other jobs that will never win Nobel prizes, but without which scientific research would grind to a halt.

To that end, I thank my family, the Bannister–Tinker–Ooi–Patel clan, and my friends, for climbing trips, Mr Bean marathons, support through tough times, stag dos and weddings, Sunday-morning trail runs, bad jokes and good fun, Nicholas Cage evenings, sleepless nights bivvying, over-ordering at restaurants, and all the other things that give life its fizz. I love you all. A special mention to my parents, Mark and Julia, for instilling in me a fascination with the natural world, and for their example of how to live with joy and courage. Thank you to Elliot for their boundless love and for being my inspiration. To my daughter Tao-Mei—your progressively robust wriggles have buoyed my spirit through the difficult months since we lost your 公公. Finally, to my wife, Kristina. Whenever I see a PhD thesis thanking a life partner, I grin because I know this is someone who gets it. It is no exaggeration to say I could not have done this without you. I love you more than you could know. These ‘repetitive, squiggly’ graphs are for you.

* * *

It is my pleasure to acknowledge that this work was funded by the UK Natural Environment Research Council (NERC) via a studentship with the Central England NERC Training Alliance (grant NE/L002493/1). I also made use of the BIFoR FACE facility, whose infrastructure and research are supported by the JABBS Foundation, the University of Birmingham, the John Horseman Trust, the Ecological Continuity Trust, and NERC (grant NE/S015833/1). I am grateful for access to, and support using, the BlueBEAR high-performance computing service, funded by the University of Birmingham.

Table of Contents

List of Figures	vii
List of Tables.....	x
List of Symbols	xi
List of Abbreviations.....	xv
Chapter 1 – Preface and Thesis Overview	16
1.1 Introduction and motivation.....	16
1.2 Aims and objectives	18
1.3 Thesis overview	18
1.4 Main novel contributions	19
1.5 The presentation of this thesis.....	20
1.5.1 Presentation of the research chapters	20
1.5.2 Stylistic considerations.....	21
1.5.3 Notation.....	21
Chapter 2 – Theory and Background	22
2.1 The atmosphere and the atmospheric boundary layer (ABL)	22
2.1.1 Basic properties of the atmosphere	22
2.1.2 Conceptual scales in the troposphere	23
2.1.3 Basic properties of the ABL.....	25
2.1.4 Sublayers of the ABL.....	27
2.1.5 Scalar quantities in the ABL	28
2.2 Turbulence in the ABL.....	30
2.2.1 Basic properties of turbulence in the ABL.....	30
2.2.2 The continuum assumption and Reynolds decomposition	31
2.2.3 Common descriptive statistics.....	33
2.2.4 Taylor’s hypothesis	34
2.2.5 Turbulence spectra in the ABL	35
2.3 Turbulent flow equations	37
2.3.1 Conservation equations	37
2.3.2 Statistical approaches to the conservation equations	38
2.3.3 The closure problem.....	39

2.3.4 RANS closure schemes	40
2.3.5 Large-eddy simulation and direct numerical simulation	41
2.3.6 Application of LES in this thesis.....	42
2.4 Flow through canopies in the ABL	43
2.4.1 Description of the flow in canopies of obstacles.....	43
2.4.2 The porous media model of canopy flow	44
2.4.3 Approximating the aerodynamic drag term fi	45
2.5 Simplifications and conceptual scalings.....	46
2.5.1 Monin–Obukhov Similarity Theory	46
2.5.2 The logarithmic wind profile.....	47
2.5.3 The mixing-layer analogy for canopy flow	48
Chapter 3 – Equipment and Methods.....	51
3.1 The Birmingham Institute of Forest Research Free-Air Carbon Dioxide Enrichment (BIFoR FACE) facility	51
3.1.1 Overview of BIFoR FACE.....	51
3.1.2 The meteorological towers at BIFoR FACE	55
3.2 The Weather Research and Forecasting model	58
3.3 Eddy-covariance measurements	60
3.4 Data management and processing in this thesis	61
3.4.1 Overview of data management and processing	61
3.4.2 Processing algorithms used for the BIFoR FACE meteorological tower measurements	62
3.4.2.1 Data cleaning and despiking algorithm	62
3.4.2.2 Coordinate rotation to correct sensor misalignment.....	63
Chapter 4 – Neighbourhood-Scale Flow Regimes and Pollution Transport in Cities.....	64
4.1 Introduction	64
4.2 Porous model of neighbourhood-scale flow.....	66
4.2.1 Use of a porous model in urban areas	66
4.2.2 Applicability of the porous model to the urban boundary layer.....	67
4.2.3 Spatial inhomogeneity and adjustment.....	68
4.3 Method	69
4.3.1 Transport equations	69

4.3.2 Approximating the drag force	71
4.3.3 Simulated cases	72
4.3.4 Numerical details and post-processing.....	73
4.4 Results – Dynamics.....	75
4.4.1 Comparison with published data.....	75
4.4.2 Adjustment of the flow.....	77
4.4.3 Dynamical patterns induced by adjustment to density changes	79
4.5 Results – Behaviour of pollutants	82
4.5.1 Two-dimensional patterns in pollutant concentration	82
4.5.2 Two-dimensional patterns in the kinematic turbulent pollutant flux	84
4.5.3 Adjustment of scalar concentrations and fluxes.....	86
4.6 Discussion and conclusions.....	88
4.6.1 Neighbourhood-scale flow regimes.....	88
4.6.2 Pollutant concentrations	89
4.6.3 Limitations and effect of other variables.....	90
4.6.4 Applications and outlook	91
Appendix 4A – Conceptual background to the porous-media model	93
4A.1 Conceptual background.....	93
4A.2 Implementation in WRF.....	94
Appendix 4B	95
Chapter 5 – Realistic Forests and the Modelling of Forest-Atmosphere Exchange.....	97
5.1 Introduction	98
5.1.1 A sense of scale	98
5.1.2 The extent of the literature	98
5.1.3 The scope of this review.....	99
Part I: Forest-atmosphere exchange around heterogeneous forests	100
5.2 The flow in and around idealised forests.....	100
5.2.1 Definition of terms	100
5.2.2 The double-average method	102
5.2.3 The double-average method in numerical models	103
5.2.4 Representing forests through distributed drag.....	104

5.2.5	The turbulence structure around forests	105
5.2.6	Atmospheric stability and the turbulence structure	107
5.3	Realistic landscape effects	109
5.3.1	Adaptation to wind loading	109
5.3.2	Flow adjustment around forest edges	110
5.3.3	The edge regions in context	112
5.3.4	Patches and gaps	113
5.4	Scalar quantities in realistic landscapes	116
5.4.1	Scalar transport at the upstream edges of forests	117
5.4.2	Scalar transport in the lee of forests	119
5.4.3	Topographical effects on forest-atmosphere exchange	119
5.4.3.1	Boundary-layer flow over hills and forest-atmosphere exchange	119
5.4.3.2	Looking forward.....	121
5.4.4	Air-parcel residence times.....	122
Part II: Improving ecosystem-scale models of forest-atmosphere exchange		123
5.5	Canopy structure	123
5.5.1	Drag and plant reconfiguration	123
5.5.2	Terrestrial laser scanning	126
5.5.3	Stochastic drag forcing.....	128
5.5.4	Waving plants and biological backscatter.....	129
5.5.5	Resolved trees	130
5.6	Atmospheric physics and chemistry.....	131
5.6.1	Modelling in-canopy chemistry	131
5.6.2	Modelling particle deposition.....	133
5.6.3	Heterogeneous sources and sinks of scalar quantities	135
5.6.4	Calculations of dispersive fluxes.....	136
5.6.5	A note on the resolution and domain size in LES models.....	137
5.7	Future challenges	139
5.7.1	Customised numerical models of real sites	140
5.7.2	Connection to larger scales	141
5.7.3	Challenging weather and atmospheric conditions.....	142

Appendix 5A: Numerical details of LES model	142
5A.1 Drag parametrisation and simulated cases	142
5A.2 Transport equations	143
5A.3 Drag parametrisation and simulated cases	144
Appendix 5B: Summary of modelling investigations of flow around forests.....	146
Appendix 5C: Image acknowledgements.....	149
Chapter 6 – Air-parcel Residence Times in a Mature Forest: Observational Evidence From a Free-Air CO ₂ Enrichment Experiment.....	150
6.1 Introduction	151
6.2 Methods.....	153
6.2.1 Site description.....	153
6.2.2 Observational details.....	155
6.2.2.1 Observation period and canopy density	155
6.2.2.2 Fumigation and meteorological measurements	156
6.2.3 Calculation of residence times	157
6.2.4 Data processing	159
6.2.5 Notation and meteorological tower calculations	160
6.3 Results and Discussion.....	161
6.3.1 Wind conditions at BIFoR FACE	161
6.3.2 Basic distributions of τ values.....	162
6.3.3 Dependence of τ on u^* and atmospheric stability.....	162
6.3.3.1 Dependence of τ on u^*	162
6.3.3.2 Dependence of τ on atmospheric stability.....	163
6.3.4 Dependence of τ on wind direction.....	165
6.3.5 Seasonal (leaf-on/leaf-off) differences in τ	166
6.3.6 Comparison with published residence time values	167
6.3.7 Longer residence times evidenced by evening venting events.....	170
6.4 Conclusions	173
Appendix 6A – Estimating Keq in Equation (6.1).....	174
Appendix 6B	175
Chapter 7 – Conclusions and Further Work.....	176

7.1 Summary of findings and their limitations.....	176
7.1.1 Objective 1: Formulate and assess a model of flow over a spatially inhomogeneous urban area at the neighbourhood scale.....	176
7.1.2 Objective 2: Use the urban model with LES to investigate the transport of pollutants in a spatially inhomogeneous urban area.....	177
7.1.3 Objective 3: Review and synthesise current understanding of turbulent exchange around forests, with a particular focus on patchiness, real forest properties, and scalar quantities.....	178
7.1.4 Objective 4: Identify ways in which numerical models of forest-atmosphere exchange, especially LES models, can be made more realistic without compromising their ability to resolve turbulence.....	179
7.1.5 Objective 5: Use the observations from a free-air carbon dioxide enrichment (FACE) facility to investigate air-parcel residence times in a real forest, open to the atmosphere.....	180
7.2 Recommendations for further work	181
7.2.1 Micrometeorological research.....	181
7.2.2 Connecting the microscale to larger scales	182
7.2.3 A case for empiricism in investigations of canopy-atmosphere exchange.....	182
7.2.4 Illustrative example: using opportunistic experiments to extend existing theory	183
7.2.4.1 Advection-speed approximation.....	183
7.2.4.2 Opportunistic ‘pulse and trace’ experiments.....	184
7.2.4.3 Comparison of the mean wind speed and pulse advection speed.....	186
References.....	188
Appendix A.....	214

List of Figures

2.1	Schematic of the lower layers of the atmosphere
2.2	Typical time and space orders of magnitude for meteorological phenomena.
2.3	Schematic spatial scales of for the interaction of the flow of air with canopies of obstacles in the ABL.
2.4	Schematic of the troposphere from Stull (1988), the lowest sublayer of which is the atmospheric boundary layer (ABL).
2.5	Schematic spectrum of the wind speed in the ABL.
2.6	Conceptual sublayers above large obstacles in the daytime ABL on (a) logarithmic and (b) linear scales.
2.7	Timeseries of the wind speed observed in the early afternoon of 27 Aug 2019 at BIFoR FACE.
2.8	Schematic spectra of a velocity component or turbulence kinetic energy in isotropic turbulence.
2.9	Schematic wind-speed profiles over short grass and a tall crop.
2.10	Schematic of the mixing-layer analogy for canopy flow.
3.1	(a) Aerial view of the BIFoR FACE infrastructure, looking north-east. (b) Schematic of the BIFoR FACE facility.
3.2	A schematic view of the sensor deployment and tissue and data flow through BIFoR FACE and Wood Brook.
3.3	Schematic of the meteorological towers at BIFoR FACE and the equipment mounted on them.
4.1	Schematic of the simulated domain, showing alternating density patches within an urban neighbourhood.
4.2	Canopy spatially averaged mean vertical profiles of the (a) mean streamwise velocity component U/u_H , (b) shear stress F_u/u_* , and (c) streamwise turbulence intensity σ_u/u_* .
4.3	Effect of patchiness on the mean vertical velocity component, W .
4.4	Effect of patchiness on the mean streamwise velocity component U .
4.5	Vertical perturbation profiles of (a) $([\bar{e}]_{alt} - [\bar{e}]_{hom})/u_*^2$ and (b) $(F_{u_{alt}} - F_{u_{hom}})/u_*$.
4.6	Effect of patchiness on pollutant concentration.
4.7	Effect of patchiness on the kinematic turbulent concentration flux F_c .

4.8	Adjustment of (a) the normalized scalar concentration $[\bar{c}]/(QH/u_*)$ at $z = 0.5H$; and (b) normalized turbulent fluxes of momentum $(-[\overline{u'w'}])/u_*^2$ (solid line) and scalars F_c/u_*c_* (dashed line) at $z = 0.5H$
4.9	Schematic of neighbourhood-scale flow regimes.
4.10	Location of concentration maxima and minima at $z = 0.5H$ downstream of the leading edge of the dense (red) and sparse (grey) patches.
4.11	Adjustment of pollutant concentration between patches of different emission rates into an area with a homogeneous urban form.
4A.1	Conceptual overview and detail of a porous medium
4A.1	Vertical profiles of the area density A used in the drag parametrisation in Equations (4.10) and (4.11)
4B.1	Effect of patchiness on TKE $[\bar{e}]/u_*^2$.
4B.2	Effect of patchiness on the square root of magnitude of the shear stress F_u/u_* .
5.1	Sublayers of the daytime atmospheric boundary layer (ABL) over a forest.
5.2	(a – left) A wind modified hawthorn (<i>Crataegus monogyna</i>) on the Isle of Wight, UK; and (b – right) windswept trees at Slope Point, South Island, New Zealand (Aotearoa).
5.3	Flow streamlines around a shelter belt standing perpendicular to the flow of air from left to right.
5.4	Dynamical flow patterns around a small forest in neutral atmospheric conditions.
5.5	Openings in various forest canopies.
5.6	Schematic of the flow over a forested hill.
5.7	(a – left) leaves of a cottonwood (<i>Populus deltoides</i>) curling in high wind. (b – right) trees at the edge of a forest reconfiguring under wind loading.
5.8	(a) Vertical profile of PAD, $a(z)$, calculated using the formula derived by Lalic and Mihailovic (2004); (b) the southern edge of the oak-dominated woodland at the Birmingham Institute of Forest Research (BIFoR) free-air carbon dioxide enrichment (FACE) facility; and (c) open trunk space of an even-aged <i>Pinus taeda</i> monoculture plantation.
5.9	3D complexity of a Simple Notophyll Vine Forest (Robson Creek, Australia)
5.10	(a) Percentage difference in Sk_u ; and (b) Kt_u between Case 1 and Case 2, as a total of the maxima for Case 1.
5A.1	Vertical profile of PAD $a(z)$ (PAI ≈ 5) used in the LES model.
6.1	(a) schematic of the BIFoR FACE facility. (b) The perforated FACE vent pipes in array 4. (c) The two-dimensional sonic anemometer in array 1.

6.2	Timeseries of the green chromatic coordinate (GCC) derived from PhenoCam measurements.
6.3	(a) Linear- and (b) logarithmic-scale PDFs of τ from BIFoR FACE during the lowest 50% (solid black) and highest 25% (black dashed) of wind speeds of the leaf-on period, and GCF17's model in Equation (6.1) (navy-blue dot-dash).
6.4	Wind roses for BIFoR FACE during the 2019–2021 leaf-off (a, b) and leaf-on periods (c, d).
6.5	(a) PDFs and statistics of the residence times for the leaf-on and leaf-off periods. (b) As for (a), with PDFs presented on log-log axes with τ normalised by h_c/u_* .
6.6	Combined scatter and density plots, showing the variation of τ with u_* for the leaf-off (a) and leaf-on (b) periods.
6.7	Statistics of normalised residence times binned by stability class. (a) Box-whisker plots of normalised residence times for stable (S), near-neutral (NN), and unstable (U) conditions. (b) and (c) PDFs of residence times for the leaf-on period, plotted on linear and logarithmic axes (base 10), respectively.
6.8	Residence-time quintiles by wind direction for the leaf-on (a–c) and leaf-off (d–f) periods.
6.9	Solid black and red lines show PDFs of τ from BIFoR FACE during the leaf-on and leaf-off periods, respectively. Dashed lines show PDF estimates on the BIFoR FACE observations using Equation (6.7). Dot-dash navy line shows PDF from GCF17 in Equation (6.1). $\tau_{c(on)}$ and $\tau_{c(off)}$ denote $\tau_c = h_c/u_*$ for the leaf-on and leaf-off periods. All τ values normalised by $\tau_c = h_c/u_*$.
6.10	Timeseries of 1-minute averages in (a) the $[\text{CO}_2]$, (b) wind speed, and (c) wind direction after shutdown on 17 Aug 2020.
6.11	Timeseries after shutdown on 27 Aug 2019 of (a) the magnitude of the velocity vector components (m s^{-1}) and TKE ($\text{m}^2 \text{s}^{-2}$) at $z = 25 \text{ m}$, (b) T ($^\circ\text{C}$), (c) z/L (where L is the Obukhov length), and (d) $[\text{CO}_2]$.
6B.1	(a) and (b) PDFs of residence times binned by stability class for the leaf-off period, plotted on linear and logarithmic axes (base 10), respectively.
7.1	(a) A neighbourhood in Melbourne, Australia comprising buildings of varying shapes and sizes and a large proportion of vegetation. (b) A neighbourhood in Nur-Sultan (formerly Astana), Kazakhstan in which the landscape is dominated by a relatively small number of large, irregularly shaped buildings.
7.2	$[\text{CO}_2]$ timeseries for P1_on; and (b) P3_off.

List of Tables

3.1	Details of the meteorological towers at BIFoR FACE, including the heights of the platforms.
3.2	Incorrect alignments of some of the sonic anemometers on the meteorological towers at BIFoR FACE
5B.1	Chronological summary of highly cited modelling investigations of flow around forests at the ecosystem scale.
6.1	Geometries of the BIFoR FACE control (c) and fumigation (f) arrays.
6.2	Descriptive statistics of τ values for the leaf-on and leaf-off periods binned into three stability regimes.
7.1	Details of the pulse and trace experiments.

List of Symbols

Italicised Roman characters

$a(z)$	Layer-wise canopy-area density.
$a[\text{CO}_2]$	Ambient CO_2 mixing ratio (at BIFoR FACE).
A_f	Frontal area.
A_t	Total plan area.
B	Vogel number.
C_d	Drag coefficient.
d	Displacement height.
$D_{med}(\alpha)$	Median absolute deviation of a quantity α .
E_ϕ	Efficiency of particle deposition.
$e[\text{CO}_2]$	Elevated CO_2 mixing ratio (at BIFoR FACE).
f	Cyclic frequency.
$F(\alpha)$	Fourier transform of some quantity α .
f_i	Aerodynamic drag.
f_0	Natural frequency of moving plants.
g	Gravitational acceleration.
H	Mean canopy height (urban areas).
h_c	Mean canopy height (forests and other vegetation canopies).
H_s	Scale height (e -folding depth) of the atmosphere.
K_{eq}	Eddy diffusivity.
Kn	Knudsen number.
Kt_α	Kurtosis of a quantity α .
L	Obukhov length.
L_c	Canopy-drag length scale.
L_h	Hill half length.
L_p	Patch length.
L_s	Shear length scale.
\mathbb{L}	Characteristic length scale.

ℓ_m	Prandtl mixing-length scale.
M_r	Molar mass (of CO ₂).
$\mathcal{O}(\alpha)$	In the order of (α).
O_d	Diameter of opening.
p	Atmospheric (perturbation) pressure.
p_n	Normalised pulse advection speed.
\mathbb{P}	Time period over which an eddy passes a sensor.
\mathbb{P}_w	Wave period.
Q_{h_c}	Specific flux at the canopy top.
\mathcal{R}	Molar gas constant.
Re	Reynolds number.
$r_{\alpha\beta}$	Correlation coefficient of quantities α and β .
Sk_α	Skewness of a quantity α .
$S_\alpha(f)$	Power spectral density of α .
S_{ϕ_i}	Source/sink of a scalar quantity ϕ_i .
T	Air temperature.
T_a	Averaging time period.
T_l	Lagrangian integral timescale.
T_s	Sonic air temperature.
U_{h_c} or \bar{u}_{h_c}	Mean streamwise wind speed at the crown top.
u_*	Friction velocity.
V	Magnitude of the wind velocity.
V_f	Volume of the fluid within a given volume.
V_s	Volume of the solid obstacles within a given volume.
V_t	Total volume, including both solid and fluid constituents ($V_t = V_f + V_s$).
V_a	Effective volume.
\mathbb{V}	Characteristic velocity scale.
w_s	Particle settling velocity.
w_*	Deardorff convective velocity scale.

x_A	Adjustment distance.
z_i	Boundary-layer depth.
z_{rel}	Air-parcel release height.
z_0	Roughness length.
z_*	Blending height in the ABL.

Greek Letters

α_c	Attenuation coefficient.
α_s	Shape parameter of inverse-gamma distribution.
β	u_*/U , evaluated at $z = h_c$.
β_s	Scale parameter of inverse-gamma distribution.
δ_{i3}	Kronecker delta.
δ_ω	Vorticity thickness.
Δ_f	LES filter width.
Δ_g	LES grid resolution.
Δ_i	LES filter width in the i^{th} direction.
η	Terrain-following hydrostatic-pressure vertical coordinate in WRF.
η_m	Kolmogorov microscale.
θ	Potential temperature.
θ_v	Virtual potential temperature.
θ_0	Reference temperature.
κ	von Kármán constant ($\kappa \approx 0.4$).
κ_n	Eddy wavenumber.
Λ_α	Eulerian integral length scale of some quantity α .
λ_d	Frontal-area density of dense patches.
λ_e	Eddy diameter.
λ_f	Frontal-area density.
λ_m	Mean free molecular path.
λ_p	Plan-area density.
λ_s	Frontal-area density of sparse patches.

λ_w	Wavelength.
ν	Kinematic molecular viscosity.
ν_{SGS}	Sub-grid scale eddy viscosity.
ν_ϕ	Dry deposition velocity.
σ_α	Standard deviation of a quantity α .
ρ	Air pressure.
τ	Air-parcel residence time.
τ_c	Canopy-turnover timescale (h_c/u_*).
ϕ_l	Resolved local scalar concentration.

List of Abbreviations

ABL	Atmospheric boundary layer.
ASL	Atmospheric surface layer.
BIFoR	Birmingham Institute of Forest Research.
(B)VOCs	(Biogenic) volatile organic compounds.
CHATS	Canopy Horizontal Array Turbulence Study
CLM	Community Land Model.
DNS	Direct numerical simulation.
FACE	Free-air carbon dioxide enrichment.
FCP	FACE control program.
GCC	Green chromatic coordinate.
ICR	In-canopy recirculation region.
IQR	Interquartile range.
ISL	Inertial sublayer.
LAI	Leaf-area index.
LES	Large-eddy simulation.
LSM	Lagrangian stochastic model(ling).
MOST	Monin–Obukhov similarity theory.
PAD	Plant-area density.
PAI	Plant-area index.
PDF	Probability density function.
RANS	Reynolds-average Navier–Stokes.
RSL	Roughness sublayer.
SGS	Sub-grid scale.
SRT	Surface-renewal theory.
TKE	Turbulence kinetic energy.
UFP	Ultra-fine particles.
WRF	Weather Research and Forecasting (model).

Chapter 1 – Preface and Thesis Overview

1.1 Introduction and motivation

The portion of the atmosphere most affected by the Earth’s surface is known as the atmospheric boundary layer (ABL). The ABL never makes up more than a couple of percent of the total depth of the atmosphere, and often much less, although it can comprise up to a fifth of the atmosphere’s mass. Despite its modest depth—tens of metres to a kilometre or two within a total depth of about 100 km of atmosphere—the ABL is very important to us indeed. It is where terrestrial plants and animals spend most of their lives. It is where we human beings build our cities, plant our crops, experience the weather, and go about our business. The ABL is home.

The systematic scientific investigation of the ABL has a short but active history. Inquiry began in earnest in the late 1950s and, until around the 1980s, was mostly devoted to the simplest situation, the ABL over flat, open terrain. Over the past few decades, the development of powerful computers, fast-response sensors, and robust theoretical frameworks have allowed researchers and practitioners to address increasingly difficult problems. However, many problems remain. The root of most difficulties in ABL research is that the air in the ABL is nearly always turbulent, containing superimposed three-dimensional swirls, known as *eddies*, whose diameters range from around a millimetre to around a kilometre (Kaimal and Finnigan 1994). As Chapter 2 discusses further, these turbulent eddies cause chaotic and seemingly random variations in the atmospheric properties, right down to very small time and space scales (Stull 1988). ABL turbulence is seldom easy to approximate robustly (Stull 1988; Finnigan 2008). Numerically simulating turbulent flow, even approximately, is extremely computationally expensive (Bou-Zeid 2014). The situation is particularly complex around assemblies of large obstacles, such as in urban areas and forests, and in uneven terrain (Belcher et al. 2012). Chapter 2 introduces common numerical methods for approximating or resolving turbulent flow. Large-eddy simulation (LES) is discussed in particular detail, because it is used in Chapters 4 and 5 of this thesis. The essence of LES is that the large-scale motions of turbulent flow (i.e., the large eddies) are resolved directly from the governing equations and the small-scale motions (i.e., the small eddies) are modelled. Despite the seemingly intractable problem of atmospheric turbulence, applications across an array of disciplines means that ABL research remains vigorous. For a sense of the known unknowns, it is useful to distinguish between two broad areas of application.

The first is within the engineering and micrometeorological communities (including air-pollution studies). Micrometeorologists and engineers are interested in the atmospheric characteristics in particular locations for applications including wind power, building and infrastructure design, vegetation-atmosphere gas exchange, storm damage, and pollution assessments. The various sub-disciplines use different techniques and have different scales of focus—e.g., micrometeorologists typically seek cases that can be considered

‘typical’ or ‘general’, whereas extreme events are of particular interest in engineering and insurance applications. However, the fundamental question is the same: what are the properties of the small-scale turbulent flow at the Earth’s surface, at scales of meters to around a kilometre, and how is it affected by the large-scale synoptic conditions?

40

The second area of application of ABL research is in numerical weather prediction (NWP) and general circulation models (GCMs) (I include regional and global climate prediction and Earth-system models under the broad umbrella of GCMs). The current horizontal spatial resolution of NWP models is at best $\mathcal{O}(1\text{ km})$ and each time step at least $\mathcal{O}(10\text{--}100\text{ s})$ (Boutle et al. 2016). GCMs are coarser still. Therefore, even if all the information required for micrometeorological or engineering applications were available, it could not usefully be applied in NWP. For NWP and GCM applications, the precise details of the surface features and the flow over it are of less interest than the net effect of those features on the resolved variables at scales of $\mathcal{O}(1\text{--}1000\text{ km})$. In particular, ABL turbulence is significant only to the extent that it affects the average flow and the average fluxes of matter, momentum, and energy to and from the surface.

50

While the two areas of application overlap, for some time the two communities largely worked on different problems and moved in separate professional circles. Over the last decade or so, however, the interests of the two areas have begun to converge. The strongest motivations for this convergence are the searches for (i) connections between time and space scales in ABL phenomena and (ii) numerically efficient ways to make models more realistic, such as including a wider variety of ABL phenomena.

55

For example, micrometeorologists and engineers working at smaller scales wish to reflect that their work does not sit in some isolated portion of space but is actually immersed in the messy and chaotic reality of the atmosphere. Including more of this reality may alleviate issues encountered when working at smaller scales, for example, that real-world micrometeorological observations often do not square with the theory—for example, real-world flows are rarely statistically horizontal and homogeneous (Belcher et al. 2012; Bou-Zeid et al. 2020; Brunet 2020)—or that engineers’ assessments of the wind environment around buildings do not always reflect the winds that occur after construction (Vita et al. 2020).

60

Similarly, while NWP models and GCMs include approximations of land-surface processes (Sellers et al. 1986; Bonan et al. 2018), the degree of simplification that is sufficient to capture the dominant behaviour under all conditions is unclear. In most operational NWP and GCMs, urban areas, forests, and crops are represented through canopy-exchange schemes. These schemes reduce the landscape to tiles consisting of layers, often a single layer, with predetermined properties regarding the exchange of quantities such as radiation, water vapour, and heat with the atmosphere (Bonan et al. 2018, 2021; Garuma 2018). (Earth system models allow dynamic evolution of surface properties but still within a small number of possible surface types (e.g., Hourdin et al., 2017; Shi et al., 2019).) For computational workability, many of these canopy-exchange schemes rely on assumptions that are known to be false, e.g., that urban areas and forests are spatially homogeneous or that the turbulence within them displays Gaussian statistics. NWP models

65

70

75 and GCMs are therefore not suitable for applications where detailed vertical distributions of momentum, heat and moisture are needed—e.g., for air-quality or plant-response studies—because concentrations and fluxes are calculated at insufficient space and time resolutions.

1.2 Aims and objectives

80 This thesis aims to address some of these known simplifications and limitations by investigating specific aspects of turbulent exchange in the ABL. I pay particular attention to the transport of *scalar quantities*—e.g., pollutants, CO₂, or bioaerosols—in distinction to vector quantities such as wind or fields such as pressure. I focus on *patchy, inhomogeneous landscapes*, particularly those comprising canopies of large obstacles, such as forests and urban areas. This investigation is mainly limited to exchange over *ground that is approximately flat* (i.e., topographical effects are not discussed in detail). This thesis focuses
85 particularly on *timescales of seconds to around an hour*, and over *length scales of metres to around a kilometre*. I refer to these scales as the ‘**neighbourhood scale**’ in the context of urban areas, and the ‘**ecosystem scale**’ in the context of forests and other vegetated landscapes.

The primary objectives of this study are to:

- 90 1. Formulate and assess a model of flow over a spatially inhomogeneous urban area at the neighbourhood scale. This model should be able to reproduce important flow statistics, while being simple enough to be deployed with large-eddy simulation (LES) turbulence closure (Chapter 4).
2. Use the urban model with LES to investigate the transport of pollutants in a spatially inhomogeneous urban area (Chapter 4).
- 95 3. Review and synthesise current understanding of turbulent exchange around forests, with a particular focus on patchiness, real forest properties, and scalar quantities (Chapter 5).
4. Identify ways in which numerical models of forest-atmosphere exchange, especially LES models, can be made more realistic without compromising their ability to resolve turbulence (Chapter 5).
- 100 5. Use the observations from a free-air carbon dioxide enrichment (FACE) facility to investigate air-parcel residence times in a real forest, open to the atmosphere (Chapter 6).

1.3 Thesis overview

This thesis is organised as follows:

Chapter 2 presents an overview of the important areas of meteorology and atmospheric physics relevant to this work.

105 **Chapter 3** is a short chapter that provides additional information the experimental equipment and methods used in this work. Chapter 3 introduces the Birmingham Institute of Forest Research FACE facility (BIFoR FACE), which provides the bulk of the observational data used in this thesis.

Chapter 4 uses LES to investigate the transport of pollutants in an urban area, where the buildings and other obstacles are represented as patches of porous media.

110 **Chapter 5** reviews and synthesises current understanding of forest-atmosphere exchange at the ecosystem scale. The chapter then sets out practical ways to make numerical models of forest-atmosphere exchange more realistic.

Chapter 6 presents an investigation of air-parcel residence times using observations from BIFoR FACE.

115 **Chapter 7** summarises the findings of this work and discusses the implications of those findings. This chapter includes novel experiments at BIFoR FACE, which extend existing theory concerning the transport of scalar quantities through a forest.

During my PhD, I contributed to projects not wholly contained in this thesis, including Hart et al. (2020) (DOI: <https://doi.org/10.1111/gcb.14786>) and Baird et al. (2022) (DOI: <https://doi.org/10.5194/bg-2021-162>). The first pages of these publications are included in **Appendix A**, and the full open-access documents are available via the DOI links.

1.4 Main novel contributions

The main novel elements of this work can be summarised as follows:

- Conceptual arguments and large-eddy simulation are used to identify and diagnose two urban flow regimes based on the size of patches of different density. These arguments provide:
 - 125 ○ possible locations of pollution hot spots in patchy cities
 - quantification of what is loosely referred to as the ‘urban background’ in the air-pollution literature
 - a conceptual basis for further research into neighbourhood-scale air-pollution problems and fluid flow in other porous media.
- 130 • A thorough review and discussion of the current understanding of forest-atmosphere exchange, particularly in patchy and inhomogeneous landscapes. This work sets out practical ways to improve numerical models of forest-atmosphere exchange, including:
 - synthesising recent work, such as efforts to modify efficiently the transport equations to account for patchy forests and moving plant elements
 - 135 ○ assessing whether a given inhomogeneity ought to be modelled, or can be assumed to be smoothed by averaging

- providing rules-of-thumb for forest areas in which edge effects dominate, and a minimum size constituting a gap from an aerodynamic perspective
 - suggestions on computing resources effectively when faced with the dilemma of improving a model's scale versus its resolution.
- 140
- Air-parcel residence times are calculated from observations at BIFoR FACE. These are among the very few reported observational estimates of air-parcel residence times in forests. This is the first study to (a) use FACE observations to investigate forest residence times and (b) to include detailed observational statistics of air-parcel residence times. The study shows:
 - median daytime residence times in the tree crowns are twice as long when the trees are in leaf versus when they are not
 - residence times increase with greater atmospheric stability, as does the variability around their central values
 - large volumes of pooled air are sometimes sporadically and unpredictably vented during calm evenings (evidence of forest venting, under different conditions (i.e., nocturnal sustained venting), has previously been reported e.g., Cook et al. (2004))
 - robust parametrisations of air-parcel residence times can be obtained using gamma-like distributions, with the parameters estimated from widely measured flow variables.
- 145
- 150
- Evidence that, under certain circumstances, simple models can be used to model the passage of passive scalar quantities in forests. To my knowledge, this is the first time these models have been compared with observations in a real forest.
- 155

1.5 The presentation of this thesis

1.5.1 Presentation of the research chapters

This thesis uses the 'Alternative Format' pursuant to 7.4.1(g)–(i) Regulations of The University of Birmingham 2021–2022 (the 'Regulations'). Chapters 4–6 consist of published or submitted material.

160

This thesis adopts the Springer Basic Style for references—used in the journal *Boundary-Layer Meteorology*, for example. The Springer Basic Style is based on the Harvard style and the recommendations of the Council of Biology Editors.

165

Chapters 4–6 are written as journal-style manuscripts. I am the lead author on each, with contributions, guidance or supervision from my co-authors. The work contained in these chapters and elsewhere in this thesis is substantially my own. At the beginning of each of Chapters 4–6, I set out the details of the publication/submission, and present the specific contributions of my co-authors, in accordance with the Regulations.

170

175 Because I wrote Chapters 4–6 as self-standing manuscripts, there is a small amount of repeated information, particularly between Chapters 2, 4, and 5, which discuss the method of double-averaging the flow equations in surface-layer canopies. The inclusion of these details is necessary for each chapter to properly describe the experimental design and the topics being discussed.

Chapter 7 also contains novel material that has not been published or submitted for publication outside of this thesis.

180 **1.5.2 Stylistic considerations**

This thesis uses British English spelling, e.g., ‘centre’ rather than ‘center’, and adopts ‘-ise/-isation’ endings rather than ‘-ize/ization’.

185 Because Chapters 4–6 have been submitted in full or in part as peer-reviewed papers with multiple authors, they are written using the first-person-plural or third-person-singular pronouns, which are retained in this thesis. The remainder of this thesis uses the first person singular ‘I’ to avoid tedious constructions such as ‘it is this author’s opinion that...’ and over-use of the passive voice.

190 I have tried to avoid any unnecessarily gendered or otherwise exclusionary language in this thesis. Where a characteristic-specific term or connotation remains, please understand it to include people from all backgrounds and experiences.

1.5.3 Notation

195 This thesis adopts right-handed Cartesian tensor notation. Most discussions of the transport equations use the Einstein summation convention, with indices (i, j, k) taking values $(1, 2, 3)$ respectively. For example, u_i is the velocity in the x_i direction, with $i = 1, 2, 3$ representing the streamwise (x), spanwise (y) and vertical (z) directions. This thesis denotes $\mathbf{x} = (x, y, z)$, $(u_1, u_2, u_3) = (u, v, w)$, and time as t .

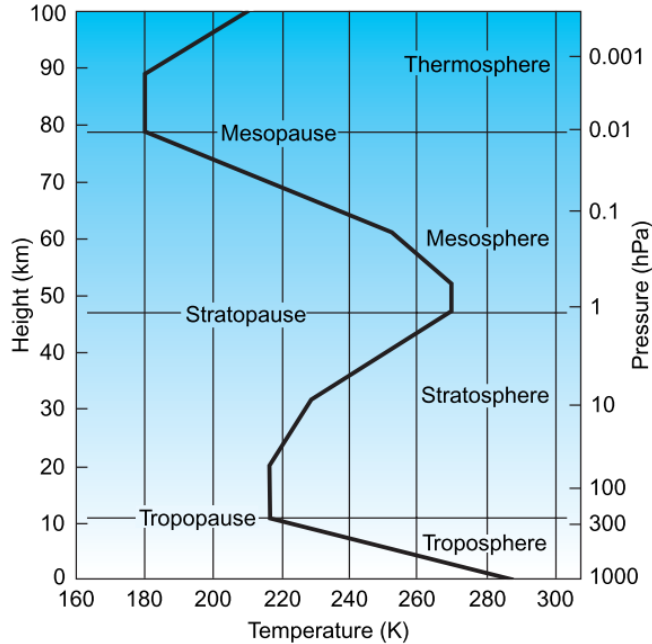
Chapter 2 – Theory and Background

200 **Abstract.** This chapter presents an overview of the important areas of meteorology and atmospheric physics relevant to this thesis, which focuses on turbulent exchange in and around canopies in the atmospheric boundary layer (ABL). Section 2.1 introduces some basic properties of the atmosphere and the ABL. Section 2.2 discusses turbulence in the ABL. Section 2.3 introduces the equations governing flow in the ABL. Section 2.4 highlights differences between flow in canopies and that elsewhere in the ABL, and
205 introduces the porous media model for canopy flow. Section 2.5 introduces helpful conceptual models in the ABL, most notably the mixing-layer analogy for canopy flow. This chapter outlines the principles of common numerical turbulence-closure scheme which are discussed in more detail in Chapters 4–7.

2.1 The atmosphere and the atmospheric boundary layer (ABL)

2.1.1 Basic properties of the atmosphere

210 The Earth’s atmosphere, i.e., the air, is the gaseous envelope that surrounds the planet. In dry air, nitrogen accounts for around 78% of the molecules by volume, oxygen around 21%, with the remaining fraction composed of a mixture of trace gases, most notably argon (around 0.9%), and carbon dioxide (0.04%). Near the Earth’s surface, water vapour usually accounts for 0–5% of the molecules by volume, although this proportion varies more in space and time than the proportions occupied by the other major constituents.
215 The portion of the atmosphere relevant to meteorology is commonly divided into four layers on the basis of the layers’ typical vertical profiles of temperature. The layers are, in order from the Earth’s surface, the *troposphere* (0–12 km above the surface), *stratosphere* (12–50 km), *mesosphere* (50–80 km), and *thermosphere* (80–700 km), with their upper limits denoted by the suffix *-pause* (Figure 2.1).



220 **Figure 2.1: Schematic of the lower layers of the atmosphere, from Wallace and Hobbs (2006). The vertical temperature profile (solid black line) is typical of a midlatitude location.**

Beyond the *thermosphere* is the *exosphere* (700–10,000 km), which is the final layer of the atmosphere before it transitions to outer space. Within the exosphere, the molecules are gravitationally bound to the Earth, but at such low densities that collisions are rare.

225 Within the troposphere, stratosphere, and mesosphere, the air pressure p decreases approximately exponentially with height such that:

$$p(z) \approx p_0 e^{-z/H_s}, \quad (2.1)$$

230 where p_0 is the pressure at some reference level (usually sea level, $z = 0$) and H_s is the scale height (the e -folding depth), which ranges from around 7–8km. The air density ρ decreases with height in the same manner (Wallace and Hobbs 2006).

235 This thesis considers only the troposphere, particularly the portion closest to the Earth’s surface, which is the ABL. The troposphere contains around 80% of the mass of the atmosphere, nearly all of its water, and consequently nearly all of its weather. On average, the air temperature, T , decreases with height in the troposphere such that $\partial T/\partial z \approx -6.5 \text{ }^\circ\text{C km}^{-1}$.

2.1.2 Conceptual scales in the troposphere

240 Meteorological phenomena in the troposphere are often classified by their characteristic time and horizontal space scales, which are usually much larger than the vertical scales, until one considers phenomena of a few kilometres or less. Figure 2.2 shows a representative categorisation by horizontal scale, with examples of the phenomena that can occur at each scale. This thesis focuses on processes occurring over the

meteorological microscale and γ -mesoscales. The meteorology of these scales is virtually synonymous with the meteorology of the atmospheric boundary layer (ABL).

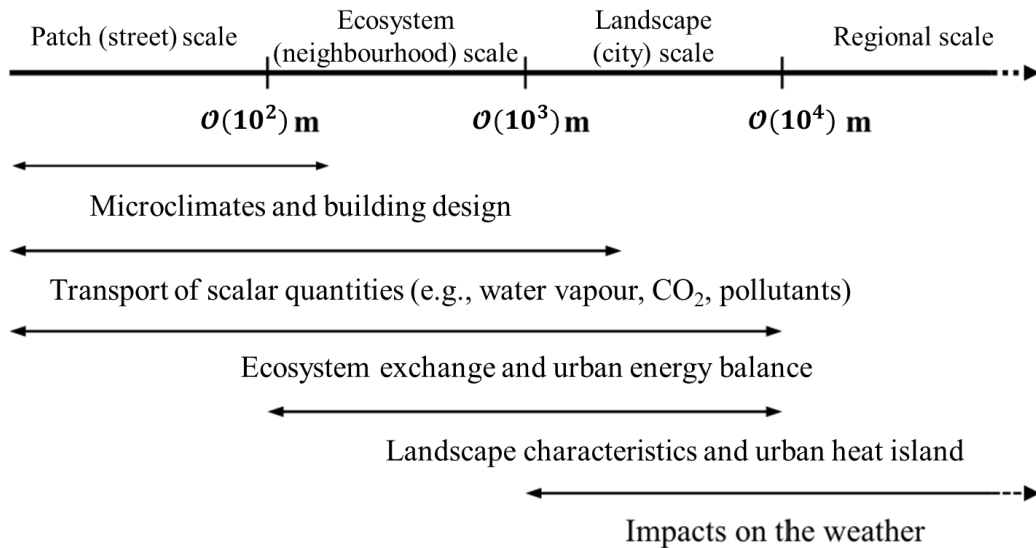
Temporal scale →	1 month	1 day	1 hour	1 min	1 sec	↓ Spatial scale
↓ Spatial scale	Standing waves Ultra-long waves					Macro α scale
10,000 km		Tidal waves				
2,000 km		Baroclinic waves				Macro β scale
200 km		Hurricanes Fronts				Meso α scale
20 km			Nocturnal jet Squall lines Inertial waves Cloud clusters Mountain waves Sea breezes			Meso β scale
2 km			Clear air turbulence Thunderstorms Gravity waves Urban Heat Island (UHI)			Meso γ scale
200 m				Tornadoes Deep convection Short gravity waves		Micro α scale
20 m				Patch edge effects Thermals Wakes		Micro β scale
				Plumes Turbulence Canyons		Micro γ scale
Temporal scale →	Climatological scale	Synoptic scale	Meso-scale	Micro-scale		

245 **Figure 2.2: Typical time and space orders of magnitude for meteorological phenomena. Dashed red region indicates the approximate scales of ecosystem/neighbourhood-scale phenomena. Figure after Orlanski (1975), adapted by Xiaoming Cai and the author through the addition of the dashed line and re-naming/ordering several of the meteorological phenomena.**

250 When investigating canopies of obstacles—such as forests, urban areas, and crops—it can be helpful to consider spatial scales based on interaction of the obstacles and the flow of air (Figure 2.3). Numerical conceptual frames, such as the Reynolds number, are introduced below, and canopy flow is also discussed in more detail. The spatial scales in Figure 2.3 are conceptual rather than rigidly defined. However, they provide a helpful basis for interpreting observations in terms of the relevant physical (and sometimes chemical) processes. As mentioned in Chapter 1, this thesis focuses on the ecosystem/neighbourhood scale.

255 This scale is interesting for a few reasons. First, it is a scale over which one can anticipate some degree of statistical homogeneity. The trees, buildings, and other obstacles can be clustered collectively into units, with their own distinct geometries and morphologies, with the units together comprising the larger landscape or city. Second, it is a scale at which one can often attempt a gross parametrisation of the flow based on coherent structures rather than wakes around individual obstacles (see below). Third, the

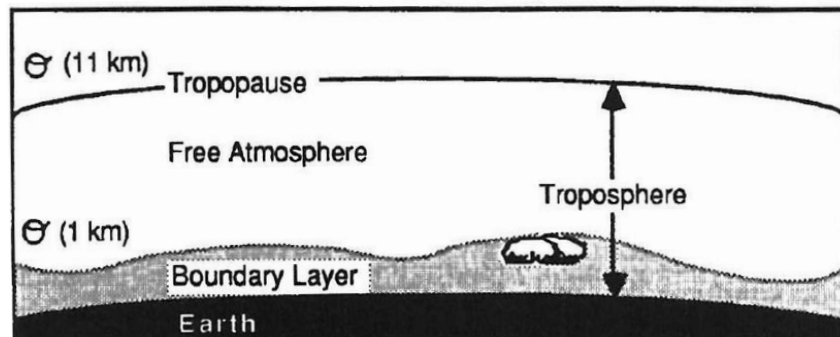
260 ecosystem/neighbourhood scale approximately corresponds to the horizontal resolution of operational meteorological models. This suggests that parametrisations at this scale may be used to couple (one way) operational models and finer scale processes.



265 **Figure 2.3: Schematic spatial scales of for the interaction of the flow of air with canopies of obstacles in the ABL. The names at the top of the figure refer to vegetated and (urban) landscapes. The urban naming protocol is adapted from Britter and Hanna (2003) and Oke (1978). Presentation of figure adapted from Zhong (2015).**

2.1.3 Basic properties of the ABL

The ABL accounts for the lowest 10% or so of the troposphere. The portion of the troposphere above the ABL is often referred to loosely as the ‘free atmosphere’ (Figure 2.4).



270 **Figure 2.4: Schematic of the troposphere from Stull (1988), the lowest sublayer of which is the atmospheric boundary layer (ABL). The \mathcal{O} on the left-hand side denotes ‘in the order of’. The scales are compressed to aid presentation.**

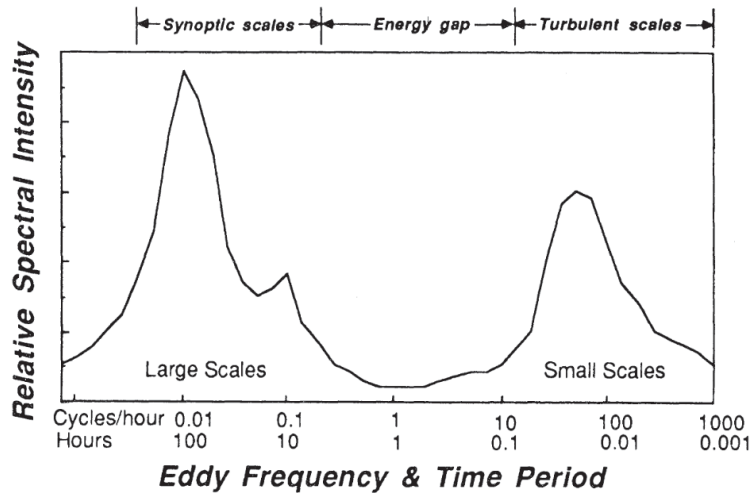
275 In the early 20th century, Ludwig Prandtl and co-workers set out the modern foundations for the dynamics of flow across surfaces and around obstacles (Prandtl and Tietjens 1957). Some of the most enduring insights of this work concern the layers of fluid next to surfaces. Prandtl and co-workers showed that, as a viscous fluid flows over a surface, the fluid elements closest to the solid boundary stick to it and therefore have no velocity, a phenomenon known as the ‘no-slip condition’. Flow continuity requirements prevent

280 sudden jumps in velocity. The no-slip condition therefore requires there to be a fluid region close to the surface within which the flow velocity increases from zero to the freestream velocity. This region is the boundary layer. As a first approximation, any flow over a surface can be split into two regions: the boundary layer, where the effects of the fluid's molecular viscosity cannot be ignored, and a region outside the boundary layer where the molecular viscosity is negligible.

285 The ABL is this concept applied to the air flowing over the surface of the Earth. For example, eddy viscosity is to the ABL as molecular viscosity is to Prandtl's boundary layer. The surface of the Earth is the lower boundary of the ABL. The ABL has no fixed upper boundary, and its depth varies in space and time from a few kilometres during sunny days near the equator, to a few tens of metres on a clear night with weak winds. The ABL is an application of what is known in English law as the 'elephant test'¹, which describes
290 phenomena that can be recognised easily from their basic features, but which are difficult to define rigorously. The ABL is the part of the troposphere that is directly influenced by the Earth's surface, and which responds to those forcings on timescales of around an hour or less (Stull 1988). The relevant surface forcings include friction, heat transfer, pollutant and volatile organic compound (VOC) emission, evapotranspiration, precipitation, and the dynamic effects of hilly terrain.

295 For most applications, the air in the free atmosphere can be treated as a collection of small parcels, which behave for a while as closed systems in the thermodynamic sense. Atmospheric motion in the free atmosphere is well approximated by resolving the forces acting on the parcels. In the ABL, however, the surface forcings generate turbulence that allow mass, momentum, and energy to be exchanged between air
300 parcels, and between the Earth's surface and the air. In the free atmosphere, kinetic energy is concentrated at periods of a day or more, a consequence of seasonal changes or large-scale disturbances. In the ABL, the kinetic energy spectrum displays an additional peak at small scales, over periods in the order of minutes or less (Figure 2.5). This additional peak is evidence of turbulence, which section 2.2 discusses further.

¹ See, for example, Stuart-Smith, LJ in *Cadogan Estates Ltd v Morris* [1998] EWCA Civ 1671



305 **Figure 2.5: Schematic spectrum of the wind speed in the ABL** (see section 2.1.3 for the basic properties of the ABL, and 2.2.5 for an introduction to atmospheric spectral analysis). Figure from Stull (1988), adapted from Van de Hoven (1957). This figure is on conceptual axes, but is derived from measurements in the inertial sublayer (ISL) (section 2.1.4).

2.1.4 Sublayers of the ABL

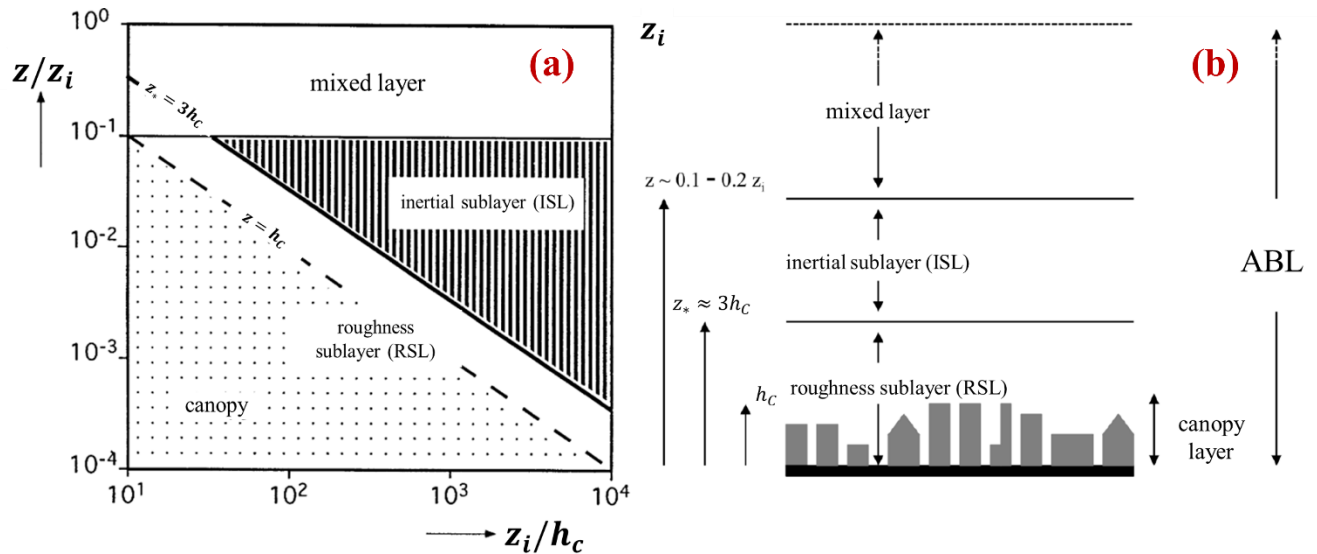
310 Observations and theory suggest the ABL can be separated into sublayers according to the dominant exchange characteristics of each sublayer (Figure 2.6). The ABL is sometimes divided into an *outer region* and an *inner region*. In the outer region, the flow is assumed to be independent of the surface obstacles and friction forces are neglected, for most applications. However, the outer region is complicated by the vertical thermal stability. During the day, the outer region consists of a *convective mixed layer* and, at night, a *nocturnal boundary layer*. There are transitions between the two forms each morning and evening.

315

The mixed layer, which is characterised by strong convection, develops during the daytime. The ABL height, z_i , marks the top of the mixed layer (Figure 2.6). The value of z_i generally increases throughout the day as the ABL entrains air from the overlying free atmosphere. The fluxes of momentum and scalar quantities generally decrease with height within the mixed layer. As its name implies, the nocturnal boundary layer forms at night. It is characterised by statically stable air which forms over the course of the night above the radiatively cooling surface. Turbulence is generally weak and intermittent when wind speeds are low. In some circumstances, short, intense bursts of turbulent mixing may occur in the nocturnal boundary layer as a result of microfronts near the ground, or jets of high velocity air aloft (Mahrt 2014,

320

325 2019).



330 **Figure 2.6:** Conceptual sublayers above large obstacles in the daytime ABL on (a) logarithmic and (b) linear scales. z_i denotes the depth of the ABL, h_c the mean height of the obstacles/canopy elements, and z_* denotes the blending height. (a) slightly modified from Rotach (1999) and (b) slightly modified from Roth (2000). The ISL and RSL together make up the atmospheric surface layer (ASL). Figure 5.1 presents a figure similar to (b) to show the daytime ABL above a forest.

In boundary-layer meteorology, the *atmospheric surface layer* (ASL) is analogous to the inner layer in wall boundary layers, where the effects of friction cannot be ignored. The Coriolis force is negligible in the ASL in comparison to the effects of friction and buoyancy. Above rough surfaces, such as forests and urban areas, the ASL can be further divided into the inertial sublayer (ISL) and the roughness sublayer (RSL) (Raupach et al. 1991). In the ISL, the turbulent fluxes of momentum and scalar quantities are approximately constant with height. The principal scaling length in the ISL is the height above the ground. The RSL extends from the ground up to around 1.5–5 times the mean height of the obstacles h_c , known as the blending height, z_* (Figure 2.6). The lowest part of the RSL, from the ground to $z = h_c$, is the canopy layer. In the canopy layer, the presence of the obstacles means that the flow dynamics are very different to those of the ISL (see 2.5.3 below). The value of h_c varies from tens of centimetres for crops, to a few metres in suburban neighbourhoods or young forests, up to tens or even a hundred metres for old-growth forests and business districts of cities. In general, the canopy layer and the RSL influence the surrounding flow more for larger values of h_c .

345 2.1.5 Scalar quantities in the ABL

Many applied problems in the ABL concern the properties of vectors, particularly the wind velocity. The most familiar example is that of operational weather forecasts, which usually try to predict average surface wind velocities at points in space and time. For many other applications, however, information on scalars is needed. In atmospheric applications, scalars refer to all the quantities in the air that can be described with a single number or physical quantity, i.e., they have a magnitude but not a direction, and can be advected on the flow. Ecologically important gaseous scalars in vegetated landscapes include water vapour, biogenic VOCs (BVOCs), carbon dioxide, signalling compounds, and oxidising agents such as hydroxyl (OH) and

ozone (O_3) (Larcher 1995; Monteith and Unsworth 2008). In urban areas, important scalar quantities include the air temperature and the concentration of pollutants. Air pollutants can be broadly classified as primary or secondary pollutants. Primary air pollutants are released directly into the atmosphere from emission sources which, in urban areas, usually means fuel combustion in vehicles and industry (Mayer 1999). Common gaseous primary pollutants include nitrogen oxides (NO_x), carbon monoxide, and VOCs. Secondary air pollutants are produced in the atmosphere when primary air pollutants undergo chemical reactions, such as photolysis or thermal decomposition (Jacobson 2005). Although chemical reaction times are often longer than the timescales of interest in this thesis—except for the oxidation of the most reactive biogenic VOCs (Chapter 6)—chemical transformations can be non-negligible when coherent flow structures increase the residence times of air near pollution sources (Dai et al. 2021).

Many ABL investigations, particularly in canopies, also concern the formation, transport, reaction, and destruction/deposition of particulate matter. In urban areas, these studies are usually motivated by questions of air quality. Particulate matter in urban areas is usually categorised by size into ‘fine particles’, particulate matter with an aerodynamic diameter less than $2.5\ \mu\text{m}$ ($PM_{2.5}$), and ‘inhalable coarse particles’, with aerodynamic diameters between 2.5 and $10\ \mu\text{m}$ (PM_{10}). Further categories include ‘large coarse’ particles, with aerodynamic diameters greater than $10\ \mu\text{m}$, and ultra-fine particles (UFPs), with aerodynamic diameters less than $0.1\ \mu\text{m}$. Most air-quality legislation around the world currently concerns $PM_{2.5}$ and PM_{10} , and particles in these categories are the most widely documented. Smaller particles ($PM_{2.5}$ and UFPs) are generally worse for human health because they are thought to be able to penetrate further into the respiratory system (Kim et al. 2015). However, the relationship between particulate matter and human and environmental health is not straightforward. Particulate matter is also important in the ecologies of forests and other vegetated landscapes. This matter includes abiotic particles—e.g., soil, dust, and particles encroaching from urban areas—and biotic particles, such as plant litter fragments, insect and animal detritus, and spores and pollen. Around forests, the oxidation of BVOCs can produce biogenic UFPs (Kulmala et al. 2001, 2007) in high number concentrations, which themselves can participate in chemical reactions, coagulate, or influence the weather by seeding clouds (Kulmala et al. 2001; Spracklen et al. 2008; Pierce et al. 2012; Rap et al. 2018). Bioaerosols are ecologically important in vegetated landscapes, but act as pollutants in urban areas.

Scalar quantities are often not easy to measure (see section 2.4.1 below regarding measurement difficulties in canopies) or even to model. The basic properties of scalar transport in turbulent flow are much less well understood than momentum transport (Shralman and Siggia 2000; Katul et al. 2013; Li and Bou-Zeid 2019). Further, different scalar quantities require different observational and modelling techniques. Many numerical investigations of scalar exchange and transport treat the quantities as approximately passive and massless, at least over the space and time scales of interest. This is the approach taken in Chapter 4 of this thesis. However, these assumptions are not appropriate for reactive chemical species, whose behaviour is quite well-documented in urban settings (Jacobson 2005; Zhong et al. 2015; Dai et al. 2021) but much less well understood for vegetation canopies. Chapter 5 discusses different ways to represent scalar quantities

in numerical models of forests, and Chapter 6 discusses some of the implications of air-parcel residence times on the probability of chemical species reacting within forests.

2.2 Turbulence in the ABL

395 2.2.1 Basic properties of turbulence in the ABL

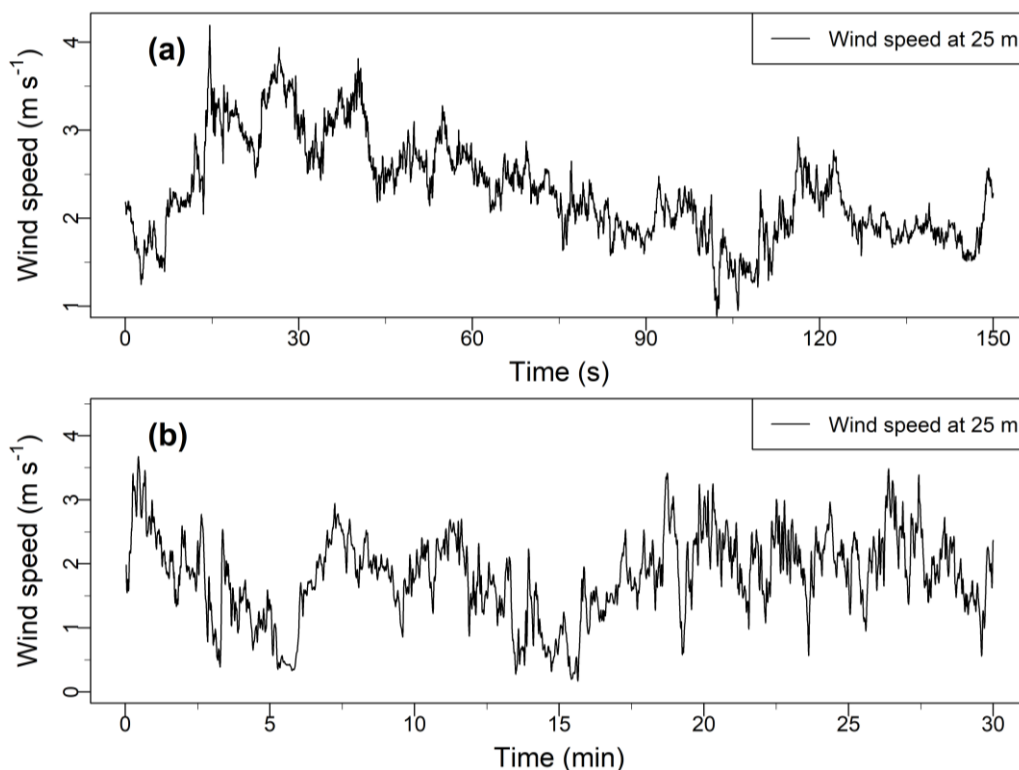
There is no single fixed definition of turbulence in fluid flow. We describe a flow as ‘turbulent’ when it is (i) comprised of three-dimensional eddies of various sizes; (ii) *chaotic*, in that small changes to the initial conditions result in large changes in the ensuing flow patterns; and (iii) *dispersive*, in that different parts of the fluid are mixed together. A criterion for the onset of turbulence in fluids is the dimensionless Reynolds number Re , which can be interpreted as the ratio of inertial to viscous forces, such that $Re = \mathbb{L}\mathbb{V}/\nu$, where 400 \mathbb{L} and \mathbb{V} are length and velocity scales that characterise the flow and ν is the kinematic molecular viscosity (in this case of the air). Flows with Re greater than a critical value of a few thousand are turbulent, provided the effect of thermal stratification is low. For air in the ABL, $\nu \approx 1.5 \times 10^{-5} \text{ m}^2 \text{ s}^{-1}$, $\mathbb{L} \approx 1\text{--}1000 \text{ m}$ and $\mathbb{V} \approx 0.1\text{--}10 \text{ m s}^{-1}$, which gives $Re \gg 10^4$. The air in the ABL is therefore nearly always turbulent, comprising a 405 cascade of rotating eddies of spatial scales 10^{-3} to 10^4 m that exchange mass, heat, and momentum between air parcels. In fact, the very presence of turbulence near the Earth’s surface is sometimes used to define the ABL’s boundaries.

We see evidence of this turbulence in high-resolution observations taken in the ABL. Take Figure 2.7, for 410 example, which shows the wind speed at $z = 25 \text{ m}$ at BIFoR FACE on an unremarkable day in August 2019. (See Chapters 3 and 6 for a description of BIFoR FACE.) A few important features can be identified.

1. The signal is very disorganised and appears to move unpredictably. Certain aspects of the signal are quite similar from moment to moment, but the finer details are completely different. It is not possible to predict the detailed behaviour of the signal from samples taken only seconds before. 415 This quasi-randomness distinguishes turbulence from other complex atmospheric motions, such as waves.
2. The signal shows structure across a range of scales, i.e., there appears to be a variety of timescales of flow variation superimposed on top of one another. For example, the smallest detectable variations in Figure 2.7a are about 0.05 s long. Looking at Figure 2.7b, we see that the time period 420 between each local peak in wind speed is about 5 minutes. Assuming each of these variations roughly corresponds with a different size turbulent eddy (see Taylor’s hypothesis below), we are seeing the signature of eddies ranging in diameter from about 0.1 m to about 600 m. In other words, we see evidence of the spectrum of turbulence. Notice that both the small (fast) changes and the longer timescale changes appear in no certain order. The diameters of eddies in the ABL more 425 generally range from $\mathcal{O}(10^{-3}\text{--}10^3) \text{ m}$. The largest eddies scale with the height of the ABL, z_i , and the smallest correspond to the smallest scales over which coherent motion occurs, before the kinetic energy is dissipated as heat.

430

3. Despite the complexity of the signal in Figure 2.7, we observe some constraints on the flow's behaviour, for example, that it varies over a limited range of speeds. In other words, the turbulent flow has a measurable and definable intensity that is visible in Figure 2.7 as the vertical spread of the wind speed. This is a clue that certain properties of turbulent flow are reproducible, even if the flow appears to behave randomly in its detailed behaviour. This reproducibility is rarely apparent from the signal and requires one to look at the flow's statistics.



435

Figure 2.7: Timeseries of the wind speed observed in the early afternoon of 27 Aug 2019 at BIFoR FACE. Measurements taken at $z = 25$ m. (a) Shows 2.5 minutes of 20Hz values. (b) Shows 30 minutes of 2-second rolling average values, calculated on 20 Hz observations. See Chapters 3 and 6 for details of the equipment setup at BIFoR FACE. These observations are taken at the interface between the canopy layer and the roughness sublayer (RSL) (section 2.1.4 and Figure 2.6).

440

2.2.2 The continuum assumption and Reynolds decomposition

A full knowledge of the movement and properties of individual molecules is not needed for most atmospheric applications, and the air can usually be treated as a continuum. This assumption is justified by the very low Knudsen number (Kn), which is the ratio of the mean free molecular path λ_m to the characteristic length scale of the turbulent motions \mathbb{L} . In the ABL, $Kn = \lambda_m/\mathbb{L} \ll 1$, usually in the order of 10^{-7} – 10^{-11} (the relevant turbulent length scales are in the order of 1–1000 m and the mean free path of air is approximately 10^{-7} – 10^{-8} m). This thesis adopts the meteorological convention of treating the atmosphere as a continuum.

445

450 Consider an instantaneous observation of an ABL flow variable α , for example, a velocity component or a scalar quantity. To account for the stochastic nature of the turbulent flow, we can consider this variable to be random. A complete description of the variable is given by its probability density function (PDF), $P(\alpha)$, where $P(\alpha)d\alpha$ is the probability that the variable takes a value between α and $\alpha + d\alpha$, such that

$$\int_{-\infty}^{\infty} P(\alpha)d\alpha = 1. \quad (2.2)$$

455 The PDFs are defined such that $P(\alpha) \geq 0$ and $P(-\infty) = P(\infty) = 0$. We can estimate the PDF of a flow by constructing a histogram of measurements of α at a specific location. The more times we repeat the measurements, the more closely the histogram will approximate the PDF. These repetitions may be formal repetitions—which is sometimes possible with laboratory experiments and numerical simulations—or approximate repetitions where measurements are taken at different points in space or time.

460 In the ABL, it is much easier to measure the flow at fixed points over time than to construct spatial grids of sensors or perform ensembles of experiments. The time average is therefore the most commonly used operation for ABL applications. All of the statistics in the following definitions refer to time averaged quantities, although they can be similarly defined with respect to averages in space or over ensembles (the set of all possible states of the given portion of atmosphere). For an instantaneous observation of a variable $\alpha(\mathbf{x}, t)$ at a location \mathbf{x} and time t , the time average (denoted with an overbar) is taken over an interval T_a so that

$$\bar{\alpha} = \frac{1}{T_a} \int_{t=0}^{T_a} \alpha(\mathbf{x}, t) dt. \quad (2.3)$$

470 This operation is equivalent to the definition of the mean, or expected value, of a random variable α with reference to its PDF,

$$\langle \alpha \rangle = \int_{-\infty}^{\infty} \alpha P(\alpha) d\alpha. \quad (2.4)$$

The averaging operation allows us to split an instantaneous observation into the resolved mean, which corresponds to large-scale motions, and the quasi-random turbulent perturbations, denoted with a prime

$$\alpha = \bar{\alpha} + \alpha'. \quad (2.5)$$

475 We can consider α' a ‘gust’ or turbulent fluctuation superimposed on the mean flow of air. This process of separating the expectation value (mean) of a quantity from its fluctuations is known as *Reynolds decomposition* (Reynolds 1895). By definition,

$$\overline{\alpha'} = 0 \text{ and } \overline{\bar{\alpha}} = \bar{\alpha}. \quad (2.6)$$

480 In Equation (2.3), the averaging period T_a should be much longer than the timescales of the turbulent fluctuations but short enough so that the mean is approximately stationary. Micrometeorological measurements typically use $T_a \approx 30\text{--}60$ min, which is justified by the ‘spectral gap’, a theoretical energetic

separation of the synoptic and turbulent scales of motion (Figure 2.5) (Stull 1988; Moncrieff et al. 2004). Shorter averaging periods ($T_a \approx 5\text{--}30$ min) are often used around obstacles such as forests and buildings in the canopy layer. Measurements at long-term flux sites suggest, under certain conditions, T_a values of a few hours are needed to capture large-scale motions in the flow, such as gravity waves or drainage flows in hilly terrain (Moncrieff et al. 2004). The optimal value of T_a depends on the properties of the measurement site, the observational height, and the purpose of the observations. The exact value of T_a is less important for short-term campaigns, provided general properties of the site's turbulence are considered. But the value of T_a should be chosen carefully for long-term campaigns, particularly when the observations are used to calculate the ecosystem exchange of an entire landscape (Finnigan et al. 2003; Baldocchi 2014).

Practical constraints require atmospheric scientists to perform the decomposition steps above using time averages rather than the mathematically convenient but experimentally unattainable ensemble average. We therefore make the 'ergodic' hypothesis that the time averages, for practical purposes, equal the ensemble averages. The ergodic hypothesis can be expressed as

$$\lim_{T_a \rightarrow \infty} \frac{1}{T_a} \int_{t=0}^{T_a} \alpha(t) dt \approx \int_{-\infty}^{\infty} \alpha P(\alpha) d\alpha, \quad (2.7)$$

or by saying that time and ensemble averages should approximately converge (Stull 1988). This assumption appears to hold for turbulence in laboratory fluids (Galanti and Tsinober 2004) but is less likely to hold in canopy sublayers, especially when the atmosphere is stable (Katul et al., 2004). Unfortunately, the violation of Equation (2.7) is very difficult to rectify in practice.

2.2.3 Common descriptive statistics

We can use Reynolds decomposition to consider other statistical moments by

$$\overline{\alpha'^n} = \frac{1}{T_a} \int_{t=0}^{T_a} \alpha'^n(t) dt, \quad (2.8)$$

where n is the 'order' of the moment. The variance is the second moment, with $n = 2$, and its square root is the standard deviation,

$$\sigma_\alpha = \sqrt{\overline{\alpha'^2}}. \quad (2.9)$$

The higher-order moments are usually presented in non-dimensional form. The third moment, with $n = 3$, is known as the skewness. The skewness is a measure of the asymmetry of a variable's PDF about its mean and is defined as

$$Sk_\alpha = \frac{\overline{\alpha'^3}}{\sigma_\alpha^3}. \quad (2.10)$$

The fourth moment is known as the kurtosis, which indicates the combined weight of the tails of a variable's PDF relative to the rest of the distribution. The kurtosis is defined as

$$Kt_\alpha = \frac{\overline{\alpha'^4}}{\sigma_\alpha^4}. \quad (2.11)$$

515 For normally distributed, real-valued random variables, $Sk_\alpha = 0$ and $Kt_\alpha = 3$, which are the values approximately found in isotropic Gaussian turbulence in fluids. For two variables α and β , where $\alpha \neq \beta$, the general mixed moment is

$$\overline{\alpha'^n \beta'^m} = \frac{1}{T_a} \int_{t=0}^{T_a} \alpha'^n(t) \beta'^m(t) dt, \quad (2.12)$$

520 where $n + m$ is the order of the moment. The most useful mixed moment for atmospheric applications is the covariance of the two variables, where $n = m = 1$. Although $\overline{\alpha'} = 0 = \overline{\beta'}$, the nonlinear product $\overline{\alpha' \beta'}$ is not necessarily zero and can be very important, e.g., in eddy-covariance measurements (Chapter 3). The correlation coefficient is the covariance scaled by the standard deviation of each variable

$$r_{\alpha\beta} = \frac{\overline{\alpha' \beta'}}{\sigma_\alpha \sigma_\beta} \quad (2.13)$$

The correlation coefficient $r_{\alpha\beta} = 1, -1$, and 0 , respectively, if α and β are perfectly positively correlated, perfectly negatively correlated, or perfectly uncorrelated.

525 2.2.4 Taylor's hypothesis

It is useful to know the scales of the motion in the ABL, including the size of the eddies. However, it is rarely possible to create a snapshot picture of the ABL using observations. Instead, we observe the flow at a small number of points in space over a long time, and try to infer spatial patterns from the timeseries. Taylor (1938) hypothesised that, for certain cases, turbulent flow may be considered to be 'frozen' as it moves past a sensor, i.e., the statistics of the turbulent flow are similar to what would be measured if the turbulent field did not evolve while travelling on the mean flow. In those cases, the total wind magnitude (speed) can be used to estimate the size of eddies from timeseries of turbulence measurements. Let V denote the wind speed such that $V^2 = u^2 + v^2 + w^2$. The eddy diameter λ_e can be estimated as $\lambda_e = V\mathbb{P}$, where \mathbb{P} is the time period over which the eddy passes a sensor. A rough estimate of \mathbb{P} can sometimes be obtained 535 by observing the period between regular peaks in timeseries. For any variable α , Taylor's hypothesis states that turbulence is frozen when $d\alpha/dt = 0$. Taylor's hypothesis can also be expressed in terms of a wavenumber κ_n and cyclic frequency f such that

$$f = \kappa_n V, \quad (2.14)$$

540 where $\kappa_n = 2\pi/\lambda_w$ and $f = 2\pi/\mathbb{P}_w$, for wavelength λ_w and wave period \mathbb{P}_w . Taylor's hypothesis is most valid for situations where the time taken for the eddy to advect past a sensor is shorter than the timescale over which the turbulence evolves. In the ASL, this is most likely to be true when considering eddies with

diameters larger than the measurement height (Higgins et al. 2012). As a first approximation, Taylor’s hypothesis is reasonable for situations where $\sigma_V \ll V/2$, where σ_V is the standard deviation of the wind speed, using Equation (2.9) (Garde 2010). Taylor’s hypothesis is widely used for scaling arguments in boundary-layer meteorology, including in this thesis.

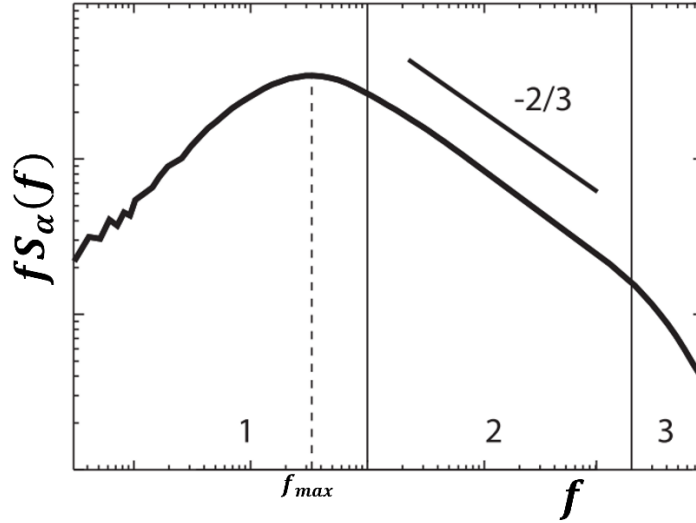
2.2.5 Turbulence spectra in the ABL

Spectral techniques can be used to estimate how much a certain frequency band contributes to the total energy of a turbulent flow. This thesis does not lean heavily on spectral arguments. However, I used spectra to test the BIFoR FACE measurements. Spectral arguments are also important throughout boundary-layer meteorology, and it is helpful to introduce their basic principles. If Taylor’s hypothesis is assumed to be approximately true, this information can be used to infer information regarding the size and structure of the flow’s eddies from temporal measurements at single locations. The fundamental tool in spectral analysis is the Fourier transform, which transforms timeseries or ensemble measurements to the frequency domain (and vice versa). During this transformation, the physical reference—the time or space dependency of the signal—is lost. However, one gains statistical information on the relative contributions of the different frequency bands, which can be associated with different eddy sizes.

For some quantity α , which could be velocity component or a scalar quantity, we have

$$\int_0^\infty F_\alpha(\kappa_n) d\kappa_n = \sigma_\alpha^2 = \int_0^\infty S_\alpha(f) df, \quad (2.15)$$

where F_α is the Fourier transform of α , and $S_\alpha(f)$ the power spectral density of α (Kaimal and Finnigan 1994). The frequency of the peak in $S_\alpha(f)$ provides an inverse timescale for the most energetic eddies. Equation (2.14) translates between the wavenumber and frequency (assuming Taylor’s hypothesis). In practice, Equation (2.15) is calculated on observations using discrete Fourier transform algorithms, such as fast Fourier transforms. For meteorological applications, the frequency weighted version of the power spectral density, $fS_\alpha(f)$, is usually plotted against f in log-log coordinates (see Figure 2.8). Plotting $fS_\alpha(f)$ allows easier scaling than using $S_\alpha(f)$, because $fS_\alpha(f)$ has the same units as the variance σ_α^2 (e.g., $\text{m}^2 \text{s}^{-2}$ for a velocity), and also emphasises the peak frequency, which can be difficult to determine in plots of $S_\alpha(f)$ against f . The area under the curve is not proportional to σ_α^2 when $S_\alpha(f)$ or $fS_\alpha(f)$ are plotted in log-log coordinates.



570

Figure 2.8: Schematic spectra of a velocity component or turbulence kinetic energy in isotropic turbulence. f_{max} denotes the peak frequency. The numbered regions refer to the (1) energy containing range, (2) inertial subrange, and (3) dissipation subrange (section 2.2.5). Figure adapted from Christen (2005).

The spectra of atmospheric velocity components, or of the turbulence kinetic energy (see definition below), display three major regions, numbered in Figure 2.8:

575

1. The *energy-containing range*, where kinetic energy is produced by buoyancy and shear in the flow. This region contains the bulk of the turbulent energy.
2. The *inertial subrange*, where kinetic energy is neither produced nor dissipated, but transferred from large eddies to progressively smaller eddies.
3. The *dissipation range*, where the kinetic energy of the air is dissipated to heat.

580

Together these steps comprise the energy cascade of turbulent flow. The energy-containing and dissipation ranges have characteristic length scales. The length scale of the energy-containing range is the Eulerian integral length scale Λ_α

585

$$\Lambda_\alpha = V \int_0^\infty R_{\alpha\alpha}(\zeta) d\zeta, \quad (2.16)$$

where $R_{\alpha\alpha}$ is the autocorrelation function for α (e.g., where α is the velocity component u), and ζ is some lag with respect to time t . The value of Λ_u ranges from around 10–500 m. The length scale of the dissipation range is the Kolmogorov microscale, η_m , such that

$$\eta_m = \left(\frac{\nu^3}{\epsilon} \right)^{\frac{1}{4}}, \quad (2.17)$$

590

where ν is the kinematic viscosity of air and ϵ is the rate of dissipation of turbulence kinetic energy. In the ABL, $\eta_m \sim \mathcal{O}(10^{-3})$ m.

Kolmogorov's theory of high- Re flow states that, if there is a large enough separation between Λ_α and η_m , then an inertial subrange will exist (region 2 in Figure 2.8). Here, the spectrum of u becomes

$$S_u(f) = k_1 \epsilon^{2/3} f^{-5/3}, \quad (2.18)$$

where k_1 is the Kolmogorov constant, whose value is estimated 0.5–0.6 (Batchelor 1953; Kolmogorov 1991). Equation (2.18) gives the well-known $-5/3$ power law for the inertial subrange (Figure 2.8 displays a slope of $-2/3$, because $fS_u(f)$ is plotted on the y -axis). Kolmogorov's theory is actually formulated in terms of wavenumbers. To obtain Equation (2.18), we assume Taylor's hypothesis can be used to convert
600 between wavenumber and frequency space. This is often not a sound assumption in the high turbulence intensities of canopy flow. However, Taylor's hypothesis is a helpful conceptual assumption, because it also allows Equation (2.18) to be couched more intuitively: within the inertial subrange, the kinetic energy (KE) of the eddies is proportional to a power law of their diameters λ_e

$$KE \propto \lambda_e^{5/3}. \quad (2.19)$$

605 2.3 Turbulent flow equations

2.3.1 Conservation equations

The Navier–Stokes equations express the conservation of mass, momentum, and energy for a viscous fluid, such as the air (i.e., the continuity equation, Newton's Second Law, and the First Law of Thermodynamics, respectively). For applications in the ABL, the Navier–Stokes equations can be simplified slightly from
610 their most mathematically complete form (Foken 2008). For turbulent motions smaller than the mesoscale, the air is approximately incompressible, so that the continuity equation

$$\frac{\partial \rho}{\partial t} + \frac{\partial(\rho u_j)}{\partial x_j} = 0 \quad (2.20a)$$

simplifies to

$$\frac{\partial u_j}{\partial x_j} \approx 0. \quad (2.20b)$$

615 The momentum equations can also be simplified by ignoring the Coriolis forces and assuming the Boussinesq approximation, i.e., neglecting the differences in the air's density ρ except where they appear in terms multiplied by the acceleration due to gravity, g . These assumptions give

$$\frac{\partial u_i}{\partial t} + u_j \frac{\partial u_i}{\partial x_j} = g \delta_{i3} - \frac{1}{\bar{\rho}} \frac{\partial p}{\partial x_i} + \nu \frac{\partial^2 u_i}{\partial x_j^2}, \quad (2.21)$$

where δ_{i3} is the Kronecker delta, which assumes gravity acts only vertically, because $\delta_{i3} = 1$ when $i = 3$, and is zero otherwise (Stull 1988). Similarly, for the mass concentration of a scalar quantity ϕ , the conservation of mass requires

$$\frac{\partial \phi}{\partial t} + U_j \frac{\partial \phi}{\partial x_j} = \nu_\phi \frac{\partial^2 \phi}{\partial x_j^2} + S_\phi, \quad (2.22)$$

where ν_ϕ is the molecular diffusivity of ϕ , and S_ϕ is the source/sink term for the processes not already in the equation, such as chemical reactions or deposition.

625

The deterministic momentum equations in Equation (2.21) do not sit comfortably with the randomness that can be observed in turbulent flow, e.g., in the timeseries in Figure 2.7. How can randomness arise in the apparently deterministic context? The most truthful answer is that we do not know for sure. It has not yet been rigorously proven whether or not well-behaved solutions to the Navier–Stokes equations always exist

630

in three dimensions in high- Re flow. Some fundamental properties of turbulent flow remain unresolved (Tao 2008). The details of these issues lie (way) outside of the scope of this thesis. But there are more practical considerations, relevant to the task of interpreting observations and making predictions in the ABL. The Navier–Stokes equations are nonlinear, second-order, partial differential equations. These features make them notoriously difficult to solve exactly, even using modern high-performance computers.

635

Resolving each individual eddy to the size of the Kolmogorov microscale would require an enormous number of numerical cells, $\sim \mathcal{O}(Re^9)$. The equations are acutely sensitive to perturbations in that small differences in their initial conditions cause the equations to evolve very differently through time. The sensitivity to perturbations imposes limits on the predictability of the atmosphere (Lorenz 1963), with important consequences for weather forecasts (Orrell et al. 2001). Small perturbations, including

640

observational errors, are unavoidable in practice because we can never measure a flow completely, and to perfect accuracy and precision. These perturbations mean the detailed behaviour of atmospheric timeseries is indistinguishable from randomness, even if the Navier–Stokes equations are eventually proven to be entirely deterministic.

2.3.2 Statistical approaches to the conservation equations

645

The difficulties in obtaining exact solutions to the Navier–Stokes equations force us to retreat to statistical approaches. Reynolds decomposition can be applied to the conservation equations of mass, momentum, and scalar quantities to generate forecast equations for the mean flow (see Kaimal and Finnigan (1994) and Stull (1988) for derivations and detailed discussion). For example, applying this process to the momentum equations in Equation (2.21) separates the variables into their mean and turbulent parts. After some algebra,

650

this process gives the following equation for the mean flow

$$\frac{\partial \bar{u}_i}{\partial t} + \bar{u}_j \frac{\partial \bar{u}_i}{\partial x_j} = \delta_{i3} g - \frac{1}{\bar{\rho}} \frac{\partial \bar{p}}{\partial x_i} + \nu \frac{\partial^2 \bar{u}_i}{\partial x_j^2} - \frac{\partial \overline{u'_i u'_j}}{\partial x_j}. \quad (2.23)$$

From left to right, the terms in Equation (2.23) represent the storage of momentum (inertia), advection of momentum, vertical gravitational acceleration, pressure gradient forces, viscous stress on the mean motions, and the Reynolds stress (i.e., the divergence of turbulent momentum flux). A similar process can

655

be applied to the conservation equations of a scalar quantity ϕ to give

$$\frac{\partial \bar{\phi}}{\partial t} + \bar{u}_j \frac{\partial \bar{\phi}}{\partial x_j} = \nu_\phi \frac{\partial^2 \bar{\phi}}{\partial x_j^2} + S_\phi - \frac{\partial \overline{u'_j \phi'}}{\partial x_j}. \quad (2.24)$$

The usual definition of the kinetic energy is $KE = 0.5mV^2$, where m is the mass. For fluids such as air, it is usually preferable to consider the kinetic energy per unit mass, $KE/m = 0.5V^2$. Recalling $V^2 = (u^2 + v^2 + w^2)$, Reynolds decomposition allows the kinetic energy per unit mass to be separated into its mean, with a turbulent component superimposed on top (Stull 1988)

$$KE/m = 0.5(u^2 + v^2 + w^2) = 0.5[(\bar{u} + u')^2 + (\bar{v} + v')^2 + (\bar{w} + w')^2], \quad (2.25a)$$

from which one can extract a portion of the kinetic energy associated the mean flow, i.e., the mean kinetic energy (MKE)

$$MKE/m = 0.5(\bar{u}^2 + \bar{v}^2 + \bar{w}^2) \quad (2.25b)$$

and an instantaneous turbulence kinetic energy per unit mass, e_m

$$e_m = 0.5(u'^2 + v'^2 + w'^2). \quad (2.25c)$$

The value of e_m varies rapidly with time. To find a variable that is more representative of the overall flow, we can define a mean turbulence kinetic energy per unit mass (TKE) by averaging the instantaneous values of e_m

$$TKE = 0.5(\overline{u'^2} + \overline{v'^2} + \overline{w'^2}) = 0.5\overline{u'_i u'_i}. \quad (2.26)$$

Equations (2.25b) and (2.26) can also be obtained by Reynolds averaging Equation (2.26a) directly, for which the average of the product terms equal zero, e.g., $\overline{\bar{u} u'} = \bar{u} \cdot \bar{u}' = \bar{u} \cdot 0 = 0$.

2.3.3 The closure problem

The main difference between Equations (2.21) and (2.23) is the appearance of the product of fluctuations term, $\overline{u'_i u'_j}$, which is associated with the non-linearity of the Navier–Stokes equations. This term looks innocuous but is actually symptomatic of a serious problem in that it cannot be expressed as a function of \bar{u}_i without introducing further assumptions about the flow. Equation (2.23), for \bar{u}_i , is actually a set of three equations, one for each spatial direction. However, $\overline{u'_i u'_j}$ comprises six unknowns, the unique components of the velocity covariance tensor \mathbf{M}_{ij}

$$\mathbf{M}_{ij} = \overline{u'_i u'_j} = \begin{pmatrix} \overline{u' u'} & \overline{u' v'} & \overline{u' w'} \\ \overline{u' v'} & \overline{v' v'} & \overline{v' w'} \\ \overline{u' w'} & \overline{v' w'} & \overline{w' w'} \end{pmatrix}. \quad (2.27)$$

Deriving equations similar to Equation (2.23) to solve for $\overline{u'_i u'_j}$ only compounds the problem, because triple correlations (third moments) $\overline{u'_i u'_j u'_k}$ are introduced. Instead of three equations and six unknowns, we have six equations with ten unknowns. This pattern continues as one attempts to resolve the increasingly higher order moments. In other words, the number of unknowns in the equations for turbulent flow is always larger

685 than the number of equations (Stull 1988). This is the *closure problem* of turbulent flow: a complete statistical description of turbulence is not possible using a finite number of equations (Orszag 1970).

2.3.4 RANS closure schemes

690 Researchers have developed a variety of turbulence closure schemes to navigate this issue. Some of these schemes use scaling arguments to simplify the equations before solving them analytically (e.g., Finnigan and Belcher, 2004). Many applied problems, however, do not yield easily to analytical solutions. Instead, researchers use physical models in flumes and wind tunnels, or numerical methods under broad umbrella of computational fluid dynamics (CFD), where computers are used to find approximate solutions to the equations of motion. The most widely applied CFD turbulence closure schemes deal directly with the Reynolds-averaged Navier–Stokes (RANS) equations, such as Equations (2.23) and (2.24). RANS closure methods are quite varied in their details. But they share a common basic principle in that the turbulent flow is expressed using a small number of equations, with the unknowns expressed as approximate functions of the known quantities. The simplest RANS method is known as ‘K-theory’ or ‘gradient transport theory’, among other names. K-theory is a first-order closure scheme that assumes the Reynolds stress/product of fluctuations term in the RANS equations is related to the gradient in the mean flow. For some quantity α , 700 which may be a velocity component or a scalar quantity, K-theory approximates the stress term as

$$\overline{u'_i \alpha'} = -K_\alpha \frac{\partial \bar{\alpha}}{\partial x_i} \quad (2.28)$$

where K_α is usually called the ‘eddy viscosity’ when α is a velocity component or the ‘eddy diffusivity’ when it is a scalar (Stull 1988; Foken 2008). At the crudest level, K_α is assumed to be a constant, although various other approximations have been proposed, most notably those based on Prandtl’s mixing-length model (e.g., Harman and Finnigan, 2007; Stull, 1988). This model assumes a fluid parcel conserves its properties over some characteristic length scale, ℓ_m , before it is mixed with the surrounding fluid (Obermeier 2006). The mixing length model is most commonly applied in simple (horizontally homogeneous and statistically steady) shear flows, where the turbulent shear stress $\overline{u'w'}$ and the mean horizontal shear $\partial \bar{u} / \partial z$ are related through 705

$$-\overline{u'w'} = -K_\alpha \frac{\partial \bar{u}}{\partial z} = -\ell_m^2 \left| \frac{\partial \bar{u}}{\partial z} \right| \frac{\partial \bar{u}}{\partial z}, \quad (2.29)$$

which gives

$$K_\alpha = \ell_m^2 \left| \frac{\partial \bar{u}}{\partial z} \right|. \quad (2.30)$$

715 In neutral atmospheric conditions away from obstacles, $\ell_m \approx \kappa(z - d)$, where $\kappa \approx 0.4$ is the von Kármán constant, and d is the displacement height (see section 2.5.2 below).

Other popular RANS schemes include ‘1.5–order’ closure based on the transport of the turbulence kinetic energy and its (specific) rate of dissipation, often denoted ‘ $k-\epsilon$ closure’ (Katul et al. 2004). Variants of

720 $k-\epsilon$ closure have been widely applied in numerical simulations of urban micrometeorology and pollutant transport (Wang and McNamara 2006; Toparlak et al. 2017). Researchers have also developed second-order (and higher) RANS closure schemes, which involve approximating the triple (and higher) covariance terms in the RANS equations (Katul et al. 2004; Shirzadi et al. 2020). For many applied problems in land-atmosphere exchange, RANS closure schemes above the second order provide little practical benefit over second-order schemes (Juang et al. 2008).

725 **2.3.5 Large-eddy simulation and direct numerical simulation**

Large-eddy simulation (LES) is another popular CFD technique. LES emerged from early work in NWP through the efforts of Smagorinsky, Deardorff, Killy, and colleagues (Killy 1962; Smagorinsky 1963; Deardorff 1970). The basic idea of LES is that the equations of motion are filtered, reducing or removing the high-frequency signal (the smaller times and space scales) and retaining the low-frequency signal (the larger time and space scales). This is achieved by applying a low-pass filter of kernel G to the flow field variables,

$$\tilde{\phi}(\mathbf{x}) = \int_{-\infty}^{\infty} G(\mathbf{x} - \mathbf{y})\phi(\mathbf{y})d\mathbf{y}, \quad (2.31)$$

735 where the overtilde denotes ‘resolved’ field variables, corresponding to larger scales of motion (e.g., Deardorff, 1970; Nottrott et al., 2014). Motions larger than the filter width Δ_f are resolved directly using numerical integration schemes. The filter width Δ_f is greater than or equal to the grid resolution Δ_g , with ratios $\Delta_f/\Delta_g = 1$ or 2 common in practice (Geurts 2003; Basu and Porté-Agel 2006). The filtered equivalent of the RANS momentum equations in (2.23), ignoring buoyancy effects, are

$$\frac{\partial \tilde{u}_i}{\partial t} + \tilde{u}_j \frac{\partial \tilde{u}_i}{\partial x_j} = -\frac{1}{\rho} \frac{\partial \tilde{p}}{\partial x_i} - \frac{\partial \tau_{ij}}{\partial x_j} + \tilde{D}_i, \quad (2.32)$$

740 where \tilde{D}_i accounts for forcings such as the geostrophic wind, an imposed pressure gradient, or distributed drag from obstacles smaller than the filter width, Δ_f (e.g., Nottrott et al., 2014). The sub-grid scale (SGS) stress term τ_{ij} accounts for the unresolved scales, those below Δ_f ,

$$\tau_{ij} = \tilde{u}_i \tilde{u}_j - \tilde{u}_i \tilde{u}_j. \quad (2.33)$$

745 A variety of schemes have been developed to approximate the SGS stresses and fluxes (see Chapters 4 and 5 for examples). Using LES, the statistics of the flow variables are calculated by averaging the resolved quantities in time and space. The turbulent perturbations are taken as the departures from those averages (again, see Chapters 4 and 5 for examples).

750 Direct numerical simulation (DNS) involves solving the Navier–Stokes equations without any turbulence model. The Navier–Stokes equations are discretised and then solved in space and time (Coleman and Sandberg 2010). The strength of DNS compared with LES and RANS is that it resolves all the spatial and temporal scales of the turbulence, from the Kolmogorov scale η_m to the integral scale Λ_α . DNS therefore

provides complete knowledge of all points within the flow, at all times within the simulation period, without approximation errors. DNS is an excellent tool for investigating the fundamental properties of turbulent flow in simplified settings, e.g., for identifying turbulence structures around idealised rigid obstacles (Coceal et al. 2007; Blunn et al. 2022). The main drawback of DNS is its extreme computational expense, which heavily constrains the Reynolds number of the flow that can be simulated. As an illustration, the total operation count for DNS simulations scales with $\mathcal{O}\left(Re^3 \left(\frac{3}{4} \log(Re)\right)^3\right)$ (Coleman and Sandberg 2010). Increasing the Reynolds number from $Re \approx 6000$ (Coceal et al. 2007; Sharma and García-Mayoral 2020a) to a more realistic ABL value of $Re \sim \mathcal{O}(10^7)$ would require more than 32 billion times the already extensive computational resources. Further, DNS of real landscapes, particularly those with flexible bodies such as trees and other plants, would require unfeasibly fine-scale structural and biomechanical information. DNS is therefore not yet a viable method for most applied problems in the ABL, particularly at the scale of ecosystems or neighbourhoods.

2.3.6 Application of LES in this thesis

The suitability of each closure scheme depends on the problem under investigation. K-theory is conceptually simple and numerically efficient, and it is therefore widely applied in air-pollution (Nguyen 2014) and ecosystem-exchange models (Ashworth et al. 2015; Banerjee et al. 2017). However, around canopies of obstacles, such as in forests and urban areas, K-theory is fundamentally flawed. Here the turbulent fluxes do not necessarily correspond to the mean gradients (Finnigan 2000; Monteith and Unsworth 2008) and K-theory does not account for transfer by large, coherent turbulent structures (Banerjee et al. 2017). In complex landscapes, especially those with canopies of vegetation or buildings, K-theory is a useful approximation only under a limited range of circumstances, which sections 5.6.1 and 6.3.6 discuss in more detail (Finnigan et al. 2015).

Most numerical studies of turbulent exchange in canopies use either RANS or LES. LES is inherently superior to RANS in that it resolves more of the flow for a given domain and set of boundary conditions. However, RANS remains a popular and useful method, especially for engineering applications and investigations of urban microclimates. The physics of certain problems, such as channelled winds (Blocken 2018), do not justify the additional complexity of LES. RANS is also much less computationally demanding than LES, meaning larger domains can be simulated, and commercial software packages using RANS have a more established user base. Although out of the scope of this thesis, researchers have formulated various hybrid RANS–LES schemes, particularly for urban applications. Hybrid RANS–LES methods try to balance computational expense and accuracy by only using LES in the regions of the flow which are challenging to RANS models, with RANS closure used elsewhere (Ashton et al. 2016; Letzgus et al. 2018; Wang et al. 2019).

This thesis uses LES, for two main reasons. First, the spatial scale of focus—up to a kilometre or two—is small enough for LES to be viable. Second, the focus of this work is turbulent exchange in and around

790 canopies in the ABL, which LES resolves better than RANS because of its ability to capture unsteady and
intermittent fluctuations of the flow field (e.g., Salim, Buccolieri, et al., 2011; Salim, Cheah, et al., 2011;
Tominaga and Stathopoulos, 2013; Zheng et al., 2020 and references therein).

2.4 Flow through canopies in the ABL

2.4.1 Description of the flow in canopies of obstacles

795 The Earth's surface is covered by obstacles, such as forests and buildings over land, and waves on the
ocean. For some applications, particularly at large space and time scales, it is not possible, and sometimes
not necessary, to consider the effect of the obstacles on the flow or the exchange of momentum, mass, and
energy. However, in many situations, it is important to understand what is happening around and between
the obstacles, for example, when measuring the air quality of a city, the spread of airborne pathogens
through crops, or the exchange of CO₂ between forests and the atmosphere.

800 When the obstacles are large—such as with buildings and infrastructure, forests, and crops—and relatively
densely packed, they begin to behave as *canopies* in that they impart a collective effect on the flow, but air
is also able to move beneath and between the obstacles. This creates the canopy layer in Figure 2.6.
Researchers have proposed various thresholds to define when the flow over obstacles transitions from
805 wakes around individual elements to collective canopy flow (e.g., see discussion in Brunet, 2020; Monteith
and Unsworth, 2008; Oke, 1978). These transitions occur at quite low densities, smaller than those in most
forests, crops, and urban areas. The urban areas and vegetated landscapes discussed in this thesis all impart
a collective canopy effect on the flow.

810 In situ observations are usually among the most important tools in any ABL investigation. However, it is
not easy to measure the properties of the air in the canopy layer. A major difficulty comes in obtaining
spatially representative measurements using a realistic number of sensors (Christen 2005; Finnigan 2008;
Finnigan and Shaw 2008). For example, in a forest or a city, where does one place sonic anemometers to
measure the wind velocity? If the sensors are placed in clearings or gaps, one may obtain a relatively clean
815 timeseries, but it will show the velocity to be higher than the true volume average (Muller et al. 2013a).
Placing the sensors in gaps also discounts the behaviour of the flow at surfaces, where many important
scalar exchange processes occur. However, there is usually little alternative, because measurements of
turbulent flow taken very close to surfaces are often very difficult to interpret, at least as regards inferring
the properties of the ecosystem-scale flow (e.g., it may be possible to detect wake-scale structures, but not
820 a local mean wind speed and direction).

Physical models in wind tunnels and flumes can help navigate some of these difficulties (a detailed
discussion of the methodology of physical modelling is outside the scope of this thesis). Physical models
are particularly useful for investigating the flow velocity and momentum transport, and are an indispensable
825 tools in engineering applications (e.g., Baker, 2007) and scientific research (Poggi et al. 2004b; Poëtte et

al. 2017; Lemone et al. 2019). Physical models do not solve all measurement difficulties, however. Scalar exchange processes of interest must be incorporated into the physical model. This is feasible for some processes such as pollutant dispersion and heat transport in urban areas (Ahmad et al. 2005; Heist et al. 2009; Cui et al. 2016), but more difficult for forests, for which scalar exchange processes are more spatially
830 diverse than in urban areas. Scale physical models take time to set up and adjust, particularly for complex landscapes such as real urban areas (as opposed to idealised arrays of cubes (Cheng and Castro 2002)) or vegetated terrain. Wind-tunnel scale models of forests also require higher Re values than investigations of bluff bodies (Gromke 2018).

835 CFD models offer researchers an additional tool to investigate canopy flow, alongside field observations, physical models, and theory. In some situations, it is possible to represent canopies at the neighbourhood/ecosystem scale by directly resolving the canopy obstacles, using CFD to simulate the flow around them, including the exchange of scalar quantities. This approach is sometimes feasible for urban areas, particularly those made up of buildings but few other obstacles, such as trees and shrubs, signage,
840 and small infrastructure elements. Chapter 4 discusses the strengths and weaknesses of using this resolved-building approach. For forests and other vegetation canopies, resolving the obstacles directly is much more difficult. Because trees and crops are smaller than buildings, very high grid resolutions are needed to sufficiently resolve each element. This severely constrains the size of the domains that can be simulated to well below the ecosystem scale, even using high-performance computing resources. In addition, directly
845 resolving flexible, fine-scale plant elements requires one either to specify artificially the elements as a bluff body, or to try to formulate the elements' porosity or biomechanics, which is not at all easy (De Langre 2008, 2019; Spatz and Theckes 2013). Chapter 5 discusses these difficulties in more detail.

2.4.2 The porous media model of canopy flow

An alternative approach at the neighbourhood/ecosystem scale is to represent the canopy layer as porous
850 media, through which the air can move, rather than attempting to resolve the individual obstacles explicitly. An overview of the porous-media model is presented here, with further detail in Chapters 4 and 5. In particular, Chapter 4 discusses in detail the applicability of the porous-media model to inhomogeneous urban areas. Chapter 5 then synthesises and discusses the application of the model to vegetation canopies, particularly to real-world forests.

855 The porous-media model is formalised by averaging the momentum and transport equations in time, as for the RANS equations, and over a volume (Raupach and Shaw 1982; Howes and Whitaker 1985; Finnigan 2000; Lien et al. 2004; Finnigan and Shaw 2008). The averaging volume is taken to be large enough in the horizontal to include a number of canopy obstacles, but not so large as to smooth out spatial variation in
860 the morphology or density of the obstacles. The volume is assumed to be thin in the vertical to properly resolve the gradients in the flow variables, which can be steep in the canopy layer (Kruijt et al. 2000; Monteith and Unsworth 2008). Under the two operations of space and time averages, the prognostic flow variables have three components, e.g., for the streamwise velocity u these are

$$u = U + u'' + u', \quad (2.34)$$

865 where $U = \langle \bar{u} \rangle$ denotes the space (angled brackets) and time (overbar) averaged velocity, $u'' = \bar{u} - U$ is the spatial variation of the time-averaged flow around the obstacles, and $u' = u - U - u''$ is the turbulent fluctuation (Finnigan and Shaw 2008). The double-averaged equivalent of the RANS momentum equations above (ignoring buoyancy effects and momentum transfer from viscosity) are

$$\frac{\partial U_i}{\partial t} + U_j \frac{\partial U_i}{\partial x_j} = -\frac{\partial P}{\partial x_i} - \frac{\partial \langle \bar{u}'_i \bar{u}'_j \rangle}{\partial x_j} - \frac{\langle \bar{u}''_i \bar{u}''_j \rangle}{\partial x_j} + f_i, \quad (2.35)$$

870 where the capital letters denote the double-averaged quantities (P is the kinematic pressure) and f_i is a forcing term that accounts for the aerodynamic drag from the canopy of obstacles (Finnigan 2000; Coceal and Belcher 2004; Patton and Finnigan 2012). Analogous equations can be obtained by double averaging the scalar transport equations. The term $\langle \bar{u}''_i \bar{u}''_j \rangle$ on the right-hand side of Equation (2.35) is the dispersive flux of mean momentum, which accounts for spatial correlations in the time-averaged velocity field.
 875 Dispersive fluxes are very difficult to measure using field observations (Patton and Finnigan 2012) and not easy even using physical models (Poggi et al. 2004a; Poggi and Katul 2008a). Dispersive fluxes are often quite small in homogeneous canopies (Poggi et al. 2004a; Patton and Finnigan 2012) and most studies do not include them in the budgets of momentum and scalar transport. However, recent evidence shows the dispersive fluxes can be quite large in heterogeneous canopies (Boudreault et al. 2017; Li and Bou-Zeid
 880 2019; Blunn et al. 2022), i.e., most canopies in the real world. Chapter 5 discusses this point further in the context of forests and other vegetation canopies.

2.4.3 Approximating the aerodynamic drag term f_i

The aerodynamic drag term f_i in Equation (2.35) accounts for the transfer of momentum from the flow to the canopy obstacles, such as the trees, plants, or buildings. The transfer of momentum results from two
 885 mechanisms. The first is viscous drag, which is generated in the thin viscous boundary layers which form near solid surfaces when the flow is brought to rest at the surface by the no-slip condition. The second is pressure or ‘form’ drag, which results from the pressure differences that develop around the canopy obstacles. That is,

$$f_i = -\left\langle \frac{\partial \bar{p}''}{\partial x_i} \right\rangle + \nu \left\langle \frac{\partial^2 \bar{u}''_i}{\partial x_j \partial x_j} \right\rangle. \quad (2.36)$$

890 The most common parametrisation of the drag force f_i is obtained by spatially averaging the localised drag from the individual canopy obstacles, assuming the drag force is proportional to the square of the flow speed, as is the case around bluff bodies. The viscous component of the drag is assumed negligible because the total aerodynamic drag f_i is dominated by form drag in high- Re flow (Coceal and Belcher 2004; Hamlyn and Britter 2005; Cheng et al. 2007; Patton and Finnigan 2012).

895 For the form-drag term, consider an array of obstacles distributed over a total plan area A_t , where each obstacle has mean height h_c , frontal area A_f and a drag coefficient $C_d(z)$ (Belcher et al. 2003; Coceal and Belcher 2004). The drag force over a thin layer dz of each element at height z is

$$\rho U^2(z) C_d(z) A_f \frac{dz}{h_c}. \quad (2.37)$$

900 The thin averaging volume at height z is $A_t dz$. The total force per unit volume (including both the solid and fluid elements) is, therefore,

$$\rho f_i = \rho \frac{C_d(z) \Sigma A_f}{h_c A_t} (\langle u_j \rangle \langle u_j \rangle)^{\frac{1}{2}} \langle u_i \rangle. \quad (2.38)$$

This amalgamates the spatially discontinuous drag force from each obstacle into a continuous resistive body force throughout the canopy layer (Belcher et al. 2003). In Equation (2.38), $C_d(z)$ is a height-dependent sectional drag coefficient, which is difficult to calculate for real canopies such as forests and urban areas. 905 Instead, a constant height-averaged sectional drag coefficient \bar{C}_d is often used (Martilli et al. 2002; Coceal and Belcher 2004; Belcher et al. 2012), with the morphology of the canopy represented through a frontal area per-unit-volume function $a_v(z)$. In urban areas, this may be the height-averaged frontal-area density $\lambda_f/h_c = \Sigma A_f/A_t h_c$ (see Chapter 4). In forests and other vegetation canopies, $a_v(z)$ is usually taken as a function of the plant area facing the direction of the flow per unit volume (Finnigan and Shaw 2008; Belcher 910 et al. 2012). Taking this $a_v(z)$, $|U| = (\langle u_j \rangle \langle u_j \rangle)^{\frac{1}{2}}$, and cancelling the air density ρ , Equation (2.38) simplifies to

$$f_i = -\bar{C}_d a_v(z) |U| \langle u_i \rangle. \quad (2.39)$$

Chapter 4 compares flow statistics obtained with this parametrisation to published values for an urban canopy. Chapter 5 discusses the formulation of this parametrisation for forests and other vegetation 915 canopies, with a particular focus on real-world heterogeneous forests and the reconfiguration of flexible plant elements.

2.5 Simplifications and conceptual scalings

2.5.1 Monin–Obukhov Similarity Theory

Monin–Obukhov Similarity Theory (MOST) is a type of zero-order turbulence closure in the ASL (in the 920 ISL over large obstacles, Figure 2.6) (Monin and Obukhov 1954; Foken 2006). MOST is a special application of dimensional analysis which assumes that the turbulent fluxes of mass, heat, and momentum are approximately constant with height. The local mean gradients and the magnitudes of the second order moments are assumed to be dictated by four main parameters: (i) the shear stress τ ; (ii) the height above the ground, z ; (iii) the kinematic heat flux density $\overline{w'\theta_0'}$ (where θ_0 is the surface temperature); and (iv) the 925 ratio g/θ_0 , which accounts for buoyancy effects (Stull 1988; Christen 2005; Foken 2006). These four

parameters are related in the Obukhov length L (Obukhov 1946), which expresses a ratio of shear-produced turbulence to buoyancy-produced turbulence in the ASL

$$L = -\frac{u_*^3 \theta_0}{\kappa g w' \theta_0'}, \quad (2.40)$$

930 where κ the von Kármán constant and $u_* = (\tau/\rho)^{1/2} = (-\overline{u'w'})^{1/2}$ is the friction velocity, a measure of surface stress.

The Obukhov length can be interpreted as a conceptual height at which shear-produced turbulence is about the same magnitude as buoyancy-produced turbulence. For heights $z < |L|$, shear-produced turbulence dominates and for $z > |L|$, buoyancy-generated turbulence dominates. $L \rightarrow \infty$ in statically neutral conditions. MOST suggests that vertical profiles of momentum, temperature, and humidity can be derived using z/L (which is sometimes used as a measure of local atmospheric stability, see Chapter 6). The details of these approximations are not discussed here. MOST is theoretically sound only for stationary, homogeneous turbulence over a flat surface, with a negligible mean vertical velocity. MOST does not hold in the RSL, and especially the canopy layer, because the fluxes of momentum and scalars vary with height.

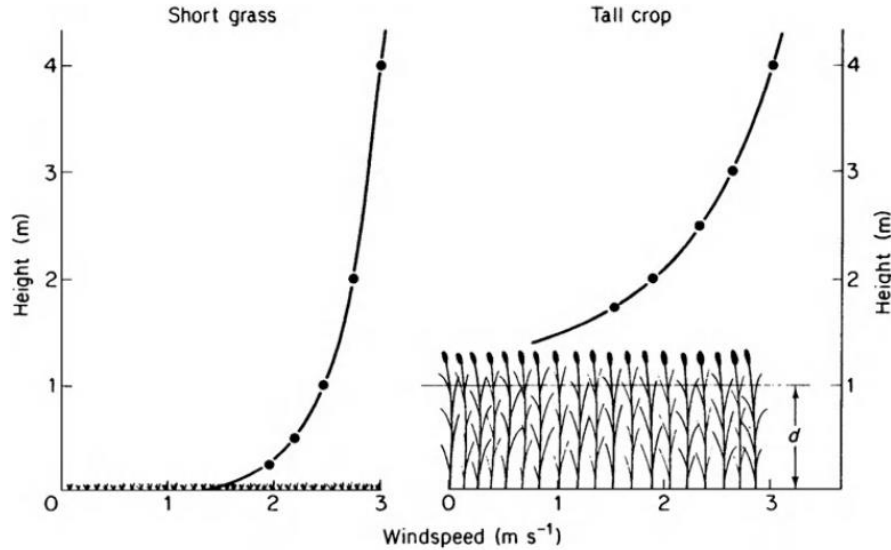
940 Nonetheless, it is helpful to be aware of MOST because it is used in nearly all operational NWP models and GCMs (Hari Prasad et al. 2016). MOST scaling parameters such as L and u_* are also widely used for other micrometeorological applications, although their practical definitions may deviate from the theory. For example, u_* is a helpful scaling variable for many applications, and is used throughout Chapters 4–6. Under the MOST assumptions, the measurement coordinates are rotated into a single reference frame, and the mean vertical velocity is taken as zero. The traditional MOST definition of u_* is calculated only on the streamwise momentum flux, but practical applications of u_* sometimes incorporate a crosswind component for measurements for which the MOST assumptions are not appropriate or necessary (e.g., see the definitions of u_* in Chapters 4 and 6).

950 2.5.2 The logarithmic wind profile

Another application of dimensional analysis in the ASL is the mean wind-speed profile. In neutral conditions over relatively homogeneous terrain, the wind speed increases approximately logarithmically with height (Figure 2.9, left). This relationship is expressed in a coordinate system aligned with the mean flow, where the mean wind speed U at each height

$$955 \quad U(z) = \left(\frac{u_*}{\kappa}\right) \ln\left(\frac{z}{z_0}\right), \quad (2.41)$$

where z_0 is a constant known as the ‘roughness length’, which varies depending on the surface obstacles, such that $U = 0$ when $z = z_0$ (Stull 1988; Foken 2008). The value of z_0 varies from around $\mathcal{O}(10^{-2})$ m to $\mathcal{O}(10^1)$ m for crops, forests, and urban areas, and generally increases with the size of the obstacles. z_0 is a mathematical convenience to avoid undefined integrals, rather than a physical height.



960

Figure 2.9: Schematic wind-speed profiles over short grass and a tall crop. The displacement height d is marked on the right-hand panel (see section 2.5.2). The filled circles indicate representative anemometer measurements. Figure from Monteith and Unsworth (2008).

A more general form of Equation (2.41) accounts for the presence of large obstacles on the surface by assuming there exists a height d , known as the displacement height, at which the mean flow velocity approaches zero because of momentum absorption by the obstacles (Figure 2.9, right). Using this assumption, Equation (2.41) becomes

965

$$U(z) = \left(\frac{u_*}{\kappa}\right) \ln\left(\frac{z-d}{z_0}\right). \quad (2.42)$$

If there are no large obstacles on the surface, $d \approx 0$ but z_0 remains non-zero. The wind speed increases faster than logarithmically with height in statically unstable conditions, and slower than logarithmically with height in stable conditions (Foken 2008; Monteith and Unsworth 2008).

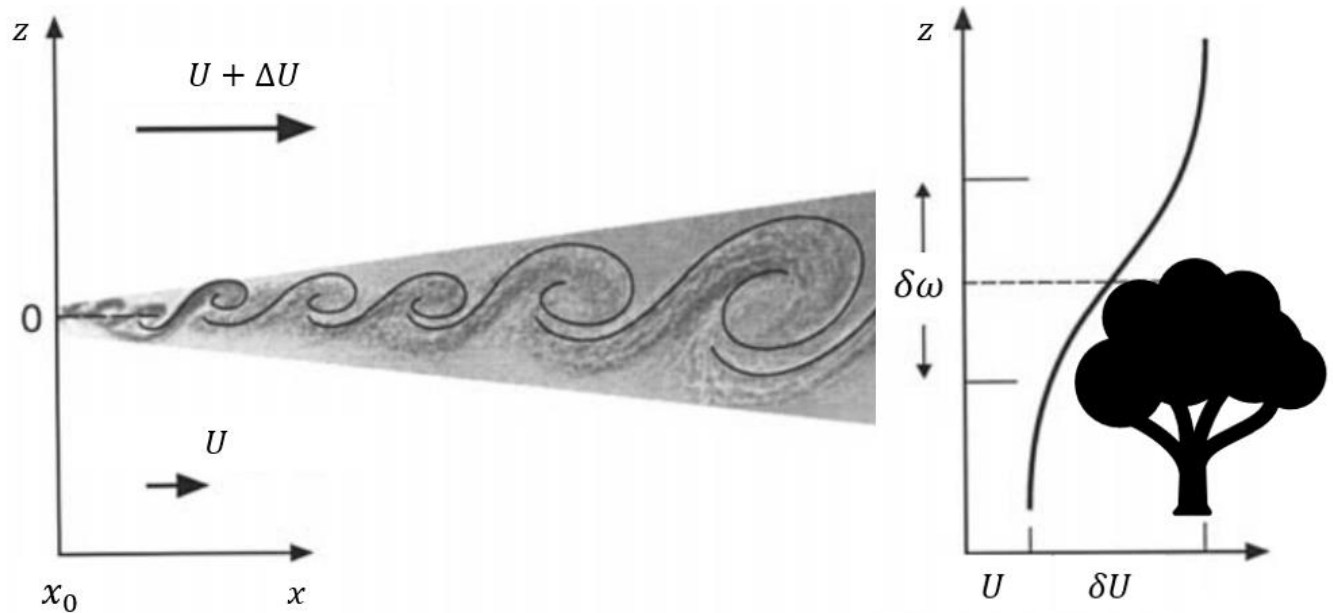
970

2.5.3 The mixing-layer analogy for canopy flow

975

Experimental evidence shows that canopy flow is very different to that in the ISL, or in the idealised ASL envisaged by MOST. The most visible evidence of these differences appears in canopies in the large turbulent transport term in the TKE budget (the transport term is approximately zero in the ISL), and in an inflected mean wind-speed profile (Figure 2.10, right). On the basis of this evidence, the seminal paper of Raupach et al. (1996) proposed that canopy flow is more similar to a plane mixing layer than to an unobstructed boundary layer. A plane mixing layer forms when two co-flowing streams of different velocities are allowed to mix (Figure 2.10, left). This is analogous to fast moving air flowing above a canopy, such as a forest or an urban area, with slower moving air flowing within the canopy. Mixing layers are turbulent and self-preserving, with a depth that scales the vorticity thickness $\delta_\omega = \Delta U / (dU/dz)_{max}$, where $\Delta U = U_1 - U_0$ is the difference between the two freestream velocities.

980



985 **Figure 2.10: Schematic of the mixing-layer analogy for canopy flow (section 2.5.3). U is the mean wind speed in the direction of the flow and δ_ω is the vorticity thickness. Note the inflected profile on the right-hand side, as compared to the logarithmic profile in Figure 2.9. Figure modified from Raupach et al. (1996).**

The elegance of the mixing-layer analogy lies in the observation that the canopy turbulence is reduced to a single variable, the vorticity thickness δ_ω . The same principle is sometimes alternatively expressed using the shear length scale $L_s = U_{h_c}/(\partial U/\partial z)_{z=h_c}$, where $\delta_\omega \approx 2L_s$. The mean wind speed increases approximately exponentially with height within canopies and approximately logarithmically above them, with an inflection point at $z \approx h_c$ (Finnigan 2000; Coceal and Belcher 2004; Brunet 2020). The height of this inflection point is sometimes taken as the mean aerodynamic height of the canopy elements.

995 According to the mixing-layer analogy, turbulent exchange in canopies is dominated by large eddies that scale with L_s (alternatively δ_ω), rather than fine-scale wakes around individual canopy elements. The flow statistics in canopies are highly non-Gaussian, evidence of the ejection (where $u' < 0$ and $w' > 0$) and sweep motions (where $u' > 0$ and $w' < 0$) that transport most of the momentum and scalar quantities within and just above the canopy. A distinctive feature of the large canopy eddies is that they are *coherent*, i.e., the ‘gusts’ superimposed on the flow are correlated. The inflected canopy velocity profile is unstable, causing two-dimensional Kelvin–Helmholtz (KH) waves to develop at the top of the canopy, with a wavelength proportional to L_s (alternatively δ_ω). These KH waves quickly evolve into transverse Stuart-type ‘roller’ vortices centred at $z \approx h_c$. There is some debate in the literature as to what happens from that point. Finnigan et al. (2009) propose that the rollers pair off to form large three-dimensional hairpin structures over the canopy, which eventually dissipate. High-resolution LES of flow over a homogeneous plant canopy supports this idea (Gavrilov et al. 2013). However, Bailey and Stoll (2016) argue that the dominant coherent structures are predominantly two-dimensional, where the main vortices split into smaller ones before stretching into hairpins. They suggest, while three-dimensional deformation of the main rollers can occur, the overall effect on the flow may be overestimated, depending on how the observational data is

1010 filtered. In complex, real-world canopies, this debate is largely irrelevant, because the observational resolutions are nowhere near fine enough to test the theories.

1015 The mixing-layer analogy has been demonstrated to be remarkably robust in forests and other vegetation canopies, showing excellent agreement with both field observations and physical models (Raupach et al. 1996; Finnigan 2000; Brunet 2020). As will be discussed in Chapter 5, numerical models formulated with the mixing-layer analogy in mind tend to be better at reproducing the mean flow variables than the higher-order moments such as the skewness and the kurtosis. The applicability of the mixing-layer analogy to urban canopies is less clear. There is some evidence that in urban areas with buildings and few other obstacles, turbulence length scales are comparatively small around the top of the canopy (Coceal et al. 2007; Barlow 2014; Blunn et al. 2022), despite there being efficient transport of momentum from the flow to the obstacles. This could be because, in urban areas, the buildings are large in relation to L_s (which is not the case with small plant elements), so eddy structures shed from individual buildings are more important than the canopy-top eddies (Coceal et al. 2007). However, most ‘urban’ investigations at this level of detail have been conducted on very simplified urban forms, such as cuboids with no other obstacles (Coceal et al. 2007; Castro 2017; Blunn et al. 2022). This approach probably overestimates the contribution of wake eddies to turbulent transport, and neglects the momentum transfer onto building adornments, such as pitched rooves, balconies, and awnings, and onto other smaller obstacles, such as trees, parked cars, and infrastructure. Chapter 4 discusses this point further in the context of representing an urban area as a patch of porous media.

1020

1025

1030 **Chapter 3 – Equipment and Methods**

Abstract. This short chapter provides additional information on the experimental equipment and methods used in the main research chapters of this thesis (Chapters 4–6). Section 3.1 describes the motivation for, and the basic properties of, the BIFoR FACE facility. Section 3.1 also lists the equipment mounted on the BIFoR FACE meteorological towers. Section 3.2 describes the Weather Research and Forecasting model. Section 3.3 introduces the principles of eddy-covariance measurements and their application in measuring land-atmosphere exchange. Section 3.4 summarises the data management protocol for the results in this thesis, with the details presented in the main research chapters. Section 3.4 includes the coordinate rotation and de-spiking algorithms used in Chapter 6 for the BIFoR FACE meteorological tower measurements.

1040 **3.1 The Birmingham Institute of Forest Research Free-Air Carbon Dioxide Enrichment (BIFoR FACE) facility**

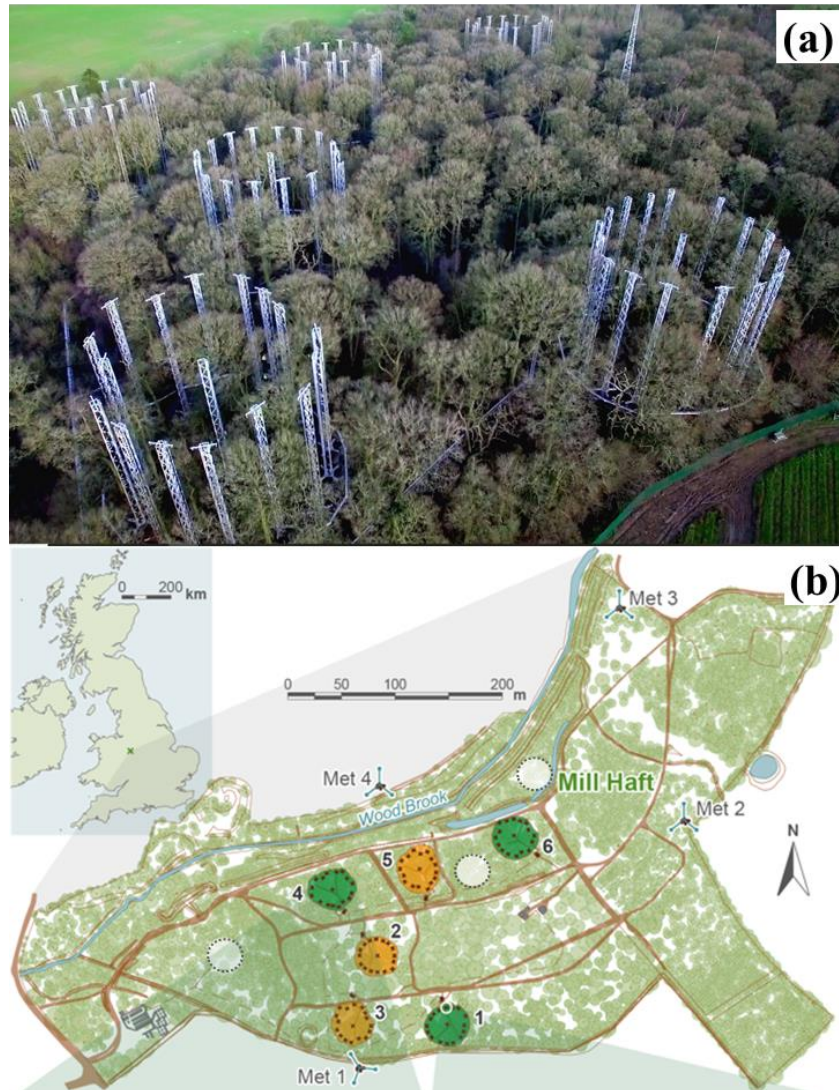
3.1.1 Overview of BIFoR FACE

There are large gaps in our understanding of how vegetation is likely to respond to increasing levels of atmospheric carbon dioxide (CO₂). Part of this uncertainty stems from a lack of experimental measurements on mature vegetated ecosystems under future elevated CO₂ mixing ratios (e[CO₂]) (Norby et al. 2016; Ellsworth et al. 2017; Hart et al. 2020; Gardner et al. 2021). Most of our experimental understanding in this area comes from FACE measurements of young trees and other plants (e.g., McLeod and Long, 1999; Norby et al., 2006, 2016). The details of the FACE protocol vary between the various experiments. The basic idea is that several large plots in an ecosystem are fumigated with air containing an e[CO₂], usually a constant increment large enough to stimulate a detectable treatment effect (e.g., +150 μmol mol⁻¹ or +200 μmol mol⁻¹) or a variable increment to maintain a concentration, such as that expected in around 2050, e[CO₂] ≈ 550 μmol mol⁻¹. FACE experiments generally show that e[CO₂] stimulates the growth of young plants in conditions with adequate nutrient and water availability (Norby et al. 2016; Brodrigg et al. 2020), as would be expected from our understanding of photosynthesis. The strength of FACE is that it examines ecosystem-level responses rather than responses of individual plants (e.g., Norby et al., 2016).

FACE experiments on forests include the Duke FACE measurements in an evergreen loblolly pine stand (Hendrey et al. 1999; Schlesinger et al. 2006), the AspenFACE experiment on aspen and poplar seedlings (Dickson et al. 2000; Kubiske et al. 2015), and the Oak Ridge National Laboratory FACE in a young deciduous sweetgum plantation (Norby et al. 2006). Together, Duke FACE, AspenFACE, and Oak Ridge FACE are sometimes referred to as the ‘first-generation’ forest FACE experiments (Norby et al. 2016; Hart et al. 2020). This first-generation also includes shorter-lived experiments such as BangorFACE (FACE on mixed-species seedlings) and POPFACE (FACE on a poplar plantation) (Miglietta et al. 2001; Hoosbeek 2016). The pioneering first-generation forest experiments produced many fascinating results regarding the growth of young trees under e[CO₂]. However, the long-term (years to decades) response of mature forests remains relatively unknown. This knowledge gap is concerning because these ecosystems account for a

large proportion of the land carbon sink (Friedlingstein et al. 2022). For example, mature seasonal forests dominate the sink in the northern hemisphere, where around 40% of the net carbon uptake takes place (Luysaert et al. 2008). The scientific community has for some time called for ‘second-generation’ ecosystem-scale FACE experiments in mature forest ecosystems (Calfapietra et al. 2010; Norby et al. 2016).
1070 So far, two have begun operating. The first, the ‘EucFACE’ experiment in an open, Mediterranean-type sclerophyll forest in Australia (Drake et al. 2016), began fumigating in September 2012. The second, BIFoR FACE, began fumigating in Spring 2017 (Hart et al. 2020; MacKenzie et al. 2021). Funding to begin building AmazonFACE, in the Amazon rainforest in Brazil, was announced towards the end of 2021 and the facility is now under construction (Met Office 2021).

1075 BIFoR FACE is located in Staffordshire, UK (52.801°N, 2.301°W) within a 19 ha patch of mature northern temperate broadleaf deciduous woodland. The BIFoR FACE woodland consists of an overstorey dominated by English oak (*Quercus robur*) and a dense, mixed-species understorey. The woodland was planted with the existing oak standards in the late 1840s. It has been largely unmanaged for the past 30–40 years. The
1080 mean canopy height, $h_c \approx 24\text{--}26$ m. The region is characterised by cool wet winters and warm, relatively dry summers. The mean air temperatures in January and July are 4 and 17 °C, respectively. There is a frost-free growing season from early April to late October. The BIFoR FACE infrastructure comprises nine experimental patches of forest, which are approximately circular, with diameters of around 30 m (Figure 3.1). There are three ‘fumigated’ patches, in which infrastructure arrays maintain the [CO₂] at
1085 150 μmol mol⁻¹ above ambient during daylight periods of the growing season. There are three further ‘control’ patches, which are dosed with ambient air only, and three ‘ghost’ patches, which are ecologically similar to the fumigated and control patches, but do not contain any of the supporting infrastructure. Throughout the growing season, the fumigated patches are treated with air with e[CO₂] from dawn (solar zenith angle, $sza = -6.5^\circ$) to dusk ($sza = 6.5^\circ$). The control patches are treated with air at similar flow rates
1090 as those in the fumigated patches. However, in the control patches, the air has an ambient [CO₂] rather than e[CO₂]. The BIFoR FACE infrastructure maintains the target e[CO₂] within the fumigated patches around 98% of the time, with adverse weather, faults, and CO₂ supply issues accounting for the time lost. There is very little contamination of the control and ghost patches by the fumigation (Hart et al. 2020).



1095 **Figure 3.1: (a) Aerial view of the BIFoR FACE infrastructure, looking north-east. The large circular rings are**
the fumigation and control patches (see section 3.1.1). Image taken from drone footage (copyright Dr Rick
Thomas and BIFoR FACE). The photograph predates the installation of meteorological towers around the edge
of the woodland (see (b) and section 3.1.2 below). (b) Schematic of the BIFoR FACE facility. The coloured
1100 **circles indicate the location of the FACE arrays, with green and orange denoting the fumigation and control**
arrays, respectively. The grey translucent circles with dashed circumferences mark the locations of the ghost
arrays. The meteorological towers on the edge of the forest are labelled Met 1–4.

The fundamental research questions of the BIFoR FACE experiment are ecological and span a range of scientific disciplines:

1. How does elevated CO₂ change carbon flows and storage, nutrient cycles, and water use?
- 1105 2. How does elevated CO₂ change biodiversity and ecosystem structure and function?
3. How does elevated CO₂ affect susceptibility to biotic and abiotic stress?

4. How can lessons from the global network of second-generation forest FACE experiments be generalised to other woodlands and forests?

1110 For example, regarding questions (1) and (2), recent measurements over a three-year period show that the
light-saturated net photosynthetic rates of the upper-canopy oak leaves is $33 \pm 8\%$ higher (mean and
standard error) in trees grown in the e[CO₂] fumigated patches compared with those grown in the control
patches (Gardner et al. 2021). This suggests that the mature oak trees assimilate more carbon under e[CO₂],
without photosynthetic downregulation, provided the nutrient availability is adequate. It is hoped further
research will reveal further details on the uptake mechanism and storage location of the extra carbon that
1115 the trees assimilate. Regarding question (3), understorey plants at BIFoR FACE flower earlier under
e[CO₂], but the length of the flowering period does not change (Crowley et al. 2021). Although no
significant difference was found in the number of visits made by pollinators to flowering plants under
e[CO₂], or in the amount of seeds those flowers produced, the change in the timing means that a mismatch
could develop between the plants and their pollinators in the future, which would affect pollination success.
1120 Optical particle counts of bioaerosols found no significant effect of the e[CO₂] treatment on total bioaerosol
concentrations, but identified a potential suppression of high-concentration bioaerosol events (Baird et al.
2022).

In addition to the main research questions above, BIFoR FACE also hosts research in atmospheric science,
1125 biology, plant physiology and pathology, the social sciences, soil and microbial sciences, hydrology, and
mycology. Hart et al. (2020) provides a detailed description of the FACE infrastructure and its performance.
Chapter 6 of this thesis provides additional detail on the FACE fumigation, with a particular focus on the
equipment and measurements relevant to the site's micrometeorology. MacKenzie et al. (2021) includes a
detailed description of the BIFoR FACE data and tissue protocols. Figure 3.2 below reproduces Figure 3
1130 from MacKenzie et al. (2021), which shows a schematic of the sensor deployment, and tissue and data flow,
through BIFoR FACE and Wood Brook (a stream running through the BIFoR FACE facility).

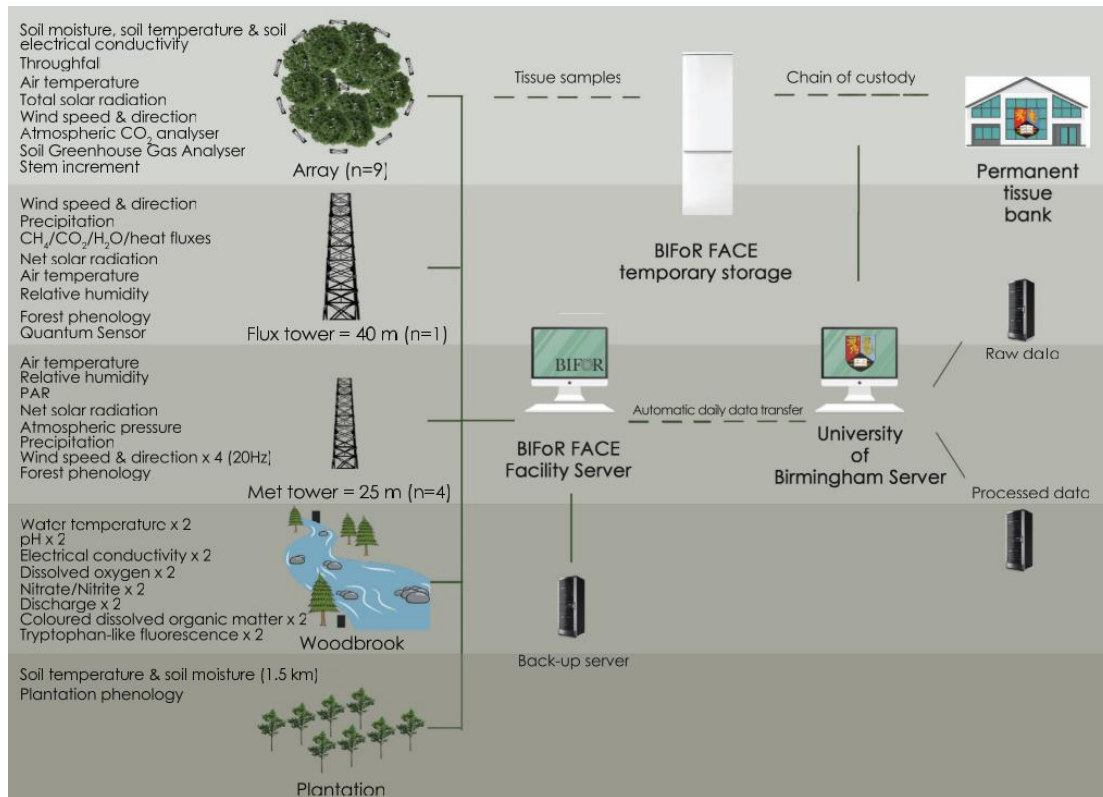


Figure 3.2: A schematic view of the sensor deployment and tissue and data flow through BIFoR FACE and Wood Brook. The main experimental infrastructure elements are shown (left); replicates are indicated by ‘n=’. Data from electronic sensors are recorded in networked field dataloggers and relayed to the facility server. Back-up is carried out on-site and by daily data download to the main University of Birmingham servers with Retrospect software (Retrospect Inc. USA). Initial quality assurance is under the control of the BIFoR Data Manager (author Giulio Curioni) before data is released to the BIFoR FACE community. A parallel system operates for physical samples, the metadata from which enters the BIFoR FACE database via chain-of-custody software (Pro-curo Software Ltd, West Sussex, UK). Figure and caption reproduced without modification from MacKenzie et al. (2021).

3.1.2 The meteorological towers at BIFoR FACE

In 2018, four meteorological masts were installed around the edge of the BIFoR FACE woodland (denoted Met 1–4, respectively; Figure 3.1(b)). The towers vary in height, depending on the characteristics of the neighbouring trees (Table 3.1). Each tower has one upper platform, and two rest platforms (Figure 3.3).

Table 3.1: Details of the meteorological towers at BIFoR FACE, including the heights of the platforms. See diagram at Figure 3.3

Tower	Lower Platform	Mid Platform	Upper Platform	Max. Height
Met 1	5.5 m	12.5 m	24.0 m	26.0 m
Met 2	5.5 m	12.5 m	22.0 m	24.0 m
Met 3	5.5 m	12.5 m	25.5 m	27.0 m
Met 4	5.5 m	12.5 m	20.0 m	22.0 m

Each tower has a three-dimensional sonic anemometer (R3-100, Gill Instruments, Lymington, UK) mounted at $z \approx 24$ m on boom arms. These anemometers sample the three-dimensional instantaneous velocity components and the speed of sound at 20 Hz. In October 2020, three additional three-dimensional sonic anemometers (Windmaster Pro, Gill Instruments, Lymington, UK) were added to each mast at heights of 7 m, 10 m, and 14 m, sampling the same variables at the same rate as the existing sensors.

Sonic anemometers can resolve atmospheric turbulence with high temporal resolution (here, sampling at 20 Hz). However, high-resolution measurements are vulnerable to distortion from surrounding obstacles, such as buildings and trees, or from the mounting infrastructure, e.g., if they are sited too close to supporting towers. At BIFoR FACE the sonics are mounted on boom arms, around 1.5 m away from the platforms, to minimise flow distortion from the tower. Despite these efforts, some measurement distortion is inevitable at spatially complex sites, because the near-surface flows are strongly deformed (e.g., partially recirculating flows in the lee of the forest) (Dellwik et al. 2010, 2014). This near-surface distortion can be reduced, with non-trivial effort, by correcting the sonic observations used matrices derived on wind-tunnel measurements—e.g., see the process in Christen (2005), which used measurements taken across two calibration campaigns.

I had no control over the siting and calibration of the equipment at BIFoR FACE, so this type of correction was not possible for the work in this thesis. The meteorological-tower measurements, which are situated within metres of the forest edges, therefore likely contain some signal of the deformed flows around the forest. This distortion would be difficult to remove entirely, even with careful sensor calibration (Finnigan 2008; Dellwik et al. 2010; Hayek et al. 2018). Regarding the net effect, the friction-velocity measurements are possibly biased slightly high, through the inclusion of wake-generated turbulence as well as shear-generated turbulence. I observed mean daytime values of around 0.7 m s^{-1} , around 20% higher than other reports—e.g., Fuentes et al. (2016). However, this difference may, in full or in part, result from the differing site structure and climate between studies. In any event, the friction-velocity calculations were used to observe the overall and directional effect of turbulence on air-parcel residence times (section 6.3.3.1), and to normalise the PDFs throughout Chapter 6. For both purposes, the exact values of individual u_* measurements are of little consequence, provided any possible net bias is acknowledged. In contrast, the calculated Obukhov lengths, L , are possibly biased slightly small. The kinematic vertical temperature flux observations, which appears in the denominator in Equation (2.40), are probably (absolutely) larger than their hypothetical stationary values, because they include the effect of recirculating eddies. Is it not possible to determine exactly the existence and extent of the bias, because of the inherent difficulties in comparing turbulent covariances between complex sites. However, the values of L were used only to define very accommodating atmospheric stability classes, over a long observational period (see 6.3.3.2), during daylight hours. Overall, I do not consider that the possible distortion in the turbulence measurements materially affects the conclusions in this thesis. It is worth emphasising here that the meteorological tower observations comprise a small component of this work—they are only used in Chapter 6, principally in section 6.3.3. That said, additional calibration or data cleaning would be required if the meteorological-

1190 tower observations were used to, for example, investigate atmospheric processes in the evening transition
—when it is necessary to determine subtle changes in the value of L (e.g., Mahrt 1981, 2017a)—or to use
 u_* to define thresholds to filter eddy-covariance observations (Gu et al. 2005; Hayek et al. 2018).

The following equipment is also installed on the meteorological towers (but whose data are not a major component of this thesis):

- 1195 1. LI-190R Quantum photosynthetically active radiation (PAR) sensor (Licor, Lincoln, NE, USA) – upper platform
2. Kipp and Zonen NR Lite 2 Net Radiometer (Kipp and Zonen, Delft, NED) – upper platform
3. Texas Electronics TR-525m tipping bucket rain gauge (Texas Electronics, Dallas, TX, USA) – maximum height and ground level
4. Vaisala PTB 210 Barometer and pressure port (Vaisala, Vantaa, Finland) – upper platform
- 1200 5. Vaisala HMP155 humidity and temperature probe and shield (Vaisala, Vantaa, Finland) – upper platform; mid platform; lower platform; $z \approx 1.4$ m.

1205 The equipment on the rest platforms is mounted on boom arms so that the sensors sit $z = 1.15$ m above the height of the platforms listed in Table 3.1 (e.g., the PAR sensor on Met 1 is at $z = 25.15$ m). All the equipment is wired into the logger enclosure near the middle platforms (Figure 3.3). Inside the enclosures are three data loggers, a Campbell CR1000x and two Campbell CR6s (Campbell Scientific, Shepshed, UK). Each logger enclosure has three 12 V power supplies (one per logger), backed up by 12 V batteries to maintain power supply in the event of a mains power outage. Each logger has its own data connection to large infrastructure cabinets at the base of the meteorological towers. Chapter 6 uses measurements from
1210 the BIFoR FACE meteorological towers to investigate the effect of the local atmospheric conditions on air-parcel residence times in the woodland. Chapter 7 uses the measurements in a ‘pulse and trace’ experiment to monitor the passage of CO₂-rich air across the BIFoR FACE woodland.

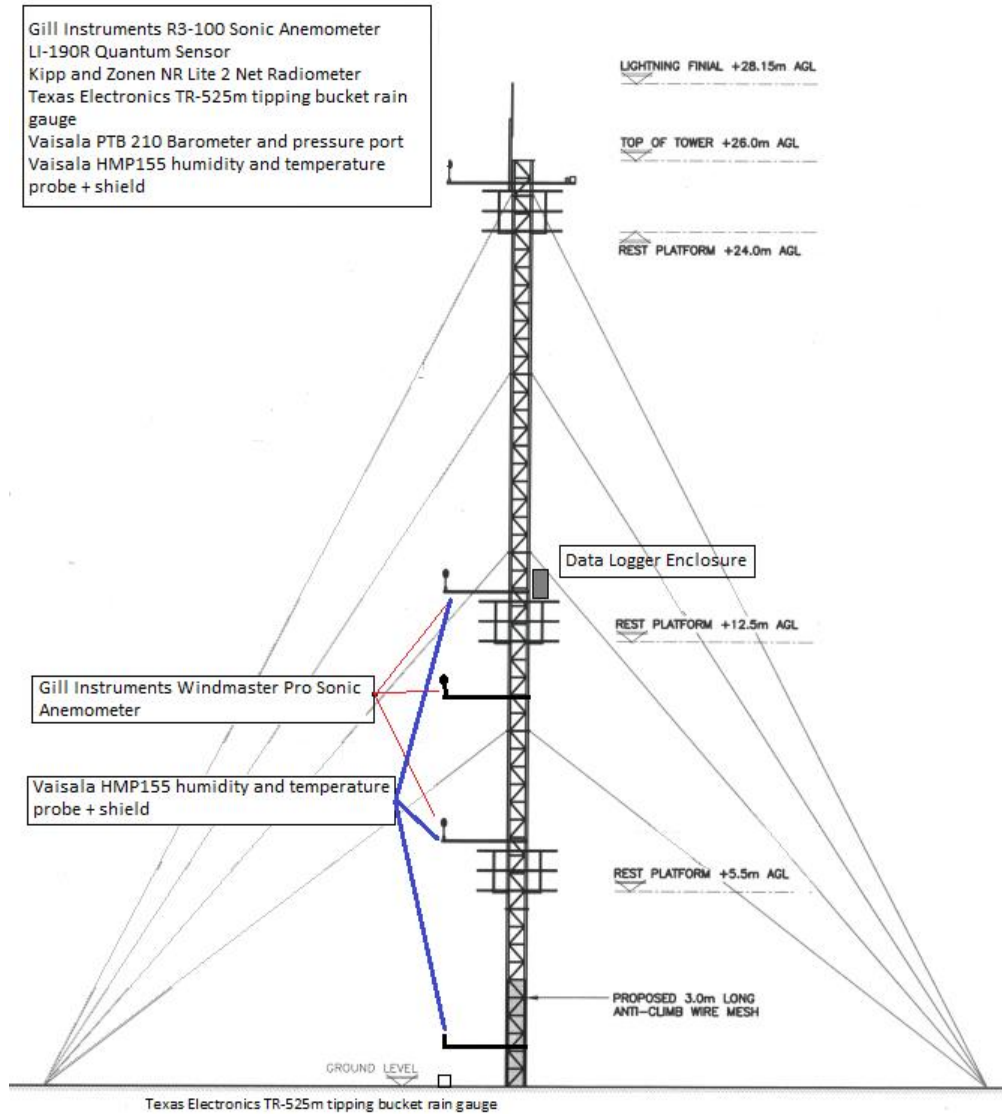


Figure 3.3: Schematic of the meteorological towers at BIFoR FACE and the equipment mounted on them. Tower shown is Met 1 (section 3.1.2 and Figure 3.1). The height of the upper platform the maximum height varies slightly from tower to tower (see Table 3.1). Image copyright BIFoR FACE.

1215

3.2 The Weather Research and Forecasting model

The Weather Research and Forecasting (WRF) model is an open-source NWP and atmospheric model developed and supported by the National Center for Atmospheric Research (NCAR), Boulder, CO, USA. WRF is designed for both NWP and research applications. WRF is the world's most widely-used atmospheric model, with more than 36,000 user registrations across 162 countries (Powers et al. 2017). WRF was developed from the Pennsylvania State University–NCAR Mesoscale Model (MM5; Grell et al., 1994) and has been extended by both the NCAR development team and its wide community of users (e.g., Powers et al., 2017; Skamarock et al., 2021). WRF currently has two atmospheric-fluid-flow solvers, known as cores, which operate within the model's software. These are the Eulerian Mass (EM) core and the non-

1220

1225

hydrostatic mesoscale model (NMM) core. The EM core is also known as Advanced Research WRF (ARW), and is intended mostly for research applications. The EM core solves the non-hydrostatic compressible Euler equations, and is designed to run on parallel networks of computers. The NMM core is designed for operational NWP, and has been widely used by private organisations, national weather agencies, and research centres for this purpose (Powers et al. 2017). WRF supports a variety of tailored configurations, including applications in atmospheric chemistry, hydrological modelling, wildfires, renewable energy, and tropical cyclones. WRF also provides 12 idealised scenarios through its ARW core, including a large-eddy simulation mode (WRF-LES), which is used in this thesis.

WRF-LES runs using the ARW dynamical solver, which integrates the compressible, nonhydrostatic Euler equations. This set of equations is very similar to those in Equations (2.20–2.22), but they are cast in flux form using hydrostatic pressure as an independent variable (Skamarock et al. 2021). (The contributions from the compressibility of the WRF equations are negligible close to the ground (Kirkil et al. 2012).) The ARW equations are formulated using a terrain-following hydrostatic-pressure vertical coordinate, denoted η , which—in version 3.6.1 of WRF-LES, used in this thesis—is defined as

$$\eta = \frac{p_d - p_t}{p_s - p_t}, \quad (3.1)$$

where p_d is the hydrostatic component of the pressure of dry air, and p_s and p_t respectively denote values of p_d along the surface and top boundaries of the simulated domain. The definition of η has been modified slightly in the most recent version of WRF, version 4 (Skamarock et al. 2021). This change is not relevant to this thesis, which focusses on processes over level terrain. The ARW solver uses a time-split integration scheme. Most of the meteorologically significant motions are captured using third-order Runge–Kutta time integration (Wicker and Skamarock 2002), a type of finite differences scheme, which is essentially a higher-order application of the Euler method of solving ordinary differential equations. ARW uses an additional, smaller time step to account for high-frequency phenomena such as acoustic waves, which are not accounted for in the incompressible flow solvers used for most NWP. WRF-LES models momentum transport and mean scalar transport well in both the neutral and convective ABL (Kirkil et al. 2012; Nottrott et al. 2014). High spatial resolutions are needed to resolve surface-layer turbulence faithfully in shear driven conditions (Kirkil et al. 2012; Nottrott et al. 2014). The model’s performance in stable ABL conditions remains relatively untested, at least against field observations. See Skamarock et al. (2021) for full technical details of the WRF model, including the governing equations and numerical integration schemes, and Powers et al. (2017) for historical overview, context, and the direction of future developments.

The WRF model incorporates several programming languages, including Fortran, C, and Perl. The main dynamical solvers are written in Fortran. WRF allows the user to configure the basic details of the simulations—e.g., the cell resolution, domain size, time step, and the geostrophic wind speed—using a ‘namelist’. Namelists are an input/output feature in Fortran that use key-value assignments to specify variables (without introducing complications or potential bugs through formatting). The WRF-LES namelist allows users to turn on and off features such as the Coriolis force (which is usually not very

1265 influential in canopy flows), and to specify options such as the SGS closure scheme, the boundary
 conditions, the surface-layer schemes, at the parametrisations for turbulent transport. In Chapters 4 and 5,
 the source code for WRF-LES physics schemes was modified to include the distributed-drag
 parametrisation. After each substantive modification, the WRF code was cleaned, configured, and re-
 compiled (using the parallel mode of an Intel Fortran compiler). The simulations in Chapters 4 and 5 took
 1270 around 50–80 wall-clock hours, running on a single node with 32–64 cores. I found the easiest way to
 navigate long queues on the university high-performance computers, while keeping within a workable
 simulation period, was to use a small number of powerful and large-memory cores. The WRF-LES outputs
 large netCDF binary data files (e.g., hundreds of GB for seven hours of simulation). I performed the
 statistical processing of the netCDF files in Fortran, outputting the time-averaged statistics in .txt files (see
 section 3.4, below).

1275 3.3 Eddy-covariance measurements

Eddy covariance is a micrometeorological technique that allows researchers to measure the exchange of
 quantities such as CO₂ and water vapour between atmosphere and the Earth’s surface. Eddy covariance is
 the most widely used technique for investigating ecosystem-scale land-atmosphere exchange, at least for
 species for which sufficiently fast sensors exist. The technique is deployed across global networks of long
 1280 term ecosystem-measurement sites, such as those in the FLUXNET programme (Baldocchi et al. 2001;
 Oliphant 2012). This thesis does not rely on eddy-covariance measurements, nor discusses the technique in
 detail. However, the challenges in obtaining robust eddy-covariance observations in certain landscapes and
 weather conditions have motivated a great deal of micrometeorological research, especially LES models of
 vegetated terrain, the focus of Chapter 5. To understand these challenges, it is informative to look at the
 1285 technique’s formulation.

In a turbulent flow, the vertical flux can be expressed as $F = \overline{\rho_a w \alpha}$, where α is the mixing ratio of some
 quantity in the air. This can be decomposed into its mean and turbulent components by Reynolds
 decomposition

$$1290 \quad F = \overline{(\bar{\rho}_a + \rho'_a)(\bar{w} + w')(\bar{\alpha} + \alpha')}. \quad (3.2)$$

Expanding Equation (3.2) and, simplifying according to the Reynolds averaging rules, gives

$$F = \bar{\rho}_a \bar{w} \bar{\alpha} + \bar{\rho}_a \overline{w' \alpha'} + \bar{w} \overline{\rho'_a \alpha'} + \bar{\alpha} \overline{\rho'_a w'} + \overline{\rho'_a w' \alpha'} \quad (3.3)$$

For eddy-covariance measurements to be at their best, one assumes that (i) there are no sources or sinks in
 the atmosphere above the surface; (ii) the surface that is horizontally uniform and level (to minimise
 1295 advective effects); (iii) the mixing ratio of the quantity does not vary significantly with time. Density
 fluctuations are also assumed to be negligible. With these assumptions, Equation (3.3) simplifies to

$$F = \bar{\rho}_a \bar{w} \bar{\alpha} + \bar{\rho}_a \overline{w' \alpha'}, \quad (3.4)$$

so that

$$F \approx \bar{\rho}_\alpha \overline{w' \alpha'} \quad (3.5)$$

1300 in level, homogeneous terrain where the mean vertical wind is assumed to be negligible (Baldocchi et al. 1988; Monteith and Unsworth 2008). The ‘ideal’ assumptions of eddy covariance are rarely satisfied at measurement sites because the landscape is not homogeneous, the terrain not flat, and the flow not statistically well-behaved. Falsely assuming that the ideal conditions are satisfied can lead to exchange estimates that are inaccurate and in, in some conditions, biased (Foken et al. 2011; Oliphant 2012; Hicks and Baldocchi 2020). These difficulties are no great secret, and the researchers who formulated the eddy-covariance technique have been refreshingly open about them since the beginning (e.g., Baldocchi et al., 1988). However, so far, attempts to fix the difficulties by refining the eddy-covariance methodology have not been successful (Wilson et al. 2002; Finnigan 2008; Aubinet et al. 2010; Mauder et al. 2020). There is strong evidence that the ideal assumptions of eddy-covariance are often violated by fluid dynamical phenomena that arise in complex terrain around hills and forest edges (Belcher et al. 2012; Brunet 2020; Finnigan et al. 2020). Physical and numerical models have proved very useful in investigating these phenomena. However, models are currently less adept at investigating theoretical violations that arise in certain weather conditions, such as during stable nights (Mahrt et al. 1998; Loescher et al. 2006; Mahrt 2017b). Chapter 5 discusses these points in more detail.

1315 **3.4 Data management and processing in this thesis**

3.4.1 Overview of data management and processing

WRF-LES is deterministic, and the LES results used in this thesis are reproducible using the model configuration and numerical details in Chapters 4 and 5. For convenience, the modified WRF physics solvers, namelists, and processing code used for the LES models in Chapters 4 and 5 are also available at github.com/foresteddy (open access, on demand).

The BIFoR FACE measurements, including the meteorological-tower observations, are managed according to the University of Birmingham and BIFoR FACE protocols set out in Hart et al. (2020) and MacKenzie et al. (2021). These measurements include the raw data used in the residence-time analysis in Chapter 6. The time-averaged measurements, supporting README files, and visualisation code from Chapter 6 are deposited in a permanent, open access repository: <https://doi.org/10.25500/edata.bham.00000836>. They are also available at github.com/foresteddy (open access, on demand).

Chapter 7 presents results from opportunistic ‘pulse and trace’ experiments at BIFoR FACE. The most important results are contained in that chapter. The raw datasets can be obtained via the BIFoR FACE repository. The processing and visualisation code for Chapter 7 is available at github.com/foresteddy (open access, on demand).

I processed and visualised the data in this thesis using version 4.0.5 of R (R Core Team 2021) and version 3 of Python. I am very grateful to the dedicated and talented community of open-source software developers in R and Python.

3.4.2 Processing algorithms used for the BIFoR FACE meteorological tower measurements

3.4.2.1 Data cleaning and despiking algorithm

Before any of the BIFoR FACE meteorological-tower measurements were used in this thesis, data points corresponding to non-physical values or instrumental failure were removed without replacement. The thresholds for data removal were defined on the basis of typical ranges local to the BIFoR FACE site. Data points were removed when any of the following conditions were satisfied:

- any of the velocity components $|(u, v, w)| > 30 \text{ m s}^{-1}$; or
- the air temperature (real or sonic) $T > 45 \text{ }^\circ\text{C}$; or
- the air temperature (real or sonic) $T < -20 \text{ }^\circ\text{C}$.

Chapter 6 discusses the tolerated quantities of missing or contaminated data for each averaging period and day before the entire period was discarded.

After data removal, the sonic data were despiked following the procedure in Højstrup (1993). The procedure in Højstrup (1993) is based on the assumption that, for each interval within the dataset, the mean variables are normally distributed, independent, and random, and for which means and standard deviations can be calculated. Researchers have applied similar protocols across a range of micrometeorological applications, including in vegetation, for aircraft measurements, and in urban canopies (Vickers and Mahrt 1997; Starckenburg et al. 2016; Barbano et al. 2021). A variety of more sophisticated algorithms have been developed for high-frequency atmospheric timeseries (e.g., Jesson et al., 2013; Starckenburg et al., 2016), but these were not applied here because sensitivity tests showed the timeseries to be quite clean.

The velocity statistics at BIFoR FACE are non-Gaussian, as is typical around vegetation (Finnigan 2000). In particular, the magnitudes of the velocity components are usually positively skewed. To account for this pattern, I modified the procedure in Højstrup (1993) so that it made no assumption of normality. This is very similar to the despiking procedure outlined in Leys et al. (2013). The modified procedure is as follows:

1. Absolute values in the measurements above a threshold $\zeta \times D_{med}$ were marked as spikes, where ζ is a discriminant factor and D_{med} the median absolute deviation over each time interval (5 min, in Chapter 6). The median absolute deviation is defined $D_{med} = \text{median}(|x_i - \tilde{x}|)$ for a univariate set x_1, x_2, \dots, x_n , with \tilde{x} the set's median (see Hampel (1974) for a technical discussion of the properties of the D_{med}).
2. A discriminant factor of $\zeta = 1.4826 \times 3.5$ was used, where 3.5 is a common discriminant factor used in previous studies (e.g., Barbano et al., 2021; Vickers and Mahrt, 1997) and 1.4826 is an

1370

additional factor to scale the D_{med} to the standard deviation, which is used to define the spikes in most similar studies² (if the data are indeed normal, the additional factor means the values of the D_{med} and the standard deviation converge).

3. The spikes were replaced with the median value of each interval.

3.4.2.2 Coordinate rotation to correct sensor misalignment

1375

When the sonic anemometers on the BIFoR FACE meteorological towers were installed, the operations team made every effort to align the sensors so that the north on the sensors aligned with Geodetic north. However, despite these efforts, subsequent testing showed that some of the sensors were slightly out in their alignment, as shown in Table 3.2. The angles in Table 3.2 refer to the direction the anemometers are pointed. Without correction, the effect of this misalignment is to introduce a bias in the measurements in the opposite direction. For example, for the sonic at 10 m on Met 1, a mean wind from 5° appears to be perfectly northerly wind (in effect rotating the measurements 5° west).

1380

Table 3.2: Incorrect alignments of some of the sonic anemometers on the meteorological towers at BIFoR FACE. The angle θ gives the direction in which the ‘north’ on the sonic anemometers is pointed

Meteorological tower	Height	Angle (θ)
Met 1	10 m	5° east
Met 2	7 m	16° west
Met 2	10 m	5° west
Met 2	14 m	16° west
Met 2	25 m	5° west
Met 3	14 m	5° east
Met 4	10 m	15° east

1385

The alignments were corrected by rotating the relevant velocity measurements around the z -axis, with the angle θ serving as a yaw angle (or $-\theta$ for the sonics on Met 2, which point θ° west). This is expressed as follows

$$\begin{pmatrix} u_1 \\ v_1 \\ w_1 \end{pmatrix} = \begin{pmatrix} \cos(\theta_r) & \sin(\theta_r) & 0 \\ -\sin(\theta_r) & \cos(\theta_r) & 0 \\ 0 & 0 & 1 \end{pmatrix} \begin{pmatrix} u_0 \\ v_0 \\ w_0 \end{pmatrix}, \quad (3.6)$$

1390

where the subscripts 0 and 1 refers to the raw and rotated vector components, respectively, and θ_r is θ from Table 3.2, expressed in radians. The velocity components were rotated after despiking but before calculating any of the time-averaged flow statistics.

² The advantage of using the D_{med} and median over the standard deviation and mean is that the despiking algorithms using the former measurements only need to be applied once and make no assumptions as to the data’s normality. Those based on the latter may need to be applied multiple times and the time intervals should be chosen carefully to ensure that the data are somewhat Gaussian.

Chapter 4 – Neighbourhood-Scale Flow Regimes and Pollution Transport in Cities

1395 **Publishing details.** This chapter is a reproduction of the article ‘Neighbourhood-Scale Flow Regimes and
Pollution Transport in Cities’ by Edward Bannister, Xiaoming Cai (XMC), Jian Zhong (JZ), and Rob
MacKenzie (AMRK), published in *Boundary-Layer Meteorology* (2021) 179:259–289
<https://doi.org/10.1007/s10546-020-00593-y>.

1400 **Author contributions.** I conceived of this study under the supervision of XMC. Under the joint supervision
of XMC and AMRK, I performed the LES model runs, wrote the processing code, conducted the formal
analysis and visualisation, wrote the original draft of the manuscript, and revised the manuscript in response
to reviewers’ comments. I am grateful to JZ for his assistance and expertise in adapting and debugging the
Fortran code in the LES mode of the WRF model. All authors (a) reviewed and edited drafts; and (b)
1405 contributed to discussions in which the methodology was refined. I am grateful to two anonymous reviewers
for constructive comments that helped improve this manuscript. I thank Chantal Jackson for her assistance
in redrawing Figures 4.1 and 4.9.

Stylistic notes. Throughout this chapter, the mean height of the canopy elements is denoted H , a common
shorthand in urban micrometeorology, rather than h_c , which is more commonly used for vegetation
1410 canopies and is adopted elsewhere in this thesis. Appendix 4B is published as electronic supplementary
material in the version of this article in *Boundary-Layer Meteorology*.

Abstract. Cities intimately intermingle people and air pollution. It is very difficult to monitor or model
neighbourhood-scale pollutant transport explicitly. One computationally efficient way is to treat
1415 neighbourhoods as patches of porous media to which the flow adjusts. Here we use conceptual arguments
and large-eddy simulation to formulate two flow regimes based on the size of patches of different frontal-
area density within neighbourhoods. One of these flow regimes distributes pollutants in counter-intuitive
ways, such as producing pollution ‘hot spots’ in patches of lower frontal-area density. The regimes provide
the first quantitative definition of the ‘urban background’, which can be used for more precisely targeted
1420 pollution monitoring. They also provide a conceptual basis for further research into neighbourhood-scale
air-pollution problems, such as parametrisations in mesoscale models, and the transport of fluid constituents
in other porous media.

4.1 Introduction

Air pollution is the greatest environmental threat to human health (World Health Organisation, 2016),
1425 particularly in urban areas (Landrigan et al. 2018), where the majority of the world’s population now lives
(United Nations 2018). However, it is difficult to assess the efficacy of air-pollution policy because in situ
observations are too sparse to monitor transport processes within a city. Permanent networks usually

comprise a handful of sites within an area of hundreds of square kilometres (World Health Organization 2016; DEFRA 2019; US EPA 2019) and typically avoid observations near large obstacles such as buildings and trees (Muller et al. 2013b). Because low-cost sensors require careful calibration (Kelly et al. 2017) and have high post-processing and maintenance costs (Kumar et al. 2015; Pope et al. 2018), they cannot simply fill the gaps in permanent networks.

Numerical simulation is a useful supplement to in situ measurements, provided the model captures the relevant physics of the problem. Numerical models provide flow information at every point in the simulated domain—sufficient to investigate the transport equations term by term, which is not usually possible with observations. Advances in affordable computing power and accessibility over the last few decades have meant numerical simulations have proliferated (Kumar et al. 2011; Tominaga and Stathopoulos 2013; Blocken 2014; Toparlak et al. 2017). However, because of the computational demands of simulating the turbulent boundary layer, numerical flow models are forced to represent urban areas differently depending on their scale of interest (Martilli et al. 2002; Hood et al. 2014; Zhong et al. 2015). The behaviour of pollutants, and of other scalar fluid constituents, around the scale of a neighbourhood (1–2 km) remains particularly difficult to interpret and model (Belcher 2005; Nikolova et al. 2018). This gap in our understanding is unfortunate because neighbourhood-scale processes disperse pollutants from peaks beside busy roads to levels treated as the ‘urban background’, and may link urban-pollution models with weather forecasts (Xie 2011). Indeed, numerical weather prediction models are beginning to resolve neighbourhood scales for certain processes, including the UK Met Office’s London Model, which has been used to forecast fog at a horizontal resolution of 333 m (Boutle et al. 2016).

As it is computationally unfeasible to resolve turbulent flow around individual obstacles at the neighbourhood scale, for most applications, researchers need a simplified approach. One route is to resolve the main features of the urban form, in the sense that boundary conditions are imposed at the surfaces of the largest obstacles (usually only the buildings are resolved). A common approach when resolving buildings at the neighbourhood scale is to apply the Reynolds-averaged Navier–Stokes (RANS) equations, which require the turbulent flow to be parametrised. Such an approach has been widely used to investigate how the urban form affects flow and dispersion at the smaller end of neighbourhood scale, such as through small networks of streets (Wang and McNamara 2006; Letzel et al. 2008; Carpentieri and Robins 2015). Many of the earlier RANS models simulated flow and scalar transport around generic urban-like structures, such as networks of cuboids or idealised street canyons (Toparlak et al. 2017 and references therein). More recently, resolved-building RANS models have been used to investigate flow in real neighbourhoods (Toparlak et al. 2015; Antoniou et al. 2017; Juan et al. 2017; Gao et al. 2018). For more information on RANS models of flow in urban areas, see Kumar et al. (2011), Tominaga and Stathopoulos (2013), Blocken (2014), and Toparlak et al. (2017).

4.2 Porous model of neighbourhood-scale flow

1465 4.2.1 Use of a porous model in urban areas

Another way of approximating neighbourhood-scale flow is to treat the urban canopy layer as a porous medium. Instead of resolving the buildings and other roughness elements in the urban area, all aerial parts of the urban area are represented indirectly through a distributed momentum sink. This is achieved by averaging the equations of motion over a volume that contains multiple roughness elements, which
1470 amalgamates the drag force from each roughness element into a continuous drag force throughout the urban canopy layer (UCL). This averaging process introduces additional terms into the momentum equation which do not appear in the equations for the freestream flow (Sect. 3 below, Coceal and Belcher 2004, and Lien et al. 2005).

1475 The porous-canopy method has been used extensively to study flow and scalar exchange in vegetation, particularly in homogeneous stands, from which a theoretical framework has emerged to explain certain statistically consistent features (Raupach and Thom 1981; Raupach et al. 1996; Finnigan 2000). A characteristic feature of flow through vegetation is that momentum is transferred over the depth of the canopy. The momentum transfer creates a strong inflection in the mean streamwise wind-speed profile,
1480 which is approximately exponential within the canopy and logarithmic above, and a layer of high shear around the top of the canopy. This shear generates Kelvin–Helmholtz type instabilities that dominate turbulence and ‘coherent’ motions, analogous to the dominant processes in a plane mixing layer (Raupach et al. 1996). Using the analogy of vorticity thickness in a mixing layer, Raupach et al. (1996) reduced canopy turbulence to a single length scale, $L_S = U_H/U'$, where U_H is the mean streamwise velocity component U at the height of the canopy H , and $U' = dU/dz$ at $z = H$. The shear length scale L_S provides
1485 a rough estimate of the diameter of the turbulent eddies, equating to around $0.5H$ for medium-density vegetation. Eddies of diameter L_S dominate the exchange of momentum and scalar quantities to and from the canopy. The inverse of the length scale L_S also represents the wavenumber of the fastest-growing instability at the top of the canopy. The coherent eddies in the shear layer induce characteristic patterns in
1490 the spatially averaged vertical profiles of higher-order moments, for example, of the variances or the skewness (Finnigan 2000).

Several studies have used the porous-canopy approach in mesoscale models to parametrise the flow through and above urban areas (Martilli et al. 2002; Santiago and Martilli 2010). Coceal and Belcher (2004, 2005)
1495 extended the work of Belcher et al. (2003) to calculate how the boundary layer adjusts upon entering an urban area (Sect. 2.3 below). Their model simulated mean velocity profiles that compared well, before and after the flow had adjusted, with wind-tunnel and field measurements reported by Davidson et al. (1995, 1996) and Macdonald (2000). Lien et al. (2005) derived a modified two-equation (k – ϵ) turbulence model, where k is the turbulence kinetic energy and ϵ is the turbulence dissipation rate, to simulate the flow through
1500 and over an array of buildings, in which clusters of buildings in the array are averaged and treated as a porous medium. Compared to high-resolution RANS simulations of flow over resolved cubes, this porous-

canopy model generated very similar vertical profiles of the mean wind speed, but less satisfactory profiles for turbulent variances, particularly in the regions around the tops of the buildings and very close to the ground (Lien and Yee 2005). Di Sabatino et al. (2008) adapted the porous model in Macdonald (2000) to simulate spatially averaged wind-speed profiles over London, Toulouse, Berlin, and Salt Lake City by varying the vertical profiles of the frontal-area density, λ_f (i.e., the total frontal area per unit ground area). Hang and Li (2010) derived a modified k - ϵ porous model to simulate the flow over arrays of aligned cubes. Compared to wind-tunnel observations, their porous model simulated macroscopic properties of the flow well, but under-predicted turbulence at the leading edges of the arrays. More recently, porous models have been used to investigate wider features of urban microclimates, such as heat-island effects (Hu et al. 2012; Wang and Li 2016) and the influence of urban trees on flow and pollutant dispersion (Krayenhoff et al. 2015; Salim et al. 2015; Wang et al. 2018).

4.2.2 Applicability of the porous model to the urban boundary layer

The porous model allows urban areas to be parametrised with a relatively small number of morphological variables. Detailed information around individual obstacles is lost, but cities can be represented simply enough to make numerical models of the neighbourhood scale, and upwards, computationally feasible. However, the model and its supporting theoretical assumptions must be used with caution when approximating urban areas. Direct numerical simulation (DNS) of idealized building arrays has shown that the eddy structure in the urban canopy shear layer is more spatially complex than its counterpart in homogeneous vegetation (Coceal et al. 2007), for example, quasi-coherent eddies may form in the wakes of the bluff elements (Böhm et al. 2013). The spatially averaged mean velocity profile in urban-like canopies—i.e., between squat, sharp-edged obstacles—is also rarely exponential (Castro 2017), having instead a sharp shear layer between the top of the canopy and the flow aloft.

However, the studies revealing the more striking differences between urban and vegetative flows have tended to use exaggerated urban forms, such as the use of arrays of cuboids (Coceal et al. 2007; Leonardi and Castro 2010; Castro 2017 and references therein). Further, because of the constraints in computational resolution and wind-tunnel capacity, even models of real urban areas typically only resolve the simplified forms of buildings and the streets (Xie and Castro 2009; Carpentieri et al. 2012; Toparlar et al. 2015; Antoniou et al. 2017; Juan et al. 2017). In reality, however, most urban areas are not just networks of buildings with small-scale irregular forms, but also have trees, street furniture, and other obstacles, all of which absorb momentum. Models of urban flow omitting those features also omit their effects on the flow and the transport of scalar quantities. For example, trees strongly influence urban flow and dispersion, particularly if they are of comparable height to buildings (Wang et al. 2018). Trees act as a direct momentum sink for the mean flow and reduce downwards turbulent transport of high velocity air from above the canopy (Giometto et al. 2017) as well as upwards turbulent transport of high-concentration air pollutants emitted along streets (Jeanjean et al. 2015).

1540 Many of the scaled vertical profiles of flow statistics are similar across vegetation and urban areas
(Finnigan, 2000; Christen, 2005 Figure 5.1). Several high-resolution studies of urban flow have also
identified Kelvin–Helmholtz instabilities in the shear layer around the tops of the buildings (Letzel et al.
2008; Salizzoni et al. 2011; Li et al. 2015), which mix air intermittently with the air aloft (Louka et al. 2000;
Cui et al. 2004; Cai 2012; Li et al. 2015) in a similar manner to the processes in vegetation. These features,
together with the comparisons with field and wind-tunnel observations in the studies cited above, support
1545 the use of the porous model for investigations of flow in urban areas as well as in vegetation. However, the
results need to be interpreted carefully. While the porous model simulates spatially averaged statistics well,
it offers no information about the flow or dispersion around the individual obstacles, which may differ
significantly from spatial averages (Coceal et al. 2007).

4.2.3 Spatial inhomogeneity and adjustment

1550 For flow into a city, such as from a rural area, there is an adjustment over a streamwise distance x_A in which
the mean flow balances the aerodynamic drag of the urban roughness (Coceal and Belcher 2004). Once the
flow has adjusted to the presence of the canopy, the net mean vertical velocity component almost totally
disappears, but the large vertical wind shear generates Kelvin–Helmholtz like instabilities around the top
of the canopy. It is worth noting that the ‘coherent structures’ generated by these instabilities refer to motion
1555 transporting a range of smaller vortices, rather than necessarily meaning the well-defined rolls of fluid that
appear in conceptual diagrams (Bailey and Stoll 2016). The spatial complexity of urban areas may prevent
coherent structures of a single length scale L_s from dominating turbulent exchange (Coceal et al. 2007). As
a rough guide, Okaze et al. (2015) calculated a turbulent length scale $\mathbb{L} \approx 0.1H$ using high-resolution large-
eddy simulation (LES) of the flow over an array of cubes.

1560 Most real urban areas are heterogeneous (i.e., patchy) in structure and density. For the flow within a city
with varying roughness, flow adjustment occurs over a distance x_A determined by the local characteristics
of the urban roughness (Coceal and Belcher 2004, 2005). We have some idea of how urban morphology
affects pollutant transport at the neighbourhood scale. For example, the mean age of air (Buccolieri et al.
1565 2010) and average pollutant concentration (Yuan et al. 2014) increase with the plan-area density λ_p (i.e.,
the total plan area per unit ground area). Urban areas are also better ventilated with increasing variation in
the height of obstacles (Hang et al. 2012).

1570 However, we do not have a clear conceptual picture of how changes in neighbourhood-scale urban form
affect the transport of pollutants and other scalar quantities. Here we present a simple model of
inhomogeneous flow within an urban area, in which air moves between areas of high and low frontal-area
density. We use the LES approach to investigate (a) the dynamical adjustment of the flow as it moves over
a neighbourhood of heterogeneous roughness; and (b) the effect of the adjustment on pollutant transport,
particularly features that may lead to improved parametrisations in mesoscale models.

1575 4.3 Method

4.3.1 Transport equations

We use right-handed Cartesian tensor notation, with the Einstein summation convention, and indices (i, j, k) take values $(1, 2, 3)$ respectively. For example, u_i is the velocity in the x_i direction, with $i = 1, 2, 3$ representing the streamwise (x), spanwise (y) and vertical (z) directions. We denote $\mathbf{x} = (x, y, z)$,
1580 $(u_1, u_2, u_3) = (u, v, w)$, and time as t .

We adapt LES models previously used for vegetation canopies by modelling the urban area as a porous body, with the obstacles represented as a momentum sink. The representation of the urban form is informed by porous models of urban areas, particularly studies by Coceal and Belcher (2004, 2005), which used
1585 mixing-length closure, and the RANS study of Lien et al. (2005). We used the ‘superficial’ or ‘extrinsic’ averaging procedure, i.e., the spatial averaging operation was performed over the total volume V_t of the UCL including both solid obstacles V_s and fluid parts V_f , where $V_t = V_f + V_s$. For a flow quantity ϕ such as velocity or stress,

$$\langle \phi \rangle = \frac{1}{V_t} \int_{V_t} \phi dV. \quad (4.1)$$

1590 Other LES studies of urban areas have used different procedures—for example, the ‘intrinsic’ average where the quantities are averaged only over the fluid volume V_f (e.g., Giometto et al. 2016). The superficial average treats pressure and velocity gradients as continuous in space, making it more straightforward to focus on the general dynamical effects of density changes, rather than discontinuities at the top of urban canopy layer. The superficial average also generates the simplest form of the averaged transport equations
1595 (Kono et al. 2010; Xie and Fuka 2018), making it easier to implement in a three-dimensional LES model than the intrinsic average. There are other situations where the intrinsic average operation may be more appropriate than the superficial, for example, when comparing simulated results to observations, because the intrinsic average produces results representative of local conditions within the fluid (Schmid et al. 2019). See Lien et al. (2005), Böhm et al. (2013), Xie and Fuka (2018), and Schmid et al. (2019) for further
1600 discussion of different averaging operations for urban areas.

Here we envisage an urban area comprising roughness elements of various shapes and sizes (buildings, trees and plants, signage, infrastructure, parked vehicles, etc.). The averaging is over an area that: (a) covers multiple roughness elements, but (b) is small compared with the distance over which the mean
1605 characteristics of roughness (e.g., the frontal-area density) varies. The vertical volume averaging is very thin in order to properly resolve the flow gradients. See Appendix 4A for conceptual background.

We used the LES mode of version 3.6.1 of the Weather Research and Forecasting model (WRF) (Skamarock et al. 2008) to solve the transport equations. The WRF model solves discretized forms of the

1610 spatially averaged momentum equations³ using the Runge–Kutta time-integration scheme (Wicker and Skamarock 2002),

$$\frac{\partial \langle u_i \rangle}{\partial x_i} = 0, \quad (4.2a)$$

$$\frac{\partial \langle u_i \rangle}{\partial t} + \frac{\partial \langle u_i \rangle \langle u_j \rangle}{\partial x_j} = -\frac{1}{\rho} \frac{\partial \langle p \rangle}{\partial x_i} + \frac{\partial \tau_{ij}}{\partial x_j} + B_i + f_c \epsilon_{ij3} (\langle u_j \rangle - U_{g,j}) + f_i, \quad (4.2b)$$

1615 where the kinematic mean stress tensor, τ_{ij} , represents the subgrid scale (SGS) stresses; $\langle p \rangle$ is the spatially averaged pressure; ρ is the air density; B_i is the buoyancy force: $B_i = -\delta_{i3} g \theta' / \bar{\theta}$, where δ_{ij} is the Kronecker delta, $\bar{\theta}$ is the potential temperature for hydrostatic balance, and θ' is the temperature variations with respect to $\bar{\theta}$; f_c is the Coriolis parameter; ϵ_{ij3} is the alternating unit tensor; and $U_{g,j}$ is the geostrophic velocity. The term f_i is related to the drag force (see Sect. 3.2 below). The angled brackets $\langle \cdot \rangle$ denote the spatially averaged quantities, for example, $\langle u_i \rangle$ is the i component of the averaged velocity field. Equation
1620 (4.2b) is closed by parametrising the stress τ_{ij} as

$$\tau_{ij} = -2\nu_{SGS} S_{ij}, \quad (4.3)$$

$$S_{ij} = \frac{1}{2} \left(\frac{\partial \langle u_i \rangle}{\partial x_j} + \frac{\partial \langle u_j \rangle}{\partial x_i} \right), \quad (4.4)$$

$$\nu_{SGS} = c_k \sqrt{\langle e_{SGS} \rangle} (\Delta x \Delta y \Delta z)^{\frac{1}{3}}, \quad (4.5)$$

1625 where $\langle e_{SGS} \rangle$ is the SGS turbulence kinetic energy (TKE) and $c_k = 0.10$ is a modelling constant. The prognostic equation for the evolution of the term $\langle e_{SGS} \rangle$ is,

$$\frac{\partial \langle e_{SGS} \rangle}{\partial t} + \frac{\partial \langle u_j \rangle \langle e_{SGS} \rangle}{\partial x_j} = \nu_{SGS} \frac{\partial}{\partial x_j} \left(\frac{\partial \langle e_{SGS} \rangle}{\partial x_j} \right) + P + F - \frac{C_\epsilon \langle e_{SGS} \rangle}{(\Delta x \Delta y \Delta z)^{\frac{1}{3}}}, \quad (4.6)$$

1630 where P represents the shear- and buoyancy-production terms (Skamarock et al. 2008), F is a cascade term to account for the SGS TKE lost due to the interaction of SGS eddies with the obstacles in the urban area (see Equation (4.11) below), and C_ϵ is the dissipation coefficient (Moeng et al. 2007).

1635 After model spin-up (see Sect. 3.4 for details), we introduce continuous sources of passive scalars to represent traffic fumes at the horizontal centres of each grid cell at $z = 0.15H$. Pollutant fluxes from traffic fumes—such as ultrafine particles—vary spatially and temporally (Levy and Hanna 2011). However, at the neighbourhood scale, scalars at a particular location can be treated as the sum of releases of many sources (Belcher 2005). Here, we focus on ‘road-to-ambient’ scalar processes, up to the neighbourhood scale

³ Strictly, the governing equations in the compressible non-hydrostatic WRF model are expressed in terrain-following eta coordinates. However, we present the Cartesian form of the equations here for ease of interpretation. See Chapter 3, section 3.2 and Skamarock et al. (2008) for further details.

(Harrison et al. 2018). We specify a unity-emission source term, Q (in $\mu\text{g m}^{-3} \text{s}^{-1}$), in the filtered advection–diffusion equation that the LES model solves to model the transport of a passive scalar,

$$\frac{\partial \langle c \rangle}{\partial t} + \langle u_i \rangle \frac{\partial \langle c \rangle}{\partial x_i} = \frac{\partial}{\partial x_i} \left(K_c \frac{\partial \langle c \rangle}{\partial x_i} \right) + Q, \quad (4.7)$$

1640 where $\langle c \rangle$ is the filtered concentration for a passive scalar, and K_c is the SGS eddy diffusivity. We applied the 'superficial' averaging operation to all of the variables, meaning the pollutant is diluted in the same volume independently of changes to the frontal-area density (see Sect. 4.3.3 below).

4.3.2 Approximating the drag force

1645 The parametrisation of the drag force f_i in Equation (4.2b) is performed by spatially averaging the localised drag from the individual elements of the urban area, assuming the drag force is proportional to the square of the flow speed. The viscous component of the drag is assumed negligible compared with the much larger inertial component (Hamlyn and Britter 2005). For the form-drag component, consider an array of roughness elements distributed over a total area A_t , where each element has mean height H , frontal area A_f and drag coefficient $C_d(z)$. The drag force over a thin layer dz of each element at height z is

$$\rho f_i A_t dz = \rho U^2(z) C_d(z) A_f \frac{dz}{H}. \quad (4.8)$$

1650 The thin averaging volume at height z is $A_t dz$. The total force per unit volume (including both solid and fluid elements) is, therefore,

$$\rho f_i = \rho \frac{C_d(z) \Sigma A_f}{H A_t} (\langle u_j \rangle \langle u_j \rangle)^{\frac{1}{2}} \langle u_i \rangle, \quad (4.9)$$

1655 which amalgamates the spatially discontinuous drag force from each roughness element into a continuous resistive body force throughout the urban area (Belcher et al. 2003). In Equation (4.9), $C_d(z)$ is the sectional drag coefficient, which is largely unknown for real urban areas, for which bulk transfer coefficients such as u_*/U are easier to measure (Nordbo et al. 2013; Peng and Sun 2014). In arrays of cubes, the drag coefficient $C_d(z)$ decreases with height because the wind speed increases from the surface (Cheng and Castro 2002; Kono et al. 2010; Castro 2017), although the value of $C_d(z)$ can vary by almost an order of magnitude depending on whether the cubes are aligned or staggered (Coceal et al. 2006). As a
1660 simplification, we adopted the common approach of taking a height-averaged sectional drag coefficient \bar{C}_d (Macdonald 2000; Martilli et al. 2002; Coceal and Belcher 2004; Yang et al. 2006b). We assumed $\bar{C}_d = 1.3$, which is derived from wind-tunnel observations (Coceal and Belcher (2004⁴), who analyse the results of Cheng and Castro (2002)), and is within the range of values measured in urban-like canopies (e.g., Castro

⁴ Coceal and Belcher (2004) calculate the height-averaged sectional drag coefficient, $\bar{C}_d = 2.6$. However, Coceal and Belcher retain the engineering convention of including a factor of 1/2 in their formulation of the mean drag force. We have not included that factor in our notation here, but have incorporated it into the estimate of \bar{C}_d .

2017). Taking the frontal-area density $\lambda_f = \sum A_f/A_t$, $|U| = (\langle u_j \rangle \langle u_j \rangle)^{\frac{1}{2}}$, and cancelling the density ρ , Equation (4.9) simplifies to

$$f_i = -\frac{\bar{C}_d \lambda_f}{H} |U| \langle u_i \rangle. \quad (4.10)$$

We also add a cascade term,

$$F = -2 \frac{\bar{C}_d \lambda_f}{H} |U| \langle e_{SGS} \rangle \quad (4.11)$$

into the transport equation for the SGS TKE, $\langle e_{SGS} \rangle$, in Equation (4.6) to account for additional dissipation of kinetic energy from air–obstacle interactions at scales below the spatial filter, bypassing the usual inertial cascade (see discussion in Lien et al. 2005 in the context of RANS modelling of urban areas; and Shaw and Schumann 1992, Shaw and Patton 2003, and Dupont and Brunet 2008 in the context of LES investigations of vegetation canopies). Without this SGS sink, the model overestimates the kinematic turbulent momentum flux within the UCL, as well as the TKE above the UCL (Lien and Yee 2005). See Appendix 4A for conceptual background and details on how these formulations are included in the WRF model.

4.3.3 Simulated cases

We used this model to simulate six different cases comprising:

- i. **a homogeneous control case** - uniform frontal-area density across the entire neighbourhood; and
- ii. **five cases of alternating values of λ_f (4H, 6H, 8H, 12H, and 16H cases)** - alternating patches of high and low frontal-area density spanning the entire domain east–west and, respectively, extending 4H (80 m), 6H (120 m), 8H (160 m), 12H (240 m), and 16H (320 m) south–north.

We simulated these patches of high and low frontal-area density by alternating the value of λ_f in Equations (4.10) and (4.11). For each simulated case, we calculate a mean frontal-area density, $\lambda_m = \sum A_f/A_t = 0.25$ across the entire domain, which we apply uniformly in the homogeneous case. For the alternating cases, we simulated alternating patches of high and low frontal-area density, which we respectively refer to as ‘dense’ ($\lambda_f = \lambda_d = 1/3$) and ‘sparse’ ($\lambda_f = \lambda_s = 1/6$) (Figure 4.1). These were chosen as typical values for sparse and dense urban areas (e.g., Oke 1988a; Nakayama et al. 2011; Kanda et al. 2013). Each of the alternating-density cases contained equal numbers of sparse and dense patches. The horizontal averages of the ratio $\bar{C}_d \lambda_f / H$ at a given height z in Equations (4.10) and (4.11) are, therefore, equal across all the simulated cases. Here we represent the effective heterogeneous frontal-area density λ_f in neighbourhoods where the plan-area density of the buildings λ_p remains approximately constant. This is not possible in the case of flow perpendicular to aligned cubes, the subject of many previous studies of urban-like areas, for which $\lambda_f = \lambda_p$. However, by considering the effect on the flow of all of the obstacles in an urban area, not just the buildings, the value of λ_f varies over small areas even within a neighbourhood (e.g., neighbouring streets having very different amounts of vegetation, or signage and infrastructure). In

these cases, the presence of non-building obstacles may contribute significantly to the total drag exerted on the flow while occupying relatively little plane-surface area and volume in comparison with the buildings (i.e., the quantities λ_p and V_s are approximately constant between patches). Alternating variations of the frontal-area density λ_f may also arise due to variations in the size, form, or arrangement of obstacles with respect to the wind direction. Formulating the model in terms of alternating variations of the frontal-area density λ_f raises the question of whether the drag coefficient \bar{C}_d also varies between patches. Wind-tunnel (Hagishima et al. 2009; Zaki et al. 2011) and LES (Nakayama et al. 2011) studies across a variety of building geometries indicate the value of \bar{C}_d does appear to vary slightly with the frontal-area density λ_f , with a peak in the range $\lambda_f \approx 0.15\text{--}0.2$. However, there is considerable scatter in the results depending on the geometry of the modelled urban areas and the value of \bar{C}_d varies relatively little for the range of λ_f values considered here. We, therefore, assume \bar{C}_d is constant across the simulated domain, while acknowledging this slightly overestimates the difference in drag between the sparse and dense patches.

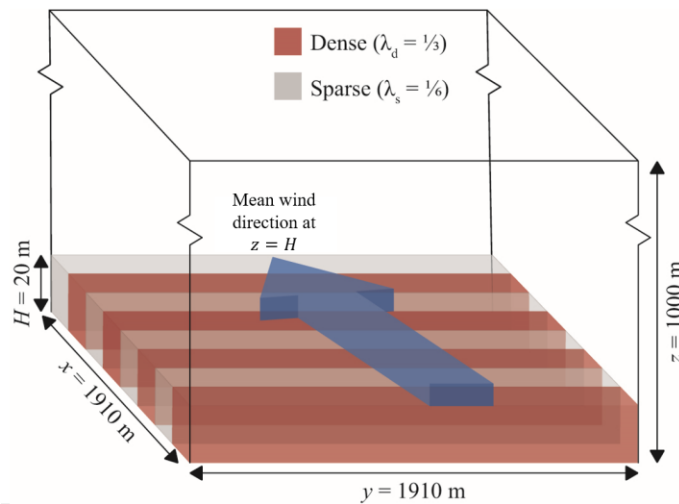


Figure 4.1: Schematic of the simulated domain, showing alternating density patches within an urban neighbourhood, with λ_d and λ_s referring to the frontal-area densities of the dense and sparse patches, respectively. The $12H$ case (section 4.3.3) is shown from the post-processing frame-of-reference with the x -direction aligned south–north, approximately with the mean wind direction.

4.3.4 Numerical details and post-processing

The simulated domain is $191 \times 191 \times 79$ grid cells in the streamwise, spanwise, and vertical directions, respectively (Figure 4.1). The horizontal grid resolution is 10 m in each direction, and increased vertically from around 0.67 m within the lower half of the UCL to around 60 m at the top of the domain. The mean height of the roughness elements (and therefore the UCL), H , is set to 20 m. We simulated the flow under neutral conditions. We included a dampening layer of 300 m at the top of the domain to minimize wave reflection because the LES model does not always maintain a deep neutral boundary layer over long simulations (Nottrott et al. 2014). The potential temperature θ was held constant at 283.15 K within the neutral layer at the bottom of the domain (up to $z = 475$ m), increasing to $\theta = 291.7$ K at the top of the

simulated domain. The geostrophic velocity components are set to $U_g = 10 \text{ m s}^{-1}$ and $V_g = 5 \text{ m s}^{-1}$, giving a mean wind speed of 1.7 m s^{-1} from a flow direction of 158° at $H = 20 \text{ m}$ —i.e., at the top of the canopy— and at an angle of 22° to the patches (see Figure 4.1). The difference in mean wind direction with respect to the geostrophic wind direction result from the balance of the shear stress force, the Coriolis force and the surface drag, with the steepest change occurring across the inversion layer at the top of the boundary layer. The spin-up time was 9 h, with cyclic boundary conditions for all dynamical variables (u, v, w, e_{SGS}, T , etc.) in both the x - and y -directions. Boundary conditions for the scalars were non-cyclic; at the inlet boundaries, all scalars were set to zero and the outlet boundaries were open. In the model set-up, we used the meteorological convention where the x -direction is aligned west–east and the y -direction south–north. For post-processing, we rotate our frame-of-reference so that the x -direction is aligned south–north, approximately with the mean wind direction, as shown in Figure 4.1.

After the spin-up, we introduced the scalars and ran the simulations for a further 120 min, taking samples at intervals of 3 s. We time averaged over the latter 100 min (denoted by T_a) of these samples (i.e., $t_0 = 20 \text{ min}$ to $t_0 + T_a = 120 \text{ min}$). Sensitivity testing (not shown) indicated scalar concentrations reached local pseudo-equilibrium 15–20 min after being introduced, where pseudo-equilibrium was defined as the time at which mean concentrations at $z = H$ deviated within $\pm 5\%$ from those at $t = 120 \text{ min}$. The concentrations before the time t_0 were therefore excluded from the analysis. This process generated a three-dimensional timeseries of 2000 resolved samples in the form $\langle \phi \rangle(x, y, z, t)$. We derived the resolved turbulent statistics using (a) time averages over the sampling period; and (b) spatial averages along the y -direction ($L_y = 1910 \text{ m}$), over which the turbulent statistics are homogeneous. For each resolved variable, $\langle \phi \rangle$ this generated a two-dimensional function,

$$[\bar{\phi}](x, z) = \frac{1}{T_a L_y} \int_0^{L_y} \int_{t_0}^{t_0+T_a} \langle \phi \rangle(x, y, z, t) dt dy, \quad (4.12)$$

where the resolved fluctuating component of $\langle \phi \rangle$ around $[\bar{\phi}]$ is defined as $\langle \phi \rangle'(x, y, z, t) = \langle \phi \rangle(x, y, z, t) - [\bar{\phi}](x, z)$. The covariance of two resolved variables $\langle \phi \rangle$ and $\langle \varphi \rangle$ is in turn defined as

$$[\overline{\phi' \varphi'}] = \frac{1}{T_a L_y} \int_0^{L_y} \int_{t_0}^{t_0+T_a} \langle \phi \rangle'(x, y, z, t) \langle \varphi \rangle'(x, y, z, t) dt dy, \quad (4.13)$$

with the autovariance $[\overline{\phi' \phi'}]$ similarly defined. The time-averaged resolved TKE is defined as $[\bar{e}] = \frac{1}{2} \overline{\langle u_i \rangle' \langle u_i \rangle'}$. We use square brackets $[\cdot]$ to denote the spatial averaging along $y \in [0, L_y]$, and we omit the angled brackets denoting the volume averaging below.

4.4 Results – Dynamics

4.4.1 Comparison with published data

We examined a selection of flow statistics: the mean streamwise velocity component $U = [\bar{u}]$, the square root of the magnitude of the shear stress $F_u = (-[\overline{w'u'}])^{\frac{1}{2}}$, and the streamwise turbulence intensity $\sigma_u = [\overline{u'u'}]^{\frac{1}{2}}$. Figure 4.2 presents (a) the vertical profiles of U for the homogeneous control case and the sparse patches of the $16H$ case; (b) F_u for the homogeneous case; and (c) σ_u for the homogeneous case. The vertical axis is normalized by $z = H = 20$ m, and the velocity moments with either (a) $u_H = |U|$ at $z/H = 1$; or (b) friction velocity $u_* = ([\overline{w'u'}]^2 + [\overline{w'v'}]^2)^{\frac{1}{4}}$ at $z/H = 1$. Also plotted are data from Castro et al. 2006 (hereafter CCR06), a wind-tunnel study; Coceal et al. 2007 (hereafter CDT07) and Leonardi and Castro 2010 (hereafter LC10), both DNS studies; and Yang et al. 2016 (hereafter YSMM16), an LES study. Each of these studies models the flow over arrays of cubes. In both CCR06 and CDT07, measurements were taken on top of a cube (which the authors denote position 0), behind (position 1), and in front of a cube (position 2), and in the gap between two adjacent cubes (position 3)—see Figure 1 of CCR06 and Figure 1b of CDT07. The measurement position 2 and the mean quantities (average of positions 0–3) provide the most meaningful comparison to our simulations because the others are strongly influenced by small-scale features that the porous model cannot capture. The spatially averaged vertical profiles in Figure 4.2a, using data from LC10 and YSMM16, were generated using the superficial averaging operation.

Our simulated U component above the canopy, where the profile is logarithmic, agrees well with both the observations at position 2 and the mean profile from CCR06⁵. Within the canopy, the vertical profile of U for our homogeneous case is approximately exponential, and closely matches that found by CCR06 for position 2 in the top two-thirds of the canopy. However, it deviates from the CCR06 mean and from LC10 for a frontal-area density $\lambda_f = 0.25$, which both reflect the non-exponential behaviour observed in flow over cubic arrays (Castro 2017). Our sparse profile ($\lambda_f = 1/6$) shows qualitative agreement with LC10 for a frontal-area density $\lambda_f = 0.16$ in that the ratio U/u_H increases at each height z compared to the case where $\lambda_f = 0.25$, but again our model does not simulate the non-exponential behaviour seen in the cubic arrays. We attribute these differences to the different model configurations, i.e., we are simulating flow through a porous medium rather than over cubes, and therefore expect a less pronounced shear region at the top of the canopy. We also suspect the filter resolution accounts for some of the difference. Our LES mesh is quite fine in the vertical ($H/20$ within the canopy), but coarse in the horizontal ($H/2$) compared with the DNS mesh of $H/32$ in LC10, for example. We note that our homogeneous profile is very similar to that in YSMM16, who simulate the flow over cubes but using a relatively coarse LES mesh ($H/8$).

Our model simulates greater F_u and σ_u values above the canopy than were observed in CCR06 and CDT07 (Figure 4.2b, c), which we attribute to the very low boundary-layer heights (H_i) in CCR06 ($H_i = 7.4H$) and

⁵ The mean profile for CDT07 is almost identical to that for CCR06 and is not plotted.

CDT07 ($H_i = 8.0H$), whilst ours is much higher at $H_i \approx 25.0H$. If the parameters F_u and σ_u are scaled vertically by $(H_i - H)$ rather than H (not shown), the shapes of the vertical profiles above the UCL differ less than in Figure 4.2b, c. We also attribute the smaller σ_u values above the UCL in CCR06 and CDT07 to the reduced amount of resolved TKE, which decreases with decreasing ratios of H_i/H (Grylls et al. 2020). Our simulated vertical profiles of these quantities do eventually decrease with height, as would be expected, for $z/H > 5$ (not shown). The most notable difference in the profiles between our simulations and CCR06/CDT07 occurs for the turbulence intensity σ_u in the lower part of the canopy (Figure 4.2c) where our model predicts less turbulence than was observed in CCR06 and CDT07. The LES model does not expressly resolve the smallest eddies (i.e., those $< 2dx = H$ in our case), which likely account for a high proportion of the total turbulence in the lower part of the canopy. Figure 4.2c includes only the resolved turbulence intensity σ_u , and therefore some of the ‘missing’ turbulence is captured by the SGS scheme. Because our mean wind direction is not completely perpendicular to the canopy, there is a small spanwise (y) component for each variable that we do not present in these results. However, the spanwise components exist along the homogeneous y -direction with a cyclic boundary condition, and the impact on the processes in the streamwise direction is, therefore, negligible. We also bear in mind that Figure 4.2b, c are not entirely direct comparisons. Our results are superficially averaged values throughout a porous medium and the published values are vertical profiles from a single position (position 2) in an array of cubes. Overall, our simulated profiles show a reasonable agreement with the published data, given that we are not simulating flow over cubes, but rather a porous medium of the same mean frontal-area density. Our choice of the \bar{C}_d value in the drag parametrisation in Equation (4.10) appears reasonable in that our simulations do not strongly under- or overestimate any of the parameters U , F_u , or σ_u at each height in the domain. Our simulated profiles differ most from the flow over cubes at the bottom of the canopy, where reversed-flow regions can occur around bluff objects, such as cubes, but only occur at quite high densities in porous media (Cassiani et al. 2008). It is also in the lower part of the canopy that our assumption of a height-independent drag coefficient is probably least appropriate, through analogy with flow through arrays of cubes (Cheng and Castro 2002; Kono et al. 2010; Castro 2017), the subject of the studies to which we compared our simulations. Of course, our results and those in the studies cited here are simplified models of urban areas, and therefore can only guide the interpretation of flow through real cities.

1815

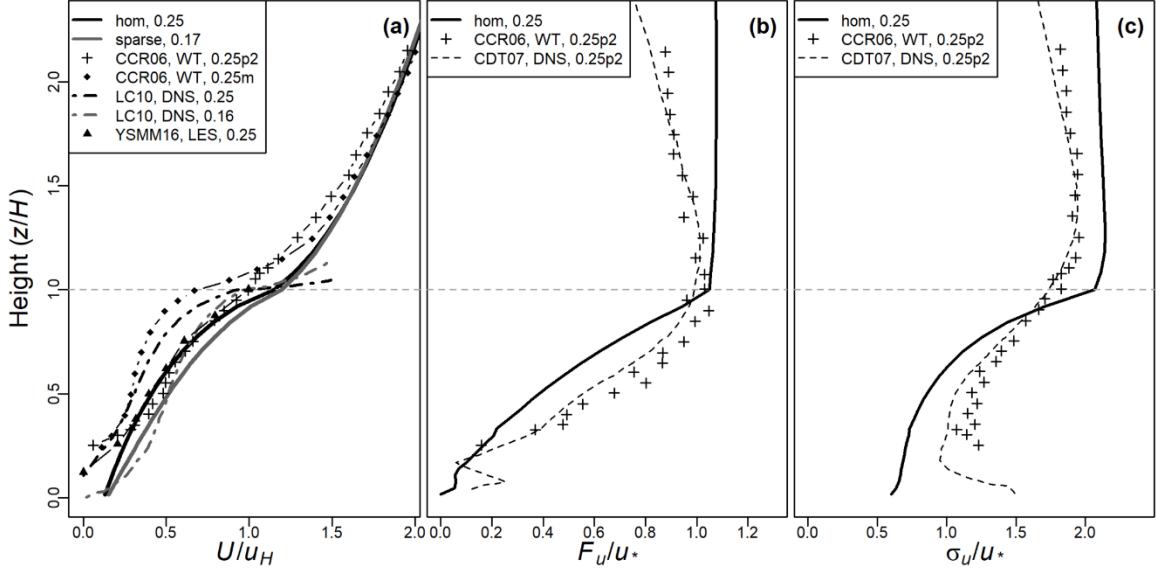


Figure 4.2 Canopy spatially averaged mean vertical profiles of the (a) mean streamwise velocity component U/u_H , (b) shear stress F_u/u_* , and (c) streamwise turbulence intensity σ_u/u_* . Values of the frontal-area density λ_f are given in the legends. The sparse profile in (a) is the spatial average of the sparse patches of the $16H$ case. The wind-tunnel (WT), DNS and LES cases in the legends denote the type of model used in each study. The m and p2 symbols in the legends for CCR06 and CDT07 (see first paragraph of section 4.4.1) respectively denote the mean (average of positions 0–3) and position 2 quantities.

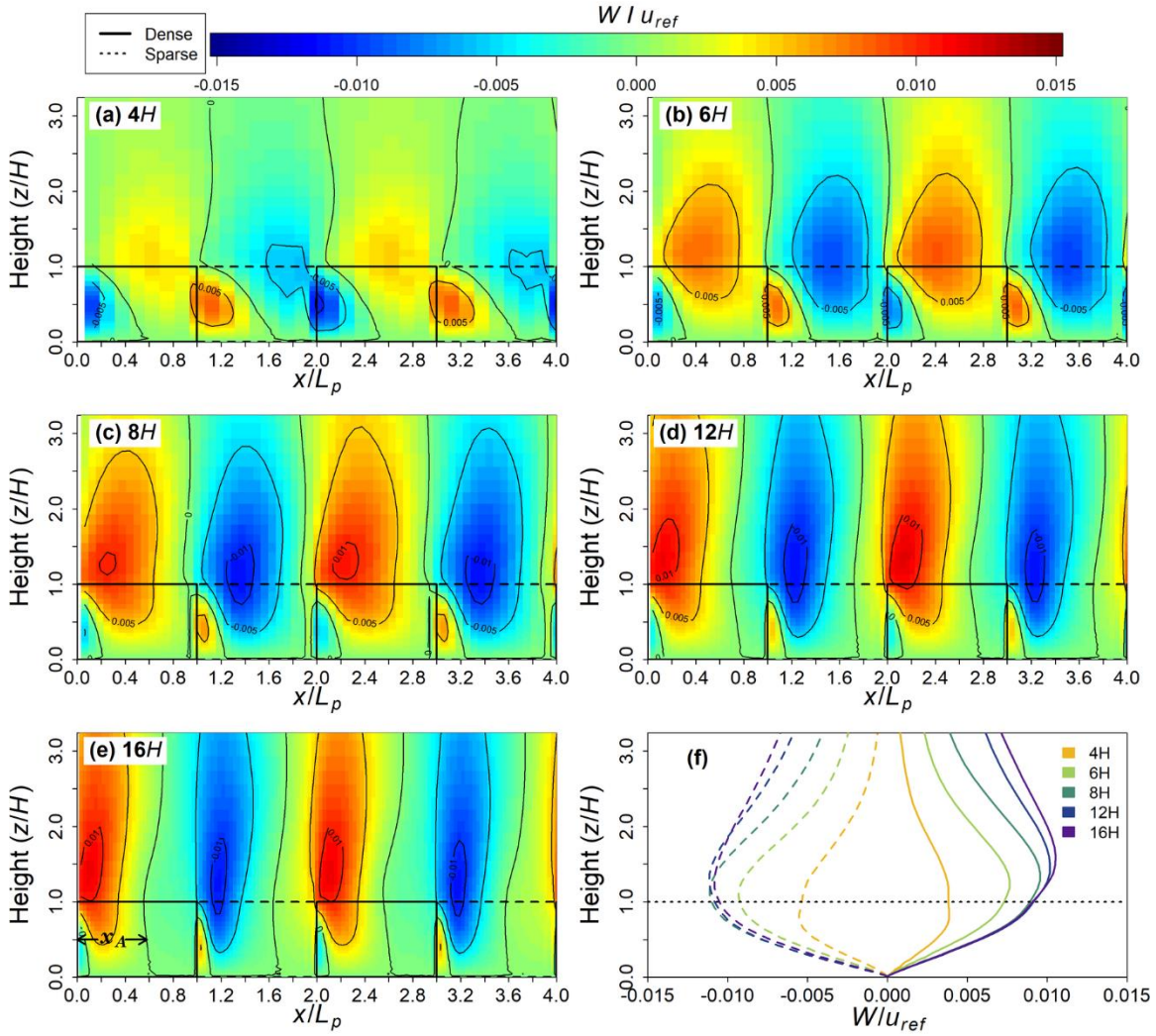
4.4.2 Adjustment of the flow

As the flow adjusts between the patches of different frontal-area density, we define the adjustment distance x_A as proposed by Belcher et al. (2003) and Coceal and Belcher (2004, 2005), as the distance in the streamwise direction at which mean vertical velocity component $W = [\bar{w}] \approx 0$ at $z = H$. Figure 4.3 shows the perturbation of mean vertical velocity component W by the alternating density patches, with the values of W normalized by $u_{ref} = |U|$ at $z/H = 7.5$. The first four patches are pictured (Figure 4.3a–e), with the streamwise distance normalized by the patch length L_p . Here $x_A \approx 8–9.5H$, which can be seen most clearly in the position of the zero contour lines in the $12H$ and $16H$ cases (Figure 4.3d, e) that occur at $x/L_p \approx 0.8$ and 0.6 , respectively, downstream of each patch edge. The adjustment distance x_A is labelled in the first patch of Figure 4.3e. In the $8H$ case (Figure 4.3c), the magnitude of x_A is visible as the zero contour lines that occur around the end of each patch.

Another measure of the minimum distance over which the flow adjusts uses the urban canopy length scale L_c , which can be interpreted as the half-distance the flow takes to accelerate or decelerate (Belcher et al. 2003; Coceal and Belcher 2004). The canopy element drag in Equation (4.10) can be expressed as

$$f_i = \frac{\bar{C}_d \lambda_f}{H} |U| \langle u_i \rangle = \frac{|U| \langle u_i \rangle}{L_c}, \quad (4.14)$$

so that $L_c = H/\bar{C}_d\lambda_f$. At the transition of the frontal-area density, the mean velocity component adjusts
1840 over a total streamwise distance $x_A \approx 3L_c \ln(K)$, where $K = (U_H/u_*)/(H/L_c)$ (Coceal and Belcher 2004).
Using our results, this gives $x_A \approx 7.8H$ and $9.2H$ for the dense and sparse patches, respectively. This
matches the range obtained using our alternative definition surprisingly well given that Coceal and Belcher
(2004) derived this formula based on linear-scaling arguments by Belcher et al. (2003) and a very
approximate linear regression of the variation of the normalized adjustment distance x_A/L_c with $\ln(K)$.
1845 Their formula also assumes the incident wind-speed profile is logarithmic, which is not the case here
because the presence of the canopy causes the profile to inflect around $z/H = 1$.



1850 **Figure 4.3: Effect of patchiness on the mean vertical velocity component, W .** (a–e) Two-dimensional patterns of W in each of the alternating-density cases. Only the first four patches are pictured, with the streamwise distance normalized by patch length L_p and the values of W normalized by u_{ref} . The dense patches and the sparse patches are bounded by the solid and dashed lines, respectively; (f) vertical profiles of W at $x = 3H$ downstream of each patch. The solid and dashed lines represent profiles at $x = 3H$ inside the dense patches and $x = L_p + 3H$ inside the sparse patches, respectively; the magnitude of x_A is marked on the first patch of (e).

4.4.3 Dynamical patterns induced by adjustment to density changes

1855 The alternating-density patches induce clear dynamical patterns in the flow, which affect the exchange between the UCL and the air aloft. Figure 4.4 shows the perturbation of the mean streamwise velocity component U by the alternating-density patches, relative to the homogeneous control case, with positive and negative values representing higher and lower U than the homogeneous case. At the top of the UCL, the value of U is higher in sparse patches than in the dense (Figure 4.4a–e). However, the flow adjusts over a distance $x_A \approx 8–9.5H$ inside the UCL as it moves between patches of different density, as indicated by the location of the maxima and minima in U values for the 12H and 16H cases, for which the mean flow fully adjusts in each patch. The adjustment distance x_A is marked on the second patch in Figure 4.4e (the 16H

1860

case). The patch length L_p relative to x_A determines the magnitude of the perturbations and the effect of density transitions on the roughness sublayer above the canopy. For the cases we investigated, the magnitudes of the perturbations increase with increasing values of L_p/x_A , and vice versa.

For the $4H$ and $6H$ cases, where $L_p < x_A$, the flow cannot fully adjust between patches, which means that each patch reflects the characteristics of the previous patch, particularly in the lower half of the canopy (i.e., the value of U is high in the dense patches and low in the sparse). However, for the $8H$, $12H$ and $16H$ cases, where $L_p \geq x_A$, the patches are sufficiently extensive for the mean flow to adjust within each patch. This is reflected in the vertical profiles of U (Figure 4.4f) where, for the $12H$ and $16H$ cases, the value of U is high in the sparse patches and low in the dense at nearly all heights in the canopy. The profiles for the $4H$ and $6H$ cases, however, invert at around $z = 0.5H$, while the profile for the $8H$ case shows a transition between the two extremes, with the magnitudes of the perturbations in U values increasing with the patch size (Figure 4.4f).

The adjustment of the streamwise flow affects vertical exchange. Figure 4.3f shows the peak magnitudes of the vertical velocity component W at the upstream edge of each patch increase with patch size for the $4H$ and $6H$ cases, where $L_p < x_A$. However, the profiles are very similar for the $8H$, $12H$, and $16H$ cases, where $L_p \geq x_A$, because the patches are sufficiently extensive for the mean flow to adjust within each patch, generating strong mean vertical exchange with the UCL. Generally, the value of W is negative (downwards) in and above the sparse patches and positive (upwards) in and above the dense patches, aside from the small reversal caused by the sudden pressure changes at the upstream edge of each patch (Figure 4.3a–e). Patch density affects the value of W above the UCL up to around $z = 5H$ in the $4H$ and $6H$ cases, rising to around $z = 15H$ in the $12H$ and $16H$ cases.

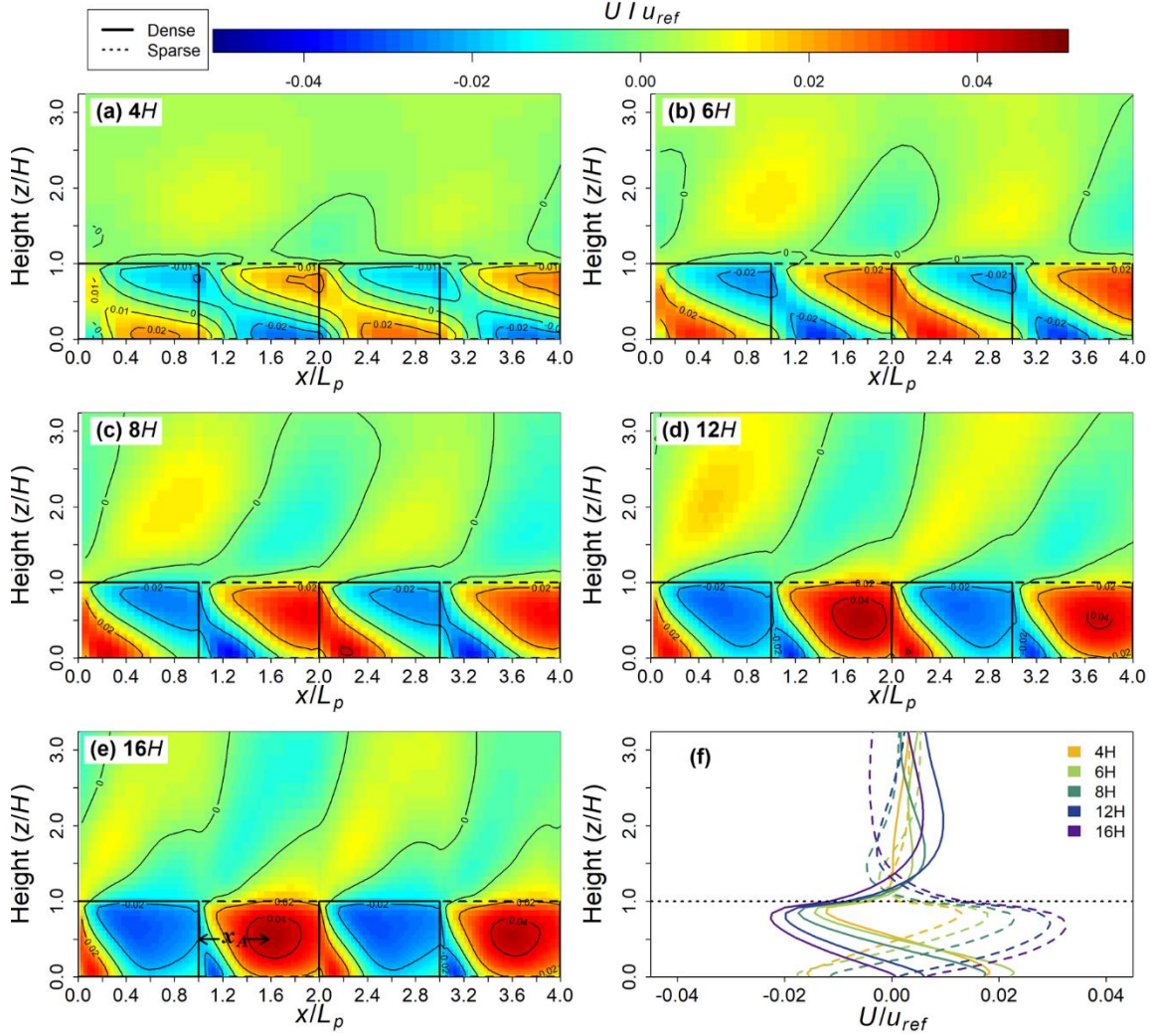


Figure 4.4 Effect of patchiness on the mean streamwise velocity component U . (a–e) Two-dimensional perturbations of U in each of the alternating-density cases. Only the first four patches are pictured, with the streamwise distance normalized by the patch length L_p and the values of U normalized by u_{ref} . The dense patches and the sparse patches are bounded by the solid and dashed lines, respectively; (f) mean vertical profiles of U in the dense and sparse patches. The solid and dashed lines represent profiles at $x = 3H$ inside the dense patches and $x = L_p + 3H$ inside the sparse patches, respectively; the magnitude of x_A is marked on the second patch of (e).

1890

1895

The alternating density of the urban form also affects the turbulent components of the flow. Figure 4.5 presents normalized vertical profiles of resolved TKE, $[\bar{\epsilon}]$, and $F_u = (-[\overline{w'u'}])^{\frac{1}{2}}$ as the perturbation of each variable by the alternating-density cases relative to the homogeneous control case. For a resolved variable ϕ , profiles of $\phi_{alt} - \phi_{hom}$ are shown, where subscripts *alt* and *hom* refer to the alternating-density and homogeneous cases. Appendix 4B presents two-dimensional plots of perturbations of the parameters $[\bar{\epsilon}]$ and F_u analogous to those for the velocity components W and U in Figure 4.3 and 4.4.

1900

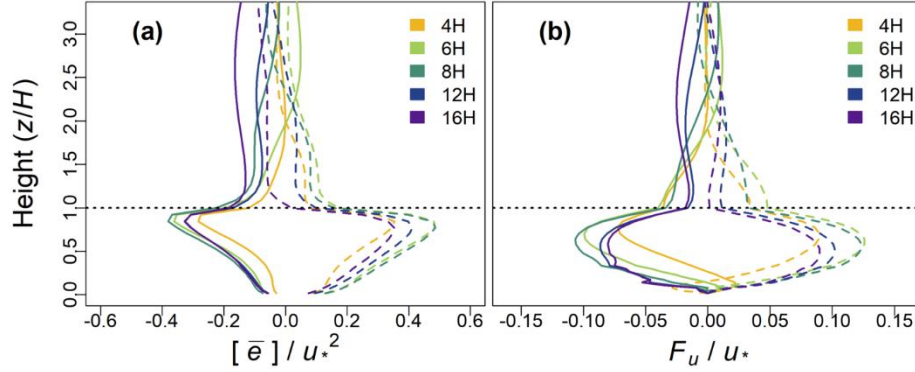


Figure 4.5: Vertical perturbation profiles of (a) $([\bar{e}]_{alt} - [\bar{e}]_{hom})/u_*^2$ and (b) $(F_{u_{alt}} - F_{u_{hom}})/u_*$ (see section 4.4.3 for definitions). The solid and dashed lines represent profiles at $x = 3H$ inside the dense patches and $x = L_p + 3H$ inside the sparse patches, respectively.

1905

Figure 4.5a shows that the resolved TKE $[\bar{e}]$ is high in the sparse patches and low in the dense, with peak positive and negative perturbations occurring just below $z = H$. The profiles for the sparse and dense patches are not symmetrical. In all cases, positive perturbations (high $[\bar{e}]$) in the sparse patches extend through the depth of the UCL, while negative perturbations (low $[\bar{e}]$) are pronounced only at the top of the UCL. The profiles show slightly higher peak magnitude perturbations for the $6H$ and $8H$ cases, because, for those cases, the spatial average includes the strongest perturbations in turbulence that occur at the upstream edge of each patch (Figure 4A.1) but only very little adjusted flow, where the perturbations are weaker (as in the $12H$ and $16H$ cases towards the downstream edge of each patch). The value of F_u is high in the sparse patches and low in the dense patches at most heights within the UCL (Figure 4.5b). The height at which the greatest mean perturbations of F_u occur decreases with patch size from around $z = 0.8H$ for the $4H$ case to $z = 0.5H$ for the $16H$ case. As previously observed for the TKE $[\bar{e}]$, the profiles show slightly higher peak magnitude perturbations for the $6H$ and $8H$ cases, again due to the proportion of adjusting versus adjusted flow that is captured in the spatial average.

1910

1915

4.5 Results – Behaviour of pollutants

1920

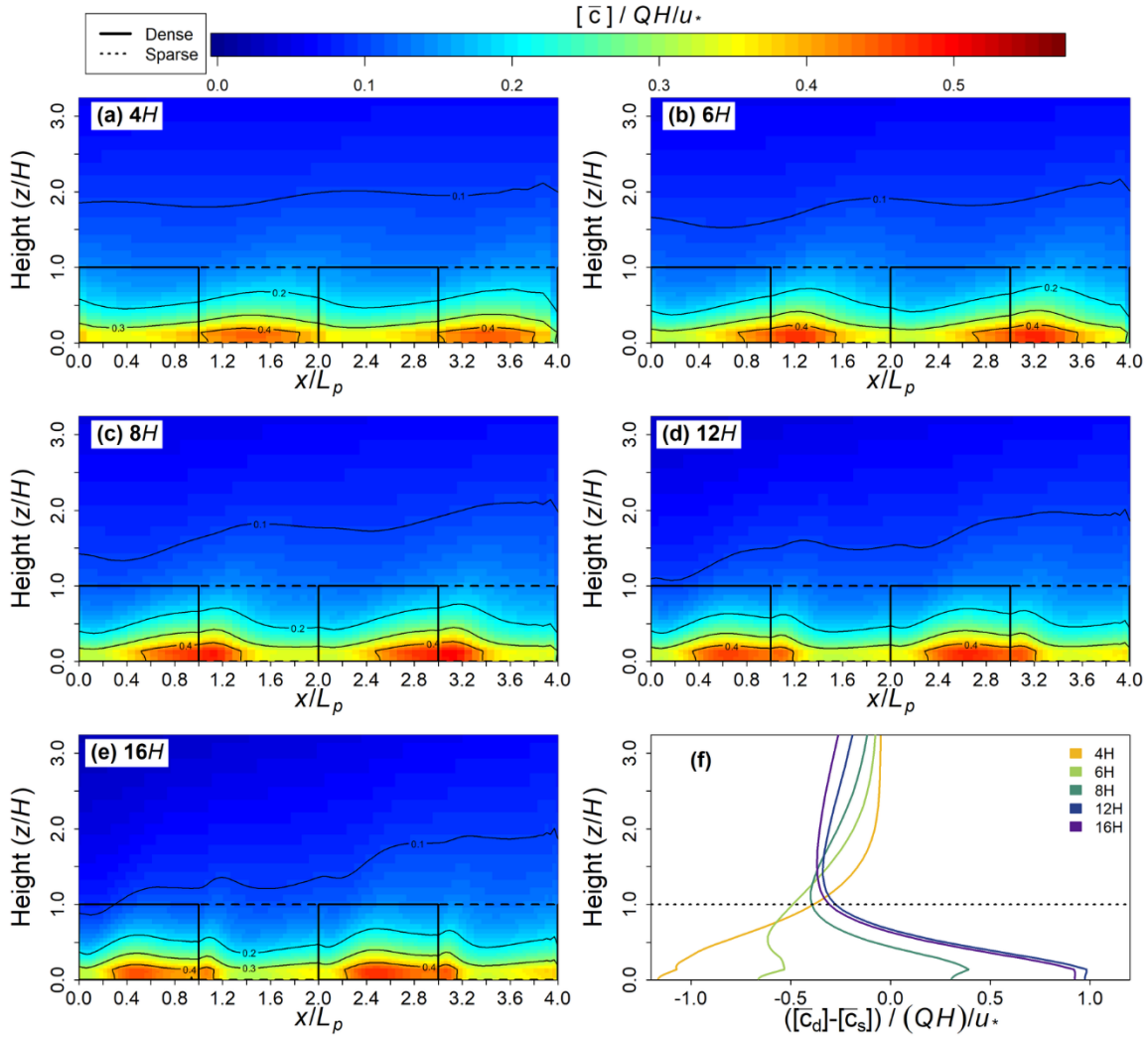
4.5.1 Two-dimensional patterns in pollutant concentration

Figure 4.6 presents two-dimensional plots of normalized pollutant concentration $[\bar{c}]/(QH/u_*)$ in each of the alternating-density cases. We used non-cyclic boundary conditions for the passive scalar. The scalar has a fixed inlet of zero at the upstream edge of the domain and is open at the downstream edge, meaning the scalar concentration increases across the domain. Figure 4.6 presents the final four patches of each domain where the scalar concentration is highest, and by which point the patterns in concentration and fluxes have had the greatest distance to establish themselves downstream of the fixed inlet.

1925

For the $12H$ and $16H$ cases, where $L_p > x_A$, concentration maxima occur in the dense patches and minima in the sparse (Figure 4.6d, e and vertical profiles in 6f). However, for the $4H$ and $6H$ cases, where $L_p < x_A$,

1930 pollutant-concentration maxima occur in sparse patches and minima in the dense patches (Figure 4.6a, b
and vertical profiles in 6f). This pattern is consistent whether a sparse or a dense patch occurs at the
beginning of the modelled domain. In the $8H$ case, where $L_p \approx x_A$, maxima and minima occur on the
boundaries at the trailing edge of the dense and sparse patches, respectively (Figure 4.6c). At the very top
of the canopy, the pollutant concentration in the sparse patches is slightly higher than that in the dense
1935 patches for all cases (Figure 4.6f). We attribute this to the higher turbulent exchange in the sparse patches,
meaning the scalar transported from the release height at the bottom of the canopy is more apparent against
the low background concentrations at this height.



1940 **Figure 4.6: Effect of patchiness on pollutant concentration. (a–e) Two-dimensional plots of normalized**
pollutant concentration $[\bar{c}]/(QH/u_*)$ in each of the alternating-density cases. The final four patches of each
domain are pictured, with the streamwise distance normalized by the patch length L_p . The dense patches and
the sparse patches are bounded by the solid and dashed lines, respectively. The wavy black lines denote
contours in the values of $[\bar{c}]/(QH/u_*)$; (f) Normalized mean vertical profiles of pollutant concentration in the
1945 **sparse patches subtracted from that in the dense patches $([\bar{c}]_d - [\bar{c}]_s)/(QH/u_*)$. Profiles include the entirety**
of each patch rather than a single x location.

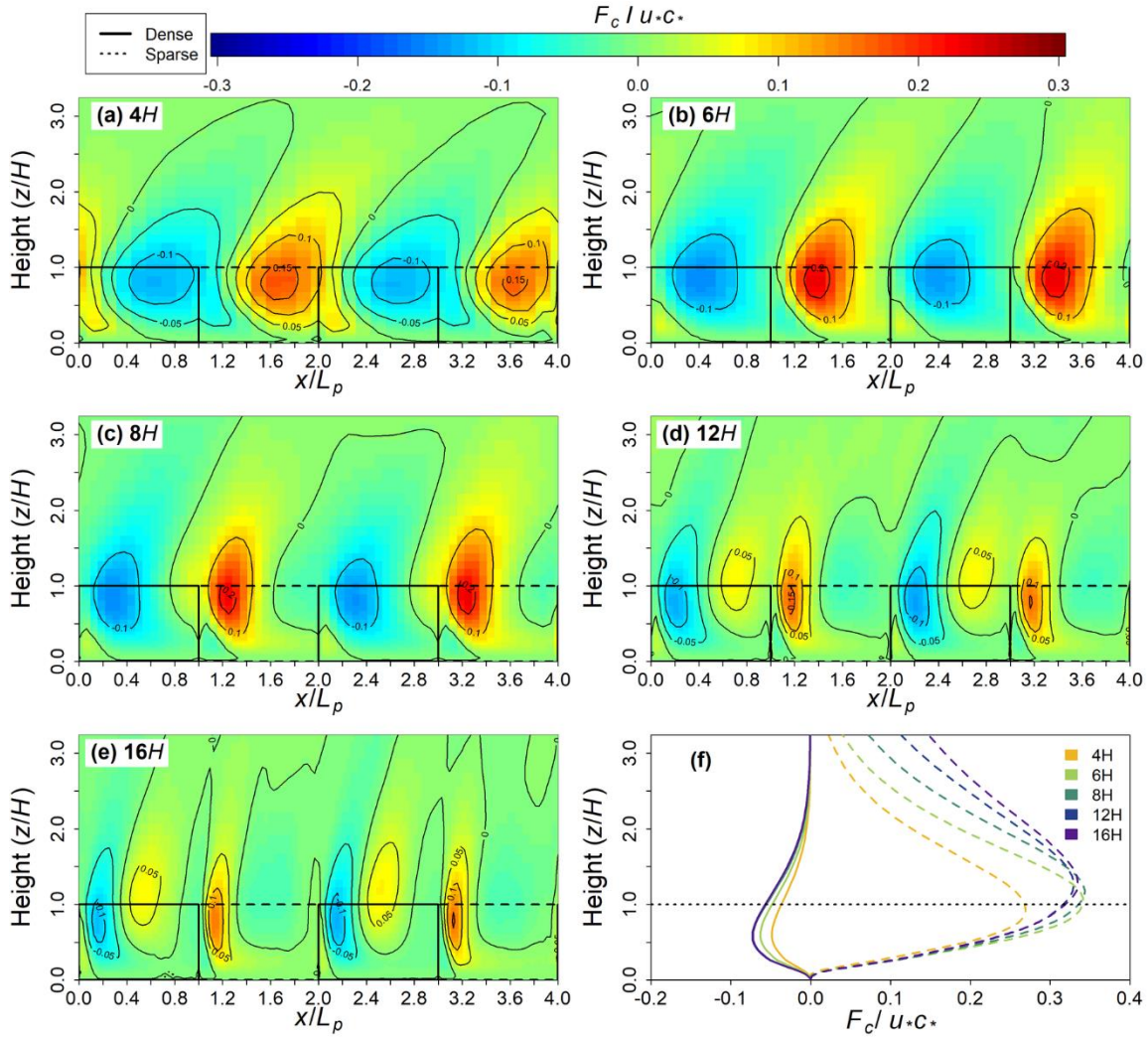
4.5.2 Two-dimensional patterns in the kinematic turbulent pollutant flux

Figure 4.7 presents two-dimensional patterns of the kinematic turbulent concentration flux, $F_c = \overline{c'w'}$ across the final four patches of each domain. The values of F_c are normalized by u_*c_* where the concentration scale $c_* = \sqrt{[c'c']_H}$, corresponding to the square root of the scalar variance at $z = H$. Figure 4.7a–e shows the difference between the flux F_c in the alternating cases versus the flux F_c in the homogeneous case; i.e., positive and negative values indicate regions where the magnitude of F_c is, respectively, higher and lower in the alternating case than in the homogeneous case. In each of the alternating-density cases, there is a clear peak in the value of F_c at the upstream edge of the sparse patches,

1950

1955 at around $x = 2.5H$ downstream of the dense-to-sparse transition. Regions of low F_c values occur at the upstream edge of the dense patches. The magnitude of the positive perturbations, the regions of high F_c values centred at $x = L_p + 2.5H$ inside the sparse patches, are around three times those of the negative perturbations, the regions of low F_c values centred at $x = 2.5H$ inside the dense patches (Figure 4.7f). The magnitudes of the perturbations are similar for each of the cases, other than the $4H$ case, for which they are slightly lower. The regions of high and low values of F_c extend from $z \approx 0.4H$ within the UCL to $z \approx 2H$ for low values of F_c to $z > 4H$ for high values of F_c .

1960



1965 **Figure 4.7: Effect of patchiness on the kinematic turbulent concentration flux F_c .** (a–e) Two-dimensional plots of perturbations of F_c in each of the alternating-density cases. The final four patches of each domain are pictured, with the streamwise distance normalised by the patch length L_p . The dense patches and the sparse patches are bounded by the solid and dashed lines, respectively; (f) normalized mean vertical profiles of perturbations of the flux F_c . The solid and dashed lines represent profiles at $x = 2.5H$ inside the dense and $x = L_p + 2.5H$ inside the sparse patches, respectively.

4.5.3 Adjustment of scalar concentrations and fluxes

1970 Figure 4.8 presents streamwise profiles of (a) pollutant concentration and (b) turbulent fluxes of momentum (solid line) and pollutants (dashed line) from the $16H$ case at $z = 0.5H$. Again, we consider the variables as adjusted once they are in equilibrium; i.e., their values lie within $\pm 5\%$ of those at the downstream edge of each patch, indicated by the two shaded areas in Figure 4.8a. Scalar concentration maxima and minima (marked with the vertical dotted lines in Figure 4.8a) occur at around $x = 8H = 0.5L_p$ in the dense patch and $x = L_p + 0.69H = 1.43L_p$ in the sparse patch. Here $L_p = 16H$, so the maxima and minima occur at $x \approx x_A$. However, equilibrium is reached slightly later (marked with the vertical dot-dash lines in

1975

Figure 4.8a), occurring at $x \approx 12H = 0.73L_p$ and $x \approx L_p + 12H = 1.77L_p$, respectively, for the dense and sparse patches. As turbulent scalar fluxes adjust to flow variations more slowly than momentum fluxes, the turbulence tends to transfer momentum more efficiently than scalar quantities (Kanani-Sühring and Raasch 2015; Li and Bou-Zeid 2019; Ma et al. 2020). This can be seen in Figure 4.8b, where the momentum flux has adjusted by $x \approx 10$ to $12H = 0.62$ to $0.75L_p$ (marked with the vertical dotted lines in Figure 4.8b), but the turbulent scalar flux only fully adjusts around $x \approx 16H$, although it takes very small absolute values before this point. To summarise section 4.5.3, maxima and minima of scalar concentration occur at around $x \approx x_A$ downstream of the density transitions, and scalar concentration almost fully adjusts by $x \approx 1.2x_A$.

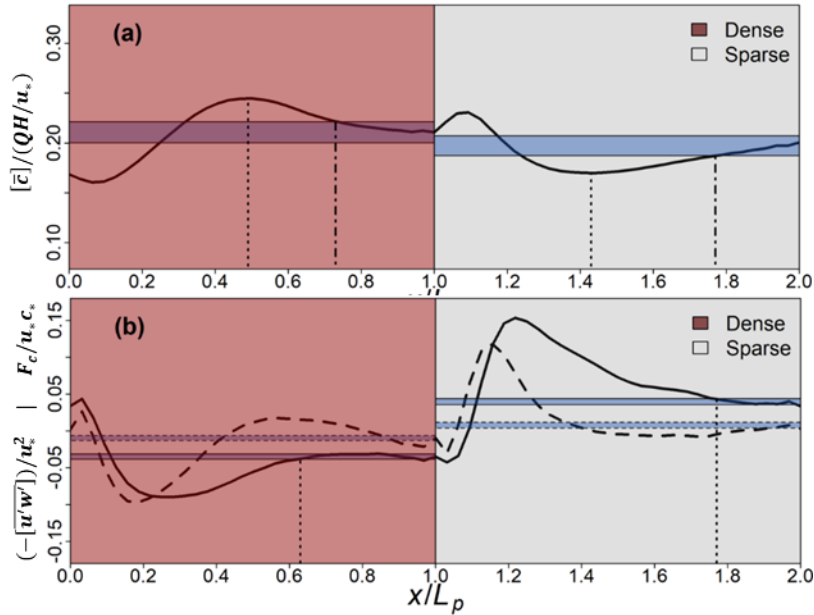


Figure 4.8: Adjustment of (a) the normalized scalar concentration $[\bar{c}]/(QH/u_*)$ at $z = 0.5H$; and (b) normalized turbulent fluxes of momentum $(-\overline{u'w'})/u_*^2$ (solid line) and scalars F_c/u_*c_* (dashed line) at $z = 0.5H$. Both fluxes in (b) are presented as perturbations relative to the homogeneous control case. Only two patches are shown, with streamwise distance normalized by the patch length L_p . Blue shaded areas show values $\pm 5\%$ of those at the downstream edge of each patch. In (a), dotted vertical lines show the approximate positions of peak scalar concentration downstream of each patch edge, and dot-dash lines show the approximate adjustment distance in scalar concentration. In (b), vertical dotted lines show estimates for x_A downstream of each density transition.

1995 **4.6 Discussion and conclusions**

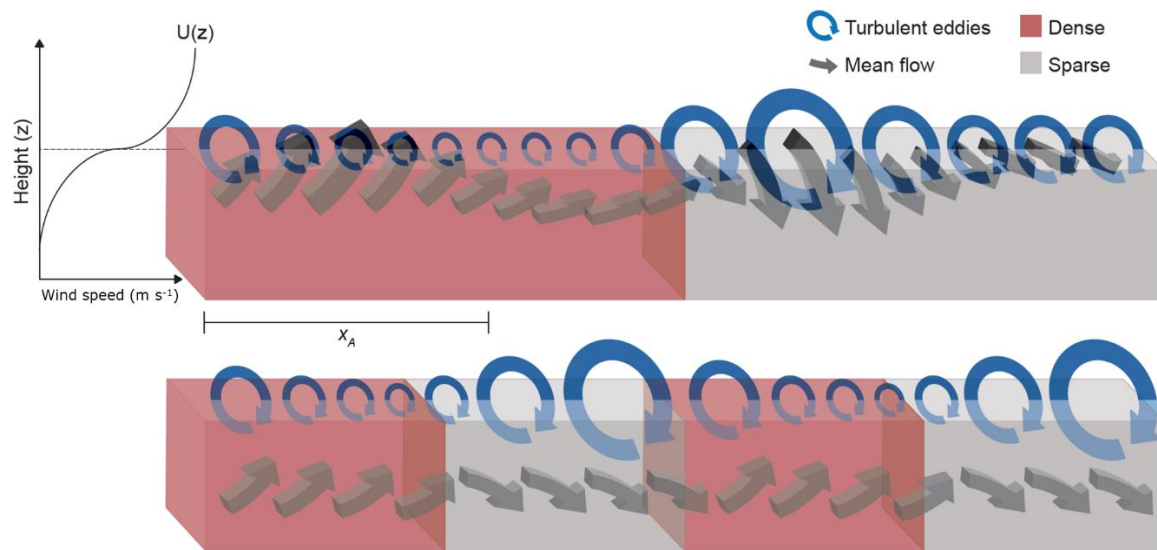
4.6.1 Neighbourhood-scale flow regimes

Using these results, we propose two conceptual regimes of neighbourhood-scale flow that emerge from the interaction of the flow dynamics with the patch size. The first is the *neighbourhood-ventilation regime*, which occurs in neighbourhoods whose frontal-area density varies in patches for $L_p > x_A$. In neighbourhoods of this type, the mean streamwise velocity component fully adjusts to the change in density for flow between patches, inducing a strong vertical velocity component for $x < x_A$ (Figure 4.3f) and weak vertical velocity component for $x \gg x_A$ (see downstream edge of the patches in Figure 4.3d, e). The second is the *neighbourhood-percolation regime*, which occurs in neighbourhoods whose frontal-area density varies in patches such that $L_p < x_A$. In these neighbourhoods, the patches are too small for the mean flow to adjust fully within each patch, which constrains the magnitude of the vertical velocity component around the top of the UCL (Figure 4.3f). Consequently, the transport of emitted pollutants within one patch is dominated by advection to the next patch. In our case, we take the $4H$ case as an example of a neighbourhood for which the percolation regime applies, and the $16H$ case as one for which the ventilation regime applies. Figure 4.9 presents a schematic of the percolation and ventilation regimes and the competing dynamical processes, illustrating enhanced turbulent vertical exchange in the sparse patches in both regimes. The dominant eddies are always small relative to the patches because turbulent exchange in urban areas is dominated by eddies much smaller than the patches, even in the $4H$ case (Okaze et al. 2015).

2000

2005

2010

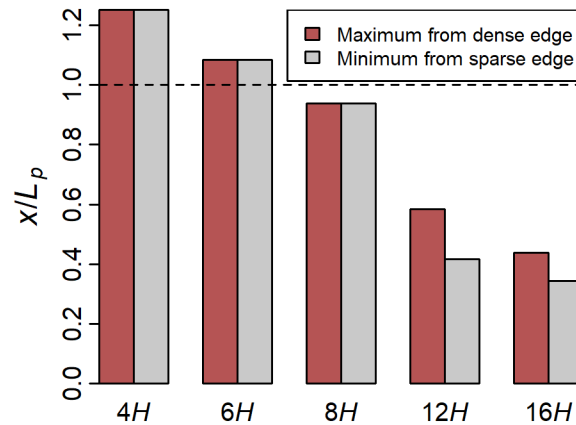


2015 **Figure 4.9: Inflected wind-speed profile between dense and sparse patches of an urban neighbourhood. Top shows the ventilation regime and the bottom the percolation regime (see section 4.6.1). The shaded volume indicates the urban canopy. Turbulent exchange is high in the sparse patches, regardless of patch length. The numbers and sizes of the arrows are conceptual and do not map directly onto a numerical scale.**

4.6.2 Pollutant concentrations

2020 The emergence of the percolation and ventilation regimes profoundly affects the distribution of pollutants. In neighbourhoods subject to the percolation regime, maximum and minimum pollutant concentrations occur in the sparse and dense patches, respectively, which can be seen by comparing the $4H$ and $16H$ cases in Figure 4.6a, e and f. This is contrary to the common interpretation that ventilation is lower, and the pollution concentration higher, in dense urban patches (Buccolieri et al. 2010). The counter-intuitive behaviour arises in neighbourhoods with the percolation regime (i.e., density changes in small patches) because turbulent exchange is suppressed in the dense patches. Therefore, pollutant accumulates over the length of the dense patch and is advected into the neighbouring sparse patches. Conversely, in the sparse patches, turbulent exchange is high and the patches better ventilated (Figure 4.7f), meaning less pollutant is advected downstream into the neighbouring dense patches.

2030 However, in neighbourhoods with the ventilation regime (i.e., density changes in larger patches), maximum pollutant concentrations occur in the dense patches (Figure 4.6e, f). The exact locations of the maxima and minima in the ventilation regime reflect the importance of both the mean flow and turbulent exchange. The turbulent pollutant flux is high at the upstream edge of the sparse patches and low at the upstream edge of the dense patches (Figure 4.7). Therefore, pollutant-concentration minima at $z \approx 0.5H$ occur at shorter distances downstream of the edge of sparse patches ($\Delta x \approx 5.5H$) compared with maxima downstream of the edge of the dense patches ($\Delta x \approx 7.5H$) (Figure 4.10). In neighbourhoods where the frontal-area density varies in patches where $L_p \approx x_A$ (the $8H$ case), we see a smooth transition between the two regimes. Pollutant-concentration maxima and minima occur around the leading edge of sparse and dense patches, respectively. The mean flow is perturbed more than in the percolation regime, but less than in the ventilation regime.



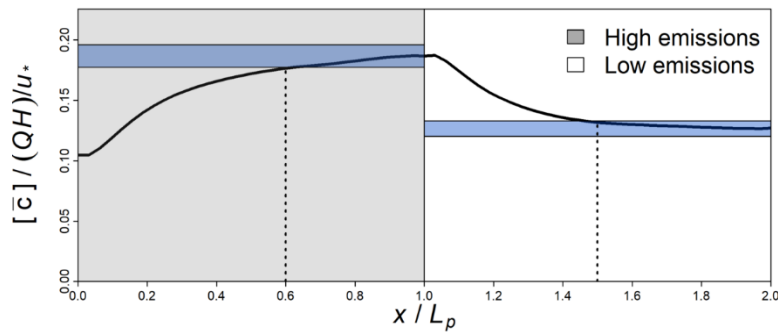
4.10 Location of concentration maxima and minima at $z = 0.5H$ downstream of the leading edge of the dense (red) and sparse (grey) patches (section 4.3.3). Values of $x/L_p > 1$ indicate maxima/minima downstream of the transition occur in the neighbouring patch (for example, scalar maxima in the sparse patches in the $4H$ case).

2045 **4.6.3 Limitations and effect of other variables**

Here we present a quasi-two-dimensional model of flow in an inhomogeneous urban area, by altering a single variable (frontal-area density), and the streamwise distance over which the density changes occur. The wind direction was held constant, and therefore our model does not capture the variations that the wind direction can induce in scalar fields even in idealised models of urban areas (Philips et al. 2013). For example, we would not expect our results to hold for flow parallel to the alternating-density patches in Figure 4.1. In real urban areas—particularly those with deep street canyons—the wind direction and urban form interact, for example, regions of high ventilation may occur at different locations depending on the prevailing wind direction (Yim et al. 2014). We also assume a constant mean obstacle height. In real urban areas, the heights of the buildings and the other obstacles vary, which affects the distance over which the flow adjusts from one patch or neighbourhood to another (Coceal and Belcher 2005) and the rate at which the UCL is ventilated (Hang et al. 2012). We also approximate the drag coefficient \bar{C}_d as constant (Sect. 3.2), which would not be a suitable simplification for a very tall canopy, for which a more empirical approach based on a real urban structure is likely to be more appropriate (Gutiérrez et al. 2015). We considered only neutral atmospheric conditions. Atmospheric stability can profoundly affect the flow, even at the neighbourhood scale; for example, in unstable conditions, scalars are transferred more efficiently with increasing instability (Wang et al. 2014). Further, while our model provides a helpful way to approximate the dynamics of air pollutants at the neighbourhood scale, careful consideration of the urban form and the behaviour of pedestrians, such as their mode of transport, is needed to assess the exposure of the population to those pollutants (Kingham et al. 2013; Tenailleau et al. 2015).

2065 Our approximation of pollutants as a homogeneous source of passive scalar may also be inappropriate for certain applications, such as for investigating species with short lifetimes, which may require a coupled chemistry scheme (Zhong et al. 2015), or for considering species with very heterogeneous sources and sinks, such as water vapour and CO₂, which behave very differently even in the same neighbourhood under the same conditions (Nordbo et al. 2013; Ramamurthy and Pardyjak 2015). In real urban areas, emission rates of even passive pollutants also vary spatially, depending on factors such as the location of busy roads. This patchiness in pollutant emissions affects concentrations within the UCL. As an illustration, we simulated a further case with the same urban form as the homogeneous control case, varying the emission rate of a passive pollutant between high ($Q = 1.5 \mu\text{g m}^{-3} \text{s}^{-1}$) and low ($Q = 0.5 \mu\text{g m}^{-3} \text{s}^{-1}$) rates in patches with $L_p = 16H$. Figure 4.11 shows the normalized concentration $[\bar{c}]/(QH)/u_*$ at $z = 0.5H$. Because the urban area is homogeneous in form, there are no dynamical patch effects induced by density transitions as in the previous subsections. However, the concentration still adjusts as it moves between patches of different emission rates. The adjustment occurs over a distance of around x_A , the point at which the concentration comes within 5% of that at the downstream edge of each patch (marked with the vertical dotted lines in Figure 4.11). Many cities worldwide have implemented measures to improve air quality, creating, for example, low emission zones in which the traffic of older vehicles is limited, with the inevitable leakage of pollutants from surrounding areas. The adjustment distance x_A appears to provide an

approximate distance over which this contamination occurs, even in the absence of dynamical effects induced by changes in density.



2085

Figure 4.11: Adjustment of pollutant concentration between patches of different emission rates into an area with a homogeneous urban form. Only two patches are shown, with the streamwise distance normalized by the patch length L_p . Solid line shows normalized concentration $[\bar{c}]/(QH)/u_*$ at $z = 0.5H$, blue shaded areas show concentrations $\pm 5\%$ of those at the downstream edge of each patch, and grey shading and no shading, respectively, show the high- and low-emission patches.

2090

4.6.4 Applications and outlook

While mean pollutant concentrations and fluxes are spatially highly variable between and within different parts of a city (Figure 4.6, 4.7), in patchy neighbourhoods subject to the ventilation regime (i.e., where the frontal-area density varies in large patches), point observations at a distance $> x_A$ downstream of a density transition in the direction of the prevailing wind direction should represent pseudo-equilibria well. The adjustment distance x_A therefore represents an approximate lower bound for fetch requirements for ‘urban background’ micrometeorological and flux observations. Further, our results suggest neighbourhood ‘hot spots’ of pollution, such as contamination downstream of a small dense patch with heavy traffic, may not be captured by relying on only roadside or ‘urban background’ observations.

2095

2100

A porous-medium approach to neighbourhood-scale processes provides a good balance between computational efficiency and flow resolution, provided the porous model is formulated to capture the characteristics of the urban area in question. The percolation and ventilation regimes (a) capture the mean and turbulent components of the transport terms for pollutants and other scalar quantities; and (b) can be described using a range of geometrical variables simple enough to be deployed in high-Reynolds-number flow models. Further, in the quasi-two-dimensional case we present here, the broad characteristics of the regimes are insensitive to the frontal-area density in the quantity f_i and the SGS sink in Equation (4.11). A greater density contrast between the sparse and dense patches would lead to more pronounced examples of the regimes but would not materially change the adjustment distance x_A either side of which the regimes emerge. A lesser contrast would simply blur the transitions between sparse and dense patches, eventually approaching flow in a homogeneous urban area. The effect of stochastic porosity and patch-scale changes on the flow dynamics would depend on the patch size. In large patches, once the flow has adjusted, it has very little ‘memory’ of the preceding urban form. To approximate flow dynamics in neighbourhoods with

2105

2110

2115 small patches, we would need to know the size of the patch of interest and its density relative to the
neighbouring patch upstream.

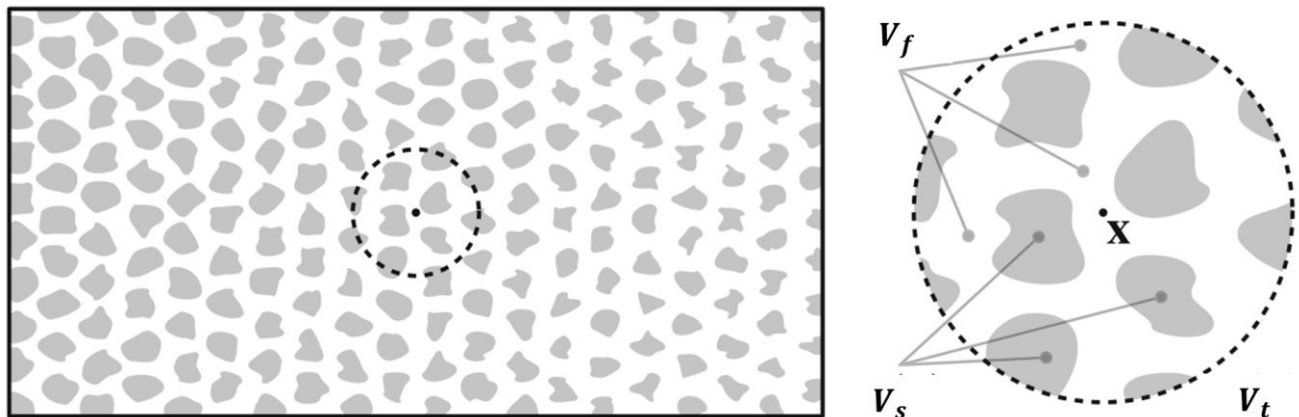
2120 Neighbourhood-scale processes provide potential boundary conditions to couple micro-scale urban-
transport models and mesoscale meteorological forecasts (Xie 2011). However, parametrisations of
neighbourhood-scale processes must be flexible enough to capture the effect of inhomogeneity in the urban
form on flow and dispersion. Here, the specifics of the urban form were captured entirely in the drag-force
2125 parametrisation in Equation (4.10). This approach adapts LES models previously used for vegetation
canopies, with the representation of the urban form informed by porous models of cities, specifically a
vertically homogeneous frontal-area density λ_f and a higher drag coefficient than in vegetation models.
Further in situ observations and experiments in wind tunnels (preferably both) would help to determine the
2130 extent to which this approach holds for real urban areas. For example, we suspect our approach would be
more appropriate for irregular cities comprising vegetation and obstacles of various shapes and sizes, rather
than regularly spaced buildings with few other features, for which a vertically varying value of λ_f or the
drag coefficient may yield better results. Further testing may allow the percolation and ventilation regimes
to be adapted to link neighbourhood and city/mesoscale models. Urban air quality motivated this study, and
2135 therefore we concentrated on scalar quantities representing pollutants emitted near the ground in urban
areas. However, with modifications, this framework could be used to model processes in other
environments, such as forests, or other scalar quantities, such as temperature. For example, in forests, after
adding a scalar sink throughout the canopy, this framework could be used to investigate the transport of
pollutants, such as ozone, into a patchy forest (Ma and Liu 2019; Ma et al. 2020). This type of investigation
is extremely difficult using observations, even with an extensive network of sampling equipment (Aubinet
et al. 2010).

Appendix 4A – Conceptual background to the porous-media model

4A.1 Conceptual background

2140 A porous medium is a material that contains a large number of voids (pores). These voids may allow fluids to flow through the material, under certain conditions (Bear and Bachmat 1990). A porous medium is most often characterised by its ‘porosity’ i.e., the fraction of the material that the voids occupy, as a proportion of the material’s total volume. All other things equal, a fluid flowing through porous media is less obstructed as the material’s porosity increases. Fluid flows through porous media are studied and used across a variety of subfields of engineering, Earth sciences, hydrology, and many others (Bear and Bachmat 1990).

The porous-media method in micrometeorology was developed from techniques in engineering and fluid mechanics (Whitaker 1973; Howes and Whitaker 1985). The method is most useful when one is interested in the flow statistics or turbulent processes around dense canopies of obstacles (e.g., urban areas and vegetation canopies), especially when the detailed morphology of the obstacles is not known, or when spatially representative measurements are unavailable (Finnigan 2008; Finnigan and Shaw 2008; Schmid et al. 2019). The porous-media method assumes we have a fluid (in this case the air) flowing through a fixed solid phase (in this case, the urban area). Instead of trying to model the obstacles directly, we focus attention on their net effect on the flow. This is achieved by treating the canopy volume as a porous medium—picture an incompressible sponge—whose size, height, and density/porosity approximately reflect the urban area in question. The solid fraction is assumed to be comprised of small, randomly shaped elements, whose properties are constant within a single averaging volume (Figure 4A.1 and section 4.3.1). However, the bulk properties of a medium may change within a porous medium, provided that the changes occur on scales large relative to the size of each averaging volume (Figure 4A.1 and Chapter 5, where the density of a forest represented by a porous medium varies with height in the canopy).



2165 **Figure 4A.1: Overview and detail of a porous medium with the total averaging region V_t centred at x containing both fluid (V_f , white) and solid (V_s , grey) regions (see section 4.3.1). In this example, the density of the material decreases from the left to right i.e., the porosity increases. In the work in the main text however, the density of the porous medium is constant within each patch, with a step change in density at the boundary between patches (section 4.3.3). Figure adapted from Schmid et al. (2019).**

4A.2 Implementation in WRF

The porous medium (the urban area) is included the WRF model by spatially averaging the localised drag from the individual solid volume elements, assuming the drag force is proportional to the square of the flow speed (see section 4.3.2 for background and derivation). We modified the dynamical solvers of the WRF model to include this additional drag force term in the momentum equations $f_i = -\frac{\bar{c}_d \lambda_f}{H} |U| \langle u_i \rangle$, Equation (4.10). A similar term was added to the solver for the TKE (Equation (4.11)). Using the values in our study (section 4.3.3), this represents the urban area through a vertically homogeneous profile of drag (Figure 4A.2), because we assume a constant drag coefficient (see discussion in section 4.3.2). We contrast this to the vertical profiles typically used in LES simulations of vegetation canopy flows, which often vary with height to indicate the region in which most of the plant area is located (Figure 4A.2 and Chapter 5).

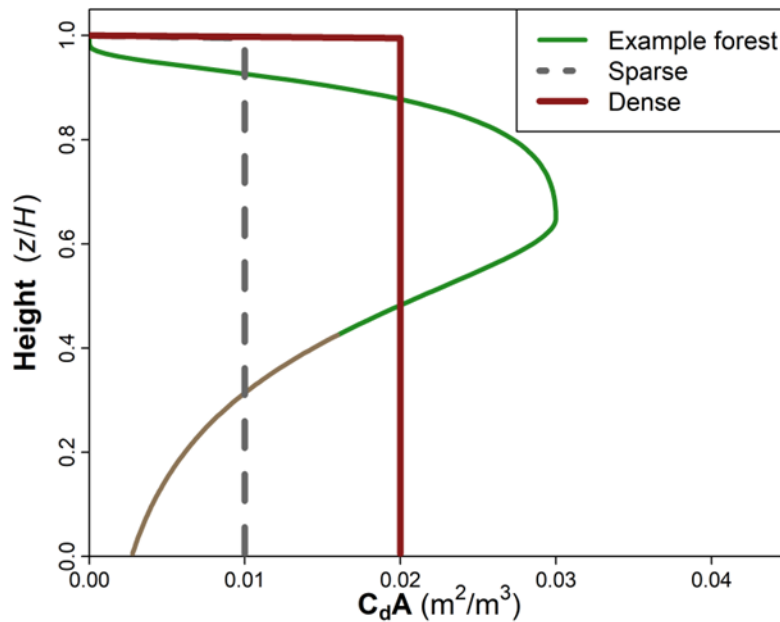
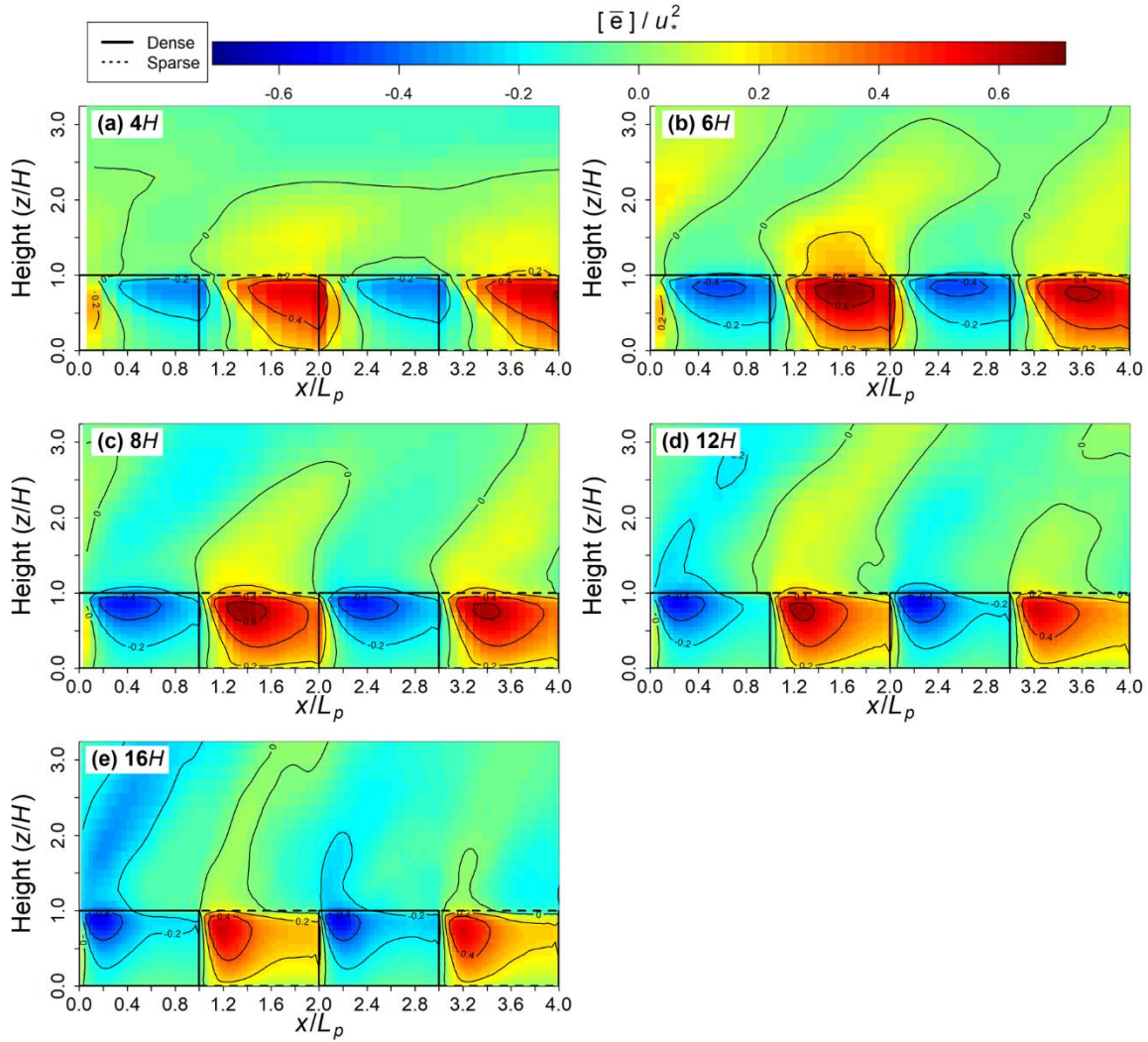


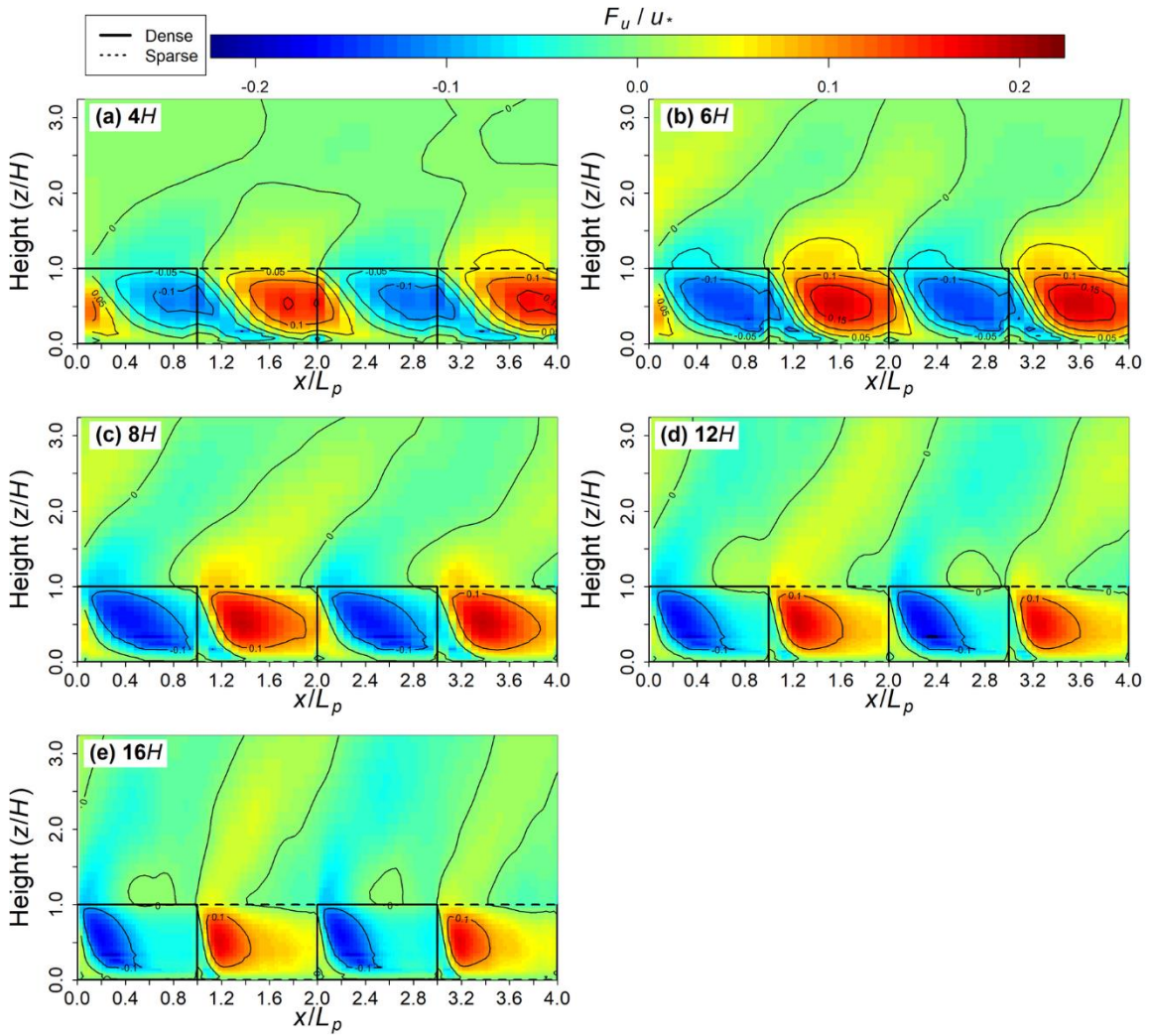
Figure 4A.2: Vertical profiles of the area density A used in the drag parametrisation in Equations (4.10) and (4.11). For the urban area, $A = \lambda_f/H$, where $\lambda_f = \lambda_d = 1/3$ for the ‘dense’ patches (solid red line) and $\lambda_f = \lambda_s = 1/6$ for the ‘sparse’ patches (dashed grey line) (see section 4.3.3). We contrast this to a typical vertical profile used in LES of forest flow (green and brown line), where the canopy has a similar net density but with a very different vertical distribution. For the example forest, A is the plant area density, calculated using the formula derived by Lalic and Mihailovic (2004), with a plant area index of 3 (see section 5.5).

Appendix 4B



2190

Figure 4B.1: Effect of patchiness on TKE $[\bar{e}]/u_*^2$. (a–e) Two-dimensional patterns of TKE in each of the alternating-density cases. Only the first four patches are pictured, with the streamwise distance normalized by patch length L_p . The dense patches and the sparse patches are bounded by the solid and dashed lines, respectively.



2195

Figure 4B.2: Effect of patchiness on the square root of magnitude of the shear stress F_u/u_* . (a–e) Two-dimensional patterns of F_u/u_* in each of the alternating-density cases. Only the first four patches are pictured, with the streamwise distance normalized by patch length L_p . The dense patches and the sparse patches are bounded by the solid and dashed lines, respectively.

2200

Chapter 5 – Realistic Forests and the Modelling of Forest-Atmosphere Exchange

2205 Publishing details. This chapter is a reproduction of the article ‘Realistic Forests and the Modelling of Forest-Atmosphere Exchange’ by Edward Bannister, Xiaoming Cai (XMC), and Rob MacKenzie (AMRK), published in *Reviews of Geophysics* (2022), 60(1) <https://doi.org/10.1029/2021RG000746>

2210 Author contributions. I conceived of this study under the joint supervision of XMC and AMRC. I reviewed and synthesised the literature, performed the LES model runs, wrote the processing code, conducted the formal analysis and visualisation, wrote the original draft of the manuscript, and revised the manuscript in response to reviewers’ comments. All authors reviewed and edited manuscript drafts.

2215 Acknowledgements. I am grateful to Dr Jian Zhong for his assistance in debugging the LES model. I thank Chantal Jackson for her assistance in redrawing Figures 5.1, 5.3, 5.4, and 5.6. Thanks also to Eric Casella of Forest Research UK for his terrestrial laser scans of BIFoR FACE, and for interesting discussions about forest structure. I am grateful to three anonymous reviewers for constructive comments that helped improve this manuscript. Image rights can be found at the end of the main text in Appendix 5C.

2220 Abstract. Forests cover nearly a third of the Earth’s land area and exchange mass, momentum, and energy with the atmosphere. Most studies of these exchanges, particularly using numerical models, consider forests whose structure has been heavily simplified. In many landscapes, these simplifications are unrealistic. Inhomogeneous landscapes and unsteady weather conditions generate fluid dynamical features that cause observations to be inaccurately interpreted, biased, or over-generalised. In Part I, we discuss experimental, theoretical, and numerical progress in the understanding of turbulent exchange over realistic forests. Scalar transport does not necessarily follow the flow in realistic settings, meaning scalar quantities are rarely at

2225 equilibrium around patchy forests, and significant scalar fluxes may form in the lee of forested hills. Gaps and patchiness generate significant spatial fluxes that current models and observations neglect. Atmospheric instability increases the distance over which fluxes adjust at forest edges. In deciduous forests, the effects of patchiness differ between seasons; counter intuitively, eddies reach further into leafy canopies (because they are rougher aerodynamically). Air-parcel residence times are likely much lower in patchy forests than

2230 homogeneous ones, especially around edges. In Part II, we set out practical ways to make numerical models of forest-atmosphere exchange more realistic, including by accounting for reconfiguration and realistic canopy structure, and beginning to include more chemical and physical processes in turbulence resolving models. Future challenges include: (i) customising numerical models to real study sites; (ii) connecting space and time scales; and (iii) incorporating a greater range of weather conditions in numerical models.

2235

5.1 Introduction

5.1.1 A sense of scale

2240 Forests cover about 30% of the Earth's surface and interact with the atmosphere in a variety of ways. Some
of these interactions are familiar enough to appear in the poetry and stories of most cultures. Fluttering
leaves and swaying branches are among the most obvious visual manifestations of wind. Trees split the
wind into flows of different velocities which, if the wind is strong enough, howl when they are reunited.
Other interactions, which occur across scales outside of human perception, are apparent only in careful
measurements. The timescales of interest in forest-atmosphere interactions begin at approximately 10^{-2} s
2245 for leaf fluttering and photosynthetic processes. The period of tree and branch swaying is typically from
 10^{-1} to 10 s. Phenomena with longer timescales include boundary-layer turbulence (10^{-1} – 10^4 s), weather
systems (10^3 – 10^6 s), and ecosystem–climate feedbacks (10^7 – 10^{12} s). Similarly, the smallest relevant space
scales are roughly 10^{-6} m, which is the size of stomatal openings, airborne spores, and small pollens. Tree
elements, such as seeds, leaves, and branches range from 10^{-3} m (seeds) to 10^2 m (entire large
2250 trees). Individual ecosystems scale from 10^2 m (small clumps of trees and plants) to 10^7 m (entire forested
landscapes, such as in the Amazon and Congo basins, or the Taiga forests of the Northern Hemisphere).
Boundary-layer turbulence contains eddies with diameters 10^{-3} – 10^3 m, and processes relevant to meso and
synoptic weather systems scale 10^3 – 10^6 m. No set of mathematical equations describes these various
interacting phenomena completely or, often, even approximately. There is also no single correct time or
2255 space scale at which to view forest-atmosphere interactions. The most important features of the interactions
depend on the scale of interest, as does the theory, experimental methods, and tools available to researchers
to study them. In this review, we concentrate on forest-atmosphere interactions across length scales of 10^{-1} –
 10^3 m and timescales of 1– 10^3 s. We refer to this as the 'ecosystem scale', which approximately corresponds
to the ecological scales from 'individuals' to 'patches' (Scholes 2017) and the meteorological micro– and
2260 γ –mesoscales (Stull 1988).

5.1.2 The extent of the literature

At the ecosystem scale, we assume the overall landscape properties to be stationary, because drivers such
as fragmentation, tree senescence, and extensive plant growth typically occur on timescales much longer
than those of plant movement or boundary-layer dynamics. With these assumptions in mind, researchers
2265 typically approach ecosystem-scale forest-atmosphere interactions from one of two directions. The first
approach focuses on the effect of the atmosphere on trees and other plants, such as on plant biomechanics
(De Langre 2008, 2019; Gosselin 2019), leaf microclimates (Vogel 2009), or water-use efficiency
(Schymanski and Or 2016). The second approach, which we use in this review, focuses on the effect of
forests on the atmosphere, especially on the structure of the turbulence and the transport of momentum and
2270 scalar quantities (Finnigan 2000; Katul et al. 2013; Brunet 2020).

Previous reviews of ecosystem-scale turbulent transport around forests have discussed land-atmosphere
interactions more generally (e.g., Bou-Zeid et al., 2020; Fisher and Koven, 2020) and ecosystem exchange

at long-term monitoring sites (e.g. Baldocchi, 2008; Hicks and Baldocchi, 2020; Oliphant, 2012). These
2275 reviews, and the work they discuss, attempt to estimate the net ecosystem exchange of carbon and other
scalar quantities, sometimes for scaling up into Earth-system and other large-scale models. Other reviews
focus on the detailed structure and statistics of the turbulence in forests and other vegetated landscapes. The
early work in this area was motivated by applied problems in agriculture and forestry, such as minimising
crop lodging and the windthrow of trees (e.g., Inoue, 1955; Ruth and Yoder, 1953). In the 1970s and 1980s,
2280 pioneering investigations of the transport equations moved the field from empirical observations to
obtaining precise knowledge about certain features of the turbulence, especially in horizontally uniform
canopies on flat ground (Raupach and Thom 1981; Van Gardingen and Grace 1991; Kaimal and Finnigan
1994; Raupach et al. 1996; Finnigan 2000). Katul et al. (2013) supplement these reviews with their survey
of scalar turbulence in uniform canopies. Lemone et al. (2019) and Brunet (2020) provide comprehensive
2285 background to boundary-layer measurements, including in plant canopies, and update earlier reviews of the
flow in homogeneous plant canopies with results obtained using high-performance computers. Other recent
reviews discuss the flow and transport of scalar quantities around forest edges (Belcher et al. 2012), the
measurement and modelling of ecological processes such as evapotranspiration (e.g., Katul et al., 2012),
and hill-induced dynamical effects on the flow and scalar fields around forests and other vegetation (e.g.,
2290 Belcher et al., 2012; Finnigan et al., 2020).

5.1.3 The scope of this review

The majority of existing work considers forests whose structure has been ‘idealised’ in some way. Often
this idealisation step occurs when physical and numerical models are configured, although occasionally
study sites are chosen on the basis of strict criteria. While there is no single definition of ‘idealised’ in the
2295 context of forest-atmosphere exchange, the majority of the literature assumes forests to be horizontally
homogeneous, with closed canopies, no large patches or gaps, and without site specific morphological or
ecological detail. Below, we describe a forest as ‘idealised’ if most of these properties are assumed. Forests
in the real world rarely fit these assumptions. For example, forests around the world are becoming
increasingly fragmented (Fahrig 2003; Bogaert et al. 2011; Taubert et al. 2018). Edge regions differ from
2300 the forest interior both in their mean local climate (e.g., less humid) and in the range of meteorological
extremes they experience (Magnago et al. 2015). Even in intact ecosystems, most forest canopies comprise
a patchwork of openings of many shapes and sizes, formed by senescence, disease, and windthrow
(Whitmore 1989; Hiron and Thomas 2018). These gaps are significant ecologically and structurally. The
floras of the northern temperate forests, for example, include many species that depend on gaps and
2305 patchiness (Fox 1977; Tinya et al. 2009). The divergence between theory and reality causes, for example,
estimates of ecosystem exchange to be inaccurate or biased (Wilson et al. 2002; Baldocchi 2008; Aubinet
et al. 2010; Stoy et al. 2013). This is no secret, and most studies end with calls for further experiments in a
wider range of ecosystems, using more detailed techniques and models.

2310 In this review, we focus on the ecosystem-scale exchange of momentum, energy, and mass between the
atmosphere and heterogeneous forests. We split our review into two parts. Part I (sections 5.2–5.4) discusses

experimental, theoretical, and numerical progress in our understanding of turbulent exchange over realistic, patchy forests. Section 5.2 summarises the methodology behind numerical investigations of forest–atmosphere exchange, and the turbulence structure around idealised forests, including the effects of atmospheric stability. The remainder of Part I discusses how structural heterogeneity and patchiness affects the exchange of momentum (section 5.3) and scalar quantities (section 5.4). We concentrate principally on forests on level ground, although section 5.4 briefly discusses recent progress in investigating scalar transport around forested hills. (See Finnigan et al. (2020), for example, for a comprehensive treatment of terrain induced effects on land-atmosphere exchange.) Part II (sections 5.5–5.6) sets out practical ways to make numerical models of forest-atmosphere more realistic, including by accounting for reconfiguration and realistic canopy structure (section 5.5) and beginning to include more chemical and physical processes in turbulence resolving models (section 5.6). We conclude in section 5.7 and provide recommendations for further research under the broader goals of (i) customising numerical models to real study sites; (ii) connecting space and time scales; and (iii) incorporating a greater range of weather conditions in numerical models.

Part I: Forest-atmosphere exchange around heterogeneous forests

We begin Part I by summarising the important fluid dynamical properties of forest-atmosphere exchange in idealised landscapes, before moving on to look at exchange in more realistic landscapes.

5.2 The flow in and around idealised forests

5.2.1 Definition of terms

We use right-handed Cartesian tensor notation, with the Einstein summation convention, and indices (i, j, k) take values $(1, 2, 3)$ respectively. For example, u_i is the velocity in the x_i direction, with $i = 1, 2, 3$ representing the streamwise (x), spanwise (y) and vertical (z) directions. We denote $\mathbf{x} = (x, y, z)$, $(u_1, u_2, u_3) = (u, v, w)$, and time as t . For a quantity, ϕ , $\langle \phi \rangle$ denotes a spatial average and $\bar{\phi}$ denotes a time average such that $\phi(\mathbf{x}, t) = \langle \phi \rangle(t) + \phi''(\mathbf{x}, t)$ and $\phi(\mathbf{x}, t) = \bar{\phi}(\mathbf{x}) + \phi'(\mathbf{x}, t)$. We refer to the quantities $\phi''(\mathbf{x}, t)$ and $\phi'(\mathbf{x}, t)$ as the ‘dispersive’ and ‘turbulent’ quantities, respectively, which reflect local departures from the space and time averages. The n^{th} moment, where n is a positive integer, is given by $\overline{\phi^n}$, when the time averaging operation is used. These moments can be similarly defined using other expectation operators, such as a spatial average. The standard deviations of the velocity components are $\sigma_{u_i} = (\overline{u_i'^2})^{\frac{1}{2}}$, the mean turbulence kinetic energy (TKE) $= \frac{1}{2} \overline{u_i' u_i'}$, skewness $Sk_{u_i} = \overline{u_i'^3} / \sigma_{u_i}^3$, kurtosis $Kt_{u_i} = \overline{u_i'^4} / \sigma_{u_i}^4$, and the friction velocity, $u_* = (\overline{u'w'^2} + \overline{v'w'^2})^{\frac{1}{4}}$.

Forests are located in the atmospheric boundary layer (ABL), the layer of atmosphere that is directly influenced by the Earth’s surface. Figure 5.1 presents a schematic of the structure of the daytime ABL. The

2345 top of the daytime ABL, at height z_i , caps the mixed layer, within which variables such as humidity and
potential temperature are approximately constant with height. The lowest 10% or so of the ABL is known
as the atmospheric surface layer (ASL), analogous to the ‘inner region’ in wall boundary layers. Above
rough surfaces, such as forests and urban areas, the ASL can be further divided into the inertial sublayer
(ISL) and the roughness sublayer (RSL) (Raupach et al. 1991). Within the ISL, the turbulent fluxes of
2350 momentum and scalar quantities are approximately constant with height. These constant fluxes are used as
scaling parameters in a set of relationships known as Monin–Obukhov similarity theory (MOST) (Monin
and Obukhov 1954; Stull 1988; Foken 2006). MOST is widely used in surface-layer parametrisations for
numerical weather prediction and climate modelling (Skamarock et al. 2008; Hari Prasad et al. 2016). The
RSL extends from the ground up to around 1.5–5 times the mean height of the obstacles h_c , known as the
2355 blending height. The lowest part of the RSL, from the ground to $z = h_c$, is the canopy layer, in which
obstacles and air are intimately intermingled. In neutral atmospheric conditions, turbulent structures that
scale with the mean canopy height h_c control the exchange of momentum and scalar quantities between the
flow and the surfaces of the obstacles. The friction velocity u_* is a scaling variable that is often used as a
shorthand for ASL turbulence, with higher values indicating more turbulent conditions. The friction
2360 velocity is easiest to interpret in when most of the turbulence is mechanically generated by friction over
level ground, for example, in the ISL in statically neutral conditions. In conditions where u_* varies slowly
in the x, y plane, u_* measured at the canopy top ($u_{*z=h_c}$) acts as a local velocity scale, a state known as
‘moving equilibrium’ (Yaglom 1979). This scaling allows landscapes, such as forest stands, to be
represented as homogeneous patches, with each patch characterised by its own velocity (u_*) and length (h_c)
2365 scales (Katul et al. 1999). In these patches, the local turbulence statistics scaled by $u_{*z=h_c}$ become
independent of their horizontal position. The moving equilibrium hypothesis approximately holds for flow
over simplified vegetated hills in neutral conditions (Chen et al. 2019a), although it has unfortunately not
been widely tested. However, in terrain and atmospheric conditions where the turbulence structure varies
strongly in the x, y plane—for example, around patchy forests, or in strongly stable or unstable conditions—
2370 then u_* alone provides limited information about the turbulence (Wharton et al. 2017).

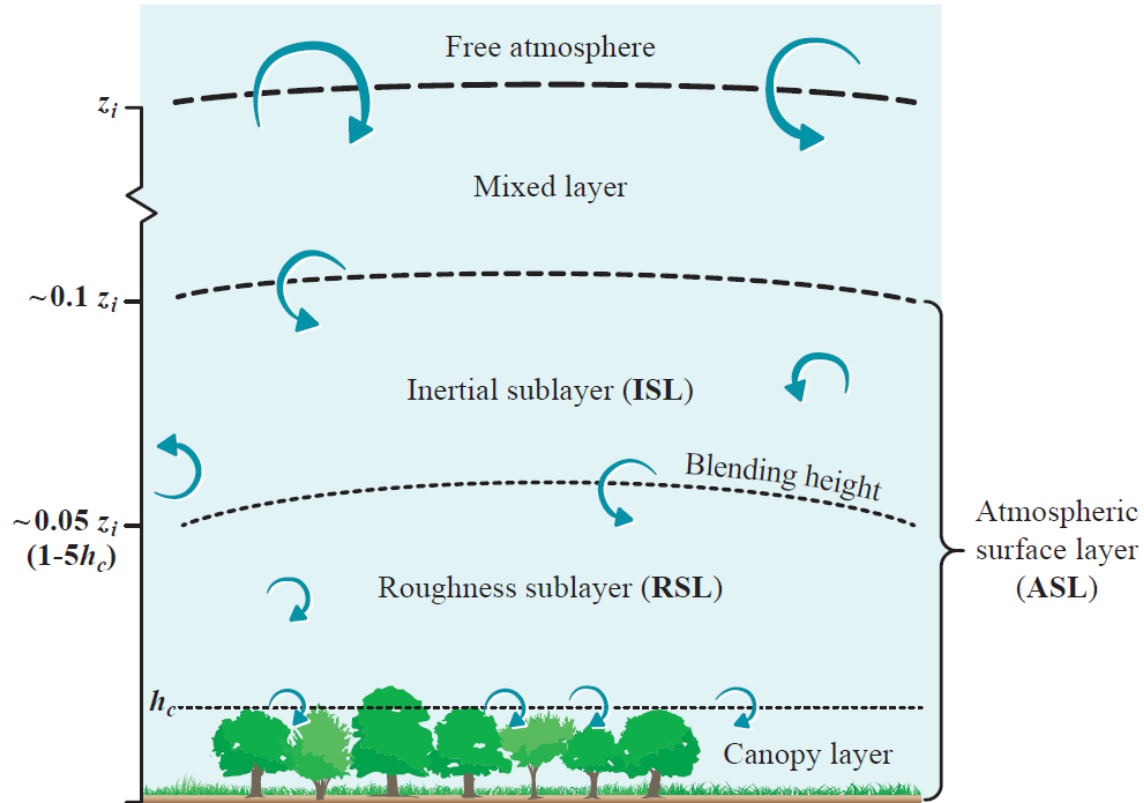


Figure 5.1: Sublayers of the daytime atmospheric boundary layer (ABL) over a forest. The figure follows the classification in Oke (1988) for an urban boundary layer. The height of the mixed layer, which typically accounts for around 90% of the daytime ABL height, is suppressed to aid presentation. The variables z_i and h_c denote the depth of the ABL and the mean height of the forest, respectively.

2375

5.2.2 The double-average method

Early models of flow in vegetation canopies accounted for the presence of the plants through empirical drag terms based on spatially averaged velocity measurements (Inoue 1963; Cionco 1965). In the 1970s and 1980s, researchers developed a more formal basis for the plants' presence, often referred to as the 'double-average method', which proceeds directly from the transport equations (Wilson and Shaw 1977; Raupach and Shaw 1982; Finnigan 1985; Raupach et al. 1986). This is achieved using a volume average operation such that, for a quantity ϕ ,

2380

$$\langle \phi \rangle(\mathbf{x}, t) = \frac{1}{V} \iiint \phi(\mathbf{x} + \mathbf{r}, t) d\mathbf{r}. \quad (5.1)$$

2385

The spatial average in Equation (5.1) is over a volume that (a) includes multiple trees and plants, but (b) is small compared to the distance over which the structure of the forest varies. The vertical resolution is high in order to properly resolve the flow gradients (Finnigan and Shaw 2008). Around the same time, researchers applied similar procedures to investigate mass transfer in engineering applications (Whitaker 1973; Howes and Whitaker 1985). Because plant elements occupy a small proportion of the available volume, no distinction is typically made between the 'superficial' averaging operation (including air and

2390

plant elements in the average) and the ‘intrinsic’ average (within the body of fluid only). This distinction can be important in urban areas (Schmid et al. 2019) and probably also in dense monoculture plantations where the tree crowns overlap, although this has not been tested. The averaging operation is followed by a time average over a period sufficient to capture the dominant scales of motion, but short enough for the flow to be approximately stationary. Applying the two operations to the continuity and momentum equations, ignoring the Coriolis force and the momentum transfer from viscosity, gives

$$\frac{\partial U_i}{\partial x_i} = 0, \quad (5.2a)$$

$$\frac{\partial U_i}{\partial t} + U_j \frac{\partial U_i}{\partial x_j} = -\frac{\partial P}{\partial x_i} + \frac{g}{\theta_0} \langle \bar{\theta}_v \rangle \delta_{i3} - \frac{\partial \langle \bar{u}'_i \bar{u}'_j \rangle}{\partial x_j} - \frac{\partial \langle \bar{u}_i'' \bar{u}_j'' \rangle}{\partial x_j} + f_i, \quad (5.2b)$$

where P is the kinematic pressure, g is the gravitational acceleration, θ_0 is a reference temperature, θ_v is the virtual potential temperature, and δ_{ij} is the Kronecker delta (the second term on the right-hand side of Equation (5.2b) is non-zero when $i = 3$). Capital letters denote the double-averaged quantities, which we refer to as the mean quantities—e.g., the mean streamwise velocity component U . The term $-\partial \langle \bar{u}_i'' \bar{u}_j'' \rangle / \partial x_j$ is the dispersive flux of mean momentum, which accounts for spatial correlations in the time-averaged velocity field. The dispersive flux is usually assumed to be low in homogeneous forests and is therefore typically disregarded in numerical models (Patton and Finnigan 2012). However, recent evidence suggests that the dispersive fluxes of momentum and scalar quantities can be significant around patchy forests (see section 5.6.4). See Finnigan (2000) and Finnigan and Shaw (2008) for more formal discussion of the double-average method.

5.2.3 The double-average method in numerical models

In applications as complex as forest-atmosphere exchange, numerical models will only ever serve as incomplete models, rather than mini versions of the real world, or even computational wind tunnels. Nonetheless, numerical models have emerged as one of the most powerful tools to investigate forest-atmosphere exchange, supplementing experimental observations, theory, and physical models. Their main advantage is that the flow is defined at every cell within the simulated domain, allowing timeseries of interest to be extracted easily. With post-processing and visualisation software, numerical models also provide a picture of the flow that is impossible to replicate with observations or physical models. Researchers have adopted various approaches to approximate solutions to the double-averaged equations, including first-order analytical closure (Finnigan et al., 2015, and references therein), modified gradient-diffusion theory (Zeng and Takahashi 2000), Reynolds-averaged Navier–Stokes (RANS) solvers (Boudreault et al., 2015; Brunet, 2020, and references therein; Katul and Albertson, 1998), and large-eddy simulation (LES) (Shaw and Schumann 1992). RANS methods span first-order closure, ‘1.5–order’ closure based on the transport of the turbulence kinetic energy and its (specific) rate of dissipation, and second-order and higher closure schemes (Katul et al. 2004). For a variety of applications dealing with land-atmosphere exchange, second-order closure appears to be sufficient (Juang et al. 2008). Direct numerical simulation (DNS) has recently been used for small, idealised plant canopies (Sharma and García-Mayoral

2430 2020a, b). However, the computational expense of DNS means it can still be employed only for relatively low Reynolds number (Re) flow and that it remains unsuitable for ecosystem-scale investigations around forests. LES has emerged as the most popular method for investigating ecosystem-scale exchange around forests, although analytical closure schemes and RANS remain popular for situations that do not require the turbulence to be resolved.

Using LES, a low-pass filter of kernel G is applied to the flow field variables,

$$\tilde{\phi}(\mathbf{x}) = \int_{-\infty}^{\infty} G(\mathbf{x} - \mathbf{y})\phi(\mathbf{y})d\mathbf{y}, \quad (5.3)$$

2435 where the overtilde denotes ‘resolved’ field variables, whose prognostic equations are solved. The filter in Equation (5.3) directly resolves motion larger than the filter width Δ_f , which is greater than or equal to the grid resolution Δ_g , with ratios $\Delta_f/\Delta_g = 1$ or 2 common in practice (Geurts 2003; Basu and Porté-Agel 2006). The filtered equivalent of the averaged momentum equations in Equation (5.2b) are

$$\frac{\partial \tilde{u}_i}{\partial t} + \tilde{u}_j \frac{\partial \tilde{u}_i}{\partial x_j} = -\frac{1}{\rho} \frac{\partial \tilde{p}}{\partial x_i} + \frac{g}{\theta_0} \tilde{\theta}_v \delta_{i3} - \frac{\partial \tau_{ij}}{\partial x_j} + \tilde{D}_i, \quad (5.4)$$

2440 where \tilde{D}_i accounts for forcings such as an imposed pressure gradient, the geostrophic wind, or distributed drag from vegetation and other obstacles smaller than the filter width, Δ_f . The sub-grid scale (SGS) stress term τ_{ij} accounts for unresolved scales, those smaller than Δ_f ,

$$\tau_{ij} = \tilde{u}_i \tilde{u}_j - \tilde{u}_i \tilde{u}_j. \quad (5.5)$$

2445 The SGS stresses and fluxes must be parametrised, for which a variety of schemes have been developed (section 5.6.5) (Kirkil et al. 2012; Rozema et al. 2015; Gadde et al. 2021; Moser et al. 2021). Once the LES model has been ‘spun up’—i.e., the flow reaches a statistical equilibrium—the statistics of the flow variables are generated by averaging the resolved quantities, usually in space and time (e.g., Cai et al., 2008; B. Chen et al., 2019). The turbulent perturbations are calculated as the departures from those averages (see Appendix 5A for an example). The main advantage of LES over RANS and analytical models is that LES expressly resolves the largest scales of turbulent motion in the simulated domain. Provided that Δ_f and the model’s forcings are chosen carefully, LES also allows a visualisation and term-by-term analysis of the turbulent flow of air that is impossible to achieve using observations or physical models. To avoid distracting switches between notation, we use the double-average notation throughout this manuscript. References to LES results and models should be interpreted as referring to the resolved variables, unless otherwise stated.

2455 5.2.4 Representing forests through distributed drag

The aerodynamic drag of the forest (per unit mass of air) is accounted for through the term f_i (m s^{-2}) on the right-hand side of Equation (5.2b). This term is the net sum of (i) the form drag from pressure differences either side of each plant element, and (ii) the viscous boundary layers that develop over each plant element,

$$f_i = - \left\langle \frac{\partial \bar{P}''}{\partial x_i} \right\rangle + \nu \left\langle \frac{\partial^2 \bar{u}''}{\partial x_j \partial x_j} \right\rangle, \quad (5.6)$$

2460 where ν is the kinematic viscosity of air. This term is typically parametrised⁶ by spatially averaging the localised drag from the individual plant elements as

$$f_i = -C_d a(z) |U| \langle u_i \rangle, \quad (5.7)$$

2465 where $|U| = (U_j U_j)^{\frac{1}{2}}$ and C_d is a dimensionless drag coefficient. This parametrisation, which we refer to as the ‘distributed-drag parametrisation’, assumes the aerodynamic drag from the forest increases with the square of the velocity, as is the case around bluff bodies (Wilson and Shaw 1977; Shaw and Schumann 1992). The viscous component of the drag is usually neglected in the approximation of f_i because form drag dominates in high- Re flow through forests (Thom 1971; Shaw and Patton 2003). The local forest density $a(z)$ is typically assumed to be a function of the plant area density (PAD), the total one-sided plant area per unit layer volume (m^2/m^3). The plant area index (PAI) is the PAD integrated over the height of the
 2470 forest h_c , i.e., $\text{PAI} = \int_0^{h_c} a(z) dz$.

It is difficult to determine a robust approximation of the drag per unit volume, f_i , in real forests. The parametrisation is based on the form drag imposed by the frontal area of the various tree and plant elements (Wilson and Shaw 1977). In closed canopies such as forests, it is typically assumed that more of the plant
 2475 material is sheltered from the flow than in clumps of leaves or isolated trees, resulting in a lower value of the product $C_d a(z)$ for closed canopies (Sogachev and Panferov 2006; Queck et al. 2012). Relatively low values of C_d are often used in modelling studies to accommodate this shelter effect, with values ranging from 0.1–0.5 (Table 5B.1). These values are usually assumed to be constant and invariant with height. Although sheltering effects, and therefore low values of C_d , have been observed at moderate to high wind
 2480 speeds (Amiro 1990a; Koizumi et al. 2010), there is much more scatter at low wind speeds (Koizumi et al. 2010; Queck et al. 2012). This is probably because the leaves of the trees and plants are mostly relaxed at low wind speeds, but will streamline temporarily in response to gusts, significantly altering the drag. At higher wind speeds, the plant elements spend more time in the streamlined position, so there is less scatter in the drag measurements during the passage of gusts. We discuss this reconfiguration in more detail in
 2485 section 5.5.

5.2.5 The turbulence structure around forests

As the air moves through a forest, momentum is transferred from the flow to the aerial parts of the plants and trees. This reduces the streamwise wind speed throughout the depth of the canopy and a region of high

⁶ This parametrisation is based on the aerodynamic drag equation, used in fluid mechanics and engineering applications. In the fluid mechanics literature, the drag equation (per unit mass) is usually written with a factor of $\frac{1}{2}$, which originates from the formula for the kinetic energy of the fluid in front of the body. By meteorological convention, the factor of $\frac{1}{2}$ is included in the drag coefficient and does not appear expressly here.

2490 wind shear forms around the crown top. The shear region is evidenced by an inflection in the mean
streamwise wind-speed profile, which is approximately exponential within the canopy and logarithmic
above it (Raupach et al. 1996; Finnigan 2000). Below the main crown, a secondary wind-speed maximum
may occur (Shaw 1977), especially near edges and in forests with sparse understories (Dupont et al. 2011).
The source of this secondary maximum is not certain, although it may result from the turbulent transport of
2495 momentum from the upper canopy (Shaw 1977) or mesoscale pressure gradients (Holland 1989). The high
shear around the crown top generates Kelvin–Helmholtz-type instabilities, which in turn generate coherent
large eddies around the tops of the trees, analogous to the dominant processes in a plane mixing layer
(Raupach et al. 1996). Using this mixing-layer analogy, Raupach et al. (1996) reduce canopy turbulence to
a single length scale, $L_s = U_{h_c}/(\partial U/\partial z)_{h_c}$, where U_{h_c} is the mean streamwise velocity component U at
 $z = h_c$. The shear length scale L_s , which equates to around $0.5h_c$ for medium density vegetation, provides
2500 a rough estimate of the diameter of the dominant turbulent eddies. It is difficult to determine the value of
 L_s exactly for real forests because dU/dz varies quickly with height around the crown top (i.e., d^2U/dz^2
is not easily defined). However, L_s can be estimated from the spectral energy peaks in wavelet cospectra of
momentum and scalar quantities (Katul et al. 1998).

2505 The second-order moments $\langle \overline{u'^2} \rangle$, $\langle \overline{w'^2} \rangle$, $\langle \overline{u'w'} \rangle$ and the TKE increase with height within plant canopies,
but are roughly constant above the canopy (Raupach et al. 1996; Brunet 2020). The turbulent velocity
components u' and w' are more correlated and skewed in the RSL than they are in the ISL above, where
many velocity statistics display approximately Gaussian behaviour. Streamwise and vertical skewness (Sk_u
and Sk_w) are approximately zero in the ISL but take values $0.5 \leq Sk_u \leq 1$ and $-1 \leq Sk_w \leq 0$ in forests
2510 (Amiro 1990b; Lee and Black 1993; Raupach et al. 1996; Kruijt et al. 2000; Villani et al. 2003). The values
of Sk_u and Sk_w may be higher, absolutely, at forest edges (Dupont and Brunet 2008b). The association of
positive Sk_u and negative Sk_w values indicates that turbulent transfer is dominated by strong but infrequent
downward penetrations of air into the canopy, known as ‘sweep motions’ ($u' > 0$ and $w' < 0$). Frequent
upward motions of low-momentum air from within the canopy, known as ‘ejections’ ($u' < 0$ and $w' > 0$),
2515 also account for a large proportion of the turbulent transfer (Shaw and Patton 2003), although sweep
motions contribute more to the total transfer of momentum around the crown top (Shaw and Tavangar 1983;
Raupach et al. 1996). Together sweep motions and ejections account for between 60% and 80% of the
exchange of scalar quantities from homogeneous forest canopies to the atmosphere aloft (Gao et al. 1989).
The greater magnitudes of the skewness statistics around forest edges reflect the significant differences in
2520 momentum and scalar exchange in patchy and gappy forests as compared to homogeneous canopies.

The mixing-layer analogy—where shear generated eddies around the crown top dominate turbulent
exchange—has proved remarkably robust in forests and other vegetation. However, current understanding
of canopy turbulence is far from complete. Further LES studies and targeted observations will help to reveal
2525 to what extent three-dimensional structures dominate the turbulence and the conditions under which the
mixing-layer analogy breaks down when the canopy is patchy. Another knowledge gap concerns forest
density. The vast majority of reported investigations have been on relatively dense tropical, Taiga, and

northern temperate forests, usually in the growing season. In these forests, mixing-layer-type turbulence has been observed at low densities (Brunet 2020). However, other sparse tree-dominated landscapes—say, the Guinea Savannah or temperate deciduous forests in winter—have similar mean densities (e.g., PAI 1–2) (Xiao et al. 2017) but entirely different structural and meteorological drivers. These important landscapes remain poorly understood. For further discussion of plant-canopy turbulence see Finnigan (2000) for flow statistics and technical background, Finnigan et al. (2009) and Bailey and Stoll (2016) for the emergence of coherent fluid structures, Belcher et al. (2012) for scaling analysis in complex terrain, and Brunet (2020) for historical background and a review of recent studies in homogeneous plant canopies.

5.2.6 Atmospheric stability and the turbulence structure

Air in the ASL is, on average, statically unstable during the day and stable at night, although the true dynamics are more complicated (Stull 1991). The mixing-layer analogy of canopy turbulence assumes near-neutral conditions, with the dynamics controlled by the high shear in the mean wind velocity around the tops of the trees. However, in strongly stable or unstable conditions, the velocity shear can be much less influential (Brunet and Irvine 2000; Lemone et al. 2019). As the ABL becomes more unstable, the turbulence structure around forests transitions from a shear-driven to a convection-driven regime, i.e. thermal cells govern the flow dynamics, and the mixing-layer type turbulence becomes less prominent (Mahrt 2000; Dupont and Patton 2012; Lemone et al. 2019). Conversely, when the ABL is stable, the buoyancy of the air dampens vertical motion. Mixing-layer-type coherent structures may still develop around a forest, but they are smaller and less energetic than those that form in near-neutral conditions (Dupont and Patton 2012). ABL turbulence is generally more intermittent in space and time in stable conditions (Mahrt 2014). In very stable conditions, fluxes of scalar quantities are driven by an interaction of mesoscale phenomena, such as gravity waves and nocturnal jets, and the local turbulence. This interaction is observed in the large, intermittent variations in temperature and CO₂ concentration around forest that occur when extended calm periods are interrupted by short bursts of intense turbulence (Wohlfahrt et al. 2005; Heinesch et al. 2007; Aubinet 2008).

Simulations of flow around idealised forests in non-neutral conditions are beginning to add detail to this general picture. Patton et al. (2016) used LES to investigate the entire ABL over an interactive forest canopy, across five stability classes (near neutral to free convection). In strongly unstable conditions, thermal plumes may bubble up from the forest floor or the canopy top, and the vertical profiles of the atmosphere in the RSL approach those predicted by MOST. As stability decreases from near neutral to free convection, the dominant turbulent structures around the forest change from shear layer vortices to thermal plumes, and momentum and scalar fluxes become less correlated. It is not clear whether this transition is gradual, with shear and thermally driven structures coexisting, or sudden, with a flip between regimes upon reaching a stability threshold. Nascent research indicates the transition may be sudden (Brunet 2020). In unstable conditions, scalar quantities are transported predominantly by thermal plumes. The Canopy Horizontal Array Turbulence Study (CHATS) observations provide the strongest observational evidence as to the effect of atmospheric stability on exchange in a tree dominated landscape (Dupont and Patton, 2012;

Patton et al., 2011). These measurements found the velocity variances, momentum stresses, and momentum transport efficiency decrease as the atmosphere becomes less stable, indicating that thermal plumes become increasingly influential.

2570 In stable conditions, wind shear at the crown top is higher than in unstable or neutral conditions, and momentum penetrates less deeply into the forest (Su et al. 2008; Nebenführ and Davidson 2015; Chaudhari et al. 2016). Within the forest, turbulence is much weaker and more intermittent than in neutral or unstable conditions, and the pressure transport term of the TKE budget becomes more significant with greater stability (Nebenführ and Davidson 2015). In open forests, intermittent turbulence, driven by shear in the air
2575 aloft, may penetrate into the canopy and dramatically alter the distribution of scalars (Wharton et al. 2017). These intermittent events in stable conditions are not well understood and are seldom resolved well by numerical models because they do not result from resolved shear generated turbulence at the microscale or the MOST parametrisations used in larger scale models. The events are thought to result from nonturbulent ‘submeso’ motions, which fall between the scale of the largest turbulent ABL eddies ($\sim\mathcal{O}(100\text{ m})$) and the
2580 smallest γ -mesoscale ($\sim\mathcal{O}(2\text{ km})$) (Mahrt 2014). There is some evidence that parametrisations of submeso motions may be possible by analogy with ‘self-organised criticality’, the tendency of dynamical systems to organise their microscopic behaviour to be scale independent (Cava et al. 2019). However, this remains an active area of future research, requiring careful comparison between numerical model results and observations (Sun et al. 2015).

2585 The atmospheric stability within forests often differs to that of the surrounding atmosphere. For example, on a sunny day, warm convective thermals may form above a forest, while the air within it remains stable (Ramos et al. 2004; Stull 2006). At night, the situation is reversed when the forest crown loses heat through radiative cooling, forming a capping layer of very stable air around the tops of the trees that can decouple
2590 the forest air space from its surroundings (Nebenführ and Davidson 2015; Xu et al. 2015; Paul-Limoges et al. 2017). The decoupling is sensitive to site-specific meteorological conditions, such as local temperature gradients (Alekseychik et al. 2013; Russell et al. 2016). When the ABL and forest air space decouple, eddy-covariance measurements are difficult to interpret because CO_2 and other scalars can accumulate within the canopy, and the measured turbulent flux is unrepresentative of the forest as a whole (Massman and Lee
2595 2002; Aubinet 2008). In hilly terrain, the decoupling can trigger drainage flows, transporting CO_2 , heat, and water vapour to and from forests (Sun et al. 2012; Xu et al. 2015; Wharton et al. 2017; Finnigan et al. 2020). Drainage flows and other below-canopy transport contribute a large proportion to the total scalar transport in certain meteorological conditions, such as during stable nights with weak winds (McHugh et al. 2017; Paul-Limoges et al. 2017).

2600

5.3 Realistic landscape effects

5.3.1 Adaptation to wind loading

Wind affects all aerial parts of forests on time and space scales from those of the smallest eddy to those of climate variation and tree lifetimes. Many plants respond to wind by reducing their surface area to minimise drag, and therefore lowering the likelihood of damage from wind loading. On longer timescales, plants may apportion biomass in such a way as to acclimate to the wind's prevailing direction and intensity, a process known as thigmomorphogenesis. Figure 5.2 presents examples of trees that show thigmomorphogenetic changes as a result of sustained wind loading. For example, trees at the upstream edge of a forest may have stiffer wood than those further inside the stand (Cucchi et al. 2004; Brüchert and Gardiner 2006), and trees exposed to high winds develop lower crown densities, comprising a smaller number of smaller leaves (Telewski and Pruyn 1998; Telewski 2009). This adaptation is a trade-off for the trees, with increased resistance to wind loading and other environmental stresses coming at the expense of slower growth (Hirons and Thomas 2018). For further background on the permanent response of trees to wind loading, see, for example, Telewski and Pruyn (1998), Telewski (2009), Hirons and Thomas (2018).

2615

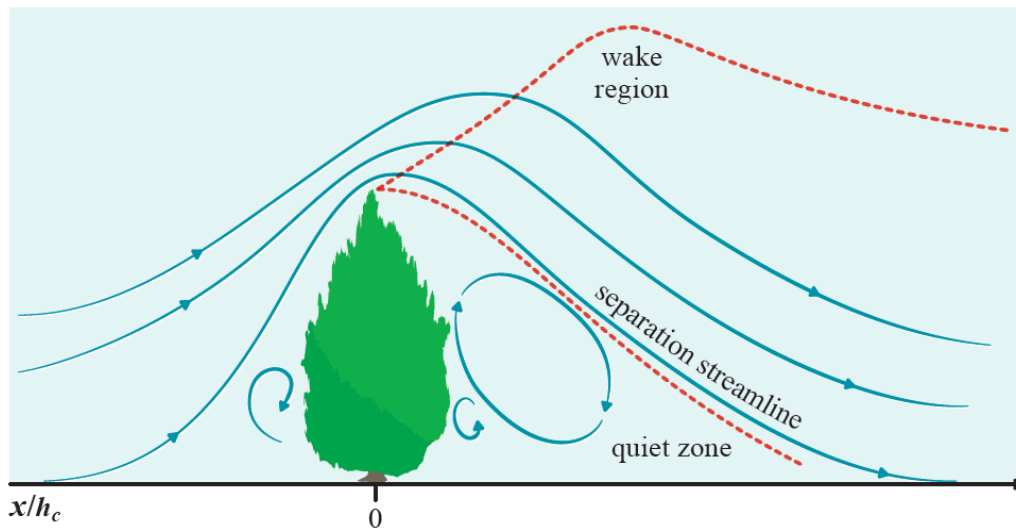


Figure 5.2: (a – left) A wind modified hawthorn (*Crataegus monogyna*) on the Isle of Wight, UK; and (b – right) windswept trees at Slope Point, South Island, New Zealand (Aotearoa).

Windbreaks, also known as shelter belts, exploit the ability of trees and shrubs to adapt to windy environments. Windbreaks have been used for centuries to shelter coastal buildings, to modify the microclimates around crops and grazing land, to protect woodland and wildlife, and, more recently, to modify pollutant transport around urban or industrial areas (Palmer et al. 1997; Pearce et al. 2021). Figure 5.3 shows a sketch of the streamlines around a windbreak for wind blowing from left to right. The ‘quiet zone’ is the region behind the barrier where the mean wind speeds are low and turbulence is dominated by recirculating eddies (Raine and Stevenson 1977). The quiet zone extends $x/h_c \approx 8\text{--}17$ downstream of the windbreak, with higher values observed in conditions with low atmospheric turbulence. The ‘wake region’ is above the quiet zone. The air in the wake region is highly turbulent because of the interaction of downward fluxes of momentum, and sharp velocity gradients as the flow adjusts around the barrier (Finnigan and Bradley 1983). The sizes and energies of the vertical fluctuations are enhanced in the

2625

2630 wake region compared to the incoming stream, whereas those of the vertical components are suppressed (McNaughton, 1989; H. Wang et al., 2001 and references therein).



2635 **Figure 5.3: Flow streamlines around a shelter belt standing perpendicular to the flow of air from left to right. Strong turbulent mixing occurs in the wake region. Figure after McNaughton (1989).**

5.3.2 Flow adjustment around forest edges

2640 Compared to the flow around relatively isolated windbreaks, the flow around a forest is more complicated. Figure 5.4 presents a schematic of the statistical patterns in momentum transfer that emerge as the flow adjusts around a small forest in neutral atmospheric conditions (Belcher et al. 2003, 2012; Dupont and Brunet 2008b, 2009).

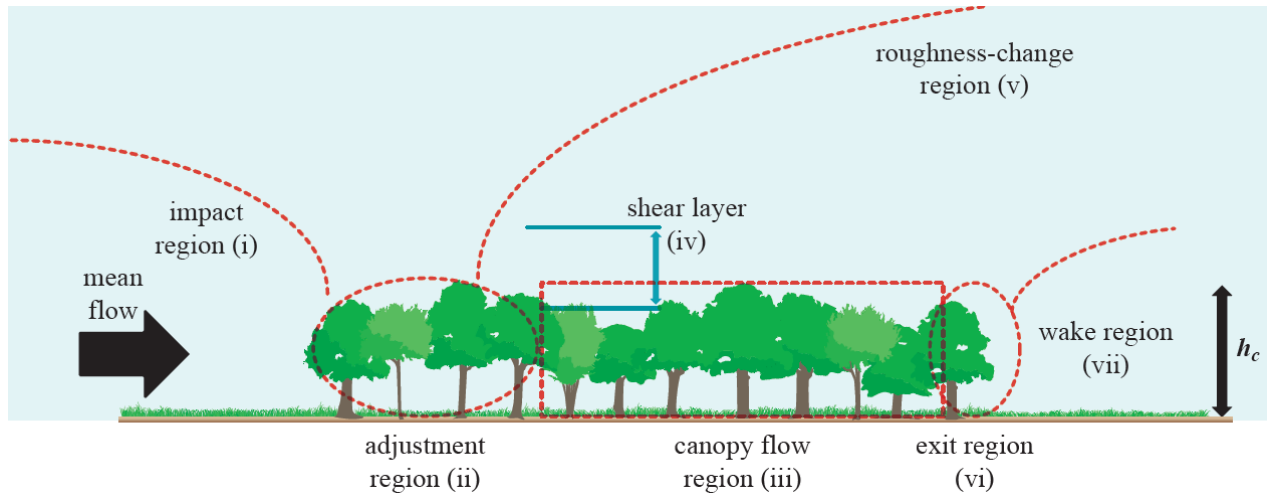


Figure 5.4: Dynamical flow patterns around a small forest in neutral atmospheric conditions. Each pictured tree represents approximately three trees in the streamwise direction. Figure after Belcher et al. (2003) and Dupont and Brunet (2009).

2645 In the *impact region*, (i) in Figure 5.4, the forest acts as a step-change in porosity, inducing a pressure gradient to slow the flow. Just downstream of the forest edge is the *adjustment region*, (ii) in Figure 5.4, in which the drag from the trees decelerates the flow over a distance x_A proportional to a canopy-drag length scale $L_c = 1/C_d a(z)$. The length scale L_c emerges from quasi-inviscid solutions to the momentum equations in one-dimensional flow. It can be interpreted as a distance constant over which the velocity and drag adjust to balance the pressure gradient (Finnigan and Brunet 1995). At the edge of homogeneous canopies, assuming constant shear and neutral atmospheric conditions, the canopy-drag length scale L_c is related to the shear length scale L_s by

$$L_c \approx L_s/2\beta^2, \quad (5.8)$$

2655 where $\beta = u_* / U$ measured at the canopy top ($z = h_c$) (Ross and Vosper 2005; Brunet 2020). Because L_c is inversely proportional to the plant density, the flow adjusts more quickly with increasing forest density⁷, provided the density varies on scales greater than the volume averaging operation. The length scale L_c is only an approximation for three-dimensional flow around real forests, for which the variables C_d and $a(z)$ may not be clearly defined (section 5.5). Nonetheless, numerical simulations, field observations, and flume investigations of vegetation canopies show the adjustment distance x_A downstream of a forest edge is indeed proportional to L_c , with $x_A \approx 4-6L_c \approx 8-10h_c$ (Morse et al. 2002; Yang et al. 2006b; Rominger and Nepf 2011; Belcher et al. 2012). The canopy-drag length scale permits an alternative expression for the PAI of a forest: $\text{PAI}/h_c = a(z) \approx a$, so that $\text{PAI} \approx h_c/C_d L_c$. This is only a rough approximation, because it assumes

⁷ Planted forests are planted at a high density and then thinned repeatedly over the years to reach the final stocking density. It's not unusual for new forests to be planted at 1,000 stems per ha, or 3 m spacing (U.S. Department of Agriculture 1982; Forestry Commission 2021)(U.S. Department of Agriculture 1982; Forestry Commission 2021). Diameter at breast height measurements can then convert stand number density into basal area (i.e. m^2 (stem) ha^{-1}). Converting basal area into PAD requires knowledge of the allometry (i.e., size and shape) of the trees in the stand from standard models or remote sensing (section 5.5.2, below). Variations from the planted-and-thinned density arise from introduction of rides for timber extraction, topographic features, and mortality from disease and windthrow.

the plant area is evenly distributed in all directions. Modelling studies have used PAI values in the range 1–8, with most studies concentrating at the low-to-medium end of the range (Table 5B.1). The relative
2665 scarcity of studies using $PAI > 5$ is surprising given that values in tropical and conifer forests often fall in
the range 8–12 (Lefsky et al. 1999; Fleischbein et al. 2005). In the *canopy-flow region*, (iii) in Figure 5.4,
the flow is fully adjusted to the presence of the forest. The *canopy-shear layer* (iv) is characterised by the
shear-generated turbulent eddies that exchange most of the energy, mass and momentum between the forest
and the atmosphere. These eddies are generated by processes analogous to those in a plane mixing layer
2670 (section 5.2.5 above) (Raupach et al. 1996). Downstream of the adjustment region, an internal boundary
layer may begin to develop above the trees, known as the *roughness-change region* (v).

If there is low vegetation or a large clearing in the lee of the forest, an *exit region* (vi) forms, within which
mean wind speed increases, with a corresponding downwards flow, over a streamwise distance $1-4h_c$. The
2675 exit region may or may not contain a quiet zone of recirculating eddies, as behind windbreaks. Quiet zones
are more likely to form in the lee of dense forests, especially those with an extensive understorey, because
the mean wind speed in the canopy flow region is typically low, meaning there is little exit flow at the
leeward edge (Cassiani et al. 2008; Detto et al. 2008). However, because forest edges are typically more
porous than purpose-built windbreaks, the recirculating eddies are more time intermittent than those behind
2680 windbreaks (Bergen 1975; Cassiani et al. 2008). Recirculating eddies become increasingly common in
forest lees as the forest density increases, although Cassiani et al. (2008) report a threshold $PAI \approx 6$ after
which further increases in density have little effect on the turbulence structure in the lee. The formation and
strength of the recirculating eddies appears to be relatively independent of a forest's foliage distribution
(Ma et al. 2020), although the influence of edge morphology has not been carefully tested. A turbulent *wake*
2685 *region* (vii) occurs above the exit region. Because tree foliage creates substantial drag, the air above forests
is typically more turbulent than that over the bare ground, sea, or fields typically found upstream of
windbreaks. This higher turbulence decreases the distance over which the wake region reaches the ground
behind forests as compared to windbreaks. The quiet zone is therefore relatively smaller behind forests
($x/h_c = 2-5$) than behind windbreaks ($x/h_c = 8-17$) and wake turbulence decays faster in the former.
2690 Banerjee and co-workers offer interesting arguments as to why the edge regions in Figure 5.4 appear to be
so reproducible. Provided the forest is dense enough, the main features in Figure 5.4 are recovered from
turbulently inviscid solutions of the momentum equations (Banerjee et al. 2013). This suggests that the
local forest structure and corresponding turbulence modifies the details of the features in Figure 5.4, but
not their existence. In other words, the turbulently inviscid solution determines the spatial patterns in the
2695 mean flow field and turbulence displaces them locally or smooths them.

5.3.3 The edge regions in context

Only about half of the world's remaining forest area, mostly in the Amazon and the Congo Basin, lies more
than 500m from the nearest edge (Haddad et al. 2015). In much of the Northern Hemisphere, forests are
small and patchy because they are located close to areas where large populations of humans have lived for
2700 centuries. As an extreme example, approximately three-quarters of English woodland lies less than 100 m

from the nearest edge (Riutta et al. 2014). Simple geometric considerations indicate the area of forest subject to edge effects, the ‘edge region’, is surprisingly large. Among two-dimensional shapes with the same area, a circle has the shortest perimeter, i.e., it is the most compact shape in terms of its edge to area ratio. By approximating the plan of a forest stand as a circle, we obtain a lower limit to the area of the edge region from the annulus of width x_A , where x_A is the flow’s adjustment distance. The lower limit for the ratio R_0 of the area of the edge region to the total stand area is therefore

$$R_o = \frac{x_A(2r - x_A)}{r^2} = \frac{\pi \cdot x_A \left(2\sqrt{\frac{A}{\pi}} - x_A \right)}{A}; r \geq x_A > 0, \quad (5.9)$$

where A is the area of the forest stand and r is the radius of the equivalent-area circle. Taking $R_0 > 1/2$ in Equation (5.9) shows the edge region comprises over half the forest stand where $\sqrt{A/\pi} < (2 + \sqrt{2})x_A$, i.e., where $A < (6 + 4\sqrt{2})\pi x_A^2$. Because most forest stands are not even approximately circular, the area subject to edge effects is substantially larger than this minimum. As a conservative heuristic for non-circular forests, we suggest edge effects dominate an area 25% greater than the area of the equivalent-area circle, therefore, where $A < 1.25 \times (6 + 4\sqrt{2})\pi x_A^2 \approx 46x_A^2$. Taking $x_A \approx 8h_c$ —the lower end of reported values of x_A —provides a rule-of-thumb that edge effects dominate in forest stands where $A < \sim 3000h_c^2$. Since forested areas are usually reported in hectares and canopy heights in meters, a dimensional version of the rule-of-thumb is

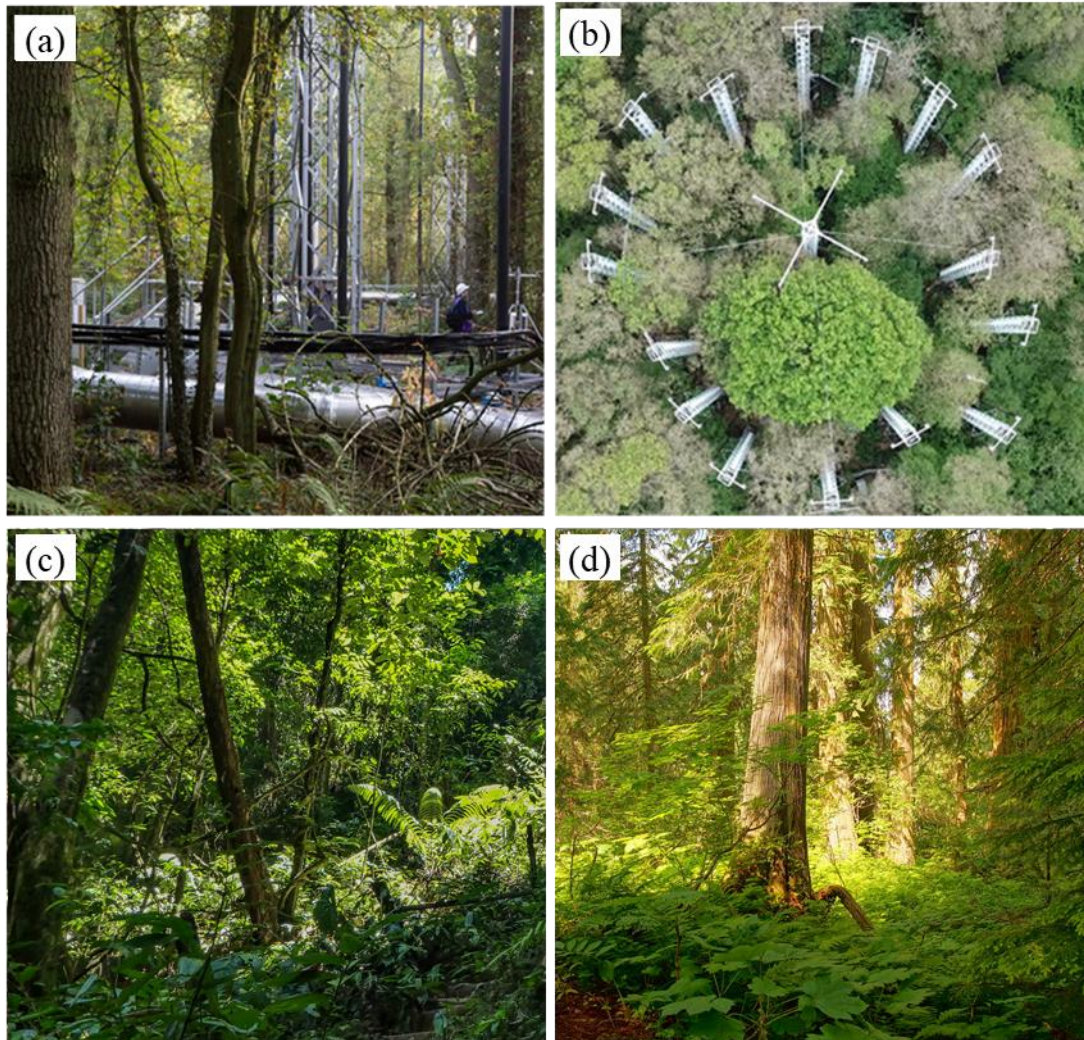
$$A(\text{ha}) < 0.3[h_c(\text{m})]^2. \quad (5.10)$$

For example, for a mature forest with a canopy height of 20 m, edge effects dominate for patches whose area are less than 120 ha. In many parts of the world (Haddad et al., 2015), edge effects dominate most of the forested area.

5.3.4 Patches and gaps

Most real forests contain openings of all shapes and sizes, some examples of which are shown in Figure 5.5. At which scale do these openings begin to influence forest-atmosphere exchange? As regards light penetration, Zhu et al. (2015) propose three categories of gap sizes in temperate forests: ‘small’ $0.49 < R_{O_d/h_c} \leq 1$; ‘medium’ $1 < R_{O_d/h_c} \leq 2$; and ‘large’ gaps, $2 < R_{O_d/h_c} < 3.5$, where R_{O_d/h_c} is the ratio of the opening’s diameter (O_d) to the mean height of the trees surrounding the gap. Openings with diameters such that $R_{O_d/h_c} \geq 3.5$ are considered clearings with their own edges. Small openings, such that $R_{O_d/h_c} \leq 0.49$ are not treated as gaps, because they remain in shade for much of the day. Regarding the flow of air, it is not clear at which size a canopy opening is a ‘pore’, in that the filtering operations smooth out its effect on the flow, and at which size it is a ‘gap’, in that it induces non-random dynamical effects. Determining a numerical threshold between pores and gaps is not possible using observations alone because of the difficulties inherent in obtaining spatially-representative velocity observations in forests (Finnigan 2000; Finnigan and Shaw 2008), and is not straightforward even using idealised LES models, because the threshold likely to be around the scale of, or smaller than, the spatial filter. We propose, as a first

2735 approximation, that openings with horizontal diameter greater than or equal to the shear length scale ($O_d \geq L_s$) can be considered ‘gaps’, because they are likely to induce fluid dynamical effects on the scale of the dominant turbulent eddies. Openings where $O_d \ll L_s$ can be considered ‘pores’ in that they have only wake-scale effects on the flow and contribute little to the overall TKE budget (Raupach and Shaw 1982; Raupach et al. 1996; Finnigan 2000). The length scale L_s is most soundly defined in homogeneous, dense vegetation
2740 canopies, so this is only rough approximation for patchy forests. Because $L_s \approx 0.5h_c$, this dynamical definition of canopy gaps corresponds to the minimum size of the ‘small gaps’ proposed by Zhu et al. (2015), which they determined with respect to light penetration rather than fluid dynamics.



2745 **Figure 5.5: Openings in various forest canopies. In-canopy (a) and aerial (b) views of the BIFoR FACE facility, situated in a mature deciduous woodland in the United Kingdom (Hart et al. 2020). The FACE infrastructure is sited in natural gaps in the forest canopy. Note the variation in foliage colour and density in (b), which was caused by insect herbivory during an outbreak of the European winter moth; (c) canopy openings in the understorey layer of a tropical rainforest in Suriname; (d) canopy openings in the understorey layer of a boreal forest in British Columbia, Canada.**

2750

Few studies have modelled the effects of patchiness on ecosystem-scale exchange. Bohrer et al. (2009) use a virtual canopy generator (Bohrer et al. 2007) to simulate three-dimensional deciduous canopies, including gaps smaller than a tree crown. The heterogeneity caused turbulent fluxes to become spatially correlated in some parts of the forests, such as stronger and more frequent ejection events occurring over shorter trees.

2755 Bohrer et al. (2009) also show that canopy gaps affect the flow differently depending on season. In winter, when deciduous forests are sparse, heterogeneity in the forest canopy causes the dominant turbulent eddies to penetrate less deeply into the canopy relative to the homogeneous case. This decreases the forest's roughness length z_0 , a common measure of surface roughness, and the displacement height d , which reflects the height of the bulk sink of momentum. By the end of spring, however, when the PAI is higher, gaps in

2760 the forest canopy cause the dominant turbulent eddies to penetrate further into the canopy, and the values

of z_0 and d to increase. In other words, in winter, the flow perceives a patchy forest as smoother than a homogeneous one but, after spring leaf-out, it perceives a patchy forest as rougher. This probably results from there being a smaller density contrast between the gaps (high eddy penetration) and full canopy cover (low eddy penetration) in winter, as well as lower wind speeds in spring. It is not clear why Bohrer et al. (2009) focused on spring rather than summer as their leaf-out season, since, for deciduous forests, spring is a time of rapid change in terms of weather and canopy structure. The changes to the values of z_0 and d induced by the transitions in canopy morphology are relevant to large-scale atmospheric models, which employ these parameters to represent forests' effect on the atmosphere. Bohrer et al. (2009) propose that variables such as the maximum PAI and the fractional area of gaps may be used in regional models to adjust the parametrised values of z_0 , d , and the eddy penetration depth, each of which may vary by around 25% in patchy forests relative to homogeneous forests of the same density. Maurer et al. (2015) find that varying z_0 and d seasonally, as a function of the canopy structure, produces more precise and less biased estimates of u_* than models taking constant values of those parameters. In section 5.6.4, we discuss the dispersive fluxes arising from canopy gaps and patchiness.

5.4 Scalar quantities in realistic landscapes

Scalar processes remain far less well understood than velocity adjustment and momentum transport, in terms of both the fundamental flow statistics (Shralman and Siggia 2000) and in geophysical applications around forests (Katul et al. 2013; Bou-Zeid et al. 2020). However, the desire to understand forest-atmosphere scalar exchange is a major motivation for measuring and modelling forests in the first place. Important scalar quantities in forest ecology include energy; trace gases such as CO_2 , water vapour, ozone, and volatile organic compounds (VOCs); ultrafine particles (UFP); litter fragments; soil particles; insect and animal detritus; and spores and pollen. In this section we focus on the numerical modelling of species that can be approximated as being passive and massless at the ecosystem scale. These include CO_2 , as well as other gases and UFPs whose lifetimes are longer than the longest air-parcel residence times (Petroff et al. 2008; Janhäll 2015; Kanani-Sühring and Raasch 2015; Bannister et al. 2021). Other scalars, such as litter, animal detritus, and certain pollens, are much larger and must be treated differently (section 5.6 below). For a scalar quantity ϕ_i , the conservation equation (neglecting molecular diffusion) is

$$\frac{\partial \phi_i}{\partial t} + U_j \frac{\partial \phi_i}{\partial x_j} = - \frac{\partial \tau_{j\phi_i}}{\partial x_j} + S_{\phi_i}, \quad (5.11)$$

where $\tau_{j\phi_i}$ is the SGS scalar flux (this term is not present when the equation is not spatially filtered, see section 5.2.2 above). The term S_{ϕ_i} is a source/sink accounting for the emission, deposition, and production or destruction of the scalar quantity. Equation (5.11) can be double filtered into mean, turbulent and dispersive components, as for Equation (5.2). We retain the forest edge terminology from section 5.3 (Figure 5.4) in this section.

5.4.1 Scalar transport at the upstream edges of forests

2795 Scalar quantities accumulate in the adjustment region at the upstream edge of the forest (region (ii) in
Figure 5.4) over a streamwise distance $x \approx 9-12L_c \approx 2x_A \approx 16-20h_c$. Here, concentrations of the scalar
quantity can be several times higher than in the air upstream of the forest. This pattern appears consistent
across field observations of heat transport around forest edges (Klaassen et al. 2002), and in RANS
(Sogachev et al. 2008) and LES (Kanani-Sühring and Raasch 2015; Ma et al. 2020) models of flow around
2800 idealised forests. The turbulent fluxes of scalar quantities above the adjustment region are 1.2–3.8 times
larger than the surface source rate, and are therefore compensated by horizontal fluxes from elsewhere in
the forest (Kanani-Sühring and Raasch 2015). The location of the peak scalar concentrations and turbulent
fluxes is dictated by (a) the adjustment of the flow and (b) the streamwise turbulent scalar transport. The
mean and turbulent fluxes are of the same order, with the turbulent component more influential in sparser
2805 forests. Strong turbulent fluxes occur above the end of the adjustment region at $x \approx x_A$, and $z \approx 1.5h_c$
(Kanani-Sühring and Raasch 2015; Ma et al. 2020). Ma et al. (2020) attribute these fluxes to scalar-rich air
being swept upwards by the mean and turbulent components of the flow (σ_w^2 is high in this region).
Horizontal and vertical advection, which eddy-covariance measurements do not usually account for
(Aubinet et al. 2010), dominate CO₂ transport in the adjustment region (Ma et al. 2020).

2810 Concentration peaks are more pronounced in forests with a higher mean density and are located closer to
the upstream edge, for example, at $x \approx 9-12L_c \approx 8h_c$ for $PAI \approx h_c/C_d L_c = 8$ but $x \approx 5-6L_c \approx 14h_c$ for
 $PAI = 2$. Forest succession and management, both of which can change PAI will, therefore, greatly
influence scalar concentration gradients close to edges. This is because denser forests impose more drag on
the flow than sparser ones, which suppresses turbulent mixing and causes the flow to adjust more quickly,
2815 i.e., the canopy-drag length scale L_c is reduced. Turbulent scalar fluxes are greater in magnitude and located
closer to the edge with increasing density. The magnitude of the fluxes increases with increasing wind speed
but, because the turbulent components w' and ϕ' vary inversely with increasing wind speed, the locations
of the fluxes do not change. Higher concentrations and scalar fluxes occur at the upstream edges of forests
2820 in which the foliage is distributed uniformly than those in which the foliage is concentrated in the upper
canopy (Ma et al. 2020). Forest management induces a step-change in the aerodynamics of the forest by
substantially decreasing forest density. The subsequent flow pattern must then continuously adjust as the
forest density increases steadily over the timescale of the management period, $\mathcal{O}(10)$ years).

2825 As to the vertical distribution of sources and sinks, scalar concentrations in the lower two-thirds of the
canopy are generally higher for scalars with ground sources than for those with canopy sources (Edburg et
al. 2012). The turbulent fluxes of scalar quantities are high throughout the depth of the canopy for ground
sources, but their magnitudes decrease sharply towards the ground for scalars with canopy sources. Scalar
quantities with canopy sources are stirred by the large turbulent eddies near the tops of the trees, whereas
2830 ground sources of scalars require intermittent turbulent motions to permeate the entire canopy depth. Scalars
emitted from the canopy are therefore more evenly mixed vertically throughout the forest and have shorter

residence times compared with those emitted from the ground (Edburg et al. 2012). With decreasing source height, there are larger variations in the concentrations and turbulent fluxes of scalar at the upstream edges of forests (Ross and Harman 2015; Ma et al. 2020). This is primarily due to low wind speeds and thus less
2835 turbulent mixing within the lower canopy layers, resulting in local accumulation of scalar concentration and large gradients. The lowest scalar concentrations coincide with the vertical locations of the sinks, if one exists (e.g. for CO₂, in the upper canopy during the daytime in the growing season). The depth of the region of low concentration increases with distance from the upstream edge.

2840 Around forest edges, the TKE and momentum transfer are much higher in unstable conditions than when the ABL is approximately neutral, and the flow takes longer to adjust upon meeting the canopy (Ma and Liu 2019). In the adjustment region, the skewness of the streamwise Sk_u and vertical Sk_w velocity are smaller in magnitude in unstable conditions than in neutral conditions, indicating that sweep motions do not penetrate as easily into the forest canopy when the air is buoyant. In neutral conditions, CO₂ accumulates
2845 in the adjustment region at the upstream edge of the forest, and water vapour in the canopy flow region, but these patterns largely vanish in unstable conditions (Ma and Liu 2019).

Scalar fluxes appear to adjust more slowly than momentum as the flow meets the forest, but the patterns in scalar transport are not always intuitive. Scalars are represented in models through the source term S in
2850 Equation (5.11) as either a concentration or flux boundary condition. In numerical models specifying flux boundary conditions, such as those discussed in the previous few paragraphs, one would expect scalar quantities to be slave to the flow because no additional length scales are introduced in the model. Based on Sogachev et al. (2008), Belcher et al. (2012) suggest scalar concentrations and fluxes ought to reach equilibrium after a distance of $x \approx 2x_A$ downstream of the edge, where the value of x_A decreases with
2855 increasing forest density. Following this reasoning, we expect the fluxes of scalars to adjust more rapidly in denser forests. However, Kanani-Sühring and Raasch (2015) find the opposite: scalar fluxes adjust more slowly with increasing PAI, $x/x_A \approx 2$ for sparse forests, where $PAI \approx h_c/C_d L_c = 1-2$, and $x/x_A \approx 3-4$ for forests with $PAI = 4.5-8$. The relative sizes of sparse and dense patches of heterogeneity in forests may also affect scalar concentrations. For example, for flow through idealised porous media, maximum scalar
2860 concentrations occur in sparse patches where the patch size is less than the adjustment distance x_A , but occur in in the dense patches where the patch size is greater than x_A (Chapter 4). The patterns in scalar transport are likely to be ecologically significant. For example, the simulations of Ma et al. (2020) indicate the air can be a few degrees warmer at the upstream edge of the forest. If this temperature variation is correct, a forest edge in the prevailing wind direction may provide very different habitats to forest only tens
2865 of meters away (Zellweger et al. 2020). Turbulent fluxes of scalar quantities adjust slowly around patchy forests and in other complex terrain. For example, turbulent fluxes of water vapour and CO₂ respectively adjust over distances $x \approx 30h_c \approx 38L_c$ and $x \approx 60h_c \approx 76L_c$ downstream of a forest edge (Ma et al. 2020). This amounts to some 500–1000 m for mature forests which, given the abundance of edges in contemporary forested landscapes, indicates scalar concentrations and fluxes are out of equilibrium for
2870 much of the world’s forested area.

5.4.2 Scalar transport in the lee of forests

The area behind the leeward edges of forests shares some obvious similarities with that in the lee of windbreaks in that they are both sheltered from the flow of air. Because of the long history of windbreaks, their micrometeorology is quite established, and gives some idea of what to expect in the lee of forests, for which little observational evidence exists. The turbulent transport of scalar quantities is generally enhanced in the wake region behind windbreaks but is suppressed in the quiet zone (McNaughton 1989), i.e. for a uniform ground source, we expect higher scalar concentrations in the quiet zone and lower concentrations in the wake region, compared to the landscape mean. LES studies of scalar transport in forest lees supports this assessment. Kanani-Sühring and Raasch (2017) show that scalars accumulate in the exit region over a distance $x/h_c \approx 2$ downstream of the trailing edge of the forest, with peak concentrations up to twice as high as those at a reference point far downstream. Ma et al. (2020) obtained similar results using a coupled radiation-LES model, although the magnitudes of the concentration and fluxes depended on the specification of the sources and sinks. Turbulent transport accounts for around half the total scalar transport in the exit and wake regions. The locations of the highest concentrations and turbulent fluxes do not vary with wind speed. Higher concentrations in the exit region occur at lower wind speeds, but the magnitudes of the turbulent fluxes are not affected (Kanani-Sühring and Raasch 2017). In the exit region, the magnitudes of both the concentrations and turbulent fluxes increase non-linearly with forest density. For example, the magnitude of the turbulent fluxes for forests of $PAI \approx h_c/C_d L_c = 8$ are around two and a half times those of forests with $PAI = 2$.

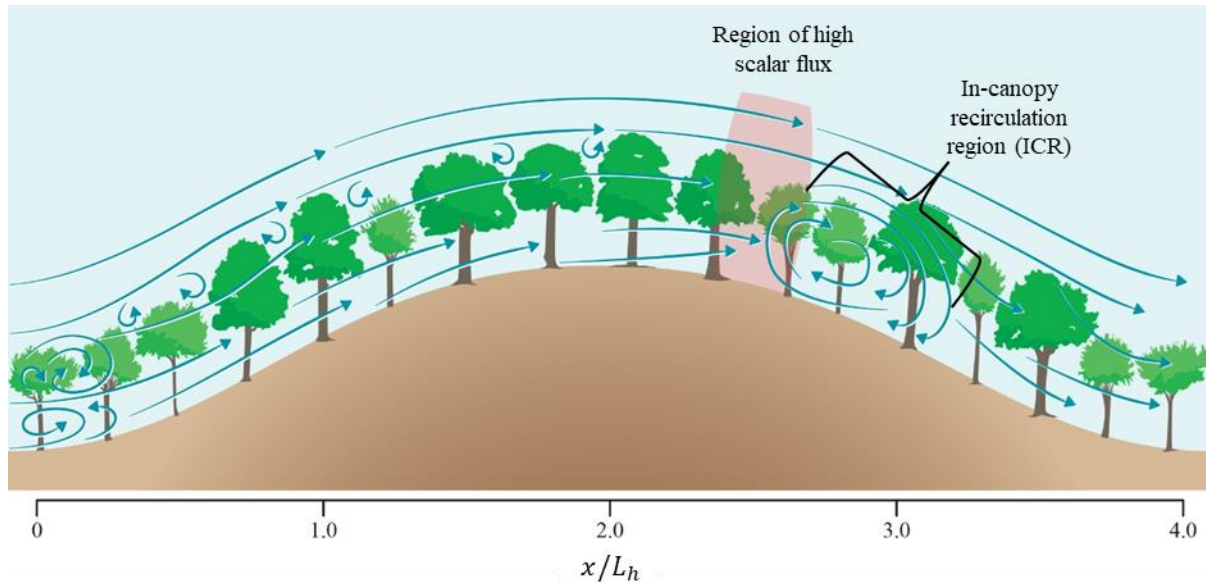
5.4.3 Topographical effects on forest-atmosphere exchange

Topographical effects on forest-atmosphere exchange are not random and can introduce notable horizontal fluxes that are not captured by eddy covariance or smoothed out by time averaging. In heavily populated regions, forests are overwhelmingly confined to land of marginal agricultural value, which often means sloping land (Sabatini et al. 2018). The effect of topography on forest-atmosphere interactions is therefore of wide applicability. Finnigan et al. (2020) review boundary-layer flow in hilly terrain, including sections discussing flows around vegetated hills. We refer readers to their paper for a thorough overview of topographical effects on land-atmosphere exchange. Before moving on, however, we highlight notable results from recent studies that relate to ecosystem-scale forest-atmosphere exchange of scalar quantities.

5.4.3.1 Boundary-layer flow over hills and forest-atmosphere exchange

A large proportion of the literature investigating land-atmosphere exchange over complex terrain studies the flow over simplified topography, such as two-dimensional Gaussian hills or sinusoidal ridges. These studies reveal phenomena around forested hills that appear remarkably robust, despite the studies' differing treatments of the physics (Katul et al. 2006; Ross and Harman 2015; Chen et al. 2019a; Finnigan et al. 2020). In the lee of a forested hill, an in-canopy recirculation region (ICR) may form within the forest, particularly when (a) the hills are steep, so there is a large pressure gradient at the upstream slope; and (b) in tall, dense forests, in which there is little mixing of high momentum air from above the forest with that

near the forest floor. Another ICR may form at the foot of the slope at the upstream side of the hill. The ICRs result from a balancing act between the aerodynamic drag, the pressure perturbation induced by the hill, and the shear stress induced by the forests. A helpful scale to interpret flow in hilly terrain is the hill half length, L_h , defined in Finnigan and Belcher (2004) as a quarter of the wavelength of the topography. The ICR upstream of the hill occurs at $x/L_h \approx -1$ to 0 , and another in the lee of the hill at $x/L_h \approx 2-4$ (Figure 5.6) (Ross and Harman 2015; Chen et al. 2019a). The air in the wake of the lee ICR is often highly turbulent (Finnigan et al. 2020). Forests absorb lots of momentum, meaning ICRs are more common in forested landscapes than in those with low vegetation, and may form in the lee of even gentle hills (Finnigan and Belcher 2004; Patton and Katul 2009). Both the forest density, through its effect on the canopy-drag length scale L_c , and the absolute height of the canopy influence the likelihood of ICRs forming. In ‘shallow’ canopies, where $h_c/L_c < 2\beta^2 \approx 0.2$ (Poggi et al. 2008), not all of the momentum is absorbed by the foliage and ICRs are less likely to form than for ‘deep’ canopies, where $h_c/L_c \gg 0.2$.



2920 **Figure 5.6: Schematic of the flow over a forested hill. A region of high scalar flux occurs at the upwind edge of the in-canopy recirculation region (ICR) in the lee of the hill. This region acts as a chimney for air parcels leaving the forest air space (section 5.4.3.1).**

Figure 5.6 shows the region of strong vertical fluxes of scalar quantities forms between the crest of the hill and the upwind edge of the lee ICR. In this region, scalar fluxes may be up to nearly an order of magnitude larger than the mean landscape flux, depending on the emission location and sampling height (Ross and Harman 2015; Chen et al. 2020). Scalar fluxes around the lee ICR are stronger for ground sources of scalars than for canopy sources, because the topography affects the flow and turbulent mixing more near the forest floor (Ross and Harman 2015). In models for which multiple sources and sinks are specified, the net effect of the sources depends on the balance of the individual transport terms. Chen et al. (2019) propose two pathways by which air parcels leave the forest: (i) the ‘local’ pathway, where ejection events transport air parcels out the forest, approximately vertically; and (ii) the ‘advection’ pathway, where parcels are transported horizontally until they encounter and are entrained into the lee ICR, before turbulent fluxes eject them from the forest. The local and advection pathways are, respectively, the dominant passages for

air parcels moving from the upper and lower parts of the forest air space. The whole forest air space
2935 contributes air parcels that leave via the advection pathway, although sources from the forest floor
contribute a greater proportion of the total escape. The region of high flux acts as a chimney for air parcels
leaving the forest. This behaviour is amenable to observational testing but has not been verified by field
measurements. Zeri et al. (2010) observed higher CO₂ concentrations around a forested hill when the wind
blew from certain directions, which they attributed to CO₂ accumulating in the hill's lee. However, the
2940 accumulation region fell just outside of the observational area, so the authors could not investigate this
behaviour further. LES simulations over realistic topography show a region of enhanced fluxes develops
downstream of hill crests, near the separation point, consistent with the chimney effect that has been
observed for simplified two-dimensional terrain (Chen et al. 2020).

5.4.3.2 Looking forward

2945 Few recent studies have modelled boundary-layer flow over hilly terrain using topographical data from real
sites (Grant et al. 2015; Liu et al. 2016; Chen et al. 2020), highlighting difficulties in interpreting
measurements in complex terrain, even when armed with theory and conceptual models. Measurement
towers are typically sited on the tops of hills. When considering simplified topography, this decision is not
controversial. The fluxes at the crest of the hill are similar to the landscape flux, although the terrain may
2950 induce biases that cause the flux measurements to be higher or lower than the landscape mean (Chen et al.
2020). Over realistic topography, while the crest usually remains the best observational location,
measurements consistently underestimate the landscape flux and there is a large variability in flux
measurements at different hill locations (Chen et al. 2020). Further testing at other sites will reveal whether
this tendency to underestimate flux measurements is a common problem. Chen et al. acknowledge that they
2955 performed their experiments in neutral conditions; mixing promoted by daytime buoyancy may alleviate
some of the discrepancy between the crest measurements and the mean landscape flux.

Flows induced by gravity—as opposed to pressure perturbations in the flow, as in Figure 5.6—are an
important topic of ongoing research in forest-atmosphere exchange. In mountainous regions, gravity flows
2960 often interact with one another across time and space scales larger than the focus of this review, so we do
not discuss these flows in detail here (see Oke (1978) for an introduction to gravity flows, Mahrt (1982)
and Belcher et al. (2012) for related scaling analysis, and Finnigan et al. (2020) for a review of recent
studies and wider discussion). Downhill (katabatic) flows can occur at night when valley surfaces emit
long-wave radiation, causing the air near the surface to cool and accelerate downslope under the influence
2965 of gravity. Katabatic flows tend to decouple soil CO₂ fluxes from eddy-covariance measurements above the
canopy (Aubinet et al. 2003; Feigenwinter et al. 2008), which can introduce significant errors into diurnal
carbon budgets (Van Gorsel et al. 2011). In stable conditions, even gentle slopes can generate strong gravity
flows (Belcher et al. 2012), meaning that, at certain sites, advection complicates the interpretation of eddy-
covariance measurements at night but not during the day (Leuning et al. 2008). However, night-time
2970 advection it is not easily addressed even with careful measurements within the forest (Aubinet et al. 2010).
An interesting line of future research would be to compare low-wind night-time eddy-covariance

observations around forested hills to high-resolution LES simulations. This type of work may reveal much-needed scaling laws to determine the onset of gravity flows, the strength and even direction of which are sensitive to the balance of the inertial forces and the buoyancy (Belcher et al. 2012; Finnigan et al. 2020).

2975 **5.4.4 Air-parcel residence times**

2980 Once a molecule or particle enters a forest from outside, or is released from a leaf or the soil, it is mixed within the forest air space. This is easiest to visualise in terms of the stretching and dissipation of small air parcels. During the passage of these air parcels, the molecules or particles contained within may react, diffuse across leaf boundary layers, or deposit on surfaces. Air-parcel residence times therefore affect forest ecology—e.g. influencing chemical signalling (Szendrei and Rodriguez-Saona 2010) and VOC chemical processes (e.g., Pugh et al. 2011; Batista et al. 2019), or varying the likelihood of nutrients (Fowler et al. 2009) or fungal spores (Norros et al. 2014; Pan et al. 2014a) being deposited. The lifetimes of some VOCs emitted by forests are on the order of tens of minutes (Wolfe et al. 2011), similar to the residence times of parcels moving from close to the ground. Reactive scalar quantities emitted from the ground are therefore 2985 more likely to be chemically transformed within the forest than scalars emitted in the tree crowns.

The initial vertical position of an air parcel affects its residence time, with parcels ‘released’⁸ near the ground having much longer residence times than those released higher in the forest canopy (Fuentes et al. 2007; Edburg et al. 2012). Estimates of parcel residence times vary from a few seconds for parcels moving 2990 from the crown, to around 30 minutes for parcels moving from the forest floor, with spatially averaged values in the order of a few minutes (Fuentes et al. 2007; Edburg et al. 2012; Gerken et al. 2017; Hart et al. 2020). The density and morphology of vegetation influences air-parcel residence times. For example, in a short, trellis-trained crop, parcel residence time increases with canopy PAI, other than for parcels released high in the canopy (Bailey et al. 2014). Residence times increase with increasing PAI, because mixing- 2995 layer-type eddies and TKE do not penetrate as deeply into the canopy (Gerken et al. 2017). Air parcels remain in the canopy for longer when they are released from approximately the height at which most of the plant area is located. For example, for parcels released in the upper canopy, residence times are longer for top-heavy PAI profiles, such as pine plantations, than for forests with more plant area lower down. We expect longer residence times in stable atmospheric conditions, such as at night or on overcast days, because 3000 turbulent mixing is suppressed. We are not aware of any previous investigations into stability effects on parcel residence times in forests (see Chapter 6). Observations and RANS simulations in urban areas indicate parcel residence times generally increase with greater atmospheric stability, although they also heavily influenced by the wind velocity and the geometry of local obstacles (Mavroidis et al. 2012).

⁸ Numerical models allow the flow to be studied from a Eulerian or Lagrangian point of view. The Eulerian specification of the flow focuses on specific locations in space through which the air flows with time, whereas the Lagrangian specification follows an individual air parcel as it moves through space and time. Studies looking at particle residence times in plant canopies often adopt a Lagrangian point of view.

3005 The next challenge in this line of enquiry is to explain quantitatively how forest canopy turbulence affects
air-parcel residence times. As rough approximation in homogeneous forests, Gerken et al. (2017) propose
that the parcel residence time (τ) is proportional to the reciprocal of the friction velocity, i.e. $\tau \propto 1/u_*$.
Unfortunately, this relationship is unlikely to hold in all landscapes. Around forest edges, and in other
3010 complex terrain, the flow is spatially variable (e.g., Figures 5.3 and 5.6). This variation means that we
cannot infer residence times across the whole forest from single variables such as u_* , i.e. we cannot assume
a moving equilibrium (Yaglom 1979). While there have been no investigations of the effect of forest
heterogeneity on air-parcel residence times, in vineyard-type canopies, heterogeneity generally decreases
residence times (Bailey et al. 2014). Lagrangian investigations in urban settings show that heterogeneity
induces spatial variations in the residence times of scalar quantities (Lo and Ngan 2015, 2017) and this
3015 method may be applied to forested environments.

Part II: Improving ecosystem-scale models of forest-atmosphere exchange

In Part II we focus on recent attempts to improve numerical modelling techniques from developments in
theory and experiments. Many of these topics, particularly those in section 5.6, are important aspects of
atmospheric science in their own right, which deserve their own reviews. However, certain techniques can
3020 be readily adapted to improve understanding of how forests and our atmosphere interact. We focus on the
application of these topics in turbulence resolving models, rather than attempting to review each area
exhaustively.

5.5 Canopy structure

5.5.1 Drag and plant reconfiguration

3025 The distributed-drag parametrisation was introduced in the 1970s and remains the starting point for
ecosystem-scale numerical investigations of forest-atmosphere exchange (see Table 5B.1), usually through
the approximation $f_i = -C_d a(z) |U| \langle u_i \rangle$, i.e., Equation (5.7). The distributed-drag parametrisation
accounts for the average aerodynamic drag the plants impose over some spatial scale larger than individual
twigs and leaves. For some applications, this averaging process is sufficient. Using this method, RANS and
3030 LES models can accurately resolve the mean flow through homogeneous forests and around bluff bodies
(Yang et al., 2006). However, the method poorly reproduces higher-order flow statistics around forests and
in other vegetation canopies (Dupont and Brunet 2008b; Pan et al. 2014a; Ma and Liu 2019). The reason
for this discrepancy may be lie in the fact that there is little in the formulation to account for the detailed
morphology and mechanics of plants and trees. In this section, we look at numerically efficient ways to
3035 improve the drag parametrisation to represent a more realistic range of forest structures.

Trees and other plants reconfigure elastically to reduce drag over short timescales, visible in the everyday
observation of leaves curling and tree branches thrashing in high wind (e.g., Figure 5.7). The

3040 reconfiguration of large trees is less extreme than of many smaller plants, which can bend elastically throughout their whole body in strong wind, significantly reducing their mean height. However, even large hardwood trees are softer geometrically and mechanically than most human-made structures, and should not be approximated as being rigid. Measurements of isolated trees in wind tunnels show that streamlining reduces the trees' frontal area by up to 54%, depending on tree species and wind speed (Rudnicki et al. 2004; Vollsinger et al. 2005). Measuring the effect of reconfiguration is more difficult in forests than on
3045 isolated trees. Trees deep inside forests are exposed to lower wind speeds than those around edges, but they are also usually suppler than edge trees (Gardiner et al. 2016). High-frequency velocity measurements in conifer forests show that trees reconfigure at the stand scale, especially around edges, large clearings, and in the region of high shear around the top of the canopy (Queck et al. 2012; Dellwik et al. 2014). The reconfiguration of dense forests and other plant canopies is also evident in coherent 'honami' waves passing
3050 through a field of wheat (Inoue 1955; Maitani 1979), from wavelet analysis of pine plantations (Schindler et al. 2012), and in video footage of forests taken above the crowns (Harper, BIFoR FACE site, private communication 2021).

At low wind speeds, the movement of individual leaves dominates foliage reconfiguration (Tadrist et al. 2018), e.g., curling up to form cones and cylinders (Vogel, 1989). This foliage-dominated configuration could account for the scatter observed in the measured values of the drag coefficient C_d at low wind speeds. At low speeds, the total plant area exposed to the wind varies more than at higher speeds—at low speeds, some leaves will be sheltered only until a gust rolls through the forest. Measuring drag coefficients using instantaneous velocity measurements—i.e., calculating the drag as being proportional to $\overline{|U|u}$ rather than
3060 U^2 —reduces scatter in estimations of C_d and the wind-speed dependency of the product $C_d a(z)$ (Cescatti and Marcolla 2004; Queck et al. 2012).



3065 **Figure 5.7: (a – left) leaves of a cottonwood (*Populus deltoides*) curling in high wind. (b – right) trees at the edge of a forest reconfiguring under wind loading**

Plant reconfiguration is particularly relevant in patchy forests because the flow is constantly adjusting and readjusting as it moves across gaps and clearings. Capturing this reconfiguration directly in ecosystem-scale models is currently unworkable because of the computational expense of simulating the motion of flexible bodies in turbulent flow. However, it may be partly captured by modifying the drag parametrisation

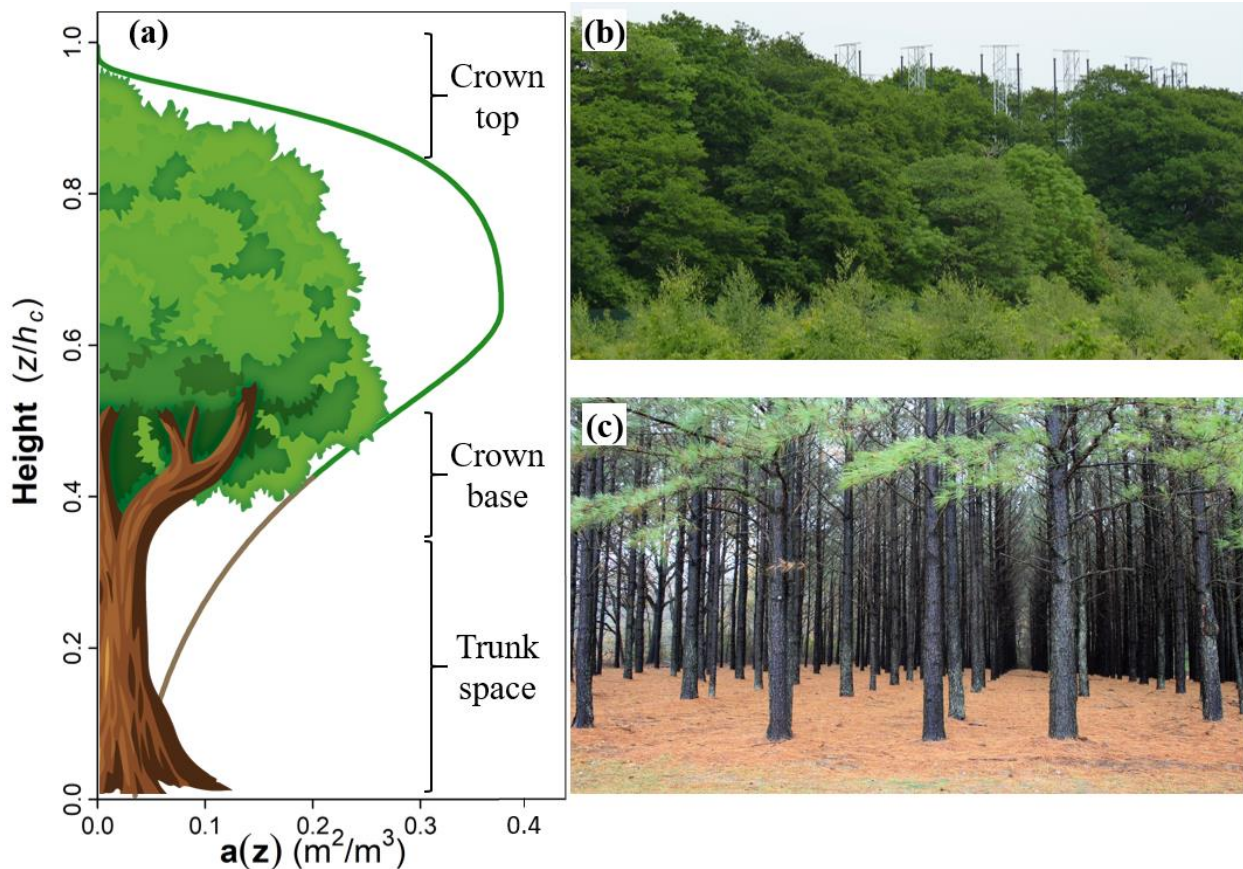
3070 in Equation (5.7). For example, one could consider the PAD, represented in $a(z)$ in Equation (5.7), as
varying with velocity (Speck 2003), or replace the drag coefficient C_d , with a shape factor that varies with
the flow (Gaylord and Denny 1997). However, these approaches require a detailed three-dimensional
knowledge of the forest structure and its response to wind loading. A more empirical approach is to proceed
from the observation that reconfiguration leads to a lower increase of drag with velocity than could be
3075 expected by assuming $a(z)$ and C_d both take constant values (Vogel 1989). Therefore, instead of having
the drag $f_i \propto U^2$, we have $f_i \propto U^{2+B}$, where B is known as the Vogel number (De Langre 2008; Vogel
2020). B therefore acts as an empirical modification to Equation (5.7) to account for the variation of $a(z)$
and C_d with velocity. Negative values of B imply that, because of reconfiguration, plant drag increases with
velocity more slowly than the usual assumption of velocity squared. Where the plants do not reconfigure,
3080 $B \rightarrow 0$ and the drag increases approximately with the square of the velocity.

Pan et al. (2014a) use LES to model the reconfiguration of a wheat canopy. They maintain the quadratic
dependence of drag on velocity in the drag parametrisation in Equation (5.7), accounting for plant
reconfiguration using a velocity-dependent drag coefficient $C_d = (|U|/A_v)^B$, where A_v is a velocity scale
3085 related to the shape and rigidity of the plants. Using the variable C_d , their LES model simulated flow with
more accurate higher order statistics than the same model with a constant C_d value (with similar
performance with respect to the mean velocities, momentum transfer and TKE). Using a variable C_d value
also improved estimates of momentum transport by sweep motions penetrating the canopy. In similar work,
Pan et al. (2014b) show plants reconfigure more at higher flow velocities, reflecting the results of lab
3090 investigations on isolated plants (Tadrist et al. 2018). In both Pan et al. (2014a, 2014b), the absolute values
of Sk_u and Sk_w increase with a more negative Vogel number—i.e. simulating more reconfiguration—as did
the ratio of sweeps to ejections. To see why, taking $B = -0.74$ from Pan et al. (2014a) gives $f_i \propto U^{1.26}$ in
Equation (5.7) rather than $f_i \propto U^2$. The drag force therefore increases more slowly with increasing velocity,
leading to a greater contrast of TKE inside and above the canopy. The decrease in the velocity exponent
3095 also increases the frequency and strength of sweep motions because strong events ($u' > 0$) penetrate further
into the canopy. The canopy-drag length scale L_c increases when the value of C_d is smaller because gusts
are able to penetrate further into the forest before drag halts their progress.

Field studies of plant reconfiguration typically focus on time-averaged adaptation over long time intervals,
3100 although measurements in poplar crowns show C_d values decrease with increasing wind speed across
averaging periods as short as 1 s (Koizumi et al. 2010). Measurements in a patchy conifer canopy found
 $B \approx -0.8$, although this value varied with the wind direction (Queck et al. 2012). Pan et al. (2014b) ran
simulations using $B = 0, -2/3, -1$, and $-4/3$, finding that a non-zero Vogel number improved the
agreement of the simulations with flume observations, with the greatest fidelity obtained using $B = -1$.
3105 Other estimates for B include $-1 < B < -2/3$ from biomechanics theory (Gosselin et al. 2010). $B \approx -1$
appears to be a robust measurement for poroelastic structures, including forests and other vegetation
canopies (Gosselin, 2019 and references therein). We suggest 0 and -1 as approximate upper and lower
bounds for the Vogel number B .

5.5.2 Terrestrial laser scanning

3110 Most studies assume that the local foliage density $a(z)$ varies only with height, if at all (Table 5B.1). For
example, Figure 5.8a shows $a(z)$ derived using the parametrisation by Lalic and Mihailovic (2004), as
employed by Yan et al. (2020), among many others. The forest is assumed to be horizontally homogeneous
at each height, reducing the forest morphology to a single dimension (z), typically with most of the density
3115 confined to the tree crowns. This is a reasonable approximation for certain forests, such as unthinned conifer
plantations (Figure 5.8c). However, it is a poor approximation for many forests, such as oak-dominated
temperate forests (Figure 5.5) and certain tropical forests (Figure 5.9), which have dense understorey layers
in which the PAD is similar to that of the crown layer or multiple modes of leaf density (Zhao et al. 2011;
Schneider et al. 2019). Most models also assume that forest edges are structural continuations of the main
body of the canopy (Dupont and Brunet 2008b; Kanani-Sühring and Raasch 2015; Ma et al. 2020). Unless
3120 the forest has been recently disturbed, this assumption is unrealistic because many trees and understorey
plants grow into the light to maximise the leaf area available for photosynthesis, thereby forming an almost
closed edge (Figure 5.8b).



3125 **Figure 5.8:** (a) Vertical profile of PAD, $a(z)$, calculated using the formula derived by Lalic and Mihailovic (2004); (b) the southern edge of the oak-dominated woodland at the Birmingham Institute of Forest Research (BIFoR) free-air carbon dioxide enrichment (FACE) facility; and (c) open trunk space of an even-aged *Pinus taeda* monoculture plantation.

3130 Terrestrial laser scanning (TLS), also known as terrestrial LiDAR, has been a major technological leap since the first LES investigation of forest-atmosphere interactions (Shaw and Schumann 1992). TLS provides non-destructive, in situ information of the three-dimensional structure of trees and forests, down to a resolution of millimetres. (Calders et al. 2020). See, for example, a captivating example of a TLS scan of an Australian notophyll vine forest in Figure 5.9 (Calders et al. 2020). Note the variety of plant forms, stem diameters, and leaf sizes for this uneven-aged, biodiverse, forest. Note also, in the right-hand panel of Figure 5.9, the pronounced increase in PAD at about 2 m, suggestive of a herbivore ‘browse line’ (Hazeldine and Kirkpatrick 2015), the relatively sparse canopy between 2 m and 10 m, and the slow drop-off of PAD with height above about 28 m, typical of a biodiverse forest. TLS is currently used for a range of ecological applications (Ashcroft et al. 2014; Momo Takoudjou et al. 2018), but has yet to be adopted widely in models of forest-atmosphere exchange.



3140 **Figure 5.9: 3D complexity of a Simple Notophyll Vine Forest (Robson Creek, Australia) captured using a time-of-flight RIEGL VZ-400 instrument. Left panel: The colours represent the distance from the scanner. Right panel: Derived plant area volume density as a function of canopy height derived for the same scan using (Calders et al. 2015). Figure and caption reproduced without modification from Calderys et al. (2020) under Creative Commons License CC BY 4.0. ‘Plant area volume density’ refers to PAD.**

3145 TLS combined with LES has the potential to revolutionise ecosystem-scale models of forest-atmosphere exchange. TLS allows real sites to be reconstructed numerically by splitting the forest volume into cells, each of which is assigned a plant density value calculated from TLS point clouds (Queck et al. 2012; Calderys et al. 2015; Raunonen et al. 2015; Boudreault et al. 2015). The few studies that have used this approach in heterogeneous forests show how much information that can be missed by assuming heterogeneity. Schlegel et al. (2015, 2012) use TLS measurements in an LES model of flow around a large forest gap. They show that small-scale plant heterogeneity creates sustained upwards motion in denser patches of forest and downwards motion in clearings and large gaps. Failing to account for the true structure of forest edges strongly overestimates the penetration of air into the forest (Schlegel et al. 2012, 2015), and neglects the possibility of dispersive fluxes of momentum and scalar quantities (Boudreault et al. 2017; Li and Bou-Zeid 2019). TKE and Reynolds stresses decay faster behind closed edges and strong cross flows may develop. Away from the edges, large gaps and clearings deflect the flow downwards, creating advective fluxes within the forest air space (Queck et al. 2016). Boudreault et al. (2017) use TLS measurements (outlined in Boudreault et al., 2015) and LES to model air flow across a forest edge. Compared to a homogeneous edge, the gaps induce variations in the flow, for example, the streamwise (U) and vertical (W) velocity components respectively vary by around 20% and 5% of their spatial means at $z = 0.5h_c$. The

turbulent momentum fluxes are likewise higher in the heterogeneous case, for example σ_w varies by around 40% of its spatial mean, because air is forced through patches of low density.

5.5.3 Stochastic drag forcing

3165 The product $C_d a(z)$ in Equation (5.7) is typically approximated as a smoothly varying function of height, with C_d taken as constant. However, Finnigan and Shaw (2008) raise the important point that the dominant large eddies around forests have diameters in the order of $L_s \propto h_c$ (Raupach et al. 1996; Bailey and Stoll 2016). To resolve the structure of these eddies in numerical models, the vertical filter needs to be much smaller than h_c , for example, a filter of $h_c/25$ is taken in the model in Appendix 5A. At this resolution, we can no longer assume $a(z)$ is a smooth function—for example, notice the structural variation of the forest understories in Figures 5.5 and 5.8. Finnigan and Shaw (2008) propose representing $C_d a(z)$ through a stochastic variation overlaying a smooth background trend, thereby introducing a stochastic forcing into the resolved momentum equations.

3175 To illustrate this argument, we consider a small, horizontally homogeneous forest patch, represented using the drag parametrisation in Equation (5.7), with the transport equations solved using LES (see Appendix 5A for numerical details). We define two cases, with the same dimensions and mean density. For Case 1, $C_d a(z)$ is uniform throughout the domain. For Case 2, $C_d a(z)$ varies randomly in space throughout the forest by $\pm 2\%$ of the value for Case 1, a small variation in comparison to the natural variation of forests. The random spatial variation of $C_d a(z)$ is almost imperceptible in the mean variables and second-order statistics such as the TKE and kinematic turbulent momentum flux. However, Figure 5.10a shows the streamwise velocity skewness Sk_u at the upstream edge of the forest ($x/h_c \approx 0-5$) is less negative for Case 2 than it is for Case 1. The value of Sk_u above the forest is more negative for Case 2 than it is for Case 1. The streamwise velocity kurtosis Kt_u at the upstream edge of the forest ($x/h_c \approx 0-5$) is smaller for Case 2 than it is for Case 1 within the forest, and larger for Case 2 than it is for Case 1 above the forest (Figure 5.10b). These statistics indicate the small stochastic forcing in Case 2 decreases the coherence of the flow at the upstream edge—i.e., the upstream edge behaves less like a bluff body than the homogeneous Case 1—leading to fewer lulls in the streamwise velocity within the forest but more lulls just above the canopy. We do not generalise these results further because the cases are idealised. But they support the conclusions of Dupont and Brunet (2008a) and Pan, Chamecki, et al. (2014), for example, that the probability distribution of gusts indicated by higher-order statistics are sensitive to the model setup, including any stochastic element. This sensitivity needs careful testing.

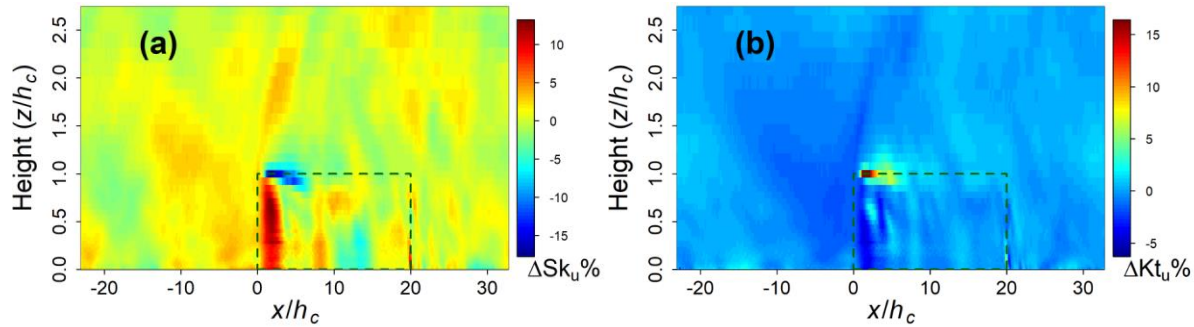


Figure 5.10: (a) Percentage difference in Sk_u ; and (b) Kt_u between Case 1 and Case 2, as a total of the maxima for Case 1. The changes are induced by the stochastic variations in $C_d a(z)$ for Case 2. The green dashed line shows the presence of the forest. The x -axis is scaled so that 0 coincides with the upstream edge of the forest. ΔKt_u is around 25 % for a few resolved cells in (b). These values are suppressed to 15% to aid presentation.

3195

5.5.4 Waving plants and biological backscatter

The velocity spectra of airflow around forests and other vegetation canopies often contain peaks that correspond to plant movement (Finnigan 1979a, b; Cava and Katul 2008; Dupont et al. 2018). These peaks indicate energy is transferred in two directions—the flow perturbs the plants, but the plants also perturb the flow. The latter effect is usually ignored in models at the ecosystem scale and above on the assumption (usually implicit) that the turbulent structures generated by plant movement are much smaller and less energetic than the dominant mixing-layer eddies. However, this neglects the possibility of resonant effects occurring when the passage frequency of the dominant eddies approaches the natural frequency f_0 of the moving plants, as has been observed in crops (Py et al. 2006). Trees near the edges of forests, such as in patchy landscapes and around clearings, are more susceptible to resonance effects than those further inside forest stands (Dupont et al. 2018).

3200

3205

Accounting for this two-way transfer of energy is not straightforward at the ecosystem scale. Dupont et al. (2010) use LES to model a crop canopy as a poroelastic continuum, with plant movement incorporated into the momentum equations as small mechanical oscillations of rigid stems. Other researchers had previously developed models coupling wind flow and plant swaying in a similar way, but with analytical solutions obtained from simplified velocity statistics rather than through LES (Gosselin and de Langre 2009; Webb and Rudnicki 2009). Pivato et al. (2014) extend this approach, using LES to model the movement of pine trees as simplified flexible cantilever beams. Their model includes the possibility large tree deflections by strong gusts, which Dupont et al. (2010) did not account for in their crop model. The model of Pivato et al. (2014) performed well against field observations and more complex small-scale plant models in terms of the instantaneous tree response to gusts.

3215

3220

The direct approaches of Dupont et al. (2010) and Pivato et al. (2014) require the plant architectures to be heavily simplified to be computationally feasible. This is not a major problem for tall, slender trees such as maritime pine, the subject of Pivato et al. (2014). However, decurrent trees, which include many broadleaf species, are structurally more complex and can have modes of vibration across several scales, for example,

3225 $f_0 \approx 0.5$ Hz in the trunks and several Hz in the branches (Schindler et al. 2013). Capturing these interactions
 at the scale of an entire forest would be very demanding computationally. A possible workaround in patchy
 landscapes is to proceed from the observation that wind velocity spectra at forest edges contain peaks
 around f_0 , the natural frequency of the trees (Dupont et al. 2018). This motion is especially visible in the
 spanwise direction because the turbulent velocity perturbations are smaller than those in the streamwise
 direction. From a modelling point of view, the trees' movement transfers energy from the SGS to the
 3230 smallest resolved scales (Piomelli et al. 1991), a process known as 'backscatter'. In general, backscatter is
 most apparent where small but energetic eddies are present (Mason and Thomson 1992), such as around
 forests and other complex structures. Studies of urban canopy flow provide a template of how backscatter
 could be incorporated into forest models. For example, O'Neill et al. represent the stochastic effects of
 backscatter in their LES simulations of the neutral surface layer (O'Neill et al., 2015) and street canyon
 3235 flow (O'Neill et al., 2016) by incorporating random acceleration fields a_i in the momentum equations. This
 gives

$$\frac{\partial U_i}{\partial t} = \dots + f_i + \underbrace{\frac{\partial}{\partial x_i} \left\{ \nu_{SGS} \left(\frac{\partial U_i}{\partial x_j} + \frac{\partial U_j}{x_i} \right) \right\}}_{\text{SGS terms}} + a_i, \quad (5.12)$$

where ν_{SGS} is SGS eddy viscosity and the ellipsis represents the other terms carried over from
 Equation (5.2b). Here, the Smagorinsky SGS scheme is shown (section 5.6.5). In principle, this approach
 3240 could be adopted for an LES of forest canopy flows, ideally with the acceleration terms a_i spaced at
 frequencies corresponding to the movement of tree parts, while ensuring zero divergence. Selino and Jones
 (2013) adopt a similar approach for a very different purpose, using synthetic SGS turbulence to improve
 video animations of trees moving in wind.

3245 5.5.5 Resolved trees

The difficulties involved in incorporating realistic structure into the distributed-drag parametrisation,
 discussed above, raise the question of whether it is possible to model the forest elements directly. Poggi
 and co-workers approximate plants as rigid circular cylinders in water-flume experiments, finding the
 wakes in the lee of the vegetation stems perturbed the dominant mixing-layer type eddies at the crown top
 3250 (Poggi et al. 2004a, 2008; Poggi and Katul 2008a). Yue et al. (2007) model corn plants as stems surrounded
 by leaves, applying a distributed-drag parametrisation at the leaf points and, at the stem points, a force
 calculated as drag around a cylinder. Chester et al. (2007) and Chester and Meneveau (2007) use LES to
 investigate the flow around isolated, solid tree-like fractals, finding that model's predictions of the drag
 imposed by the fractals were sensitive to the orientation of the branches. Böhm et al. (2013) modelled trees
 3255 in a wind tunnel as cylindrical trunks below spherical crowns. They conclude similarly to Poggi et al. (2004)
 that the partially coherent wakes of the bluff canopy elements modify the dominant eddies at the crown top,
 and that the flow within the canopy divides into wake and non-wake regions, where the wake regions scale
 with the stem diameter (Ghannam et al. 2020). Yan et al. (2017) performed high-resolution LES studies of

3260 a regular array of bluff elements, specified similarly to the wind-tunnel model of Böhm et al. (2013). In a series of separate simulations, Yan et al. (2017) configure the trees as (a) entirely bluff bodies; (b) solid trunks with the crown represented as distributed drag; and (c) as entirely distributed drag. The spatially averaged flow statistics were similar across the three cases, with slightly higher turbulence in the shear layer using the bluff-body representations. As an interesting alternative, Schrötle and Dörnbrack (2013) use LES to simulate flow around 16 Pythagoras trees⁹, treated as immersed boundary layers with the outer tree branches 3.35 K warmer than their surroundings. They show the thermally driven vortices from the trees, of diameter roughly h_c and turnover time of around 30 s, interfere with the shear-generated coherent structure at the tops of the trees. However, the study was a method prototype, and its results reveal little about real forests.

3270 For the time being, because of the computational expense of simulating turbulent flow, resolving forest structure directly remains out of reach for ecosystem-scale investigations of forest-atmosphere exchange. For example, Yan et al. (2017) use an extremely high resolution model to discretize the trees ($dx = dy = 0.03h_c$), which severely constrains the number of trees that can be simulated. Further, treating the trees as bluff bodies does not account for plant reconfiguration, may overestimate the scales of vortical wakes behind tree crowns, and excludes the possibility of resolving the cooperative waving motion that occurs in real vegetation. There are no theoretical constraints on the number of trees that can be included in wind-tunnel models, although practical considerations to preserve scale relationships may of course impose limits. It is also difficult to include canopy exchange and other ecological processes in physical models. It is challenging to maintain flow with sufficiently high Re values around model forests, for which higher values are needed than in many engineering applications (Gromke 2018). Results from bluff-body models may be useful to derive drag parametrisation schemes for use in larger scale simulations. Böhm et al. (2013) motivate this approach by identifying that wake-scale TKE in bluff-body canopies is around $1/5 L_s$ rather than $1/100$ to $1/10 L_s$ typical of vegetation canopies. This implies momentum is transferred more efficiently to vegetation than to canopies of bluff bodies. Further, information theoretical analysis of flume experiments suggests the von Kármán streets formed in the wake of stems can cause scalar variance to be transferred from small to large scales (Ghannam et al. 2020), i.e. opposing the usual turbulent cascade characterised by constant fluxes of energy and scalar variance from the scales of production down to dissipation.

5.6 Atmospheric physics and chemistry

3290 5.6.1 Modelling in-canopy chemistry

BVOCs are ecologically important in forests (Niinemets 2010; Visakorpi et al. 2018) and influence air quality, meteorology, and the climate through their interactions with oxidants such as O_3 and OH (Lelieveld et al. 2008; Peñuelas and Staudt 2010; Rap et al. 2018). Plants release a wide variety of compounds from

⁹ A type of fractal constructed iteratively from a right-angled triangle with squares erected on each of its sides.

3295 tissues above and below ground. Flowers and fruits release the widest variety of compounds, while leaves
generally have the greatest mass emission rates (Laothawornkitkul et al. 2009). The most important class
of BVOCs for air quality and climate is the terpenoid class of compounds, particularly the five-carbon (C5)
hemi-terpene, isoprene, the C10 monoterpenes such as α - and β -pinene, and the C15 sesquiterpenes such
as β -caryophyllene. Leaf-scale emissions of isoprene depend sensitively on temperature and light (and,
3300 hence, on forest structure). Emissions of terpenoids vary exponentially with leaf temperature (Guenther et
al. 2006). This class of compounds displays a great range of lifetimes with respect to reaction with OH and
O₃, from several tens of minutes for isoprene for reaction with OH (Apel et al. 2002) to 2 minutes for the
reaction of β -caryophyllene with O₃ (Shu and Atkinson 1994). BVOC molecules must be well mixed at the
molecular scales in order to react. Because the source of oxidants (i.e., OH and O₃) for the degradation of
3305 BVOCs is outside the forest, imperfect mixing acts as an apparent brake on reaction rates, a process known
as segregation (Krol et al. 2000; Butler et al. 2008; Pugh et al. 2011). Fluxes of unreacted terpenoids out of
forest patches therefore depend sensitively on air-parcel residence times, which vary with position within
the canopy, as discussed above in section 5.4.4.

3310 Studies investigating BVOC chemistry in forests are usually interested in time and space scales that are too
large for the turbulent flow to be resolved by DNS, LES or RANS, requiring the turbulent exchange to be
parametrised (Ashworth et al. 2015; Forkel et al. 2015; Wang et al. 2017). These parametrisations are
typically based on K-theory, which should be used cautiously in forests and other vegetation canopies
(Finnigan 2000; Monteith and Unsworth 2008). K-theory works well in situations where the sum of the
flux transport and buoyancy terms of the scalar flux budget is small compared to the production term (Bash
3315 et al. 2010; Freire et al. 2017)—e.g. in neutral conditions, where there is a strong vertical gradient in the
scalar concentration, such as investigating isoprene released from leaves. However, the gradient diffusion
assumptions in K-theory often fail in real forests—for example, in stable atmospheric conditions or when
considering scalars with multiple and temporally varying sources and sinks. Model predictions of BVOCs
and their oxidation products are very sensitive to the turbulence parametrisation used (Bryan et al. 2012;
3320 Makar et al. 2017). It is therefore important to make the parametrisations as robust as possible.

Ecosystem-scale LES models can simulate counter-gradient transport and are therefore likely to be
indispensable tools in developing chemistry parametrisations that scale to large space and time resolutions.
Due to the complexity of the task, there have been few attempts to investigate forest chemistry while
3325 resolving turbulence. However, the urban literature is an excellent source of relevant techniques (e.g.,
Bright et al., 2013; Buccolieri et al., 2018; Khan et al., 2020; Kwak et al., 2015; Liao et al., 2014; Zhong et
al., 2016, and references in each). One possible path is to couple chemistry models to LES, a technique
which has recently been used to investigate chemical transformation, transport, and deposition of air
pollutants in realistically shaped urban areas (Khan et al. 2020). However, the computational expense of
3330 the coupled approach heavily restricts the resolution of the domain and the number of chemical species that
can be investigated in each run. Another approach is to model chemistry inside a forest air space using ‘box
models’, which treat the air space as a fixed volume into which species are emitted and are able to react.

Box models require the characteristics of the turbulence to be specified a priori, such as through an exchange velocity between the box and its surroundings. This simplification allows computing resources to be
3335 reallocated to more complex chemistry or particle microphysics than is possible when the turbulence is highly resolved using RANS or LES. Box models are widely used to model street-canyon chemistry (Holmes and Morawska 2006; Murena 2012; Zhong et al. 2016) and have been used for one-dimensional investigations of forest-atmosphere exchange across large homogeneous canopies (Pugh et al. 2011; Ashworth et al. 2015). In patchy landscapes, multiple boxes would be required to account for the fluid
3340 dynamical regions that form around forest edges and clearings. The urban literature offers a precedent for dividing air spaces into dynamical regions. For example, models of street-canyon chemistry have used multiple boxes to represent the ‘compartmentalisation’ of fluid dynamical phenomena such as counter-rotating vortices (Murena 2012; Kwak and Baik 2014; Zhong et al. 2016, 2018; Dai et al. 2021).

5.6.2 Modelling particle deposition

3345 Ecosystem-scale investigations of forest-atmosphere interactions are often motivated by questions concerning trace gas exchange, usually representing the species of interest as passive scalars (see section 5.4). However, the behaviour of many biologically important particles cannot be approximated in this way. For example, many pollens and spores have substantial mass and are subject to inertial forces different to those on a trace gas molecule (see, e.g., Hinds, 1999; Seinfeld and Pandis, 2016). Freshly
3350 nucleated UFPs, resulting from the oxidation of BVOCs (Kulmala et al. 2001, 2007), are produced in high number concentrations around forests and may coagulate (Kulmala et al. 2001; Pierce et al. 2012). These processes introduce physics requiring a different mathematical approach to that for fluid flow or particle growth/evaporation (Jacobson 2005; Spracklen et al. 2006; Seinfeld and Pandis 2016).

3355 Many studies of scalar quantities (Poggi et al. 2006) and particles (Aylor and Flesch 2001) in vegetation adopt a Lagrangian stochastic modelling (LSM) approach, which requires the vertical profiles of turbulence statistics to be specified a priori. However, around patchy forests, determining a priori vertical profiles is extremely difficult because the dynamics are so spatially varied. There have been a handful of attempts to incorporate non-Gaussian turbulence in an LSM framework, with varying success (e.g., Reynolds, 2012).
3360 More recently, several groups have adopted an Eulerian specification of the flow field to model particle deposition. Around patchy forests, Eulerian models offer the advantage of resolving the velocity statistics directly down to the scale of their grids. This does not necessarily affect the predictive ability of the models around vegetation. For example, Gleicher et al. (2014) simulated more accurate concentrations of spores in a homogeneous maize canopy using an Eulerian LES model than using their equivalent LSM. However, an
3365 inherent difficulty using LES is that canopy deposition occurs at spatial scales much finer than the spatial filter and therefore must be parametrised. One method is to include a sink term in the conservation equation,

$$S = E_{\phi} \alpha \phi_l |U|, \quad (5.13)$$

where α is the attenuation coefficient—which accounts for the flow’s response to the forest density (Cionco 1978)— ϕ_l the resolved local particle concentration, and E_{ϕ} the efficiency of particle deposition

3370 (Friedlander 2000; Lin et al. 2012, 2018a). Pan et al. (2014a) use a similar approach, modifying the
deposition model in Aylor and Flesch (2001) to generate a sink term linked to the PAD,

$$S = E_{\phi}(P_x + P_y)a(z)\phi_l|U|. \quad (5.14)$$

This formulation considers the distribution of the forest density directly through the incorporation of the
PAD, as $a(z)$, and the projection coefficients P_x and P_y , which respectively account for the PAD facing the
3375 streamwise and spanwise directions. The ground deposition of particles can be modelled using a surface
flux boundary condition. Lin et al. (2018) and Pan et al. (2014a) use slightly different formulations for the
deposition efficiency E_{ϕ} based, respectively, on a parametrisation of molecular diffusion and on
observations of particle impaction onto cylinders. The deposition efficiency term E_{ϕ} accounts for the
momentum and size of the particles, so that Equations (5.13) and (5.14) are solved separately for each
3380 particle size, with the only difference between the solutions resulting from the approximation of the
deposition efficiency. The same is true for the surface-flux parametrisation representing ground deposition.

The mechanisms of particle deposition, and hence deposition velocities, are highly size-dependent for the
size ranges of particles commonly encountered in forests (Litschike and Kuttler 2008). Lin et al. (2018)
3385 found the deposition velocity decreased sharply with increasing particle size for the range of sizes they
investigated (diameters 10–50 nm). Pan et al. (2014a) investigate size indirectly through the ratio of the
particle settling velocity w_s to the friction velocity u_* , with ‘light’ particles having $w_s/u_* \approx 0.04 \ll 1$, and
‘heavy’ particles $w_s/u_* \approx 0.2$. They show, for large values of w_s/u_* (heavy particles) and sources near the
ground, few particles escape the canopy, reflecting their empirical observation that plant diseases initiated
3390 deep within a canopy move upward to the canopy top before spreading. Unsurprisingly, more particles are
deposited in denser vegetation (Branford et al., 2004), particularly at $z \approx h_c$, and therefore lower
concentrations of particles occur deep in the canopy. The rate of dry deposition generally increases with
increasing turbulence because the thickness of the quasi-laminar boundary layers around plant elements is
reduced, therefore increasing the probability of impaction (Fowler et al. 2009). However, the rate at which
3395 particles are deposited depends on the tree species. Studies of urban trees indicate deposition onto conifers
is more efficient than onto broadleaf trees (Chen et al. 2017; Pace and Grote 2020). Beyond these general
observations, there appears to be no clear dependence of fluxes or deposition of fine particles on broad-
brush measures of the canopy morphology (Katul et al. 2011; Lin et al. 2018a). Deposition patterns appear
to depend strongly on the complex arrangement of plant area in forests and other plant canopies (Fowler et
3400 al. 2009).

A future task, straddling in-canopy chemistry and trace-gas deposition, is to investigate how forest
patchiness and more complicated weather conditions affect the rate of deposition and stomatal uptake of
trace gases. For example, particle impaction can be several times higher in unstable conditions versus stable
3405 ones (Pryor et al. 2008; Fowler et al. 2009; Chiesa et al. 2019). This suggests leaf related removal by forests
is likely much lower at night than measurements taken during the day would suggest; impaction is much
lower in stable, nocturnal conditions and the stomata are mostly closed at night. Local atmospheric stability

gradients, such as from patchy heating from sunlight, may produce apparent fluxes when particles and gases trapped in stable conditions are eventually released in convective plumes (Chiesa et al. 2019). Most models of spore dispersal in forests consider only dry deposition, which is a major simplification in many climates where forests are found, and pay little attention to the resuspension of deposited particles. However, the rates of particle removal by rain and resuspension by depend on species composition and the local meteorological conditions, such as the frequency and intensity of rainfall events (Chen et al. 2017). Airborne fungal-spore concentrations in forests are generally higher in wet conditions (Crandall and Gilbert 2017), which are physiologically favourable to certain fungal species such as *Ganoderma* spp. (Stepalska and Wołek 2009). Air vortex rings, which can carry dry-dispersed spores away from the host plant, form around the impact site when raindrops hit plant surfaces, (Kim et al. 2019). This process, which is not accounted for in current models, is likely significant in the transmission of fungal spores because particles transported by the air vortices can reach beyond the laminar boundary layer around plant surfaces, enabling long-distance transport in the turbulent flow.

5.6.3 Heterogeneous sources and sinks of scalar quantities

Section 5.4 considered investigations where scalar quantities were approximated as having horizontally homogeneous sources and sinks. This approach provides a good conceptual template for certain processes around forests, such as the encroachment of pollutants from surrounding areas, or the release of isoprene, which is overwhelmingly from sunlit leaves in the canopy from a monoculture stand (Sharkey et al. 1996). However, in mature forests, most scalars have multiple sources and sinks, whose distribution varies temporally and spatially. This heterogeneity often requires dense networks of equipment to measure, and is therefore not widely reported, despite the known difficulties in generating spatially representative observations in forests (Massman and Lee 2002; Aubinet 2008; Finnigan 2008). Visible examples of this heterogeneity include the water vapour plumes that form over forests after it has rained, e.g. during periods of high convection but a low lifting condensation level height over tropical forests (Jiménez-Rodríguez et al. 2021). Less obvious examples include the steep temperature gradients that can form within forests on clear days. In direct sunlight, broad leaves may be 20 °C warmer than their surroundings (Schuepp 1993; Monteith and Unsworth 2008; Vogel 2009) and can therefore act as highly localised heat sources.

We are not aware of numerical investigations of how patchy sources and sinks affects scalar transport within forests. LES of unevenly heated generic surfaces suggests thermal heterogeneities drive the local mean flow in certain conditions, such as when the geostrophic wind is weak. In these conditions, the dispersive fluxes of heat account for more than 40% of the total sensible heat flux at $z = 100$ m and up to 10% near the surface (Margairaz et al. 2020). The effect of differential heating is not easy to constrain in models of forests because the locations of sunflecks (brief periods of high photon flux density) change quickly depending on branch movement (Way and Pearcy 2012). The radiative properties of the leaves may even vary between the sun and shade sides of a tree (Vogel 1968). One possible approach is to combine the modelling techniques of thermal transfer in urban areas (e.g., Martilli et al. 2002; Salamanca et al. 2010) and radiation transfer in vegetation (Ma and Liu 2019). For example, the leaves of the forest may be represented using a

probability density function (PDF) of small, flexible, surfaces with high absorptance, and the trunks through a PDF of vertically aligned cylinders of varying thickness and low absorptance. This type of testing is probably best carried out in uniform canopies to begin with, so as to differentiate between patterns in scalar transport resulting from terrain effects and those resulting from spatially heterogeneous sources and sinks.

3450 For uniform sources around forest edges, the patterns of scalar concentrations and fluxes are most complicated in the adjustment region where they are influenced by the strong turbulence, the inflow concentration from the surrounding environment, and the vertical distribution of the sources and sinks. Eventually, however, it may be possible to investigate the effect of heterogeneous source and sinks on scalar transport in patchy landscapes. Section 5.7.1 revisits this point again in the context of customised numerical
3455 models of real study sites.

5.6.4 Calculations of dispersive fluxes

Acknowledging the spatial heterogeneity of real forests raises the question of how to handle the dispersive fluxes of momentum and scalars that result from the double averaging of the momentum and transport equations. The dispersive fluxes are the spatial correlations in the time-averaged statistics; the dispersive
3460 flux of momentum, for example, is given by the term $-\partial(\bar{u}_i \bar{u}_i'')/\partial x_j$ in Equation (5.2b). The dispersive fluxes are usually excluded from analyses of forest-atmosphere exchange (Kaimal and Finnigan 1994; Patton and Finnigan 2012), which is a reasonable assumption in dense, homogeneous canopies in which the dispersive fluxes of momentum are usually small (Poggi et al. 2004a; Poggi and Katul 2008b; Moltchanov et al. 2011). However, in sparse canopies—roughly comparable to the densities found in
3465 savannahs—dispersive fluxes can be $\approx 30\%$ of the conventional momentum flux, even when the canopy is homogeneous (Poggi and Katul 2008b). Further, investigations in model canopies show structural inhomogeneities can generate large dispersive fluxes of momentum (Moltchanov et al. 2011, 2015; Harman et al. 2016). Boudreault et al. (2017) show that spatial variability in forest-canopy structure induces dispersive fluxes that account for 10–70% of the total variances of U and W at the upstream edge of the
3470 forest, across a streamwise distance of $x/h_c = 0-8 \approx 0-x_A$. Here, the dispersive momentum fluxes and skewness are greater than their turbulent counterparts, for example, with the dispersive flux of momentum accounting for over 50% of the total momentum flux. Away from the edges, gaps and other patchiness decrease the efficiency of momentum transfer at the crown top. This suggests gap-induced flow phenomena interfere with the mixing-layer-type coherent structures that form around the tops of the trees. Bailey et al.
3475 (2014) observed a similar result in row-structured versus homogeneous trellis-trained crops. This interference is probably strongest when the structural inhomogeneities are of a size $\approx L_s$, so that the vortices shed around them are of a similar scale to the coherent structures that develop around the crown top. In a more idealised example, Q. Li and Bou-Zeid, (2019) use LES to show that rough, heterogeneous surfaces—comprising cuboids of various dimensions and orientations—affect the dispersive fluxes of momentum and
3480 scalar quantities more than the turbulent components of the fluxes. As in Boudreault et al. (2017), Q. Li and Bou-Zeid (2019) show the dispersive components can comprise most of the total momentum flux.

Wind-tunnel measurements in homogeneous plant canopies found the dispersive scalar fluxes to be small (Legg et al. 1986). However, dispersive fluxes of scalar quantities generated by patchiness or spatially heterogeneous source/sinks have not been studied in real forests. Recent studies in urban areas and generalised porous media suggest the dispersive fluxes of scalar quantities should not be dismissed out of hand. Philips et al. (2013) use LES in an urban canopy to show that the dispersion of a scalar quantity is sensitive to the geometry of the obstacles surrounding the source (they observe a plume’s evolution directly, rather than investigating time-averaged quantities). Q. Li and Bou-Zeid (2019) show the dispersive fluxes of scalar quantities do not always follow the flow of momentum, with obstacle geometry typically affecting dispersive fluxes of momentum more than those of scalars. The authors attribute this difference to the physical mechanisms involved. The air’s velocity decreases before it reaches the upstream face of an obstacle, and therefore pressure affects the momentum transfer away from the surfaces. However, the air must touch an obstacle’s surface to deposit or take up scalars, so scalar transport is much more spatially confined. Another important difference between the treatment of momentum and scalar quantities is that the former is effectively continuous in atmospheric flows (see section 2.2.2). This contrasts with most atmospheric scalar quantities which, aside from the temperature and the mixing ratios of a modest number of unreactive gasses, are spatially and temporally intermittent. LES studies of ABL flow over homogeneous landscapes indicate dispersive fluxes of heat are modulated by two broad flow regimes. The first is where surface heterogeneities, such as unevenly heated ground, drive the dispersive fluxes. The second is where dispersive fluxes are driven by turbulent coherent structures in high-shear conditions (Inagaki et al. 2006; Margairaz et al. 2020). Numerical investigations of patchy forests should include calculations of the dispersive fluxes. Ignoring these fluxes may mean ignoring over half of the total momentum flux, for example, by focusing only on deviations from the time average and neglecting spatial deviations. Real forests channel air into gaps and patches, creating spatially coherent structures whose contributions can be as large as those induced by turbulence.

5.6.5 A note on the resolution and domain size in LES models

Scientists continually face a trade-off between scale and resolution. This choice is particularly relevant to fluid modelling because of the extreme computational expense of simulating turbulence. LES of ecosystem-scale interactions around forests currently use around 10^6 – 10^7 cells (e.g., Ma et al., 2020), although Patton et al. (2016) deployed some 4×10^9 cells in an enormous computational effort. Researchers decide how to deploy those cells most effectively. Two competing demands must be balanced: (i) the LES domains should be large enough to simulate the largest boundary-layer eddies; but (ii) should have a filter width fine enough to resolve the smallest eddies sufficiently (Wood 2000). As to the first requirement, we denote the domain size (L_x, L_y, L_z) , where L_i is the domain length in the i^{th} direction, and z_i the boundary-layer depth. For neutrally stratified conditions, a domain size of at least $(\approx 3z_i, \approx 3z_i, z_i)$ is probably sufficient (Mason and Thomson 1987; Wurps et al. 2020). Larger horizontal domains—e.g. $(8z_i, 8z_i, z_i)$ —are needed to capture the largest eddies in free convection conditions. In stable conditions, smaller domains are required in an absolute sense, because the largest ABL eddies scale with z_i , which may be 100 m or less, compared with $z_i \approx 1$ – 2 km in highly unstable conditions (Basu and Porté-Agel 2006; Wurps et al. 2020). However, using

too small a value of L_z , particularly over obstacles, artificially negates any interaction of the boundary layer and the residual layer aloft (Grylls et al. 2020); $L_z \geq 3z_i$ appears to be a reasonable minimum for stable conditions (Basu and Porté-Agel 2006; Wurps et al. 2020).

3525 Determining an appropriate filter resolution for LES requires careful consideration of the atmospheric
conditions, the forest structure, and the topography. A useful rule-of-thumb for ABL investigations is that
a filter width $\Delta_f < z_i/60$ is sufficient for the first- and second-order flow statistics to be well resolved
(Sullivan and Patton 2011). This equates to $\Delta_f \approx 2.5$ m, 10 m, and 20 m for stable, neutral, and convective
3530 conditions, respectively, over unvegetated ground (Wurps et al. 2020). However, for LES models of forests,
we need to consider the dominant turbulent eddies in the shear layer at the top of the canopy. In neutral
conditions, the length scale for these eddies is $L_s \approx 2\beta^2/C_d a(z)$ (by rearranging Equation (5.8)), giving
 $L_s \approx 7$ m for $\beta = 0.35$, $C_d = 0.2$, and $a(z) \approx 0.18 \text{ m}^2 \text{ m}^{-3}$, typical daytime values for mature forests. To
resolve the eddies' structure, we need the vertical filter width to be significantly smaller than L_s , say $L_s/8$.
A vertical filter width within the canopy of around a metre or less is a good first approximation. The
3535 dominant eddies have a mean streamwise spacing of around $8.1L_s \approx 50$ m (Raupach et al. 1996; Finnigan
2000), requiring a horizontal filter width of around 5 m. Smaller filters may be required in the lee of hills,
around which L_s can take smaller values (Finnigan 2000; Ross 2008). If gaps are to be simulated explicitly
(i.e., openings with $O_d \geq L_s$), then a horizontal filter width of around $O_d/8$ or smaller is required to
adequately resolve the turbulent structures in the gaps. Slightly coarser resolutions than those suggested
3540 may suffice for very unstable conditions, but finer filters may be required in very stable cases, because L_s
decreases with increasing stability. In very stable and very unstable conditions around forests, mixing-layer-
type eddies cease to dominate the turbulence structure. In very unstable conditions, the filter width should
be chosen to scale with the dominant convective plumes, rather than L_s . It is not clear whether the
distributed-drag parametrisation is appropriate to model forest-atmosphere exchange in very stable
3545 conditions, during which the turbulent exchange can be dominated by intermittent bursts rather than
mechanically generated eddies (section 5.2.6) (Mahrt 2014).

Although LES resolution has increased more slowly than the general semiconductor capacity predicted by
Moore's law (Bou-Zeid 2014), computing capacity is expected to increase with time for the foreseeable
3550 future. This raises the question of whether the extra capacity should be applied towards increasing the
resolution or the size of the simulated domain. In many fluid applications, the answer to this question is
'both'. However, the distributed-drag parametrisation assumes the averaging volume—the filter width for
LES—to be much larger than the individual tree and plant elements so that their presence is accounted for
statistically. For mature forests, where the tree trunks can have diameters of a metre or more, decreasing
3555 the horizontal filter widths below a few meters makes little physical sense without a formal re-think of the
averaging operations. In many cases, the increased computational capacity could be used more productively
(i) to increase the simulated ABL height, thereby increasing the total amount of resolved TKE (Grylls et al.
2020), (ii) to increase the size of the simulated domain, (iii) to include a wider range of physical and
chemical processes, or (iv) to account for plant movement. However, there may be instances for which a

3560 very fine filter is required, such as to investigate turbulent transfer in small gaps, in the lee of steep hills, or
in stable conditions.

Outside of these specific applications, the workhorse spatial resolution of $\Delta_x = \Delta_y \approx 5$ m, and $\Delta_z \approx 1$ m,
means a forest volume of up to tens of cubic meters is accounted for by a single grid cell, with the smallest
3565 resolved eddies ≈ 5 m in diameter. This implies a need for robust SGS schemes if LES simulations are to
be useful. Although LES has become popular over the last few decades, the development of SGS schemes
has been slow (Moser et al. 2021). The most widely used SGS parametrisation is the Smagorinsky scheme,
in which closure is achieved using empirical arguments and theory (Smagorinsky 1963). This scheme
assumes the turbulence is isotropic, which is not the case in forests (and in many other ASL applications).
3570 Recently, more suitable schemes have been developed by determining the minimum energy dissipation
needed to balance the turbulence production at SGS scales (Rozema et al. 2015; Gadde et al. 2021), but
these schemes have not yet been widely adopted. Improving SGS schemes for forest applications is an
important line of future research. Eddies larger than the plant elements lose TKE to heat and fine-scale
TKE, which short cuts the usual eddy cascade that is assumed by Kolmogorov's $-5/3$ law (Finnigan 2000).
3575 Shaw and Patton (2003) show this effect can be accounted for in LES using a TKE cascade term, without
the need for extra modifications to account for wake-scale kinetic energy transfer. However, the effect of
this short cut to fine scales has not been tested in patchy vegetation canopies, with moving plants, or with
a view to determining its impact on scalar exchange across the boundary layers of leaves.

5.7 Future challenges

3580 It is an exciting time to investigate forest-atmosphere exchange. There is a growing body of high-quality
observations from micrometeorological campaigns (e.g., Butterworth et al., 2021; Patton et al., 2011), long-
term ecosystem monitoring sites (e.g., Hicks and Baldocchi, 2020; Oliphant, 2012), and ecosystem-scale
FACE experiments (e.g., Drake et al., 2016; Hart et al., 2020; Norby et al., 2006). These observations allow
researchers to investigate an increasingly diverse range of physical and biological phenomena in an
3585 increasingly diverse range of ecosystems. Numerical models, if deployed correctly, offer a fourth pillar in
ecosystem-scale investigations, alongside measurements, theory, and physical models. However, fulfilling
the potential of observational networks and new modelling techniques requires a concerted effort across
scientific disciplines. Moving beyond idealised cases and moderate atmospheric conditions is not easy.
Firstly, the idealisations and simplifications are usually for good reason, for example, to reduce the
3590 dimensionality of investigations, or to attempt to reveal canonical processes rather than the idiosyncrasies
of individual sites. Second, because many of the experimental and modelling techniques were developed
from studies of idealised forests in moderate conditions, attempting to interpret results outside of these
scenarios is not always straightforward because the techniques are not at their best (Wilson et al. 2002;
Baldocchi 2008; Belcher et al. 2012; Stoy et al. 2013; Brunet 2020). Third, research into ecosystem-scale
3595 forest-atmosphere interactions is motivated by scientific questions across disciplines including forest
ecology, fluid mechanics, plant physiology, meteorology and climatology, air and water quality, as well as

policy and commercial need. The literature is therefore vast and widely dispersed. In a sense this dispersion is exciting because it suggests that progress may lie at the intersections of these scientific disciplines. However, it is also a barrier to progress because results familiar to one scientific community may be unknown in another, even when they relate to important coupled phenomena. We conclude by framing progress and outstanding challenges under three overlapping headings.

5.7.1 Customised numerical models of real sites

Advances in non-destructive scanning techniques, computing power, and theory are poised to allow researchers to investigate forest-atmosphere exchange at real sites, using models capable of resolving turbulence. These models could be calibrated to study a variety of ecosystem-scale processes, including the wind dispersal of spores, turbulent fluxes of important scalar quantities, or the forest's microclimate. Regarding the structural element of this challenge, TLS allows researchers to include detailed, site-specific morphological detail in their models (Raumonen et al. 2015; Boudreault et al. 2015; Wang et al. 2020), and virtual canopy generators can be used to generate realistic forest canopies from a small number of structural variables (Bohrer et al. 2007). Researchers should include a careful description of the forest morphology in their numerical models, particularly when assessing simulated results against observations, or in forests with a high proportion of edge region. Ecosystem-scale exchange models should account for the streamlining of plants in high wind conditions. This can be accounted for efficiently in LES simulations by incorporating the Vogel number B into the parametrisation of the aerodynamic drag f_i . Plant movement at an ecosystem scale can be incorporated through poroelastic and mechanical parametrisations (Dupont et al. 2010; Pivato et al. 2014) or by the inclusion of a stochastic forcing into the momentum equations at a frequency corresponding to plant movement.

However, two important knowledge gaps need to be narrowed before these customised models can be used to investigate the exchange of scalar quantities at real sites. The first is that there are few public datasets against which nascent models can be tested. The ability of turbulence-resolving models to simulate scalar transport in real landscapes therefore remains essentially unknown. The CHATS observations are the apogee of surface measurements in a tree dominated landscape (Patton et al. 2011; Dupont and Patton 2012) and a valuable resource for model developers (Ma and Liu 2019). However, the CHATS measurements were made in a homogeneous orchard on level ground and are therefore unsuitable for testing models' ability to handle patchiness, species diversity, and undulating topography. More measurements are needed, especially of scalar quantities such as CO₂, water vapour, pollutants, and spores in patchy forests. For practical reasons, these measurements may not be on the scale of CHATS. However, existing eddy-covariance and FACE facilities have generated extensive timeseries that may be exploited, especially if combined with experiments of opportunity and targeted observational campaigns around edges, gaps, and hills. For example, further experimental testing will determine the extent to which scalar fluxes reach an approximate equilibrium in patchy landscapes, and whether the chimney effect in the lee of hills is observed in nature as well as in numerical models.

3635 The second gap concerns the soil–forest–atmosphere coupling of scalar quantities. Researchers are
beginning to incorporate multi-layer canopy exchange schemes in ecosystem-scale LES models (Patton et
al. 2016; Ma and Liu 2019) and in models designed for slightly larger space and time scales (Xu et al. 2017;
Yan et al. 2020; Bonan et al. 2021). These schemes include parametrisations of phenomena such as
3640 evapotranspiration, soil fluxes, and the photosynthetic uptake of CO₂ that are designed to hold
approximately across different ecosystems. A potentially fruitful area of research would be to modify these
schemes to reflect observations at individual sites, for example, by adjusting the underlying
parametrisations, or through some combination of Bayesian data assimilation and machine learning. A point
of caution is that observations in forests tend to be sparse in space (e.g., wind measurements) and sometimes
3645 time (e.g., spore releases), and are often measured using proxies or with indirect techniques (e.g.,
photosynthetic capacity) (Gardner et al. 2021). Machine-learning techniques should therefore be carefully
adapted to account for uncertainty in our knowledge of the underlying physical processes (Geer 2021).

5.7.2 Connection to larger scales

Developments in theory and computing capacity allow researchers to begin incorporating ecosystem-scale
phenomena into numerical weather prediction and earth system models (Shao et al. 2013; Bonan et al. 2018,
3650 2021; Arthur et al. 2019; Yan et al. 2020). To be computationally feasible, these schemes rely on simplified
versions of the forest canopy (Yan et al. 2020), a priori turbulence parameters (Chen et al. 2016), or
modifications of MOST with mixing-layer length scales (Bonan et al. 2018). These approximations perform
best when the atmosphere is neutral and the surface homogeneous. Further work is needed to determine
3655 whether the length scales and approximations can be modified to account for patchy landscapes and a larger
range of atmospheric conditions. Robust parametrisations for scalar quantities are especially difficult to
find. Missing theoretical links may become apparent through further testing of customised LES models
against high-quality field measurements, as outlined above. Another relatively unexplored approach is to
reject the assumption that the scalar statistics should always relate to those of the velocity field. For
3660 example, understanding the movement of water vapour around at fragmented forest at dusk is a problem
that may not yield to a deterministic, drag-based treatment or approximate vertical turbulence profiles. The
geometries of velocity and scalar timeseries are often much less scale-dependent than their accompanying
physics (Belušić and Mahrt 2012; Kang 2015; Chen et al. 2019b). Turbulent events in these timeseries can
also be clustered by their statistical properties, with no assumption of the underlying physical structures
(Kang et al. 2015; Sun et al. 2015). The timeseries of well-chosen turbulence measurements may reveal
3665 scale-independent behaviours to parametrise forest-atmosphere exchange in terrain and conditions that are
beyond the reach of current approaches. Spectral analysis of long-term eddy-covariance measurements over
mixed hardwood forests showed smaller eddies are relatively more efficient in transporting sensible heat
than momentum, while larger eddies are relatively more important in transporting momentum (Su et al.
2004). It would be fascinating if this type of analysis were conducted over even longer measurement
3670 periods, with a larger diversity of ecosystems.

5.7.3 Challenging weather and atmospheric conditions

Numerical models permit low dimensionality experiments that are difficult to perform in the open atmosphere. A common simplification is that of an isolated forest in neutral atmospheric conditions. This removes all aspects of the atmosphere, other than a velocity field that is recycled using periodic boundary conditions. In nature, however, forests are subject to all sorts of weather, climatic, atmospheric conditions. Atmospheric stability can change quickly in time, such as around dusk, and in space, such as when the forest air space decouples from the surrounding ABL. Simulations of the entire ABL will help explore these effects further (Patton et al. 2016; Ma and Liu 2019; Yan et al. 2020). Local effects around gaps and areas of uneven heating should not be discounted and, with time, may be possible to resolve in site-specific models. However, further research is needed into the effect of submeso motions on forest-atmosphere exchange. These motions are difficult to model because they often manifest as intermittent turbulent bursts, but do not result from mixing-layer-type eddies, and therefore must be generated using mesoscale coupling or synthetic turbulence. Submeso motions are common in the atmospheric conditions that tend to be most problematic for eddy-covariance measurements, such as during stable nights, and discounting their effect from models introduces an unwelcome bias. Rainfall is a significant source of momentum into forests, affecting myriad ecological processes as well as the plants' mechanical response to the flow. Raindrop-induced vortices can carry small particles away from plant surfaces and into the turbulent flow. Wet conditions provide a major unexplored area for numerical investigations of forest-atmosphere exchange, especially given that much of the world's forested area is situated in climates where precipitation is common.

Appendix 5A: Numerical details of LES model

5A.1 Drag parametrisation and simulated cases

We simulate flow across small forests, with the presence of the aerial parts of the forests represented using the drag parametrisation in Equation (5.7), $f_i = -C_d a(z) |\tilde{U}| \langle \tilde{u}_i \rangle$ (the overtilde denotes the resolved variables, as in section 5.2). We specified a height-averaged equational drag coefficient $\bar{C}_d = 0.2$, a value commonly used in previous studies (Table 5B.1). Figure 5.11 shows the mean vertical profile of the LAD, $a(z)$, which was derived from terrestrial lidar surveys of the BIFoR FACE facility (Hart et al. 2020), using the method in Raunonen et al. (2015), giving $PAI \approx 5$. Contrast this to the urban parametrisation in Chapter 4, which assumed the density of the porous medium to be constant with height (section 4.3.2 and Appendix 4A).

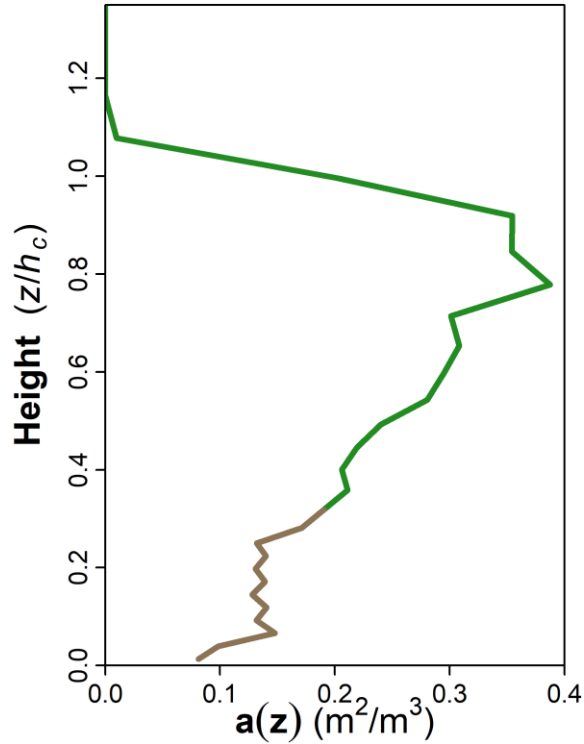


Figure 5A.1: Vertical profile of PAD $a(z)$ ($\text{PAI} \approx 5$) used in the LES model. Colouring indicates that the trunks account for much of the PAD in the lower part of the canopy, and the leaves account for much of the PAD in the upper part of the canopy. The colouring is illustrative only and does not reflect the detailed composition of the BIFoR FACE facility.

3705

We specified two cases:

- **Case 1** – We apply the distributed-drag parametrisation over a patch extending 500 m in the streamwise direction, and across the entire domain in the spanwise direction, to simulate flow across a small, isolated forest.
- **Case 2** – As for Case 1 but, for each forested cell, $\bar{C}_d a(z)$ taking a random number (uniformly distributed) within the range $\bar{C}_d a(z)$ (Case 1) $\pm 2\%$. This introduces a small spatial stochastic forcing into the momentum equations solved by the LES model via the drag term in Equation (5.7).

3715

5A.2 Transport equations

We solved the transport equations using the LES mode of WRF version 3.6.1 (Skamarock et al. 2008). The WRF model solves discretized forms of the spatially averaged momentum equations using the Runge–Kutta time-integration scheme (Wicker and Skamarock 2002),

3720

$$\frac{\partial \tilde{u}_i}{\partial x_i} = 0, \quad (5A.1a)$$

$$\frac{\partial \tilde{u}_i}{\partial t} + \frac{\partial \tilde{u}_i \tilde{u}_j}{\partial x_j} = -\frac{1}{\rho} \frac{\partial \tilde{p}}{\partial x_i} + \frac{\partial \tau_{ij}}{\partial x_j} + B_i + f_c \epsilon_{ij3} (\tilde{u}_j - U_{g,j}) + f_i, \quad (5A.1b)$$

where ρ is the air density; \tilde{p} is the resolved pressure; τ_{ij} is the kinematic mean stress tensor, which represents the SGS stresses; B_i is the buoyancy force: $B_i = -\delta_{i3} g \theta' / \bar{\theta}$, where $\bar{\theta}$ is the potential temperature for hydrostatic balance, and θ' is the temperature variations with respect to $\bar{\theta}$; f_c is the Coriolis parameter; ϵ_{ij3} is the alternating unit tensor; and $U_{g,j}$ is the geostrophic velocity. Equation (5A.1b) is closed by parametrising the SGS stress tensor τ_{ij} as

$$\tau_{ij} = -2\nu_{SGS} S_{ij}, \quad (5A.2)$$

$$S_{ij} = \frac{1}{2} \left(\frac{\partial \tilde{u}_i}{\partial x_j} + \frac{\partial \tilde{u}_j}{\partial x_i} \right), \quad (5A.3)$$

$$\nu_{SGS} = c_k \sqrt{e_{SGS}} (\Delta x \Delta y \Delta z)^{\frac{1}{3}}, \quad (5A.4)$$

where e_{SGS} is the SGS TKE and $c_k = 0.10$ is a modelling constant. The prognostic equation for the evolution of the term e_{SGS} is,

$$\frac{\partial e_{SGS}}{\partial t} + \frac{\partial \tilde{u}_j e_{SGS}}{\partial x_j} = \nu_{SGS} \frac{\partial}{\partial x_j} \left(\frac{\partial e_{SGS}}{\partial x_j} \right) + P_r + F - \frac{C_\epsilon e_{SGS}}{(\Delta x \Delta y \Delta z)^{\frac{1}{3}}}, \quad (5A.5)$$

where P_r represents the shear- and buoyancy-production terms (Skamarock et al. 2008), C_ϵ is the dissipation coefficient (Moeng et al. 2007). The term F is a cascade term, which accounts for additional dissipation of kinetic energy from air–forest interactions at scales smaller than the spatial filter (Shaw and Schumann 1992; Shaw and Patton 2003), with

$$F = -2\bar{C}_d a(z) |\tilde{U}| e_{SGS}. \quad (5A.6)$$

5A.3 Drag parametrisation and simulated cases

The simulated domain is $1435 \times 1435 \times 1000$ m in the streamwise, spanwise, and vertical directions, respectively, comprising $287 \times 287 \times 79$ grid cells. The horizontal grid resolution is 5 m in each direction, and the vertical resolution is increased from around 0.67 m in the lower half of the forest to around 60 m at the top of the simulated domain. The mean height of the forest $h_c = 25$ m. The upstream edge of the forest is situated approximately 600 m from the inflow edge of the domain. We simulate flow under neutral conditions, with the initial profile of potential temperature θ specified as a constant at 283.15 K at the bottom of the domain (up to $z \approx 475$ m) followed by a linear increase to 291.7 K at the top of the domain. We include a dampening layer of $z \approx 300$ m at the top of the domain to minimise wave reflection (Nottrott et al. 2014). The geostrophic velocity components above the boundary layer top are set to $U_g = -6$ m s⁻¹ and $V_g = -9.3$ m s⁻¹, and this specification yields a mean wind speed of 1.6 m s⁻¹ from a flow direction of 343° (approximately a northerly wind) at the crown top ($z = h_c$). We use the meteorological convention where the x -direction is aligned west–east and the y -direction south–north.

Spin-up was 5 h, with cyclic boundary conditions for all dynamical variables in both horizontal directions. After the spin-up, we ran the simulations for a further 120 min, taking samples at intervals of 3 s. We time-averaged over the latter 100 min (denoted by T) of these samples (*i.e.*, $t_0 = 20$ min to $t_0 + T = 120$ min).

3755 This process generates a three-dimensional timeseries of 2000 resolved samples in the form $\tilde{\phi}(x, y, z, t)$. We derived the resolved turbulent statistics using (a) time averages over the sampling period; and (b) spatial averages along the y -direction ($L_y = 1435$ m), over which the turbulent statistics are homogeneous. For each resolved variable, $\tilde{\phi}$, the averaging process generates a two-dimensional function,

$$\bar{\Phi}(x, z) = \frac{1}{TL_y} \int_0^{L_y} \int_{t_0}^{t_0+T} \tilde{\phi}(x, y, z, t) dt dy, \quad (5A.7)$$

3760 from which we calculate the statistics presented in Figure 5.10. The resolved fluctuating component of $\tilde{\phi}$ around $\bar{\Phi}$ is defined as $\phi'(x, y, z, t) = \tilde{\phi}(x, y, z, t) - \bar{\Phi}(x, z)$, with the skewness $Sk_{u_i} = \overline{u_i'^3} / \sigma_{u_i}^3$ and kurtosis $t_{u_i} = \overline{u_i'^4} / \sigma_{u_i}^4$.

3764 **Appendix 5B: Summary of modelling investigations of flow around forests**

3765 **Table 5B.1: Chronological summary of highly cited modelling investigations of flow around forests at the ecosystem scale. PAD and PAI, respectively,**
 3766 **refer to the plant area density/index, $a(z)$ is a height-dependent function of the PAD, and C_d is the drag coefficient**

3767

Study	Equations/ model	Distribution of PAD as $a(z)$	C_d	PAI range (m^2/m^2)	Additional Features
Shaw and Schumann (1992)	LES	Artificially generated vertical profile for a deciduous forest.	0.15	2, 5	
Dwyer et al. (1997)	LES	Artificially generated vertical profile for a deciduous forest	0.15	2, 5	Numerical setup based on Shaw and Schumann (1992)
Su et al. (1998)	LES	Artificially generated vertical profile for a deciduous forest	0.15	2	Numerical setup based on Shaw and Schumann (1992)
Shaw and Patton (2003)	LES	Artificially generated vertical profile for a deciduous forest	0.15	2	
Watanabe (2004)	LES	Uniform vertical distribution	0.2	2	
Finnigan and Belcher (2004)	Mixing-length closure	Uniform vertical distribution	0.25	≈ 4	Drag parameters are approximations. Analysis is mostly expressed in dimensionless terms
Katul et al. (2006)	Mixing-length closure	Uniform vertical distribution	0.2	3	Investigated carbon dioxide exchange over forested hills
Yang et al. (2006b, a)	LES	Artificially generated vertical profile for a deciduous forest	0.15	2	Numerical setup based on Shaw and Schumann (1992)
Dupont and Brunet (2008a)	LES	Four cases: (1) approximately vertically uniform; (2) sparse trunk space and dense crown; (3) very dense crown and very sparse trunk space; and (4) undergrowth in trunk space	≈ 0.5	2	PAI chosen so that the product $c_d a(z)$ was the same as in Raupach et al. (1987), where $PAI \approx 5$
Dupont and Brunet (2008b)	LES	Uniform vertical distribution	0.2	2	Structure of the upstream edge of the forest was varied across seven shapes and densities
Dupont and Brunet (2008c)	LES	Three cases: (1) approximately vertically uniform; (2) sparse trunk space and dense crown; (3) undergrowth in trunk space	0.2	1–5	
Cassiani et al. (2008)	LES	Artificially generated vertical profile for a deciduous forest	0.2	2–8	Forest structure approximately based on that of Duke Forest (Katul and Albertson 1998)

Sogachev et al. (2008)	RANS	Foliage distribution based on beta probability density function	0.2	0.5–3	Investigated scalar transport around a forest edge
Ross (2008)	LES	Uniform vertical distribution	0.15	5	Simulated flow over forested ridges
Bohrer et al. (2009)	LES	Randomly generated heterogeneous canopy	0.15	1.4–3	1,000 virtual canopies generated for each simulation, with randomised gaps of approximately crown width
Dupont and Brunet (2009)	LES	Artificially generated vertical profile for a deciduous forest	0.2	2, 5	Canopy structure approximately based on deciduous forest reported in Neumann et al. (1989)
Dupont et al. (2011)	LES	Dense canopy with sparse trunk space to approximate pine plantation	0.26	2	Includes five additional cases with the vertical profile gradually relaxed towards a uniform distribution
Edburg et al. (2012)	LES	Artificially generated vertical profile for a deciduous forest	0.5	1	
Schlegel et al. (2012)	LES	Forest dominated by <i>Picea abies</i> . PAD varied across simulated domain	0.15	≈ 7.1	PAD distribution derived from terrestrial Lidar
Mueller et al. (2014)	LES	Simplified vertical profiles estimates from observations in a pine plantation and a deciduous forest	0.26	2	Setup taken from Sylvain Dupont et al. (2011) and Hong Bing Su et al. (1998)
Boudreault et al. (2015)	RANS	Forest dominated by <i>Picea abies</i> . Frontal area density varied across simulated domain	0.2	≈ 2.9	Vertical profile derived from aerial lidar scans of the forested area
Xu et al. (2015)	RANS	Vertical profile from measurements in a forest dominated by spruce and pine	≈ 0.3	3.3	Two-dimensional investigation of stably stratified flow around an idealised forested hill
Kanani-Sühring and Raasch (2015)	LES	Artificially generated vertical profile for a deciduous forest	0.2	1–8	Used LES to investigate scalar transport around a forest edge
Schlegel et al. (2015)	LES	Forest dominated by <i>Picea abies</i> . PAD varied across simulated domain	0.15	≈ 7.1	PAD distribution derived from terrestrial lidar. Developed preliminary work in Schlegel et al. (2012)
Ross and Harman (2015)	LES	Uniform vertical distribution	0.25	4	Simulated flow and scalar transport over forested hills
Kanani-Sühring and Raasch (2017)	LES	Artificially generated vertical profile for a deciduous forest	0.2	1–8	Investigated scalar transport in the lee of the forest, with multiple sources and sinks
Yan et al. (2017)	LES	Simplified deciduous trees. Three cases: (1) bluff objects; (2) bluff trunks and porous crowns; (3) fully porous trees	≈ 0.2	≈ 5	Numerical details couched in terms of bluff objects (e.g. frontal area index) to be compared more easily to wind-tunnel observations in Böhm et al. (2013)
Boudreault et al. (2017)	LES	Two cases: (1) heterogeneous PAD derived from terrestrial lidar; and (2) spatially homogeneous $a(z)$ from averaged data	0.2	6	Heterogeneous case included tapered upstream edge
Chen et al. (2019)	LES	Horizontally homogeneous. Profile derived from leaf area measurements in the Amazon rainforest	0.2	7	Simulated flow and scalar transport over forested hills. PAD profiles generated from observations reported in Tóta et al. (2012) and Fuentes et al. (2016)

Ma and Liu (2019)	LES	Uniform vertical distribution	0.2	2.5	LES coupled with multiple-layer canopy exchange model
Watanabe et al. (2020)	LES (Lattice Boltzmann method)	Uniform vertical distribution	0.2	2	The equations of motion are resolved using the lattice Boltzmann method rather than solving the incompressible Navier–Stokes equations
Ma et al. (2020)	LES	Three cases: (1) vertically uniform (2) sparse trunk space and dense crown; (3) very sparse trunk space and dense crown	0.25	4	LES coupled with a multiple-layer canopy exchange model used to investigate transport of different scalars across a forest edge
Yan et al. (2020)	LES	Profile generated using empirical relationship in Lalic and Mihailovic (2004)	0.15	4.3	LES coupled to the mesoscale Weather Research and Forecasting model. Grid resolution at the mesoscale
B. Chen et al. (2020)	LES	Horizontally homogeneous. Profile derived from measurements in the Amazon (as for Chen et al. (2019))	0.2	7	Simulated flow and scalar transport over forested hills, including realistic terrain

3768

Appendix 5C: Image acknowledgements

3770 Figure 5.2b seabirdnz on Flickr. “Slope Point”. 18 February 2008. Online image with Creative Common License CC-BY-2.0. <https://www.flickr.com/photos/seabirdnz/5460426633>.

Figure 5.5c -JvL- on Flickr. “Brownsberg jungle path”. 22 October 2016. Online image with Creative Common License CC-BY-2.0. <https://www.flickr.com/photos/-jvl-/33153976490/>.

3775

Figure 5.5d R.V. on Flickr. “Forest, British Columbia, Canada”. 6 July 2013. Online image with Creative Common License CC-BY-2.0. <https://www.flickr.com/photos/bluegruen/9601965057>.

3780 Figure 5.8c Soil-Science.info on Flickr. “*Pinus taeda* plantation”. 21 May 2008. Online image with Creative Common License CC-BY-2.0. <https://www.flickr.com/photos/22503286@N06/2512091836>.

Figure 5.9 and caption reproduced without modification from Calders et al. (2020) under Creative Commons License CC-BY-4.0

3785 **Chapter 6 – Air-parcel Residence Times in a Mature Forest: Observational Evidence From a Free-Air CO₂ Enrichment Experiment**

Submission details. This chapter is a reproduction of the article ‘Air-parcel Residence Times in a Mature Forest: Observational Evidence From a Free-Air CO₂ Enrichment Experiment’ by Edward Bannister, Mike
3790 Jesson (MJ), Nicholas J. Harper (NJH), Kris M. Hart (KMH), Giulio Curioni (GC), Xiaoming Cai (XMC), and A. Rob MacKenzie (AMRK), which was submitted on 29 April 2022 to *Atmospheric Chemistry and Physics* for peer review.

Author contributions. I conceived of this study, wrote the processing code, conducted the formal analysis and
3795 visualisation, and wrote the original draft, under the supervision of ARMK, MJ, and XMC. KMH, MJH, GC are responsible for the operation of the BIFoR FACE facility and the curation of the data arising from it. All authors contributed to reviewing and editing the manuscript. The phenocam data used for Figure 6.2 was processed by Tom Downes at BIFoR FACE.

3800 **Abstract.** In forests, air-parcel residence times—the inverse of first-order exchange rates—influence in-canopy chemistry and the exchanges of momentum, energy, and mass with the surrounding atmosphere. Accurate estimates are needed for chemical investigations of reactive trace species, such as volatile organic compounds, some of whose chemical lifetimes are in the order of average residence times. However, very few observational residence-time estimates have been reported. Little is known about even the basic statistics of real-world
3805 residence times or how they are influenced by meteorological variables such as turbulence or atmospheric stability. Here, we report opportunistic investigations of air-parcel residence times in a free-air carbon dioxide enrichment (FACE) facility in a mature, broadleaf deciduous forest with canopy height $h_c \approx 25$ m. Using nearly 50 million FACE observations, we find that median daytime residence times in the tree crowns range from around 70 s when the trees are in leaf to just over 34 s when they are not. Air-parcel residence times increase
3810 with greater atmospheric stability, as does their variability. Residence times scale approximately with the reciprocal of the friction velocity, u_* . During some calm evenings in the growing season, we observe distinctly different behaviour: pooled air being sporadically and unpredictably vented—evidenced by sustained increases in CO₂ concentration—when intermittent turbulence penetrates the canopy. In these conditions, the concept of a residence time is less clearly defined. Parameterisations available in the literature underestimate turbulent exchange in the upper half of forest crowns and overestimate the frequency of long residence times. Robust
3815 parameterisations of air-parcel residence times (or, equivalently, fractions of emissions escaping the canopy) may be generated from inverse gamma distributions, with the parameters $1.4 \leq \alpha_s \leq 1.8$ and $\beta_s = h_c/u_*$ estimated from widely measured flow variables. In this case, the mean value for τ becomes formally defined as $\bar{\tau} = \beta_s/(\alpha_s - 1)$. For species released in the canopy during the daytime, chemical transformations are unlikely
3820 unless the reaction timescale is in the order of a few minutes or less.

6.1 Introduction

3825 Forests cover nearly a third of the Earth's land surface and exchange momentum, energy, and mass with the atmosphere. Forest-atmosphere exchanges are fundamental to forest ecology, involving transfers of water vapour, carbon dioxide (CO₂), trace gases including biogenic volatile organic compounds (BVOCs), and particles such as pollen and spores. Forest-atmosphere exchanges also influence air quality, meteorology, and the climate, for example, through BVOCs interacting with oxidants such as O₃ and OH (Fuentes et al. 2000; Peñuelas and Staudt 2010; MacKenzie et al. 2011; Pyle et al. 2011; Rap et al. 2018).

3830 Turbulent motions transport the air from the boundary layers around the forest elements into the canopy airspace and out into the surrounding atmosphere. The properties of these turbulent motions depend on factors such as a forest's structure and the atmospheric conditions (Finnigan 2000; Brunet 2020; Bannister et al. 2022). The turbulent exchange determines the extent to which a forest is ventilated, i.e., how quickly the air within the forest is replaced by air from the surroundings. The rate at which a forest is ventilated is especially pertinent when considering reactive compounds, such as many BVOCs, whose chemical lifetimes can be in the order of
3835 a few minutes (Kesselmeier and Staudt 1999). In this context, it is helpful to consider a 'residence time', which refers to a representative amount of time air parcels spend within the forest air space. During this time, the air parcels can exchange mass with the forest and one another, and the gases within them may participate in chemical reactions. Accurate estimates of air-parcel residence times in forests are needed to scale leaf-level chemistry and meteorology to the regional and global scales relevant to commerce and policy (Guenther et al.
3840 2012; Forkel et al. 2015). Residence times and other time-scale estimates are commonly used in urban studies, for example, to quantify how well a city is ventilated, or the time over which pedestrians are exposed to pollutants (e.g., Cai, 2012; Lau et al., 2020; Lin et al., 2014; Lo and Ngan, 2017).

3845 There is no single definition of an air-parcel residence time in forests, although a Lagrangian approach probably offers the simplest conceptual picture. For example, one can imagine an air parcel passing over a source of a BVOC, such as a sunlit leaf, then passing through the forest air space, and eventually leaving the forest. Tracking the trajectories of lots of air parcels in this way allows one to derive a statistical residence time. The first attempts to investigate the statistics of air parcels in forests adopted a Lagrangian stochastic modelling (LSM) approach to exploit this basic idea (Strong et al. 2004; Fuentes et al. 2007). These LSM studies suggest that air-parcel
3850 residence times depend strongly on the parcel's release height. The mean residence times range from a few seconds, for parcels travelling from the forest crown, to several minutes for parcels travelling from near the forest floor (Strong et al. 2004; Fuentes et al. 2007). Long residence times—ten minutes or more—have been calculated to occur almost exclusively for parcels travelling from the lower third of the canopy.

3855 The numerical simulations of Gerken et al. (2017) (hereafter GCF17) offer the most complete published statistical account of air-parcel residence times in forests. GCF17 propose an elegant model for the distribution of residence times by adapting the inverse-Gaussian distribution and representing turbulent transport using eddy-diffusivity closure. The residence times, τ , have a probability density function (PDF) given by the distribution of first passage through a plane at $z = h_c$, where h_c is the mean height of the forest. For a given
3860 release height, z_{rel} , the PDF is

$$p(\tau; z_{rel}) = \frac{|h_c - z_{rel}|}{\sqrt{4\pi K_{eq}}} \tau^{-\frac{3}{2}} \exp\left[-\frac{(h_c - z_{rel})^2}{4K_{eq}\tau}\right], \quad (6.1)$$

where K_{eq} is a constant eddy diffusivity at each z_{rel} (but may differ for different z_{rel}). GCF17 use Equation (6.1) to define turbulent transport timescale

$$\tau_{turb}(z_{rel}) = \frac{(h_c - z_{rel})^2}{4K_{eq}(z_{rel})}. \quad (6.2)$$

Equation (6.1) predicts an exponential increase in probability with increasing τ , followed by a heavy-tailed $\tau^{-3/2}$ power-law decrease beyond the mode (i.e., as τ becomes large relative to τ_{turb} , the exponential term approaches unity). In forests and other plant canopies, eddy-diffusivity closure is imperfect and may be unsuitable for certain applications (Finnigan 2000; Monteith and Unsworth 2008; Bannister et al. 2022). However, it remains widely adopted in larger scale models because it allows in-canopy turbulent transfer to be estimated from a modest number of variables, without the prohibitive computational expense of more sophisticated closure schemes. GCF17 acknowledge the limitations of eddy-diffusivity closure and find support for Equation (6.1) in that it agreed quite well with results obtained using large-eddy simulations (LES) of idealised forest canopies, particularly for parcels travelling from low down in the canopy (LES does not rely on the same closure assumptions as Equation (6.1)).

GCF17 find that the median values of τ range from a few seconds in the upper crowns to around 30 minutes near the forest floor, with the spread in τ values decreasing rapidly with height. GCF17 also showed that the density and morphology of vegetation influences air-parcel residence times. The values of τ values increase with the leaf area index (LAI)—the ratio of total projected leaf area per unit ground area—other than for parcels released high in the canopy. Bailey et al. (2014) obtained similar results in LES investigations of exchange around short, trellis-trained crops. Bailey et al. (2014) also found residence times were longer in homogeneous canopies than heterogeneous ones. In an LES investigation of flow over forested hills, residence times of Lagrangian air parcels emitted in the lower part of the canopy were shorter than those moving over flat terrain (Chen et al. 2019a).

Researchers have also used Eulerian frameworks to investigate residence times in forests. Edburg et al. (2012) use LES to calculate mean residence times of 8.6, 3.6, and 5.6 min for ground, canopy, and mixed sources of passive scalars released in a homogeneous forest, within the range of reported values using LSMs. Wolfe et al. (2011) use a simple canopy resistance model to estimate air-parcel residence times of around 2 min for a ponderosa pine plantation.

Because of the challenges in calculating air-parcel residence times from point observations, field estimates are rarely reported, meaning there is little data against which modelling estimates can be tested. A handful of studies have used ^{222}Rn , a radioactive gas produced along the α -decay chains of uranium, as an inert tracer. Because ^{222}Rn is inert and originates in the soil, provided the ground flux is known, its concentration in the forest airspace can be used to infer a canopy ventilation rate (Trumbore et al. 1990; Martens et al. 2004; Simon et al. 2005). Trumbore et al. (1990) used ^{222}Rn measurements to calculate mean canopy residence times of $\tau \leq 1$ h and

$\tau \leq 3.4\text{--}5.5$ h for day- and night-time conditions, respectively, in a mature Amazon Rainforest site ($h_c \approx 30$ m).
3900 Subsequent measurements at other Amazonian locations have reported mean residence times ranging from
around a minute during the day to several hours at night (Martens et al. 2004; Rummel 2005; Simon et al. 2005).
Measurements in a young ponderosa pine plantation ($h_c = 5.7$ m) in California, USA found daytime summer
residence times ranging from 70–420 s (Farmer and Cohen 2008). It is possible to estimate residence times
3905 through indirect methods, such as calculating the mean time between scalar ramps in the ejection–sweep cycle
that dominates turbulent exchange between forests and the atmosphere (Paw U et al. 1995; Katul et al. 1996;
Rummel et al. 2002). These methods have been used to estimate air-parcel residence times of a minute or two
during the day to around an hour at night (Rummel et al. 2002). However, there are no field reports of air-parcel
residence time statistics beyond their mean values, which provide limited information in, for example,
calculating the probability of a BVOC reacting during its passage out of a forest. Further, little is known about
3910 the influence of even basic meteorological variables on air-parcel residence times in forests.

Here, we report opportunistic investigations of air-parcel residence times in the mature, broadleaf deciduous
forest at the Birmingham Institute of Forest Research (BIFoR) free-air carbon dioxide enrichment (FACE)
facility. The primary experiment at BIFoR FACE observes forest ecosystem behaviour under future atmospheric
3915 composition. This is achieved by using large-scale infrastructure to elevate the CO₂ mixing ratio, without
containment, to 150 $\mu\text{mol mol}^{-1}$ above ambient in several large patches of the forest (Hart et al. 2020;
MacKenzie et al. 2021). BIFoR FACE is one of two ‘second-generation’ FACE experiments on mature,
ecosystem-scale forests, the other being the ‘EucFACE’ experiment in an open sclerophyll forest in Australia
(Drake et al. 2016). If we focus our attention on timescales of seconds to hours, over which the CO₂ is
3920 approximately passive, the normal course of operation of BIFoR FACE also offers a unique, daily dispersal
experiment. Across several patches of the mature woodland, the CO₂ mixing ratio is elevated around sunrise,
held at 150 $\mu\text{mol mol}^{-1}$ above ambient during daylight hours, and allowed to return to ambient after sunset, when
the CO₂ release is stopped. We use three years’ data (just under 50 million observations) to investigate the effect
of canopy structure and the surrounding atmospheric conditions on air-parcel residence times in a mature
3925 temperate forest.

6.2 Methods

6.2.1 Site description

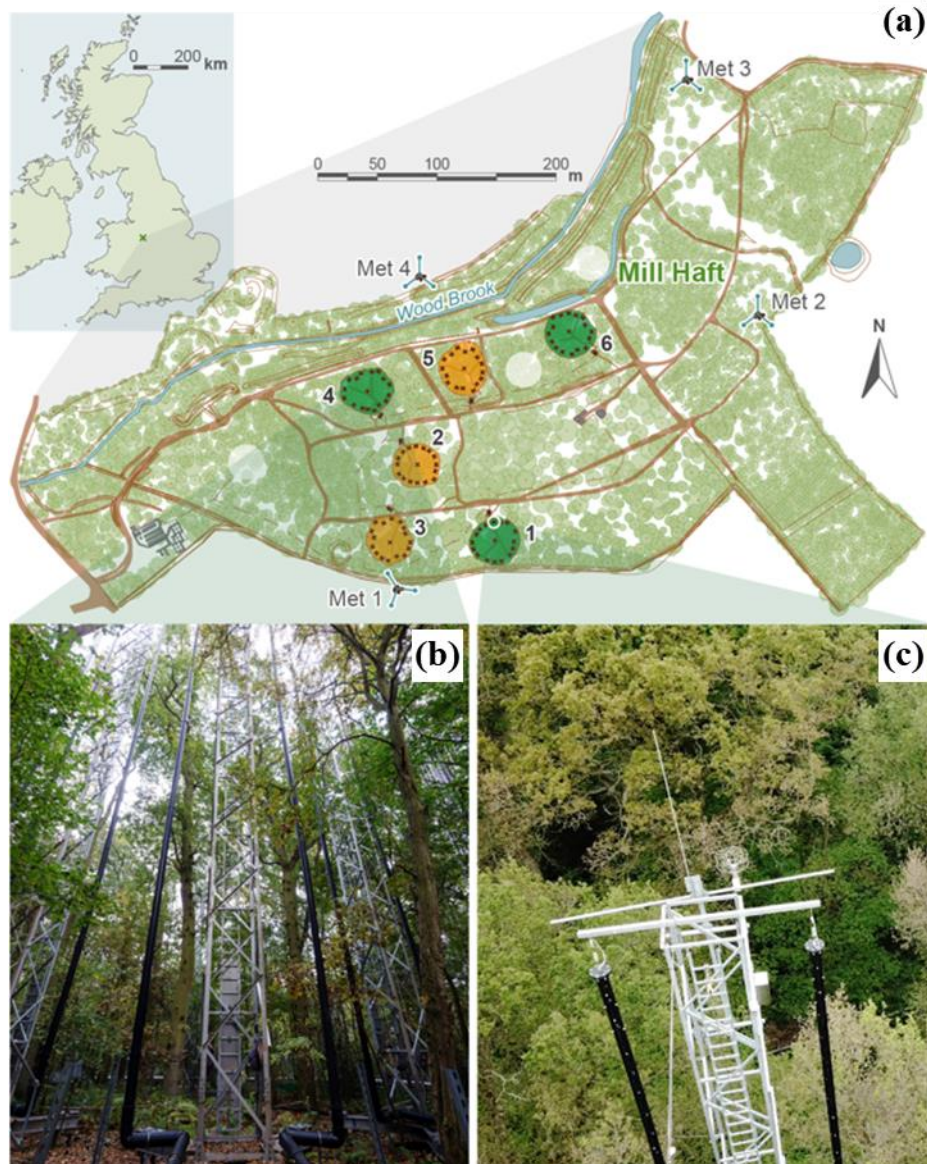
The BIFoR FACE facility is located in a mature deciduous broadleaf forest patch (≈ 19 ha) in central England,
United Kingdom (latitude, longitude: 52.7996, -2.3039). The BIFoR FACE woodland is dominated by *Quercus*
3930 *robur* (pedunculate oak), with a dense heterogeneous understorey layer of *Corylus avellana* (hazel), *Crataegus*
monogyna (common hawthorn), *Acer pseudoplanatus* (sycamore), and *Ilex aquifolium* (holly). Below the
heterogeneous understorey, the woodland supports ground flora, including *Phegopteris connectilis* (beech fern),
Rubus fruticosus (bramble), *Hedera spp.* (ivy), *Lonicera periclymenum* (honeysuckle), and, where the canopy
has been opened for access rides, various grass species (G. Platt, private communication, 2019). The BIFoR
3935 FACE woodland shows evidence of historical coppicing but it has not been managed for at least 30 years. The
largest oaks were planted in 1850. Hanging and fallen deadwood is left in place except where it poses a direct
risk to human safety. The highest point of the facility is situated in the east of the forest, at around +112 m above
sea level (a.s.l.) and the lowest point at the site offices and CO₂ storage plant, at +92 m a.s.l. The terrain below

the areas of experimental interest is quite level, at $+108 \pm 2.7$ m a.s.l. (see contour maps in MacKenzie et al. (2021)).

The BIFoR FACE facility comprises nine experimental patches of forest, which are approximately circular, with an internal radius of around 17 m (Table 6.1). There are three ‘fumigated’ (f) patches, in which infrastructure arrays maintain the CO₂ mixing ratio (denoted [CO₂] hereafter) at 150 μmol mol⁻¹ above ambient during daylight periods of the growing season. There are three further ‘control’ (c) patches, which are dosed with ambient air only, and three ‘ghost’ patches, which are ecologically similar to the fumigated and control patches, but do not contain any of the supporting infrastructure (Figure 6.1). In the fumigated arrays, premixed air/CO₂ is released in the upwind quadrant from perforated vent pipes, supported by 16 free-standing lattice towers (Figure 6.1). The wind direction and speed are updated in the FACE control program (FCP) every second, based on 20 Hz sonic anemometer measurements at the canopy top on the northernmost tower of each fumigated array (Hart et al. 2020). The forest arrays are paired, so that a control array mimics the actions of its corresponding fumigated array, but doses the forest patch with ambient air only. The pairings are numbered 1(f) and 3(c), 4(f) and 2(c), 6(f) and 5(c) (Figure 6.1). For more background on the BIFoR FACE facility and its operation, see Hart et al. (2020). Details of the measurements and data and tissue curation pipelines are provided in MacKenzie et al. (2021).

Table 6.1: Geometries of the BIFoR FACE control (c) and fumigation (f) arrays. The internal radius is defined as the mean distance between the central tower and the inside edge of the towers supporting the perforated vent pipes.

Array	Infrastructure tower heights (m)	Central tower height (m)	Height of CO ₂ sample inlet	Internal radius (m)	Research ground area (m ²)	Array volume (m ³)
1(f)	26.7	26.0	21.5	17	724	24,815
2(c)	25.6	24.9	22.5	16	628	21,107
3(c)	26.2	25.5	21	16	661	22,138
4(f)	27.2	26.5	22	17	702	24,406
5(c)	27.3	26.6	22.5	17	688	24,207
6(f)	24.7	24.0	19.8	17	678	21,641



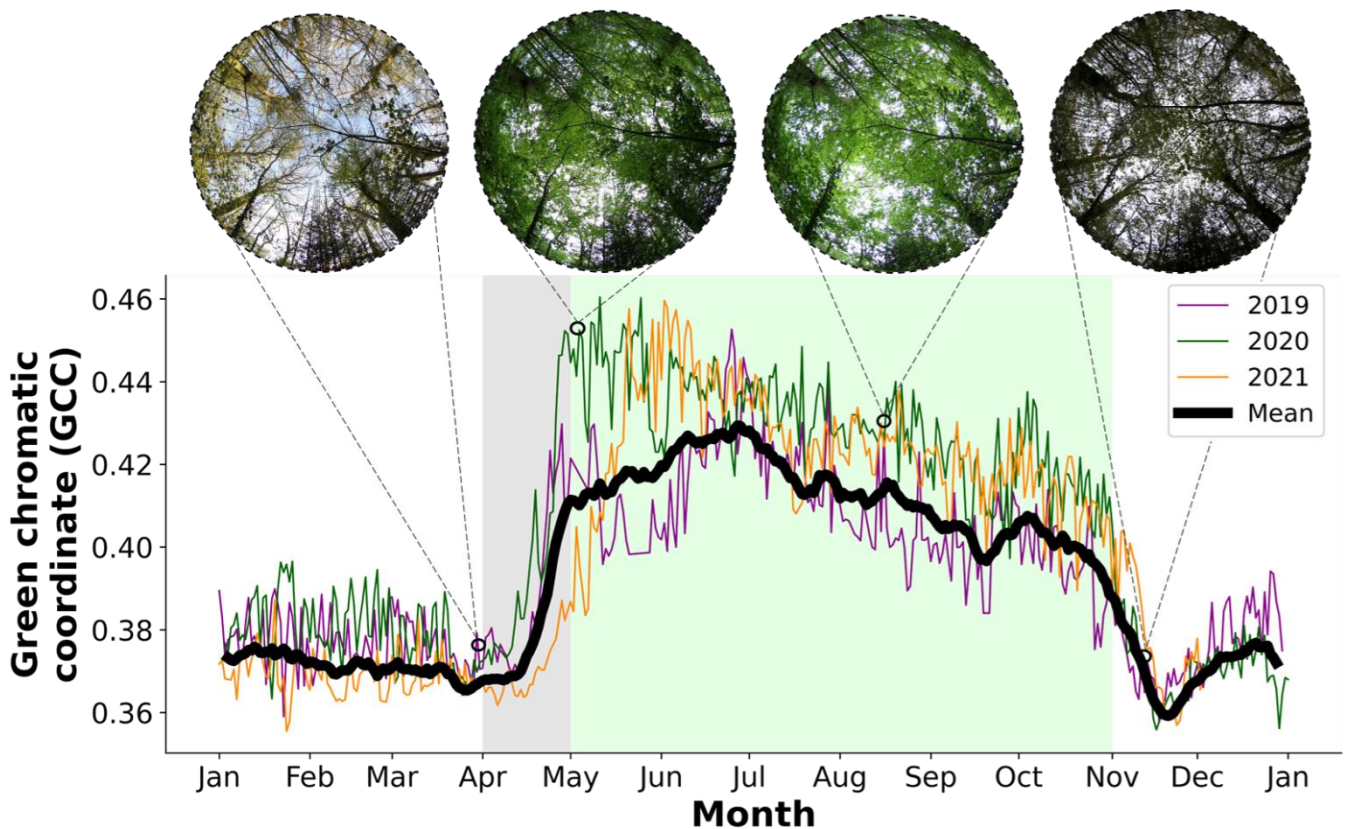
3960 **Figure 6.1:** (a) schematic of the Birmingham Institute of Forest Research free-air carbon dioxide enrichment (BIFoR FACE) facility (see section 6.2.1 for site description). The coloured circles indicate the location of the FACE arrays, with green and orange denoting the fumigated and control arrays, respectively. The grey translucent circles mark the locations of the ghost arrays. The meteorological towers on the edge of the forest are labelled Met 1–4. (b) The perforated FACE vent pipes in array 4. (c) The two-dimensional sonic anemometer in array 1 (see section 3970 6.2.2.2 for details of meteorological measurements).
3965

6.2.2 Observational details

6.2.2.1 Observation period and canopy density

The FACE arrays operate up to 18 hours a day (04:30–21:30), depending on day length, and from budburst (around 1 April) to leaf fall (around 31 October). We investigate observations from 1 April–31 October in the 3970 years 2019–2021. We refer to the April fumigation period as ‘leaf-off’, because the dominant canopy oaks put out most of their leaves in May, and the period from 1 May to 31 October as ‘leaf-on’. Together the leaf-on and leaf-off periods, as defined, make up the CO₂ fumigation period at BIFoR FACE. The LAI is much greater during the leaf-on period than the leaf-off period—see, for example, the hemispheric photographs in Figure 6.2. The LAI \approx 7–8 during the leaf-on period, calculated using extensive leaf-litter measurements throughout the

3975 season. The plant area index (PAI)—the total projected plant area per unit ground area—is approximately 1–2
 for the leaf-off period, however, this is only a rough estimate. Deriving PAI estimates from digital photographs,
 for example, is problematic in tall multi-layered forests (Yan et al. 2019) and leaf litter observations are not
 available. To show the broad phenological changes at BIFoR FACE, Figure 6.2 presents timeseries of the green
 chromatic coordinate (GCC) for the investigation period. The GCC (normalised to take values from 0–1)
 3980 measures the ‘greenness’ of the canopy from repeated digital photographs (Woebbecke et al. 1995). Figure 6.2
 shows that the greenness of BIFoR FACE forest increases sharply towards the end of April, as the canopy oaks
 begin to put out their leaves, peaks in May–June, declines slowly across the leaf-on period as the leaves mature,
 before declining sharply in November when the dominant oaks drop their leaves. A note of caution: although
 the GCC is a helpful tool to monitor seasonal canopy-scale dynamics (Toomey et al. 2015), it is not a proxy for
 3985 plant-area density in multi-layered deciduous forests. For example, in Figure 6.2, the sharp changes in GCC in
 spring and autumn correspond to changes in leaf density, but the gentle decrease in GCC over the leaf-on period
 is not reflected by changes in canopy density (i.e., the leaves become less green over the summer, but their
 number remains approximately constant).



3990 **Figure 6.2:** Timeseries of the green chromatic coordinate (GCC) derived from PhenoCam measurements (section
 6.2.2.1). The hemispheric photos are taken by cameras around 50 cm above the ground in array 1 (Figure 6.1 and
 site description in section 6.2.1). Shaded grey and green regions show the leaf-off and leaf-on periods, respectively
 (as defined in section 6.2.2.1).

6.2.2.2 Fumigation and meteorological measurements

3995 The FCP determines, based on solar elevation, the times at which the fumigation is started and shut down each
 day. Array pairings are switched on in sequence 1(f) + 3(c), 2(c) + 4(f) and 5(c) + 6(f) (Figure 6.1). Wind
 velocities for the FCP are monitored at 1 Hz using two-dimensional sonic anemometers (WMT700, Vaisala
 Oyj, Vantaa, Finland), mounted at a height $z \approx 1$ m above the canopy on the northernmost tower of each

fumigated array. The FCP logs 1-min averages of the wind speed and direction, and of other variables including
 4000 the air temperature, atmospheric pressure, and solar elevation. There are four meteorological masts around the
 edge of the forest (denoted Met 1–4, respectively; Figure 6.1), with three-dimensional sonic anemometers (R3-
 100, Gill Instruments, Lymington, UK) mounted at 25 m on each. These anemometers sampled the three-
 dimensional instantaneous velocity components and the speed of sound at 20 Hz throughout the entire
 observational period. In October 2020, three additional three-dimensional sonic anemometers (Windmaster Pro,
 4005 Gill Instruments, Lymington, UK) were added to each mast at heights of 7 m, 10 m, and 14 m, sampling the
 same variables at the same rate as the existing sensors. The $[\text{CO}_2]$ is measured at 1 Hz using infrared gas
 analysers (IRGA, LiCor 840A, LiCor Lincoln) with inlets situated in the centre of the fumigation and control
 arrays, just below the top of the canopy for each array (Table 6.1).

4010 The FCP automatically records 1-min and 5-min averages of the 1 Hz $[\text{CO}_2]$ observations. The software halts
 fumigation when the canopy-top 1-min average air temperature is $< 4^\circ\text{C}$ because broadleaf forests uptake little
 carbon below this threshold (Larcher 1995). Fumigation is also stopped during periods of high winds—where
 the 15-min average wind speed, V , at the canopy top exceeds 8 m s^{-1} —because of the high cost of maintaining
 the elevated $[\text{CO}_2]$. When $V < 0.4 \text{ m s}^{-1}$, the FCP introduces CO_2 -enriched air all around the array via alternate
 4015 vent pipes, rather than in the upwind quadrant, as under normal wind speeds. This is because advection of the
 enriched gas flow is ineffective at very low wind speeds.

6.2.3 Calculation of residence times

We calculate residence times from the FACE data using a mass balance approach. We treat each fumigated
 array as a reservoir of ‘additional’ CO_2 , i.e., as a reservoir of air with a CO_2 mixing ratio that is elevated ($e[\text{CO}_2]$)
 4020 compared to the ambient CO_2 mixing ratio, $a[\text{CO}_2]$. The residence time represents the average time each
 additional molecule of CO_2 spends in the fumigated arrays before it is transported out by turbulent and advective
 fluxes, or is taken up by the trees and other plants. Provided we choose a time period over which the mass of
 the additional CO_2 in each fumigated array is approximately steady, the residence time can be interpreted
 equivalently as the time it would take to increase the CO_2 mixing ratio from $a[\text{CO}_2]$ to $e[\text{CO}_2]$ in the absence of
 4025 significant sinks. First, we find the mixing ratio of the additional CO_2 in each fumigated array ($\chi_{e\text{CO}_2}$) during
 fumigation, i.e., the difference between the elevated and ambient mixing ratios:

$$\chi_{e\text{CO}_2} (\mu\text{mol mol}^{-1}) = e[\text{CO}_2] - a[\text{CO}_2]. \quad (6.3)$$

The value of $\chi_{e\text{CO}_2}$ is then used together with the ideal gas equation to calculate the mass of additional CO_2 in
 each fumigated array during fumigation:

$$4030 \quad M_{\text{CO}_2} = V_a M_r \chi_{e\text{CO}_2} \frac{p}{\mathcal{R}T}, \quad (6.4)$$

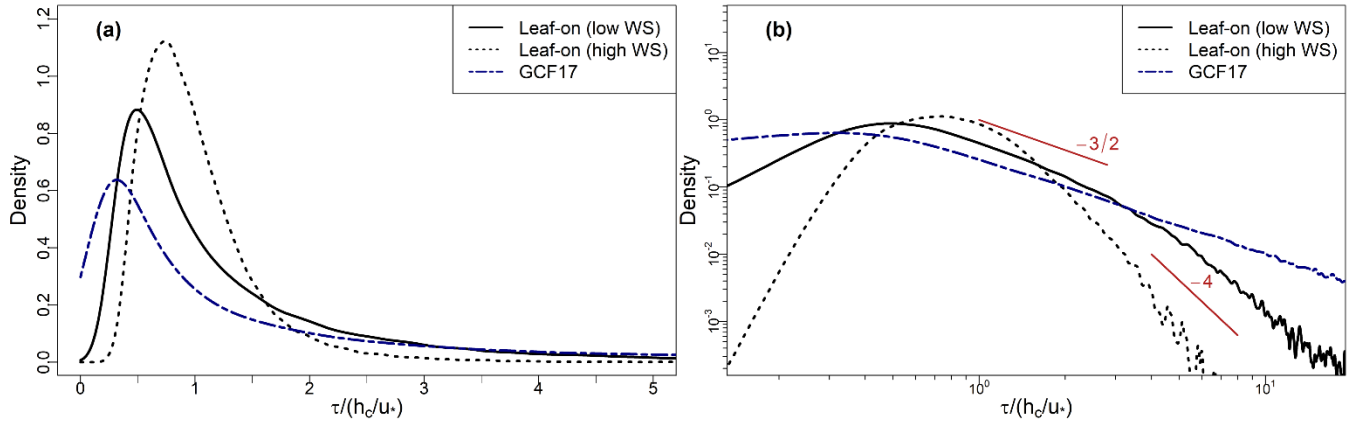
where M_{CO_2} (g) is the mass of the additional CO_2 , V_a (m^3) is the effective volume of each fumigated array
 (Table 6.1), M_r is the molar mass of CO_2 (g mol^{-1}), p is the atmospheric pressure (Pa), \mathcal{R} is the molar gas
 constant ($8.314 \text{ m}^3 \text{ Pa K}^{-1} \text{ mol}^{-1}$), and T is the air temperature (K). For the residence time analysis across the
 entire study period, we treat V_a as constant for each array. However, when examining individual events such as
 4035 venting in stable atmospheric conditions (section 6.3.7), this assumption is called into question. We define a
 residence time by dividing the mass of additional CO_2 in each array by the flow rate required to sustain it:

$$\tau = \frac{M_{CO_2}}{F_{in}}, \quad (6.5)$$

where τ (s) is the residence time and F_{in} ($\text{g (CO}_2\text{) s}^{-1}$) is the CO_2 flow rate into each fumigated array from the FACE infrastructure. Equation (6.5) ignores other sources of additional CO_2 into each fumigated array, most notably the soil fluxes (F_{soil}). This is justified because $F_{in} \gg F_{soil}$ during fumigation— $F_{in} \approx 50\text{--}550 \text{ g (CO}_2\text{) s}^{-1}$ in each array, compared with $F_{soil} < 0.1 \text{ g (CO}_2\text{) s}^{-1}$ (Von Arnold et al. 2005).

We consider the conditions under which Equation (6.5) offers a reasonable estimate of residence times. In a quasi-infinite model of a uniform forest, such as in GCF17, the only path for air parcels to leave the canopy is through vertical venting out of the top, which we denote $F_{out(top)}$. The BIFoR FACE arrays, however, are not closed at the sides, and air parcels can also exit the arrays horizontally, i.e., there is some non-zero horizontal flux, $F_{out(hor)}$, of air out of the array. In a quasi-infinite, uniform forest, we expect $\tau = M_{CO_2}/F_{in} \approx M_{CO_2}/F_{out(top)}$. In reality, however, $\tau = M_{CO_2}/F_{in} = M_{CO_2}/(F_{out(top)} + F_{out(hor)} + F_{out(sink)})$, where $F_{out(sink)}$ denotes CO_2 sink terms, most notably photosynthetic uptake. We do not include $F_{out(sink)}$ in our calculations below because $F_{out(sink)} \approx 0.5\text{--}2 \text{ g (CO}_2\text{) s}^{-1}$ during the day (Gardner et al. 2021), typically less than 1% of the total flux. Long-term analysis of the BIFoR FACE observations shows contamination events between the arrays are rare and mostly small (Hart et al. 2020), usually occurring in strong winds. This suggests that, although $F_{out(hor)}$ is always non-zero, it is likely small in conditions with weak advection. Unfortunately, horizontal fluxes in forests are difficult to measure or even estimate (Aubinet et al. 2010). Therefore, rather than trying to assign a numerical value to $F_{out(hor)}$, we identify meteorological conditions under which $F_{out(top)} \gg F_{out(hor)}$, and therefore $\tau = M_{CO_2}/F_{in} \approx M_{CO_2}/F_{out(top)}$. Figure 6.3 presents probability density functions of τ during the lowest 50% of wind speeds of the leaf-on period (solid black), during the highest 25% of wind speeds of the leaf-on period (dashed), and GCF17's model in Equation (6.1) (navy). The PDF for GCF17 takes $K_{eq} = 1.2 \text{ m}^2 \text{ s}^{-1}$, calculated using Equations (6A.1–6A.3) in Appendix 6A, $h_c = 25 \text{ m}$, and $z_{rel} = 15 \text{ m}$, which reflects that the majority of the CO_2 is released in the upper two-thirds of the canopy (see section 6.2.4 below).

Figure 6.3 shows, at low wind speeds, our method generates PDFs of τ in reasonably close agreement to GCF17, especially given the very different assumptions used to calculate each PDF. Under these conditions, the one notable deviation between our results and GCF17's theory is in the right tails of the PDFs (Figure 6.3b), which we discuss further in section 6.3.6. In the strongest winds, however, the limited diameters of the BIFoR FACE arrays constrains our method. In these conditions, the mostly small values of τ —visible in the sharp peak of the PDF in Figure 6.3a and steep decay of the right tail in Figure 6.3b—indicate that F_{in} has increased, and therefore the flux out has increased. Comparisons with GCF17 suggest this is predominantly due to an increase in the horizontal component $F_{out(hor)}$, which is difficult to approximate in our finite-size arrays. Our residence-time calculations below therefore include only observations during the lower half of wind speeds (varying the percentile cut-off between 40–60% does not qualitatively affect our results). We discuss the implications of stronger winds on τ in sections 6.3.3 and 6.3.6.



4075 **Figure 6.3:** (a) Linear- and (b) logarithmic-scale PDFs of τ , as defined in section 6.2.3, from BIFoR FACE (site description in section 6.2.1) during the lowest 50% (solid black) and highest 25% (black dashed) of wind speeds of the leaf-on period, and GCF17's model in Equation (6.1) (navy-blue dot-dash). In (b), slopes of $-3/2$ and -4 are shown for reference. The slope of $-3/2$ is the power-law decay from GCF17 (Equation (6.1)) and -4 is an arbitrary value to show the steeper decay of the right tail of the PDF if τ in strong winds. Values of τ normalised by the canopy turnover time h_c/u_* (section 6.2.4).

4080 6.2.4 Data processing

We use a 5-min averaging period for the residence time calculations in Equations (6.3–6.5) and Reynolds averaging of the meteorological tower observations below. Sensitivity testing on high-resolution velocity measurements showed this to be the most appropriate period to capture the significant turbulent structures at this structurally heterogeneous site, while being long enough so that χ_{CO_2} and F_{in} were approximately steady.

4085 In mature forests, whose largest eddies scale with the mean height of the canopy h_c (Raupach et al. 1996; Finnigan 2000; Bannister et al. 2022), the canopy turnover time $\tau_c \approx h_c/u_* \approx 30\text{--}90$ s, where u_* is the friction velocity measured at $z = h_c$ (its derivation is described in section 6.2.5 below). This averaging period therefore corresponds to 5–10 cycles of the dominant turbulent eddies and the statistics of the residence time calculations were not qualitatively altered using averaging periods of up to 1 hr.

4090 We discarded observations for dates on which at least one of the fumigation arrays was switched off for more than two hours, or switched on and off more than once during the normal fumigation period. These temporary shutdowns were usually for maintenance work, or during periods of exceptionally high winds (which we discarded in any case according to section 6.2.3). This cautious filtering threshold ensures the residence time calculations focus on periods during which the fumigation was steady, rather than when the FACE infrastructure was operating at high flow rates to increase the $[CO_2]$ following shutdown. We also discarded dates on which observations were available from neither Met 1 nor Met 4 (see Figure 6.1). The filtering process left 530 observation days (78 in leaf-off and 452 in leaf-on) from a total of 642 (90 in leaf-off and 552 in leaf-on). To avoid erroneous values of τ , we discarded entries where: (i) $F_{in} < 1 \text{ g (CO}_2\text{) s}^{-1}$; and (ii) values of $\overline{M_{CO_2}}$ lay

4100 outside the range $\overline{M_{CO_2}} \pm 4\sigma(M_{CO_2})$, where σ is the standard deviation and the overbar denotes the mean. Steps (i) and (ii) together discarded less than 0.3% of the data.

To aid comparisons with previous reports, we highlight two particular features of the fumigation at BIFoR FACE. First, the fumigation is only carried out when the trees are likely to be photosynthesising, i.e., during the

4105 daytime (with an hour or so of fumigation either side of sunrise and sunset) of the UK growing season, which

is taken as 1 April–31 October. We therefore emphasise our estimates here are of forest air-parcel residence times during the daytime of the northern temperate spring, summer, and autumn. Second, most of the e[CO₂] air at BIFoR FACE is released into the oak canopy—comprising approximately the upper two-thirds of the mean forest height—where the bulk of the photosynthesising leaves are located.

4110

Three measures of statistical variability are used in this paper: the standard deviation, the interquartile range (IQR), and the median absolute deviation, D_{med} , defined $D_{med} = \text{median}(|x_i - \tilde{x}|)$ for a univariate set x_1, x_2, \dots, x_n , with \tilde{x} the set’s median. The D_{med} is helpful when considering the spread of observations with highly skewed distributions, as is the case here. For highly skewed distributions, the more familiar standard deviation overweighs the influence of (absolutely) large values in the observations (Jobst and Zenios 2001). In such cases, the D_{med} provides a less volatile and more representative measure of a sample’s deviation. However, this paper retains the standard deviation to aid comparison to other works, because it is much more commonly reported than measures such as the D_{med} . We report the IQR because it is familiar and provides a robust measure of the spread of the middle 50% of a dataset. But, because the IQR contains no direct information on tail behaviour, we use it alongside the standard deviation and D_{med} .

4120

6.2.5 Notation and meteorological tower calculations

We use right-handed Cartesian coordinates throughout this paper. We denote $\mathbf{x} = (x, y, z)$, the velocity components u, v, w (using the meteorological convention that positive u and v values indicate westerly and southerly flow, respectively), and time as t . For a quantity $\phi(\mathbf{x}, t)$, a double overbar denotes the time average and the prime denotes the deviations from that average, which we refer to as the ‘turbulent quantities’, i.e. $\phi(\mathbf{x}, t) = \overline{\overline{\phi}}(\mathbf{x}) + \phi'(\mathbf{x}, t)$. The double overbar is used instead of the conventional single overbar to distinguish the time averages from the descriptive statistics elsewhere in the paper. The turbulence kinetic energy (TKE) per unit mass = $\frac{1}{2}(\overline{u'^2} + \overline{v'^2} + \overline{w'^2})$. The friction velocity $u_* = \left(\overline{u'w'^2} + \overline{v'w'^2}\right)^{\frac{1}{4}}$ is a scaling variable that is most meaningfully defined in the inertial sublayer of the atmosphere (Monin and Obukhov 1954). However, it is often used as a shorthand for turbulence elsewhere in the atmospheric surface layer, with higher values indicating more turbulent conditions. The Obukhov length, L , is calculated as

4130

$$L = \frac{-\overline{\overline{T_s}} u_*^3}{\kappa g \overline{w' T_s'}}, \quad (6.6)$$

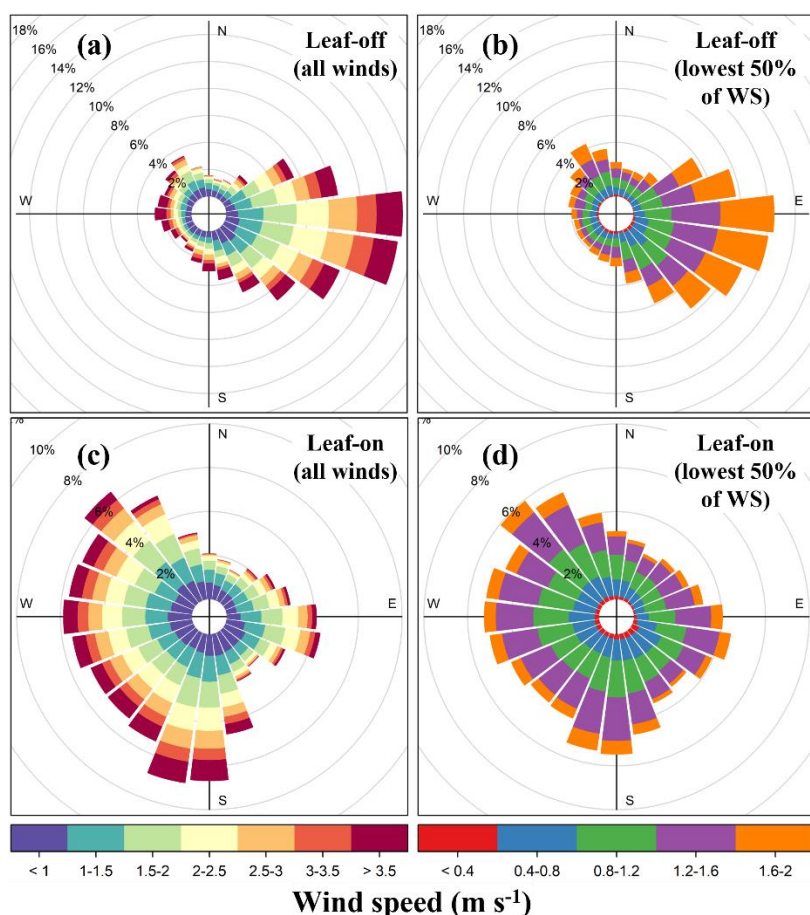
where $\kappa = 0.4$ is the von Kármán constant, g is the acceleration due to gravity, and T_s is the sonic air temperature, which is a good approximation of the virtual potential temperature (Kaimal and Gaynor 1991). The values of L , u_* and the TKE are calculated from 20 Hz observations at $z \approx 22 \text{ m} \approx h_c$ on Met 4 preferentially, because it lies at the downstream edge of the forest in the direction of the prevailing wind. On dates for which Met 4 observations were unavailable, the observations were taken from Met 1 (Met 4 and Met 1 account for 512 and 18 days, respectively, of the 530 total).

4135

6.3 Results and Discussion

4140 6.3.1 Wind conditions at BIFoR FACE

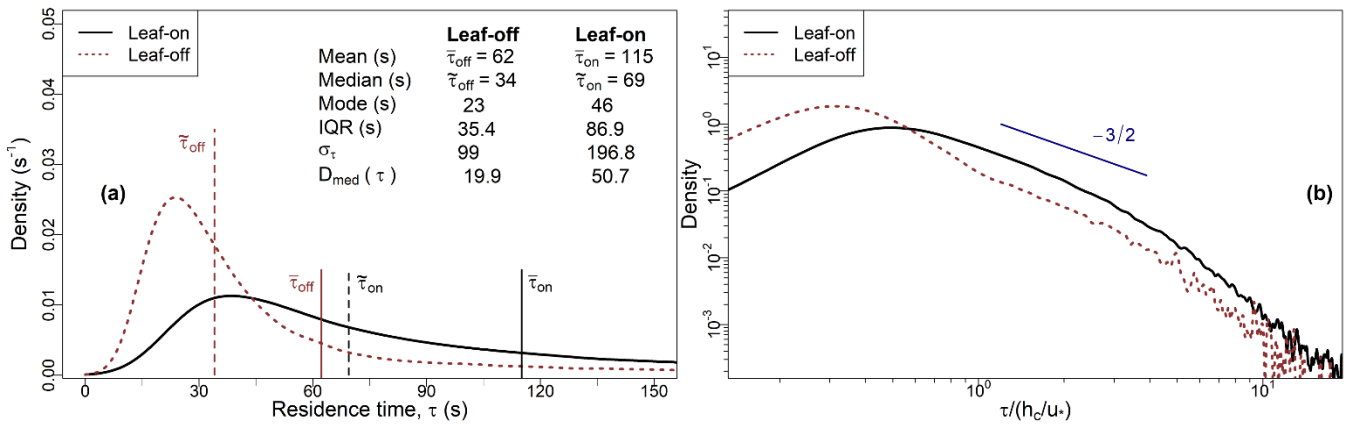
Figure 6.4 presents wind roses for the 2019–2021 fumigation period at BIFoR FACE across the period as a whole (Figure 6.4a, c) and for the observations used in the residence-time calculations, i.e., the lowest 50% of wind speeds across the whole observation period (Figure 6.4b, d). The wind speeds are generally low compared with observations from most meteorological stations because the wind measurements at BIFoR FACE are measured around the tops of the trees of each array, whereas meteorological stations are typically located away from large obstacles. The wind speeds were generally higher in the leaf-off period than the leaf-on. For example, 39% of 5-min averages were $> 2.5 \text{ m s}^{-1}$ for the leaf-off period, compared with 27% for leaf-on. The prevailing wind direction around BIFoR FACE is south-westerly, as is typical for most of the UK. However, the wind direction in the UK is highly variable in April (leaf-off) and the wind direction around BIFoR FACE was predominantly easterly during the leaf-off period 2019–2021 (Figure 6.4a, b). Predominantly easterly winds are unusual in the UK, but these observations match the local synoptic conditions over the same period. Our leaf-off period is much shorter than the leaf-on period and is therefore more susceptible to isolated meteorological events.



4155 **Figure 6.4:** Wind roses for BIFoR FACE during the 2019–2021 leaf-off (a, b) and leaf-on periods (c, d) (see section 6.2.1 for site description, and 6.2.2 for observation details). The wind roses are calculated on 5-min averages of sonic measurements in array 1. (a, c) show wind roses across all wind conditions; (b, d) show wind roses for the lowest 50% of wind speeds, used in the residence-time calculations (section 6.2.3). The wind roses for the other fumigation arrays are very similar and are omitted to avoid repetition. Note the change of scale between (a, c) and (b, d).

4160 **6.3.2 Basic distributions of τ values**

Figure 6.5 presents probability density functions (PDFs) and reports descriptive statistics of the residence times for the leaf-off (τ_{off}) and the leaf-on (τ_{on}) periods. The overbar and overtilde notation refer to the mean and median values, respectively. The modal values of $\tau < \tilde{\tau} < \bar{\tau}$ for each period, which is typical but not diagnostic (von Hippel 2005) of positively skewed unimodal distributions. Longer residence times are relatively less common during the leaf-off period than leaf-on, as indicated by the shift to the left of the τ_{off} PDF compared with the τ_{on} PDF. For example, 57% of τ_{on} observations are greater than 60 s, compared with only 24% of τ_{off} values. The τ_{on} values are more variable than the τ_{off} values. For example, the interquartile range (IQR) for τ_{on} is over twice that of τ_{off} , and $D_{med}(\tau_{on}) > D_{med}(\tau_{off})$. In Figure 6.5b, both the leaf-off and leaf-on PDFs show clear modal values, followed by a region over which the decay exhibits almost power-law behaviour, followed by steeper decay in the tails.



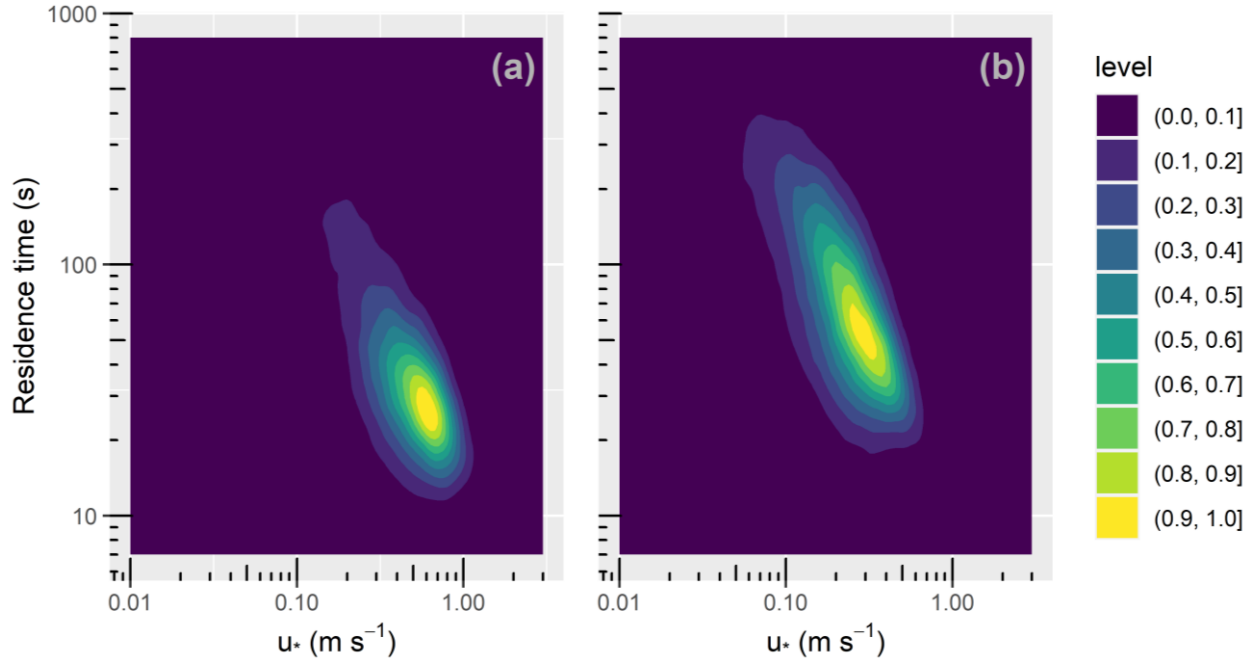
4175 **Figure 6.5: (a) PDFs and statistics of the residence times for the leaf-on and leaf-off periods (see section 6.2.2 for observation details, and 6.2.3 for calculations of the residence time, τ). Solid and dashed vertical lines mark the mean and median values for each period, respectively. The mode for each period is taken as the value at which the PDFs attain their maximum densities. (b) As for (a), with PDFs presented on log-log axes with τ normalised by the canopy turnover time, h_c/u_* (section 6.2.4). The black line is the same as in Figure 6.3, although (a) presents dimensional information whereas Figure 6.3a presents the normalised PDF.**

6.3.3 Dependence of τ on u_* and atmospheric stability

6.3.3.1 Dependence of τ on u_*

4180 Figure 6.6 presents combined scatter and density plots showing the variation of τ with u_* in the (a) leaf-off and (b) leaf-on periods. The yellow regions indicate higher density, with the decile contours shown. The colour scale is normalised to account for the different sample sizes in the two periods. Figure 6.6 shows, over both periods, the residence times decrease with increasing values of u_* . This accords with intuition that canopy residence times should progressively reduce with increasing turbulence. Most notably, (a) and (b) regress to gradients of around -1 (-0.93 and -0.95 , respectively), which indicates that, as a first approximation, the effect of turbulence levels on the residence times is given by $\tau \propto u_*^{-1}$, as proposed by GCF17. It is worth qualifying this point a little. Because our u_* values are derived from a single measurement location whereas our τ values in three nearby locations within 300 m (Figure 6.1), this argument assumes a state of ‘moving equilibrium’ (Yaglom 1979), in which u_* varies slowly in the x, y plane, with u_* measured at $z = h_c$ serving as a local velocity scale. This assumption has not been tested in patchy forests such as that at BIFoR FACE, whose

structure varies strongly in the x, y plane, likely challenging the assumption that u_* is approximately constant. Further, our results do not account for the effect of strong winds on τ , which to our knowledge remains untested.



4195 **Figure 6.6:** Two-dimensional density plots, showing the variation of the residence time τ (section 6.2.3) with the friction velocity u_* (section 6.2.5) for the leaf-off (a) and leaf-on (b) periods (section 6.2.2 for observation details). The colour scale is normalised to account for the different sample sizes in the two periods. ‘Level’ in the colour scale refers to the density of each bin, normalised by the peak density for each observational period.

6.3.3.2 Dependence of τ on atmospheric stability

To analyse the dependence of τ on atmospheric stability, we define three broad stability classes following the approach in Mahrt et al. (1998) and Dupont and Patton (2012). Our stability regimes are defined at $z \approx h_c$ according to the behaviour of the kinematic fluxes of temperature $\overline{w'T'_s}$ and momentum (via u_*), as a function of the stability parameter h_c/L from Equation (6.6).

- Near-neutral (NN): $-0.005 \leq h_c/L < 0.003$. In this regime, the momentum flux is significant, but the temperature flux is negligible.
- 4205 • Stable: $3 \leq h_c/L < 20$. This regime occurs mostly in light winds, often on cloudy mornings or shortly before fumigation shutdown in the evening. The momentum flux is small. Intermittent turbulence is a major component of turbulent exchange (Mahrt 2014).
- Unstable: $-20 \leq h_c/L < -1$. This regime mostly occurs during the day, especially in clear-sky conditions. This regime is characterized by a large temperature flux and, usually, small u_* values associated with light winds.

4210 These thresholds are not universal and are site and study specific. We define only three broad stability classes and adopt unusually demanding thresholds to define them. This is because (i) fumigation is carried out mostly during the day, so we have limited opportunity to investigate transitory sub-regimes, which typically occur in the early morning and late evening; and (ii) the observations used to calculate L are not taken at exactly the same location as the observations used to calculate τ , so we prefer to exclude potentially misleading marginal

cases. Figure 6.7a shows box-whisker plots of τ for the three stability regimes and Table 6.2 summarises their basic statistics. Figures 7b, c present PDFs for the three regimes during the leaf-on period (those for leaf off are similar and are included in Figure 6B.1 in Appendix B). The values of τ in Figure 6.7 are normalised by $\tau_c = h_c/u_*$ for each class to minimise the more trivial dependence of τ on u_* , because u_* varies between the classes. However, Table 6.2 presents the statistics in dimensional form for easier interpretation.

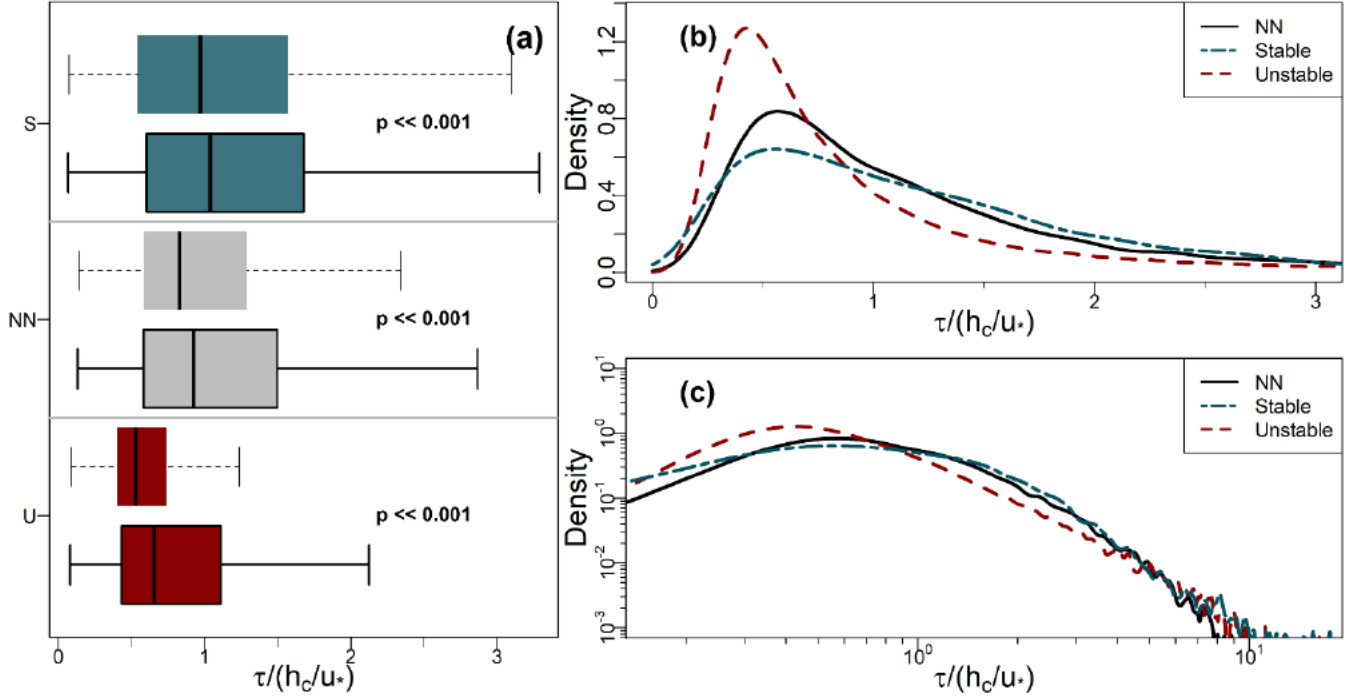


Figure 6.7: Statistics of normalised residence times (section 6.2.3) binned by the stability classes defined in section 6.3.3.2. (a) Box-whisker plots of normalised residence times for stable (S), near-neutral (NN), and unstable (U) conditions. Boxes with dashed whiskers and no border show leaf-off values; boxes with solid whiskers and borders show leaf-on (see section 6.2.2 for observation details). Solid vertical lines indicate median values. Width of the boxes shows the IQR. Lower and upper whiskers respectively indicate the 25th percentile $-1.5 \times \text{IQR}$ and 75th percentile $+1.5 \times \text{IQR}$. (b) and (c) PDFs of residence times for the leaf-on period, plotted on linear and logarithmic axes (base 10), respectively.

Table 6.2: Descriptive statistics of τ values (section 6.2.3) for the leaf-on and leaf-off periods binned into three stability regimes. All values in seconds rather than normalised units. The symbols $\bar{\tau}$, σ_τ , $\tilde{\tau}$, and $D_{med}(\tau)$ denote the mean, standard deviation, median, and median absolute deviation, respectively (see section 6.3.2 for an overview of these statistics).

	Stable		NN		Unstable	
	Leaf-on n = 11,291	Leaf-off n = 1,556	Leaf-on n = 10,668	Leaf-off n = 2,865	Leaf-on n = 32,001	Leaf-off n = 8,846
$\bar{\tau}$	229	155	100	64	89	37
σ_τ	319	198	172	83	154	45
$\tilde{\tau}$	169	117	73	45	55	27
$D_{med}(\tau)$	121	85	47	24	34	12
IQR	174	124	72	38	57	17

Air-parcel residence times increase with greater stability, as does the variability in their values. These differences are significant, both between the growing periods and between the stability classes in each period ($p < 0.001$ using the Mann–Whitney–Wilcoxon test). In unstable conditions, long residence times are much

less common than they are in the NN or stable regimes. For example, in Figures 7b, and 7c, the right tails of the unstable PDF are lighter than those for NN and the stable regime. The distributions of τ remain positively skewed for each stability class (e.g., the right whiskers are longer than the left in Figure 6.7a). These general patterns are not sensitive to the exact thresholds of h_c/L used to bin the data. Changes in the turbulence structure around the forest likely account for the main differences in the distributions of τ across the three stability classes. In NN conditions, shear generated eddies around the tops of the trees dominate turbulent exchange (Finnigan 2000; Brunet 2020; Bannister et al. 2022). However, as stability decreases from NN to free convection in the unstable regime, the dominant turbulent structures around the forest transition from shear-layer vortices to thermal plumes. These thermal plumes have typical length scales several times larger than shear-layer vortices (Patton et al. 2016), which could result in more vigorous mixing in unstable conditions than NN, resulting in the smaller τ values seen for the former than the latter (Figure 6.7). Conversely, in stable conditions, in-canopy turbulence is much weaker and more intermittent than in neutral or unstable conditions, reflected in (i) the larger average values of τ for the stable regime than the NN or the unstable regimes; and (ii) a greater likelihood of long τ values, when air remains within the canopy until it is vented by infrequent, intermittent turbulence, as reflected in the heavy tails of the stable PDFs. Section 6.3.7 discusses intermittent venting in stable atmospheric conditions in more detail. For the NN and unstable regimes, $\tau \propto u_*^{-1}$, but $\tau \propto u_*^{-0.8}$ in stable conditions.

6.3.4 Dependence of τ on wind direction

Figure 6.8 presents polar plots showing percentiles in τ values with wind direction. The values of τ are not completely symmetrically distributed with regards to wind direction. This is unsurprising because the BIFoR FACE forest is a complex, mature woodland, within which the species composition, tree age, and stand structure varies. Array 1 provides the clearest example of the heterogeneity in that the residence times are noticeably lower when the wind direction is from the south and south-east (Figures 6.8a and 6.8d). This is because array 1 is located at the southern edge of the forest (Figure 6.1) and therefore vulnerable to edge effects from southerly winds. However, in most mature forests, structural heterogeneity means that point observations are never likely to be entirely neutral with respect to wind direction, even when edges are accounted for. For example, the closest edge to arrays 4 and 6 is to the north (Figure 6.1). But arrays 4 and 6 are relatively more exposed to south-westerly and southerly winds, respectively, because the trees abutting the arrays in those directions are slightly shorter than those to the north.

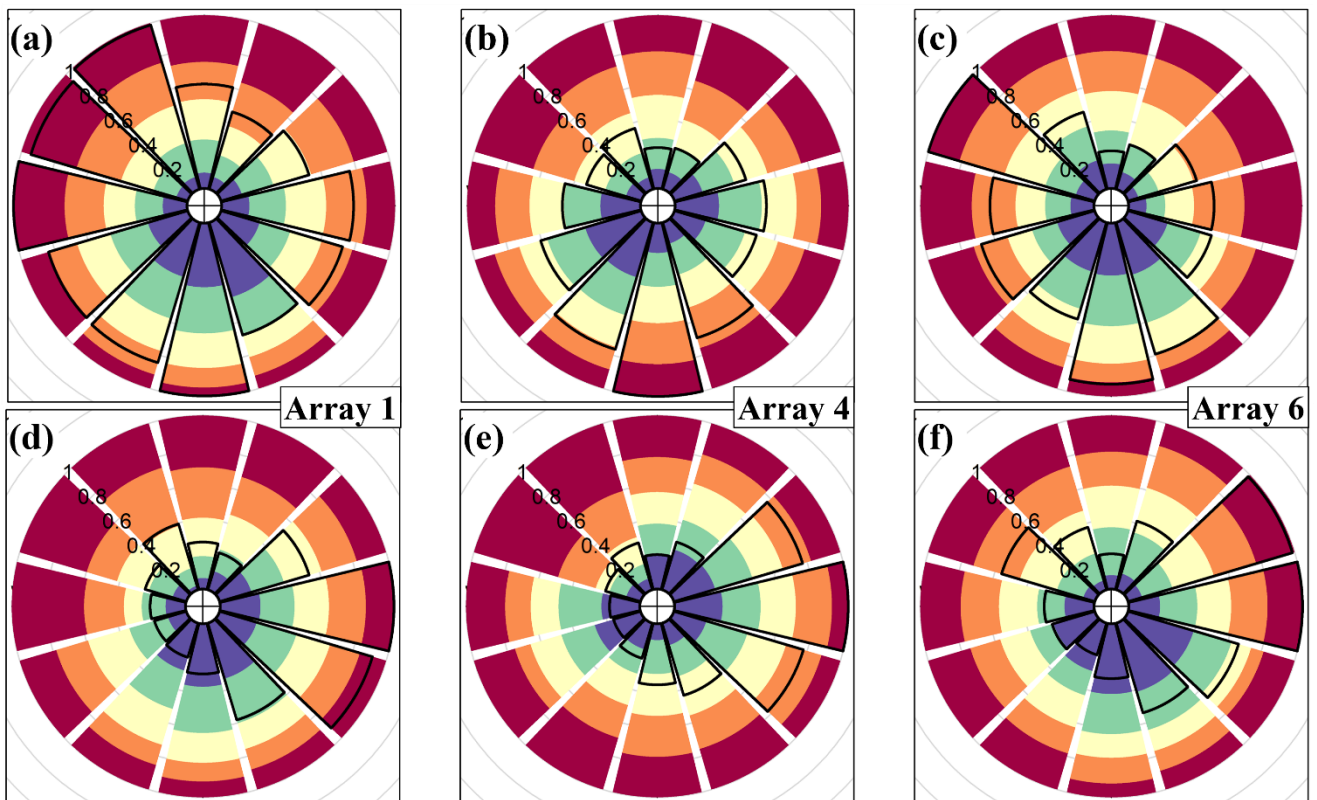


Figure 6.8: Residence-time (see section 6.2.3) quintiles by wind direction for the leaf-on (a–c) and leaf-off (d–f) periods (section 6.2.2 for observation details). (a, d) Array 1; (b, e) Array 4; and (c, f) Array 6 (Figure 6.1 and section 6.2.1). The colours indicate the proportion of τ values within each quintile, increasing from blue (lowest 20% of τ values across the whole site) to red (highest 20% of τ values across the whole site). For example, (a) shows that for southerly winds, a higher proportion of τ values are in the first and second quintiles (more blue and green in the southerly wind sectors) and a lower proportion are in the fifth quintiles (less red in the southerly wind sectors). In other words, for Array 1, lower τ values are more common for southerly winds. The solid black line shows the relative frequency of each wind sector across the whole leaf-on and leaf-off measurement periods, with the scale 0–1 indicated by the radial numbering.

4270

4275

No systematic differences or symmetries are apparent between the southern-edge array (array 1) and the northern-edge arrays (4 and 6). Because wind directional effects are so site and climate specific, it is difficult to generalise these results other than to say, where possible, observational campaigns of forest-atmosphere exchange in patchy landscapes should include at least two measurement locations, one deep in the forest, and one near any edges, especially in the direction of the prevailing wind. Forest edges experience different wind conditions, chemistry, microclimates to forest interiors (Bonn et al. 2014; Schmidt et al. 2017). It is important not to dismiss forest-edge processes as unrepresentative, however, because edges comprise the majority of the forested area in many parts of the world (Bannister et al. 2022).

4280

6.3.5 Seasonal (leaf-on/leaf-off) differences in τ

4285

As indicated by the descriptive statistics in section 6.3.2, the forest is more ventilated when the trees are not in leaf. Taking the distributions of τ across the entire fumigation period, the values of τ_{on} are significantly higher than the values of τ_{off} , with $p \ll 0.001$ using both the t -test and the Mann–Whitney–Wilcoxon test. Figure 6.8 shows that, for a given percentile, $\tau_{on} < \tau_{off}$ for most wind directions, particularly in arrays 1 and 4, which are slightly less sheltered than array 6. Figure 6.7 and Table 6.2 shows the average values of $\tau_{off} < \tau_{on}$ for the three stability classes we defined, with the distributions remaining significantly different ($p \ll 0.001$). The

4290

variability in the τ_{on} values is higher than in τ_{off} across the entire fumigation period, and in unstable conditions. However, for the NN and stable regimes, the variability in the τ values is quite similar between the two periods.

6.3.6 Comparison with published residence time values

4295 Recalling the set-up of the FACE operations, described above, our estimates are most comparable to the daytime residence times of air parcels released from approximately the upper two-thirds of the canopy, $z/h_c > 1/3$. With these considerations in mind, our calculated residence times fall within the range of modelled median values of tens of seconds to a few minutes (Strong et al. 2004; Fuentes et al. 2007; Gerken et al. 2017). There are few reported observational estimates of residence times, and none derived from measurements in ecosystems similar to the BIFoR FACE forest. To the extent a comparison is meaningful, our calculated residence times are
4300 within the range of reported field estimates e.g., mean values of a minute or two during the growing season (Martens et al. 2004; Farmer and Cohen 2008).

Our results agree with existing modelling studies that the distributions of residence times are strongly positively skewed and in certain conditions—e.g., in stable conditions (Figure 6.7) or for parcels travelling from near the
4305 ground (GCF17; Strong et al., 2004)—can be widely dispersed with quite heavy tails. For these situations, average values cannot be said to be ‘representative’, and it is preferable to be able to estimate distributions rather than single values. GCF17’s model in Equation (6.1) is appealing because it allows the distribution to be estimated from a small set of variables, making it suitable for deployment in large-scale models. The eddy diffusivity K_{eq} can be partially tuned to account for the forest structure and wind conditions. However, although
4310 GCF17’s model generates modal values similar to those we observed, it appears to overpredict the likelihood of long residence times in the upper canopy. For example, GCF17 predicts around 20% of air parcels have residence times of five minutes or more whereas, in our leaf-on data, the proportion is closer to 6%. Some of the discrepancy between our observations and GCF17’s model likely results from our underestimation of τ because of the finite-size arrays used in the mass balance calculations in Equation (6.5). However, given that
4315 GCF17’s model and our results diverge even in low winds, when advection is negligible and turbulence is weak, this factor is unlikely to be the only relevant difference. Indeed, the tails of GCF17’s own LES-generated PDFs appear to decay faster than the $-3/2$ power law predicted by analytical model in Equation (6.1)—especially for parcels released higher in the canopy—further suggesting Equation (6.1) overpredicts the likelihood of long residence times.

4320 The eddy-diffusivity closure assumptions used to formulate Equation (6.1) are most realistic when the length and timescales of the transport mechanism are smaller than the scale of the gradients in the measured quantities (Corrsin 1975). Cava et al. (2006) show this condition is most likely to be satisfied when the sum of the turbulent transport and buoyant production terms in the transport equations is small compared to the gradient in the
4325 measured quantity. In forests and other vegetation canopies in neutral conditions, this is a reasonable assumption below around $z/h_c = 1/2$, especially when considering quantities with strong gradients, such as fertilizer (Bash et al. 2010) or fungal spores. However, in forest crowns in neutral conditions, turbulent exchange is dominated by eddies with diameters that scale with h_c (Raupach et al. 1996; Finnigan 2000; Brunet 2020). These eddies create significant turbulent transport, meaning that the eddy-diffusivity model underestimates turbulent forest-
4330 atmosphere exchange in the upper canopy and therefore overestimates residence times. As a more general consideration, GCF17’s model envisages a horizontally homogeneous, quasi-infinite forest, in which the only

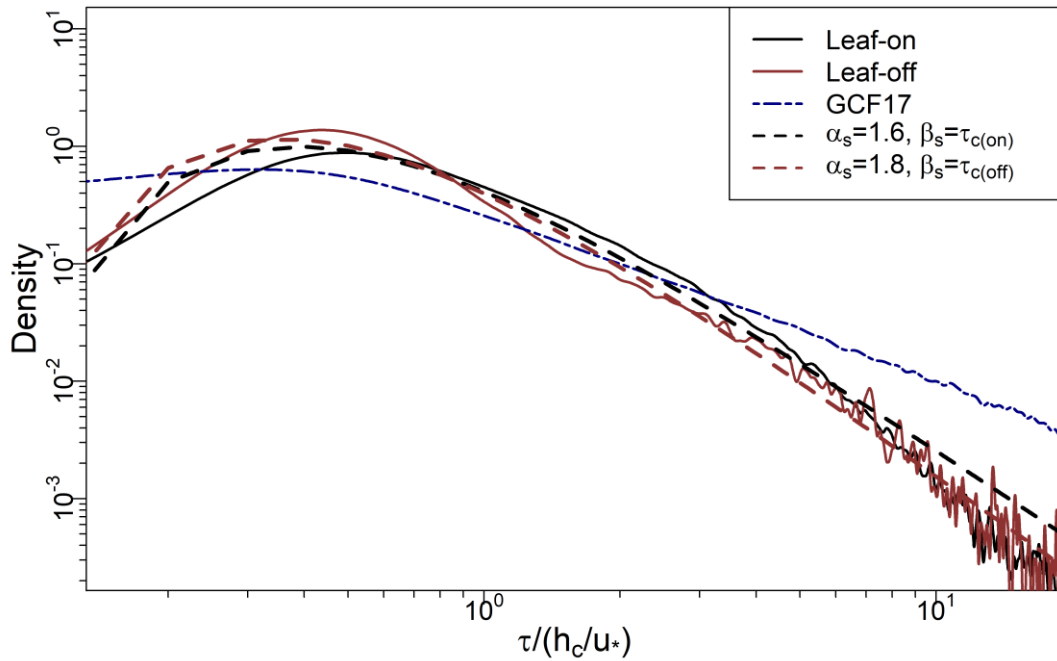
path of exit for air parcels is via turbulent exchange at the top of the canopy. However, real forests usually comprise a patchwork of gaps and clearings at all heights, caused by disease, tree senescence, human activities, and wind throw. These openings offer air parcels additional routes to exit forests, such as via advection across edges or through the regions of strong turbulent fluxes that form in patchy forest crowns. In hilly terrain, flow-separation regions in the lee of hills can create chimney-like pathways for air parcels to leave the forest, particularly for parcels moving from near the ground (Chen et al. 2019a; Bannister et al. 2022). The likely net effect of these additional pathways is to reduce the incidence of very long residence times, particularly in forests with extensive edge regions and patchy structures.

4340

Here we adapt GCF17's model to reduce the overprediction of large τ values while keeping it simple enough to be deployed in regional or global models, for which information on the canopy structure and the flow of air is typically limited. First, we observe that Equation (6.1) is a special case of the inverse-gamma distribution, the general form of which is

$$4345 \quad p(\tau; \alpha_s, \beta_s) = \frac{\beta_s^{\alpha_s}}{\Gamma(\alpha_s)} \tau^{-(\alpha_s+1)} \exp\left[-\frac{\beta_s}{\tau}\right]; \tau > 0, \quad (6.7)$$

where $\Gamma(\cdot)$ is the gamma function and α_s and β_s are, respectively, shape and scale parameters (β_s is the rate parameter from the point of view of the gamma distribution). Taking $\alpha_s = 1/2$ and $\beta_s = \tau_{turb} = (h_c - z_{rel})^2 / 4K_{eq}$ in Equation (6.7) gives Equation (6.1). The value of β_s is relatively more influential at lower values of τ , whereas α_s determines the distribution's dominant behaviour for large τ . In forest crowns, turbulent exchange scales with the canopy turnover timescale $\tau_c = h_c / u_*$, which we use as our value for β_s . The value of α_s then determines the shape of the distribution, particularly at large τ values. We find $\alpha_s = 1.4$ – 1.8 fits our observations better than using $\alpha_s = 1/2$, as in GCF17 (Figure 6.9). The main effect of the larger α_s value is to reduce the probability of very long residence times, as evidenced by the roll-off of our PDFs from GCF17 at large τ values in Figure 6.9. A helpful by-product is that, for $\alpha_s > 1$ in Equation (6.7), the mean values of τ become formally defined as $\bar{\tau} = \beta_s / (\alpha_s - 1)$ (the mean is undefined for $\alpha_s < 1$). For our data, $\tau_{c(on)} = 78$ s and $\tau_{c(off)} = 54$ s. Taking $\alpha_s = 1.6$ and 1.8 as rough estimates for the leaf-on and leaf-off periods, respectively, gives $\bar{\tau}_{on} = 130$ s and $\bar{\tau}_{off} = 68$ s, close to the values $\bar{\tau}_{on} = 115$ s and $\bar{\tau}_{off} = 62$ s calculated directly on our data.



4360 **Figure 6.9:** Solid black and red lines show PDFs of τ (section 6.2.3) from BIFoR FACE (6.2.1 and Figure 6.1) during the leaf-on and leaf-off periods, respectively (section 6.2.2). Dashed lines show PDF estimates on the BIFoR FACE observations using Equation (6.7). Dot-dash navy line shows PDF from GCF17 in Equation (6.1). $\tau_{c(on)}$ and $\tau_{c(off)}$ denote $\tau_c = h_c/u_*$ for the leaf-on and leaf-off periods (section 6.2.4). All τ values normalised by $\tau_c = h_c/u_*$.

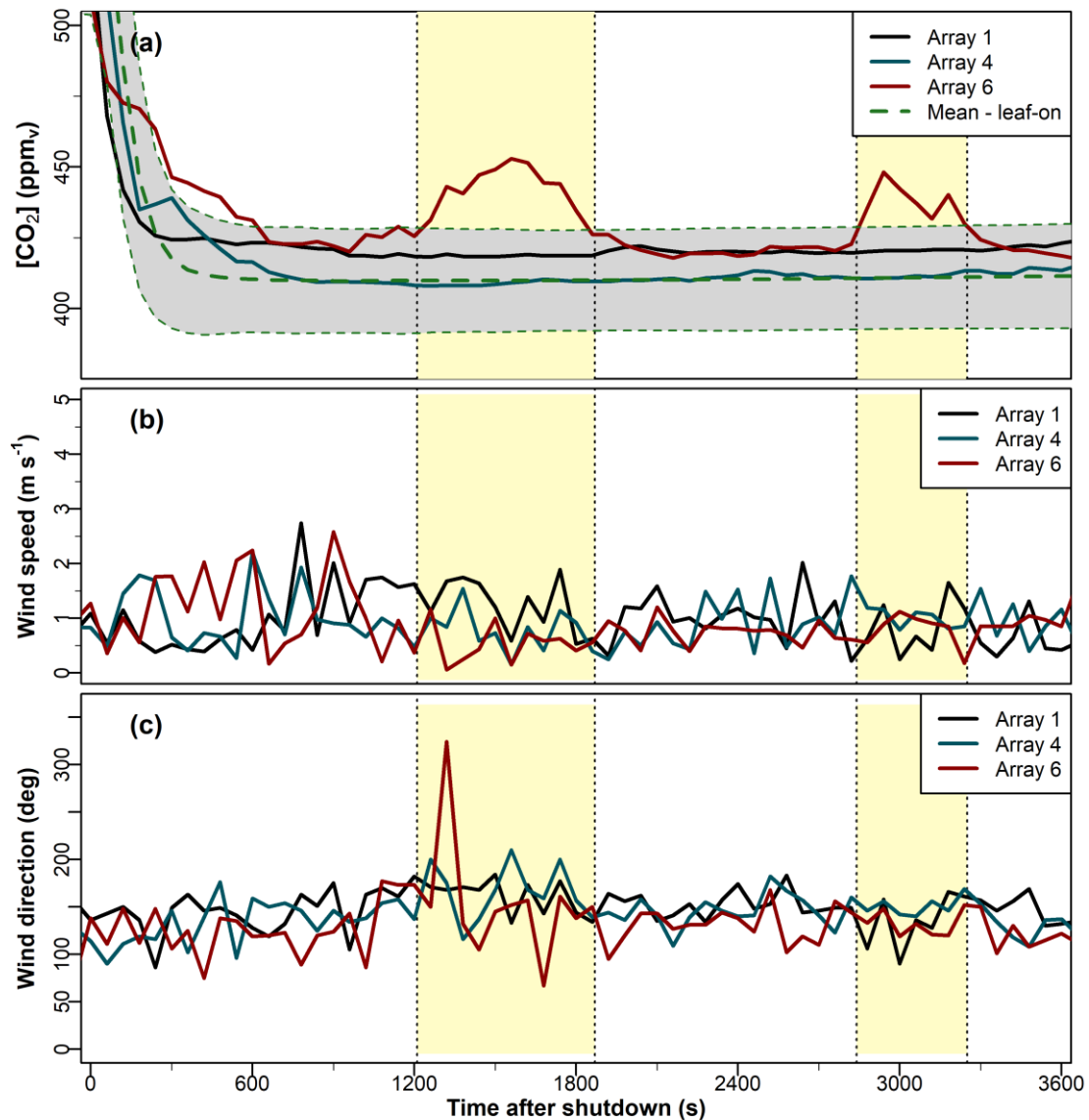
Inverse-gamma distributions are flexible and can fit observations from a variety of processes, without always reflecting the underlying physical mechanisms. However, surface-renewal theory (SRT) (Danckwerts 1951) offers a compelling analogy that warrants further testing with physical models or LES. SRT assumes the movement of individual fluid parcels near a surface may be represented as a stochastic process driven by a turbulent flow field away from the surface, which is comparable, at least conceptually, to air parcels moving to and from a porous forest canopy exposed to the open atmosphere. SRT has been used to estimate the fluxes of scalar quantities to and from forests (Paw U et al. 1995; Katul et al. 2013). Under certain SRT assumptions, it has been shown that residence times can be well approximated using distributions in the gamma family (Gon Seo and Kook Lee 1988; Haghghi and Or 2013, 2015; Katul and Liu 2017; Zorzetto et al. 2021). We hope a similar approach may be used to estimate α_s for other forest types, for example, by using LES to calculate τ across a variety of realistic forests (i.e., including openings, edges, and horizontally heterogeneous structure).

4375 We reiterate here that the above discussion does not include the effect of very strong winds on τ (see section 6.2.3), which also lends itself to further testing with LES. We expect α_s to increase slightly in strong winds, when the reconfiguration of tree crowns allows energetic gusts to penetrate further and more regularly into the forest canopy. The behaviour of τ across atmospheric stability regimes is more difficult to parametrise. We obtain good fits on both our leaf-on and leaf-off observations in unstable conditions using $\beta_s = 2h_c/w_*$ in Equation (6.7), where $w_* = (\overline{gw'T_s'}h_c/\overline{T_s})^{1/3}$, the Deardorff convective velocity scale (defined locally). However, we do not have sufficient spatial resolution in our observations to determine whether this result is robust across a range of unstable conditions, or whether it is just a consequence of the flexibility of the inverse-gamma distribution. In stable conditions, turbulence is dominated by turbulent structures that are intermittent in space and time. These intermittent structures can induce complex flow patterns that do not lend themselves to

scaling analysis. The following subsection discusses evidence of this complex behaviour and its implications for air-parcel residence times.

6.3.7 Longer residence times evidenced by evening venting events

On some evenings during the leaf-on period, we observed ‘bumps’ in the $[\text{CO}_2]$ timeseries shortly after fumigation was shut down, whereby the $[\text{CO}_2]$ decays to $a[\text{CO}_2]$, rises again by tens of $\mu\text{mol mol}^{-1}$ for several minutes, before decaying again to $a[\text{CO}_2]$. Figure 6.10 shows a representative example from 17 August 2020. Pools of CO_2 can accumulate naturally in forests, e.g., from soil respiration on calm, humid nights, creating anomalously high carbon flux values when the pools are vented from the canopy (Cook et al. 2004). The venting of natural pools typically occurs in the early hours of the morning, after the CO_2 has had time to accumulate in the stable nocturnal conditions (Cook et al. 2004), and can last for several hours. Here, the bumps occur shortly after shutdown, last for no more than a few minutes, and occur only in the fumigation arrays. We therefore believe these bump signals are evidence of the venting from the canopy of trapped fumigation CO_2 within the canopy, rather than of natural pools (although without isotope analysis it is not possible to conclude with absolute certainty). To investigate these bumps further, we filtered the data according to the following criteria: at least 15 minutes after the shutdown time, the $[\text{CO}_2]$ in one or more of the arrays rises by $\geq 15 \mu\text{mol mol}^{-1}$ from the $a[\text{CO}_2]$ for ≥ 3 minutes. These criteria are somewhat arbitrary but serve to distinguish the signal from the inevitable noise as the $[\text{CO}_2]$ decays to $a[\text{CO}_2]$. These criteria identified 41 days with bump events during the leaf-on period, from a total of 452 observation days (i.e., about 9% of the time). Using these criteria, no bumps occurred in the leaf-off period.



4405

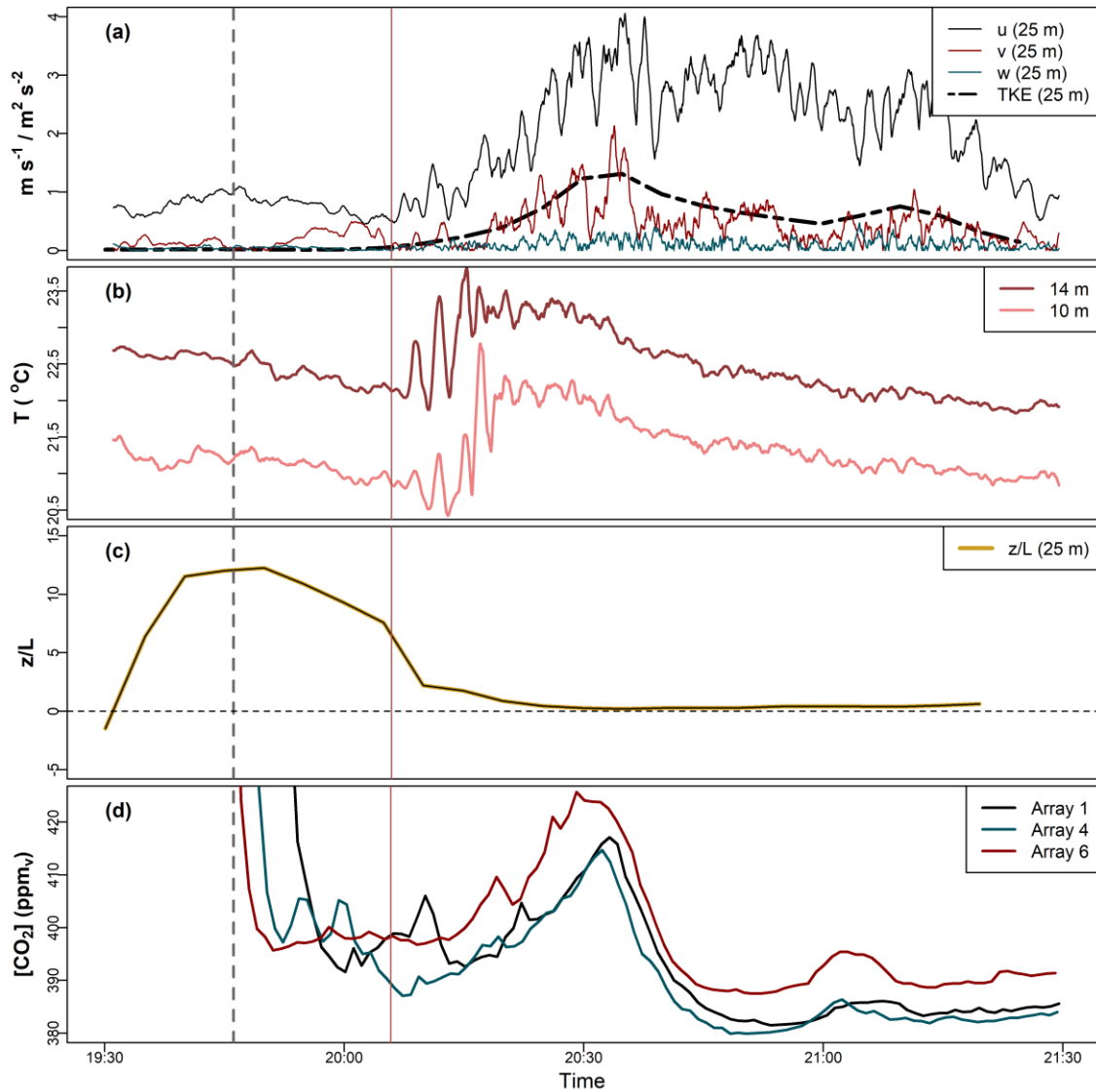
Figure 6.10: Timeseries of 1-minute averages in (a) the CO_2 mixing ratio, denoted $[\text{CO}_2]$ (section 6.2.1), (b) wind speed, and (c) wind direction after shutdown on 17 Aug 2020. In panel (a), the dashed green line shows the mean $[\text{CO}_2]$ at each 1-minute time step after shutdown for the leaf-on period (section 6.2.2 for observational details). The grey shaded confidence interval in (a) shows one standard deviation either side of the mean. The standard deviation is presented here to emphasise that these venting events are not simply symptoms of the variability of the $[\text{CO}_2]$ observations; on this dataset, it is larger than the other two measures of statistical dispersion used in this paper (the IQR and D_{med}). The shaded yellow rectangles indicate the approximate duration of the venting events.

4410

The bumps occurred only when wind speeds were low, all with $\bar{u} < 1.5 \text{ m s}^{-1}$ and typically with $\bar{u} < 1 \text{ m s}^{-1}$. This was a necessary but not sufficient condition; there were days with weak winds but no bump events in the $[\text{CO}_2]$ timeseries. These bump events may be caused by CO_2 -rich air being trapped within the dense canopy, particularly when the surrounding atmospheric conditions are very stable, which can occur on evenings with low winds and strong stratification from radiative cooling. The venting occurs when intermittent turbulent structures interact with the forest airspace (whose local stability may differ to that of the surrounding atmosphere). In very stable conditions, boundary-layer turbulence is intermittent in space and time, and may arise from with a variety of phenomena, such as differential heating, top-down turbulent bursts, or larger ‘submeso’ motions such as microfronts and short gravity waves (Mahrt 2014; Wharton et al. 2017). These turbulent structures tend to be highly localised, which could explain why the bumps in our timeseries rarely

4420

occurred in more than one array at any one time, even though they typically last for 10 minutes or so (Figure 6.10). Detecting intermittent turbulent structures around forests requires dense networks of 3D
 4425 anemometers throughout the canopy, which BIFoR FACE did not have for most of our investigation period (we have recently installed several anemometers within the forest for future investigations). However, on a few occasions, the meteorological towers around the edge of the forest were able to detect the presence of submeso structures.



4430 **Figure 6.11: Timeseries after shutdown on 27 Aug 2019 of (a) the magnitude of the velocity vector components (m s^{-1}) and TKE ($\text{m}^2 \text{s}^{-2}$) at $z = 25 \text{ m}$, (b) T ($^{\circ}\text{C}$), (c) z/L (where L is the Obukhov length, section 6.2.5), and (d) $[\text{CO}_2]$. The dashed grey vertical line indicates the shutdown time and the solid red line the approximate arrival time of the warm microfront described in the paragraph below. The high-resolution measurements in (a)–(c) are from on Met 1, at the southern edge of the BIFoR FACE facility (Figure 6.1 and section 6.2.1). (a) and (b) show 1-min rolling means.**
 4435

Figure 6.11 presents a case study from 27 August 2019, which was a warm, cloudless day with weak southerly winds. Around sunset, and therefore fumigation shutdown (marked with the dashed grey vertical line in Figure 6.11), the wind speed was very low—less than 1 m s^{-1} at $z = 25 \text{ m}$ at the forest edge (Figure 6.11a) and almost zero within the canopy. The TKE was close to zero (Figure 6.11a). A strong temperature inversion
 4440 formed (Figure 6.11b), with the temperature at $z = 25 \text{ m}$ a further few degrees warmer than at $z = 14 \text{ m}$ (not

shown). The air around the forest was very stable, with $z/L \approx 10\text{--}15$ (Figure 6.11c). Around 20 minutes after shutdown, a warm microfront reached the southern edge of the forest, marked with the solid vertical red line in Figure 6.11 and visible in a sharp increase in temperature near the ground (Figure 6.11b). The passage of a warm microfront leads to increased local wind speed and turbulent intensity, and decreased atmospheric stratification (Mahrt 2019). These changes can be seen in Figure 6.11a, where the horizontal wind speed and the TKE increase quickly, and Figure 6.11c, which shows the stability decaying quickly from very stable to approximately neutral (i.e., $z/L \approx 0$). The increased wind speed and turbulence cause trapped CO_2 to be vented from the forest in all the fumigation arrays (Figure 6.11d). As well as providing interesting micrometeorological case studies, these venting events provide observational evidence that air-parcel residence times can be much longer in stable evening conditions compared with the average daytime values, e.g., at least 20–30 minutes in the example in Figure 6.11 and nearly 60 minutes in the example in Figure 6.10.

6.4 Conclusions

Our opportunistic investigations of fumigation data from the BIFoR FACE facility provide the first observational evidence of air-parcel residence times in the upper canopy of a deciduous forest. Air-parcel residence times in the upper half of the forest canopy vary strongly with atmospheric stability, and their statistics differ significantly when the forest is in leaf compared to when it is not. Our dataset shows that air parcels in the BIFoR FACE facility have the following characteristics:

1. When the trees are in leaf, we found median daytime residence times, $\tilde{\tau}$, are around twice as long ($\tilde{\tau} \approx 70$ s) as when the trees are not in leaf ($\tilde{\tau} \approx 34$ s). The variability in the values of τ is over twice as large when the trees are in leaf versus when they are not in leaf, e.g., median absolute deviation, $D_{med} \approx 51$ s for leaf-on and $D_{med} \approx 20$ s for leaf-off.
2. For chemically reactive tracers, such as BVOCs, released in the upper canopy during daytime, our results suggest the molecules are unlikely to have time to react within the forest unless their reaction timescale is in the order of a few minutes or less.
3. Our results agree with Lagrangian modelling studies that the distributions of τ are strongly positively skewed (e.g., Figure 6.4). For these types of distributions, average values are not representative of the population as a whole. Where possible, future investigations should report the distributions of residence times, or at least a variability measure to accompany average values. Median values, accompanied by the interquartile range or D_{med} , are preferable to the mean and standard deviation because the former are more robust measures of highly positively skewed distributions.
4. The PDFs of residence times can be closely approximated using the inverse-gamma distribution. Models using eddy-diffusivity turbulence closure generate plausible average values but overestimate the probability of very long residence times in the upper canopy (i.e., the PDF tails are too heavy). We find the canopy turnover timescale, $\tau_c = h_c/u_*$, provides a good approximation for the scale parameter of the inverse-gamma distribution, with the shape parameter a function of the forest's structure. Although outside the scope of the present study, we suggest that careful testing using physical models

or LES will be able to generate robust residence time parametrisations based on simple gamma-like distributions, where the shape and rate/scale parameters can be estimated from variables such as the LAI or wind-velocity statistics, which are available at most forest research sites and, increasingly, at all forest locations from remote sensing.

5. Air-parcel residence times increase with greater stability, as does the variability in their values. In unstable conditions, long residence times are much less common than they are in near-neutral or stable conditions. In neutral and unstable conditions, the effect of turbulence levels on the residence times can be approximated $\tau \propto u_*^{-\gamma}$. Our data show $\gamma \approx 1$ in unstable and neutral conditions, but $\gamma \approx 0.8$ in stable conditions.

6. Very long residence times (tens of minutes to hours) can occur in the evening boundary-layer transition when the trees are in leaf. These are evidenced in our data by the venting of trapped CO₂ from the canopy long after FACE fumigation has been shut down for the day. This behaviour occurs on a little fewer than 10% of the days with suitable meteorology in our dataset. Cook et al. (2004) report nocturnal venting of pooled CO₂ over the course of several hours, which is different from what we see here. We are not aware of any other observational evidence of these brief evening venting events, which typically last around 5–20 minutes and are highly localised, usually in a single fumigation patch. The evening venting events occur only in low winds. We suspect they are evidence of the decoupled forest air space interacting with intermittent turbulent structures in very stable conditions. We found a single case study of a warm microfront, a type of ‘submeso’ atmospheric motion, causing venting of the forest air space, but the causes of the majority of venting events are not known.

7. The observation of these venting events, and the long residence times they imply, fits with previous field studies that nocturnal residence times are often in the order of several hours, rather than the few minutes typical of daytime values (Rummel et al. 2002; Martens et al. 2004). The stable boundary layer, particularly during the evening and at night, remains poorly understood. Further investigations of nocturnal residence times are needed to understand how physical processes determine in-canopy chemistry, e.g., the mixing ratios of monoterpenes in boreal forests are at their highest at night, but those for isoprene are at their lowest (Hakola et al. 2012). These investigations need to be centred around robust observations and physical experiments—nocturnal exchange is dominated by intermittent turbulence that is difficult to constrain in numerical models (Mahrt 2014; Sterk et al. 2016; Bannister et al. 2022).

Appendix 6A – Estimating K_{eq} in Equation (6.1)

A variety of methods can be used to estimate K_{eq} around vegetation (Monteith and Unsworth 2008; Haverd et al. 2009). We use GCF17’s simple parametrisation

$$K_{eq} = T_l g(LAI) u_* h_c, \quad (6A.1)$$

where h_c is the mean height of the canopy, u_* is the friction velocity measured at a height h_c , T_l is the Lagrangian integral timescale normalised by h_c/u_* , and $g(LAI)$ is a function that adapts the profile of the vertical velocity variance to the canopy structure such that

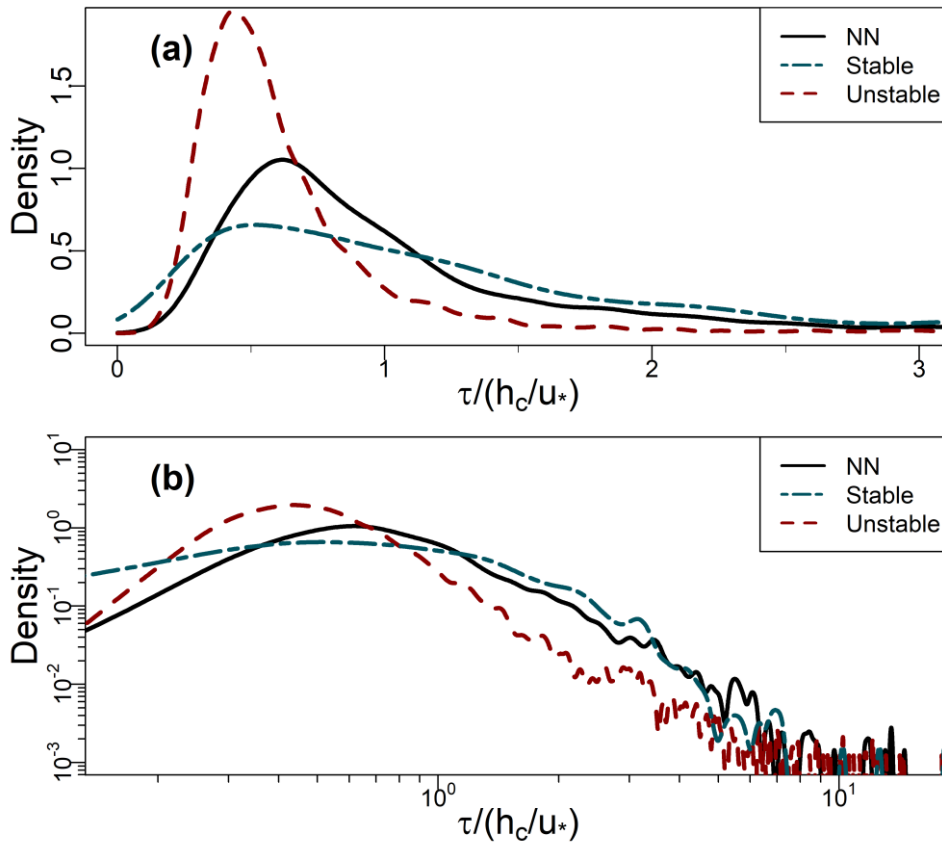
$$g(LAI) = c_1^2 \frac{2c_2 - 4 \exp(c_2) + \exp(2c_2) + 3}{2c_2(\exp(c_2) - 1)^2} \quad (6A.2)$$

4515 where c_1 and c_2 are modelling constants, with $c_1 = 0.9$ and $c_2 \approx -0.5-1.5$. GCF17 use $T_l u_*/h_c = 1/3$ from Raupach (1989), but we obtain better results on our data using the estimate of Haverd et al. (2009) such that

$$\frac{T_l u_*}{h_c} = c_4 \frac{1 - \exp\left(-\frac{c_3 z_{rel}}{h_c}\right)}{1 - \exp(-c_3)}, \quad (6A.3)$$

4520 where $c_3 = 4.86 \pm 1.52$ and $c_4 = 0.66 \pm 0.1$, which gives $T_l u_*/h_c \approx 0.6$. Taken together, these assumptions obtained $K_{eq} = 1.2 \text{ m}^2 \text{ s}^{-1}$, which was used in Equation (6.1) to generate the GCF17 PDF in Figure 6.3, for example.

Appendix 6B



4525 **Figure 6B.1:** (a) and (b) PDFs of residence times (section 6.2.3) binned by stability class for the leaf-off period (section 6.2.2), plotted on linear and logarithmic axes (base 10), respectively. NN denotes near-neutral conditions. See section 6.3.3.2 for definitions and Figure 6.7b, c for analogous results from the leaf-on period.

Chapter 7 – Conclusions and Further Work

Abstract. The first section of this chapter summarises the findings of this thesis, including a discussion of the work's main limitations. The second section of this chapter discusses the wider context of this work and provides recommendations for further research. As an illustrative example, the second section presents opportunistic experiments at BIFoR FACE, used to generate a rule-of-thumb for scalar transport through a forest.

7.1 Summary of findings and their limitations

The aim of this thesis was to investigate and narrow specific gaps and simplifications in our knowledge of turbulent exchange in the ABL. I paid particular attention to the transport of scalar quantities, such as pollutants and CO₂, in patchy inhomogeneous canopies, such as real-world forests and urban areas. I focussed mostly on spatial scales of metres to around a kilometre, over timescales of seconds to around an hour, which I refer to as the 'ecosystem scale' in the context of forests and other vegetated landscapes, and the 'neighbourhood scale' in the context of urban areas. The work in this thesis is most easily summarised by revisiting the objectives in Chapter 1, while keeping in mind the work's limitations.

7.1.1 Objective 1: Formulate and assess a model of flow over a spatially inhomogeneous urban area at the neighbourhood scale

Chapter 4 formulated a model of flow over an urban area by representing the buildings and other canopy obstacles elements in the urban area through a distributed momentum sink (i.e., as a porous medium), rather than attempting to resolve the obstacles directly. This is achieved by averaging the equations of motion over a volume that contains several obstacles, which amalgamates the drag force from each obstacle into a continuous drag force across the volume. This model, deployed with LES turbulence closure, meets Objective 1 by generating vertical profiles of selected flow statistics that compared well with published values from physical models and DNS. The main differences between the porous model and the published values occurred near the ground, where the porous model under-simulates turbulence intensity. Possible reasons for these differences include the surface parametrisation in the WRF LES, 'missing' turbulence being captured by the LES model's SGS scheme (only the resolved turbulence was included in the comparison), and over-estimation of turbulence in the published values, which mostly study flow around very simplified urban structures such as arrays of cuboids, and therefore may over-simulate structures such as reversed flow regions behind the bluff obstacles.

The key advantages of the porous medium model are that (i) it is simple enough to be deployed at the neighbourhood scale, using LES turbulence closure, generating robust flow statistics and (ii) it can be adjusted using a modest range of geometrical variables. Chapter 4 exploits the second point by simulating six different urban areas: a homogeneous case, where frontal-area density was uniform across the entire neighbourhood, and five cases with varying size patches of alternating high and low density. The main drawbacks of the porous-media method result from the representation of the urban form through distributed drag, specifically, with vertically constant values for the drag coefficient and the frontal-area density. This approach is likely to be a reasonable approximation for urban areas comprising vegetation and obstacles of various shapes and sizes (e.g., the Melbourne neighbourhood in Figure 7.1a). However, it would not be suitable for urban areas comprising

4565 buildings and little else, or neighbourhoods of large, irregular buildings, such as that in Figure 7.1b. In those cases, resolved-obstacle or street-canyon methods are likely to be more appropriate.



4570 **Figure 7.1:** (a) A neighbourhood in Melbourne, Australia comprising buildings of varying shapes and sizes and a large proportion of vegetation. (b) A neighbourhood in Nur-Sultan (formerly Astana), Kazakhstan in which the landscape is dominated by a relatively small number of large, irregularly shaped buildings. The urban form in (a) is likely to be much more amenable to that in (b) to the porous-media method in Chapter 4. The images in (a) and (b) are copyright of iStock and Getty Images, respectively.

4575 **7.1.2 Objective 2: Use the urban model with LES to investigate the transport of pollutants in a spatially inhomogeneous urban area**

Chapter 4 meets Objective 2 by simulating six urban neighbourhoods, five of which comprise patches of alternating high and low density that vary in size from four to sixteen times the mean height of the obstacles. On the basis of these results, I proposed two conceptual regimes of neighbourhood-scale flow that emerge from the interaction of the flow dynamics with the patch length L_p . The first is the *neighbourhood-ventilation regime*, which occurs in neighbourhoods whose frontal-area density varies in patches where $L_p > x_A$ (x_A is the adjustment distance of the mean flow). In these neighbourhoods, the mean streamwise velocity component adjusts to the change in density as the air moves between the patches. During this adjustment, a strong vertical velocity is induced over a distance for $x < x_A$, with a weak vertical velocity component for distances $x \gg x_A$. The second conceptual regime is the *neighbourhood-percolation regime*, which occurs in neighbourhoods whose frontal-area density varies in patches such that $L_p < x_A$. In these neighbourhoods, the patches are too small for the mean flow to adjust fully within each patch. The magnitude of the vertical velocity component around the top of the urban canopy is smaller.

The emergence of the percolation and ventilation regimes profoundly affects the distribution of pollutants, which were modelled as being passive, massless, and emitted uniformly across each neighbourhood. In neighbourhoods with the ventilation regime (i.e., where density changes in larger patches), the maximum pollutant concentrations occur in the dense patches, as intuition would have it. However, in neighbourhoods subject to the percolation regime (i.e., where density changes in small patches), the maximum pollutant concentrations occur in the sparse patches. The counter-intuitive behaviour arises in these neighbourhoods because turbulent exchange is suppressed in the dense patches. Pollutants therefore accumulate over the length of the dense patches and are advected into the neighbouring sparse patches. These arguments offer a quantitative estimate for what is often referred to as the ‘urban background’ in micrometeorological observations (e.g.,

DEFRA, 2022): point observations at a distance $x > x_A$ downstream of a density transition (in the direction of the prevailing wind) should represent pseudo-equilibria well.

4600

Now to limitations. The results in Chapter 4 are derived on an idealised version of the urban form. It is therefore easy to think of examples of urban areas where these results offer little information, e.g., where the neighbourhood comprises relatively small numbers of large, irregular buildings (see previous subsection), or when investigating a situation for which a neighbourhood spatial average is not very informative, such as
4605 investigating pollutant dispersion around a busy intersection surrounded by tall buildings. Even in cities where the model approximately applies, careful consideration of the local morphology and the behaviour of pedestrians is needed to assess the exposure of pedestrians to the emitted pollutants (Kingham et al. 2013; Tenailleau et al. 2015). An interesting line of further inquiry would be to investigate the effect of atmospheric stability on the results in Chapter 4, which considered only neutral conditions. Atmospheric stability can profoundly affect the
4610 flow, for example, in unstable conditions, scalars are transferred more efficiently with increasing instability (Belcher et al. 2012; Wang et al. 2014). Determining whether the flow regimes in Chapter 4 hold across stability classes would be useful for questions about scalar transport in porous media more generally. It would also inform our knowledge of pollutant transport in urban areas. In general, urban pollutant concentrations are higher and more sustained in stable atmospheric conditions because turbulent mixing is suppressed (Harrison 2018; Hu
4615 and Yoshie 2020). However, the effects of atmospheric stability on neighbourhood-scale processes are hard to determine from sparse networks of in situ sensors.

7.1.3 Objective 3: Review and synthesise current understanding of turbulent exchange around forests, with a particular focus on patchiness, real forest properties, and scalar quantities

Part I of Chapter 5 reviews and synthesises current understanding of exchange around forests, paying particular
4620 attention to patchiness, scalar transport, and other properties of real forests. The mixing-layer analogy—where shear generated eddies around the crown top dominate turbulent exchange—has proved remarkably robust in forests and other vegetation. However, the analogy assumes near-neutral conditions, with the dynamics controlled by the high shear in the mean wind velocity around the tops of the trees. In strongly stable or unstable conditions, the velocity shear can be much less influential. As the ABL becomes more unstable, the turbulence
4625 structure around forests transitions from a shear-driven to a convection-driven regime, i.e., thermal cells govern the flow dynamics, and the mixing-layer type turbulence becomes less prominent. Conversely, when the ABL is stable, the buoyancy of the air dampens vertical motion. Mixing-layer type coherent structures may still develop around a forest, but they are smaller and less energetic than those that form in near-neutral conditions.

Meteorologists and ecologists are often interested in the edges of forests, although the definition of an ‘edge’
4630 depends on the context. In aerodynamic applications, we can take ‘edges’ as the parts of the forest where momentum and scalar exchange is spatially and temporally variable, because the flow is adjusting to the forest’s presence. Using the concept of the adjustment distance x_A , Chapter 5 shows that edge effects dominate turbulent exchange in forest stands where $A < \sim 3000h_c^2$. Because forested areas are usually reported in hectares and canopy heights in meters, a dimensional version of this estimate is that edge effects dominate in forests where
4635 $A(ha) < 0.3[h_c(m)]^2$. Recent evidence shows that scalar transport does not necessarily follow the flow in realistic settings, meaning scalar quantities are rarely at equilibrium around patchy forests, and significant scalar fluxes may form in the lee of forested hills.

4640 Most numerical and observational studies of forests assume the landscapes to be horizontally homogeneous,
with closed canopies, no large patches or gaps, and do not include site specific morphological or ecological
detail. These assumptions are rarely realistic. For example, forests around the world are becoming increasingly
4645 fragmented. Edge regions differ from the forest interior both in their mean local climate and in the range of
meteorological extremes they experience. Even in intact ecosystems, most forest canopies comprise a patchwork
of openings of many shapes and sizes, formed by senescence, disease, and windthrow. These gaps are significant
ecologically and structurally. Chapter 5 proposes an approximation that openings with horizontal diameter
greater than the shear length scale ($O_d \geq L_s$) can be considered ‘gaps’, because they are likely to induce fluid
dynamical effects on the scale of the turbulence that dominates forest-atmosphere exchange. Openings where
 $O_d \ll L_s$ can be considered ‘pores’ in that they have only wake-scale effects on the flow and contribute little to
4650 the overall TKE budget.

7.1.4 Objective 4: Identify ways in which numerical models of forest-atmosphere exchange, especially LES models, can be made more realistic without compromising their ability to resolve turbulence

The three traditional pillars of ecosystem-scale micrometeorological investigations are observations, theory,
and physical models (Lemone et al. 2019; Brunet 2020). Over the past few decades, numerical models have
4655 become increasingly important in meteorology, and the three pillars are now very much a quartet. However, it
is currently unclear how much the models’ output can be trusted, particularly in heterogeneous landscapes and
non-neutral weather conditions. Numerical investigations usually simulate only a handful of ecological scalar
exchanges, assume neutral atmospheric conditions, and focus on forests whose structure has been ‘idealised’ in
some way. These simplifications are usually for good reason, for example, to reveal canonical processes rather
4660 than the idiosyncrasies of individual sites, or to reduce the dimensionality of investigations. However, forests
in the real world rarely resemble the neat approximations found in models.

Part II of Chapter 5 satisfies Objective 4 by discussing ways in which ecosystem-scale numerical models of
forest-atmosphere exchange can be made more realistic without compromising their ability to resolve
4665 turbulence. Due to computational expense, it is not practical to resolve directly the forest elements at the
ecosystem scale. Instead, Chapter 5 proposes ways to modify the transport equations to account efficiently for
patchy forests and moving plant elements. For example, one can account for the streamlining of plants in high
wind conditions by incorporating a ‘Vogel number’ into the parametrisation of the aerodynamic drag. Sub-grid
scale plant movement can be incorporated through poroelastic and mechanical parametrisations, or by including
4670 a stochastic forcing into the momentum equations at a frequency corresponding to plant movement. Terrestrial
laser scanning allows researchers to include detailed, site-specific morphological detail in their models, and
virtual canopy generators can be used to generate realistic forest canopies from a small number of structural
variables. The effects of non-neutral atmospheric conditions and other weather on forest-atmosphere exchange
are more difficult to constrain, and are active topics of research (see section 2 of this chapter, below). Numerical
4675 investigations of patchy vegetation canopies should include calculations of the dispersive fluxes. Real forests
channel air into gaps and patches, creating spatially coherent structures whose contributions can be as large as
those induced by turbulence. Ignoring these fluxes may mean ignoring over half of the total momentum flux.

Numerical models are at their most useful in fluid-flow research when they measure the unmeasurable—e.g.,
4680 calculating scalar fluxes in non-uniform terrain—or visualise the invisible—e.g., diagnosing coherent turbulent
structures that can be used to parametrise the flow. Here we encounter the circular limitation that these types of
models are difficult to test, because they are used to generate information that is unavailable from other methods.
Barring some great leap in our theoretical understanding, the only way around this limitation is the gradual
testing and refinement of numerical simulations against what can be measured by high-quality observations and
4685 physical models. Section 7.2.4 provides a specific example of how experiments of opportunity and targeted
observational campaigns may be used for this purpose. Another major limitation, common to all turbulent fluid
modelling, is computing capacity. For canopies in the ABL, a fine spatial resolution is needed to resolve the
dominant turbulent structures. Chapter 5 provides specific recommendations for LES models of forests—a
workhorse spatial resolution of $\Delta_x = \Delta_y \approx 5$ m, and $\Delta_z \approx 1$ m is a good first approximation, where Δ_i is the
4690 filter width in the i^{th} direction. LES models are therefore likely to remain viable only for relatively small
domains (a few square kilometres) for many years. Despite these constraints, computing capacity is expected to
increase with time for the foreseeable future. This raises the question of how the extra capacity should be used.
My opinion is that, for investigations of vegetation-atmosphere exchange, the additional computational capacity
4695 can be applied most productively (i) to increase the size of the simulated domain, (ii) to include a wider range
of physical and chemical processes, or (iii) to account for plant movement, rather than simply increasing the
grid resolution.

7.1.5 Objective 5: Use the observations from a free-air carbon dioxide enrichment (FACE) facility to investigate air-parcel residence times in a real forest, open to the atmosphere

Chapter 6 uses observations from the BIFoR FACE facility to conduct opportunistic investigations of air-parcel
4700 residence times, τ , in a mature, deciduous forest. This study used nearly 50 million FACE observations, and
several billion measurements from the meteorological towers. The results in Chapter 6 are among the very few
reported observational estimates of air-parcel residence times in forests. It is the first study to (a) use FACE
observations to investigate forest residence times and (b) to include detailed observational statistics of air-parcel
residence times. Chapter 6 shows that median daytime residence times in the tree crowns are twice as long when
4705 the trees are in leaf versus when they are not. Air-parcel residence times increase with greater atmospheric
stability, as does the variability around their central values. Very long residence times (tens of minutes to hours)
can occur in the evening boundary-layer transition when the trees are in leaf. These longer residence times are
evidenced by the sporadic and unpredictable venting of large volumes of pooled air during some calm evenings.
In neutral and unstable conditions, the effect of turbulence levels on the residence times can be approximated
4710 $\tau \propto u_*^{-\gamma}$, where $\gamma \approx 1$ in unstable and neutral conditions and $\gamma \approx 0.8$ in stable conditions. Probability density
functions (PDFs) of residence times can be closely approximated using the inverse-gamma distribution. The
canopy turnover timescale, $\tau_c = h_c/u_*$, provides a good estimate for the scale parameter of the inverse-gamma
distribution, with the shape parameter a function of the forest's structure.

4715 Chapter 6 calculates residence times from the FACE data using a mass balance approach. Each fumigated array
at BIFoR FACE is treated as a reservoir of 'additional' CO_2 , i.e., as a reservoir of air with a $[\text{CO}_2]$ that is elevated
compared to the ambient $[\text{CO}_2]$ ($a[\text{CO}_2]$; here the brackets denote the mixing ratio, as in Chapter 6). The
residence time represents the average time each additional molecule of CO_2 spends in the fumigated arrays
before it is transported out by turbulent and advective fluxes, or is taken up by the trees and other plants. As to

4720 the limitations, the FACE arrays have diameters of just over 30 m and are not closed at the sides. Air parcels
can therefore exit the arrays horizontally as well as vertically. Horizontal fluxes in vegetation are very difficult
to model or measure, and Chapter 6 does not attempt to quantify them. However, long-term analysis of the
BIFoR FACE observations shows contamination events between the arrays are rare and mostly small, usually
4725 occurring in strong winds. This suggests that, although the horizontal fluxes from the arrays are always non-
zero, they are likely small in conditions with weak advection. The investigation was therefore limited to low-
to-moderate wind speeds (taken as the lowest 50% of wind speeds). The effect of very strong winds on τ remains
untested. In strong winds, the reconfiguration of tree crowns likely allows energetic gusts to penetrate further
and more regularly into the forest canopy. The effects of the strongest winds therefore may not lend themselves
to scaling analysis, because the structure of the forest is not constant. However, the inverse-gamma distribution
4730 is probably flexible enough to account for quite strong winds, by modifying the shape parameter. Chapter 6 uses
long-term observations, but is limited to a single research site. The method is amenable to testing using
observations from other FACE facilities, most notably those from EucFACE (see Chapter 3), which has a similar
experimental setup to BIFoR FACE but in a different forest ecosystem.

7.2 Recommendations for further work

4735 To provide context and non-exhaustive recommendations, it is helpful to consider the two broad goals of
ecosystem-scale micrometeorological research. The first goal is furthering our understanding of the
microclimates and flow dynamics of cities, forests, and other vegetation canopies. This research is motivated
by a wide range of problems, from fundamental questions in fluid dynamics, to applied questions in pollution
transport, ecology, and agricultural science. The second goal is connecting the meteorological microscale to
4740 larger scales, principally to improve parametrisations in operational forecast models and GCMs.

7.2.1 Micrometeorological research

There are few public datasets against which numerical models can be tested. The ability of turbulence-resolving
models to simulate scalar transport in urban areas, forests, and crops therefore remains poorly understood. More
field measurements are needed, especially of scalar quantities such as pollutants, CO₂, water vapour, and
4745 bioaerosols. Some of these quantities are already measured extensively, e.g., for pollution monitoring or at
ecosystem-exchange sites, but usually at a single spatial point and not always at sufficient time resolutions to
test turbulence-resolving models. Targeted observational campaigns using grids of sensors at various heights
would be the best way to fill this knowledge gap (e.g., Arnold et al., 2004; Bohnenstengel et al., 2015; Patton
et al., 2011; Wood et al., 2007). Alongside dedicated campaigns, I recommend that the community also exploits
4750 the extensive timeseries generated by existing eddy-covariance and FACE facilities, for example, by comparing
ensembles of models to ensembles of real-world observations, or by using geometric analysis to study the
statistics of turbulent structures (Belušić and Mahrt 2012; Kang 2015; Chen et al. 2019b).

Further research is needed into the effect of intermediate-scale motions on land-atmosphere exchange. These
4755 are motions, often called ‘submeso’ motions in the literature, with length scales larger than those typical of
turbulence, but smaller than the mesoscale and synoptic scales of operational forecasts. Submeso motions are
difficult to measure because they often manifest as turbulent bursts, intermittent in space and time (Kang et al.
2015; Mahrt 2019). They are also difficult to model because they do not result from mixing-layer eddies, and

therefore must be generated by other means, such as through micro-mesoscale coupling or synthetic turbulence. Submeso motions are important because they are common in the atmospheric conditions that tend to be most problematic for eddy-covariance ecosystems measurements, such as during stable nights. Discounting their effect introduces an unwelcome bias into assessments of land-atmosphere exchange. The time evolution of submeso motions is not well understood—tracking them requires a detailed spatial network of instruments. I also believe we need measurements collected over deep layers in stable ABL conditions to examine the momentum disturbances that create submeso motions. The effect of precipitation on canopy-atmosphere exchange has been a topic of recent research activity in urban areas (Liang et al. 2015; Kleine Deters et al. 2017; Lin et al. 2018b; Zalakeviciute et al. 2018), but the effects are not well documented in vegetation. Rainfall, for example, is a significant source of momentum into vegetation, affecting a variety of ecological processes, as well as the plants’ biomechanical response to the flow of air. Given that much of the world’s vegetated area is situated in climates where precipitation is common, wet conditions provide an important unexplored area for further work.

7.2.2 Connecting the microscale to larger scales

The difficulties in parametrising and coupling canopy processes to larger scales is well documented for urban areas (e.g., Grimmond et al., 2010, 2011; Silveira et al., 2019; Xie, 2011) and of increasing interest in vegetation (Bonan et al. 2018, 2021). Chapter 5 makes some specific recommendations for forested landscapes, which I won’t duplicate here. An interesting related line of further enquiry, whose details are beyond the scope of this thesis, concerns the use of ‘inexact’ computing to simulate a greater range of time and space scales, but with less accuracy and precision (Düben et al. 2014; Palmer 2015). Although it is technically viable to build computers powerful enough to resolve processes below the grid scale of operational forecasts—e.g., canopy processes or thunderstorms—the electricity consumption and expense of such computers would be prohibitively high. Instead, one could acknowledge that atmospheric simulation is inherently probabilistic, because of practical insolubility of the Navier–Stokes equations. This allows researchers to trade a certain amount of accuracy and precision of the computations in exchange for significant savings in power consumption and/or computing performance. This saving is achieved at the hardware level by making the calculations partially stochastic, or by reducing the number of bits used to represent individual pieces of information. Initial tests of this idea on simplified dynamical systems are promising (Düben et al. 2014; Düben and Dolaptchiev 2015). I recommended that researchers test inexact computing hardware in ABL-canopy applications, where it could be used to resolve submeso motions, while still approximating the complexity of the flow within and around the canopy.

7.2.3 A case for empiricism in investigations of canopy-atmosphere exchange

I end these recommendations with a short argument in favour of empiricism in numerical investigations of canopy-atmosphere exchange. I use ‘empiricism’ in this subsection in the colloquial sense of solving problems using parsimonious solutions, obtained by analysing experimental data. I provide a supporting example in the final subsection. This section is not a criticism of more formal arguments, e.g., proceeding from the Navier–Stokes equations. Theory, experiments, and approximations coexist and co-depend to some extent in all scientific disciplines, and they are completely intertwined in meteorology (Stull 1988; Kaimal and Finnigan 1994). I should therefore explain what I mean.

4800 Outstanding problems in atmospheric science are usually framed with the assumption that we know the
equations we wish to solve, but we are not yet able to solve them with the accuracy and precision that we would
like. For certain applications, particularly away from the Earth's surface, this assumption is correct. However,
it is very much a physicist's perspective—equivalent equations for biological and ecological exchanges, if they
exist, are much less clear. In many surface landscapes, particularly those with lots of living matter, it is not
possible to model all of the processes completely, even with unlimited computing power. Numerical models of
4805 surface-layer exchanges, across all time and space scales, need approximations and parametrisations. My call
for empiricism is essentially a call that these approximations should be based preferentially on experiments,
rather than on theory. I consider that this is particularly important for scalar quantities, whose statistics are
currently poorly understood and do not always correspond to those of momentum (Shrimalman and Siggia 2000;
Belcher et al. 2012; Katul et al. 2013; Li and Bou-Zeid 2019).

4810 Ideally, the experiments should be specific to the task at hand, e.g., arrays of sensors deployed across different
forest ecosystems, or around busy traffic intersections in different cities. Practical constraints mean that these
dedicated studies will be infrequent, and will probably involve lead times of several years. To supplement
targeted investigations, I recommend that researchers also revisit existing experimental datasets, which may
4815 involve interpreting observations that were originally envisaged for a different purpose. For example, Chapter
6 uses FACE observations to develop a new parametrisation of air-parcel residence times in forest canopies.
Existing infrastructure in the open atmosphere may also be used creatively to extend theoretical models, as
shown in the final subsection.

7.2.4 Illustrative example: using opportunistic experiments to extend existing theory

4820 Micrometeorological measurements in forests typically consist of point observations of the wind velocity
components, occasionally in conjunction with observations of scalar quantities such as temperature, trace gases,
or aerosol particles. Scalar quantities are seldom measured at more than one horizontal location at permanent
research sites. It would therefore be useful if we had a rule-of-thumb that we can use to estimate how quickly
air parcels or scalar quantities are transported across a forest, e.g., to understand the transport of fungal spores
4825 within the forest, or pollution encroaching from outside. Such a rule is not easy to obtain using conventional in
situ observations.

7.2.4.1 Advection-speed approximation

In dense forests, the mean streamwise wind speed \bar{u} inflects around the tops of the trees, increasing
approximately exponentially with height below the inflection and logarithmically with height above it (Cionco
4830 1965; Raupach et al. 1996; Finnigan 2000). Below the main crown, a secondary wind-speed maximum may
occur (Shaw 1977), especially around the edges of forests with open trunk spaces (Dupont et al. 2011). The
source of this secondary maximum is not certain, although it may result from the turbulent transport of
momentum from the upper canopy (Shaw 1977) or mesoscale pressure gradients (Holland 1989). To derive a
an approximate lower bound for the mean wind speed, we ignore cases where a secondary maximum occurs.
4835 This is likely a reasonable assumption in many forests, such as the deciduous temperate forest at BIFoR FACE,
which have almost closed edges and dense understories. An approximate lower estimate for \bar{u} at each height z
within the forest can be approximated as

$$\bar{u}(z) = \bar{u}_{h_c} e^{-a_c \left(1 - \frac{z}{h_c}\right)} \quad (7.1)$$

where h_c is the mean height of the trees and \bar{u}_{h_c} is \bar{u} at $z = h_c$ (Campbell and Norman 1998). The attenuation
 4840 coefficient, a_c , accounts for the flow's response to the structure of the forest, taking typical values of 2–5.5 for
 mature forests (Cionco 1978). In Baird et al. (2022), I used this model in Monte-Carlo simulations to estimate
 the statistics of spore movement at BIFoR FACE (Appendix A). Rearranging Equation (7.1) slightly gives a
 non-dimensional lower estimate of the mean wind speed, \bar{u}_n , at each height,

$$\bar{u}_n = \frac{\bar{u}(z)}{\bar{u}_{h_c}} = e^{-a_c \left(1 - \frac{z}{h_c}\right)}. \quad (7.2)$$

4845 7.2.4.2 Opportunistic ‘pulse and trace’ experiments

During normal operation, the BIFoR FACE infrastructure maintains an elevated $[\text{CO}_2]$ in each of the fumigation
 arrays during daylight hours. I used the FACE infrastructure outside its usual purpose by releasing sustained
 pulses of CO_2 -rich air¹⁰ from a small number of points on a single array. I then used the FACE sensors to track
 the movement of the pulses across the forest. I performed the pulse experiments in both the leaf-off and leaf-on
 4850 periods, on days such that the local meteorological conditions allowed the orientation of the FACE infrastructure
 to capture the movement of the pulses. This approach is analogous to monitoring the passage of chemical or
 particle plumes, which is well documented in the literature relating to urban air quality (e.g., Belcher, 2005;
 Philips et al., 2013; Wang et al., 2006). Researchers have investigated tracer plumes or pulses in forested
 environments, for example, in investigations of chemical signalling (Murlis et al. 2000), water-vapour transport
 4855 (Jiménez-Rodríguez et al. 2021), and the transport of smoke from forest fires over large areas (Goodrick et al.
 2013; Vaughan et al. 2018). This is the first report of the pulse and trace approach being used to investigate
 microscale transport in a forest.

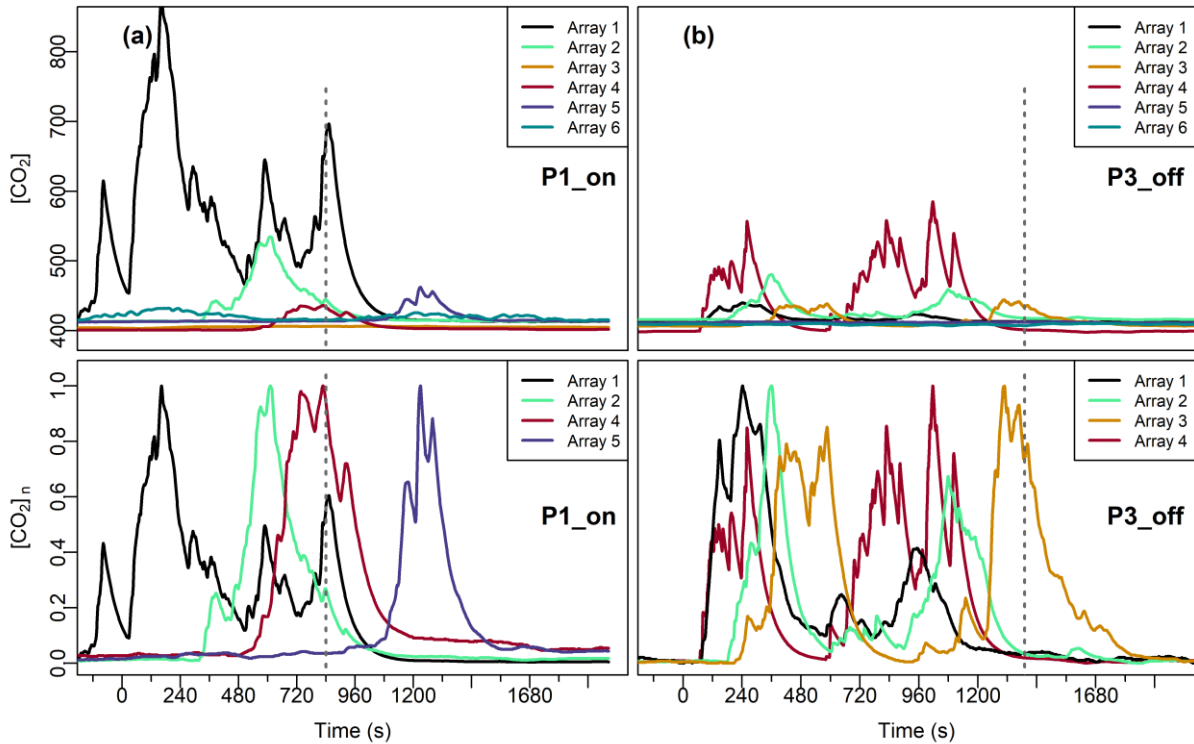
Table 7.1 presents the details of the pulses, including the meteorological conditions at the release arrays. I
 4860 performed the leaf-on experiment on 7 October 2020, after normal fumigation shutdown. Two pulses were
 released, denoted P1_on and P2_on, respectively, where ‘on’ refers to the leaf-on period. The wind direction
 was approximately southerly. The pulses were therefore released from the southern edge of Array 1, so that the
 wind carried the CO_2 -rich air north across the forest. The evening was mostly dry, although there was a brief
 rain shower just before P2_on. Atmospheric conditions were neutral to weakly stable.

4865 I performed the leaf-off experiment on 22 March 2021 during daylight hours (the site is not fumigated in March).
 Four pulses were released (denoted P_i _off, where $i = 1-4$ and ‘off’ refers to the leaf-off period.) The wind
 direction was north-westerly, and the pulses were therefore released from the north-west edge of Array 4.
 Conditions were dry. Atmospheric conditions were weakly unstable. All the pulses—in both seasons—were
 4870 released from four standing towers, spaced around a metre apart from one another, on the edge of the release
 array.

¹⁰ BIFoR FACE does not have sensors to measure the mixing ratio of the CO_2 -rich air at the moment of release. However,
 the flow rate was well over 1000 kg (CO_2) hr^{-1} , which is typically only required in strong winds to maintain the usual
 elevated $[\text{CO}_2]$ of 550 $\mu\text{mol mol}^{-1}$ at BIFoR FACE. The mixing ratio of the air was therefore probably high given that
 winds were quite light on the days of the pulses, say, 1000–2000 $\mu\text{mol mol}^{-1}$ at the moment of release.

Table 7.1: Details of the pulse and trace experiments. Mean wind speed, wind direction, and air temperature are calculated from measurements in the release arrays. In the seventh column, z/L is the dimensionless Monin–Obukhov stability ratio, where L is the Obukhov length. The ratio is calculated using observations from the meteorological towers nearest to the release arrays, respectively Met 1 and Met 4 for the leaf-on and leaf-off pulses. \bar{p}_n refers to a normalised pulse advection speed, as defined in the main text.

Pulse	Datetime (UTC)	Release Array	Wind speed \bar{u}_{h_c} (m s ⁻¹)	Wind Direction (deg)	T (°C)	z/L	Detection array; time taken from release to first detection (s)	Distance from release array to detection array (m)	Estimate of \bar{p}_n
P1_on	2020-10-07 18:22–18:36	1	1.1	163	10.3	≈ 2	Array 2; 317	105	0.30
							Array 4; 567	184	0.30
							Array 5; 915	168	0.17
P2_on	2020-10-07 19:06–19:39	1	1.7	172	10.4	≈ 0.5	Array 5; 365	168	0.27
P1_off	2021-03-22 11:06–11:27	4	3.3	306	7.5	≈ -1	Array 1; 151	184	0.37
							Array 2; 82	93	0.34
P2_off	2021-03-22 11:52–12:11	4	2.7	284	8.3	≈ -2	Array 1; 314	184	0.22
							Array 2; 105	93	0.33
							Array 5; 1164	98	0.03
P3_off	2021-03-22 12:26–13:19	4	2.6	310	9.2	≈ -2	Array 1; 75	184	0.94
							Array 2; 179	93	0.20
							Array 3; 242	143	0.23
P4_off	2021-03-22 13:44–14:04	4	2.2	317	9.4	≈ -2.5	Array 1; 283	184	0.30
							Array 2; 176	93	0.24
							Array 3; 190	143	0.34



4880 **Figure 7.2:** (a) $[\text{CO}_2]$ timeseries for P1_on; and (b) P3_off (see above in section 7.2.4.2 and Table 7.1). On the time axis, 0 corresponds to the beginning of each pulse. The dashed grey line indicates the time at which the pulse was stopped. In the lower panels, the y-axis is normalised so that the signal is expressed as a proportion of the maximum $[\text{CO}_2]$ recorded at $z \approx 24$ m for each array during each pulse. The release arrays for the leaf-on and leaf-off experiments were, respectively, Arrays 1 and 4.

4885 Figure 7.2 presents the $[\text{CO}_2]$ timeseries for (a) P1_on and (b) P3_off. The figures for the other four pulses are omitted here to avoid repetition. On the time axis, 0 corresponds to the beginning of each pulse. The dashed grey line indicates the time at which the pulse was stopped. In the lower panels, the y-axis is normalised so that the signal is expressed as a proportion of the maximum $[\text{CO}_2]$ recorded in each array during each pulse. We observe peaks in the $[\text{CO}_2]$ in the release arrays shortly after $t = 0$. In Figure 7.2a, there is a smaller peak just before $t = 0$ where the infrastructure was tested before the first pulse, P1_on. A short time later, peaks in the $[\text{CO}_2]$ appear in the timeseries for the other arrays as the CO_2 -rich air is transported across the forest. The time taken depends on the wind speed and direction, and the distance of the detecting array from the release array, as discussed in the next subsection. Even in these simple examples, we see evidence of the flow's complexity. In Figure 7.2, the $[\text{CO}_2]$ is highly variable even in the release arrays, despite the flow rate into the array being almost constant. This fluctuation is probably because of localised shifts in wind direction, and eddies of varying $[\text{CO}_2]$ moving past the sensors in the middle of the arrays. We also see inconsistent signals in the detection arrays, consisting of spikes in the $[\text{CO}_2]$ followed by an exponential decay, rather than sustained elevated $[\text{CO}_2]$ values.

4895

7.2.4.3 Comparison of the mean wind speed and pulse advection speed

4900 Table 7.1 lists the arrays in which each pulse was detected by the 1 Hz sensors mounted at $z \approx 20\text{--}23$ m on the central tower of each array. The ‘time taken from release to first detection’ is the time difference between the beginning of each pulse and the first non-trivial increase in the $[\text{CO}_2]$ at any of the other arrays. Here, ‘non-trivial’ means an increasing sequence in an array’s $[\text{CO}_2]$ timeseries that resulted in a $[\text{CO}_2] > a[\text{CO}_2]$ by at least

15 $\mu\text{mol mol}^{-1}$. In Table 7.1, the mean pulse advection speed \bar{p} is taken as the distance between the release and detection arrays divided by the time taken from release to first detection. The normalised pulse
4905 advection speed $\bar{p}_n = \bar{p}/\bar{u}_{h_c}$.

Using Equation (7.2), at a height of 16 m in a mature forest canopy of $h_c = 25$ m, we expect $\bar{u}_n \approx 0.15\text{--}0.5$ (16 m is a good estimate of the mean release height of the pulses). This range is similar to the normalised speed of the pulses through the canopy of the woodland, for which the mean and median values of $\bar{p}_n \approx 0.3$ (also at
4910 $z \approx 16$ m). Only the minimum and maximum values of \bar{p}_n (0.03 and 0.94, respectively) fell outside the expected range $\bar{u}_n \approx 0.15\text{--}0.5$. These results tentatively suggest that $\bar{u}_n \approx \bar{p}_n$, i.e., that pulses/plumes of scalar quantities in forest crowns appear to be transported on the mean flow, to a first-order approximation. The limited sample size of this experiment means one should be cautious about over-generalising this finding. However, it shows that established theory may be extended using contemporary experimental equipment, provided that researchers
4915 are willing to revisit material that is ‘well-known’.

References

- Ahmad K, Khare M, Chaudhry KK (2005) Wind tunnel simulation studies on dispersion at urban street canyons and intersections - A review. *J Wind Eng Ind Aerodyn* 93:697–717.
4920 <https://doi.org/10.1016/j.jweia.2005.04.002>
- Alekseychik P, Mammarella I, Launiainen S, et al (2013) Evolution of the nocturnal decoupled layer in a pine forest canopy. *Agric For Meteorol* 174–175:15–27. <https://doi.org/10.1016/j.agrformet.2013.01.011>
- Amiro BD (1990a) Drag coefficients and turbulence spectra within three boreal forest canopies. *Boundary-Layer Meteorol* 52:227–246. <https://doi.org/10.1007/BF00122088>
- 4925 Amiro BD (1990b) Comparison of turbulence statistics within three boreal forest canopies. *Boundary-Layer Meteorol* 51:99–121. <https://doi.org/10.1007/BF00120463>
- Antoniou N, Montazeri H, Wigo H, et al (2017) CFD and wind-tunnel analysis of outdoor ventilation in a real compact heterogeneous urban area: Evaluation using “air delay.” *Build Environ* 126:355–372. <https://doi.org/10.1016/j.buildenv.2017.10.013>
- 4930 Apel EC, Riemer DD, Hills A, et al (2002) Measurement and interpretation of isoprene fluxes isoprene, methacrolein, and methyl vinyl ketone mixing ratios at the PROPHET site during the 1998 intensive. *J Geophys Res Atmos* 107:1–15. <https://doi.org/10.1029/2000jd000225>
- Arnold SJ, Apsimon H, Barlow J, et al (2004) Introduction to the DAPPLE Air Pollution Project. *Sci Total Environ* 332:139–153. <https://doi.org/10.1016/j.scitotenv.2004.04.020>
- 4935 Arthur RS, Mirocha JD, Lundquist KA, Street RL (2019) Using a canopy model framework to improve large-eddy simulations of the neutral atmospheric boundary layer in the weather research and forecasting model. *Mon Weather Rev* 147:31–52. <https://doi.org/10.1175/MWR-D-18-0204.1>
- Ashcroft MB, Gollan JR, Ramp D (2014) Creating vegetation density profiles for a diverse range of ecological habitats using terrestrial laser scanning. *Methods Ecol Evol* 5:263–272. <https://doi.org/10.1111/2041-210X.12157>
- 4940 Ashton N, West A, Lardeau S, Revell A (2016) Assessment of RANS and DES methods for realistic automotive models. *Comput Fluids* 128:1–15. <https://doi.org/10.1016/j.compfluid.2016.01.008>
- Ashworth K, Chung SH, Griffin RJ, et al (2015) FORest Canopy Atmosphere Transfer (FORCAsT) 1.0: A 1-D model of biosphere-atmosphere chemical exchange. *Geosci Model Dev* 8:3765–3784. <https://doi.org/10.5194/gmd-8-3765-2015>
- 4945 Aubinet M (2008) Eddy covariance CO₂ flux measurements in nocturnal conditions: An analysis of the problem. *Ecol Appl* 18:1368–1378. <https://doi.org/10.1890/06-1336.1>
- Aubinet M, Feigenwinter C, Heinesch B, et al (2010) Direct advection measurements do not help to solve the night-time CO₂ closure problem: Evidence from three different forests. *Agric For Meteorol* 150:655–664. <https://doi.org/10.1016/j.agrformet.2010.01.016>
- 4950 Aubinet M, Heinesch B, Yernaux M (2003) Horizontal and vertical CO₂ advection in a sloping forest. *Boundary-Layer Meteorol* 108:397–417. <https://doi.org/10.1023/A:1024168428135>
- Aylor DE, Flesch TK (2001) Estimating spore release rates using a Lagrangian stochastic simulation model. *J Appl Meteorol* 40:1196–1208. [https://doi.org/10.1175/1520-0450\(2001\)040<1196:ESRRUA>2.0.CO;2](https://doi.org/10.1175/1520-0450(2001)040<1196:ESRRUA>2.0.CO;2)
- 4955 Bailey BN, Stoll R (2016) The creation and evolution of coherent structures in plant canopy flows and their role in turbulent transport. *J Fluid Mech* 789:425–460. <https://doi.org/10.1017/jfm.2015.749>
- Bailey BN, Stoll R, Pardyjak ER, Mahaffee WF (2014) Effect of vegetative canopy architecture on vertical transport of massless particles. *Atmos Environ* 95:480–489. <https://doi.org/10.1016/j.atmosenv.2014.06.058>
- 4960 Baird AB, Bannister EJ, MacKenzie AR, Pope FD (2022) Mass concentrations of autumn bioaerosol in a mature temperate woodland Free Air Carbon Dioxide Enrichment (FACE) experiment: investigating the role of meteorology and carbon dioxide levels. *Biogeosciences*. <https://doi.org/https://doi.org/10.5194/bg-2021-162>
- Baker CJ (2007) Wind engineering-Past, present and future. *J Wind Eng Ind Aerodyn* 95:843–870. <https://doi.org/10.1016/j.jweia.2007.01.011>
- 4965 Baldocchi DD (2014) Measuring fluxes of trace gases and energy between ecosystems and the atmosphere - the state and future of the eddy covariance method. *Glob Chang Biol* 20:3600–3609. <https://doi.org/10.1111/gcb.12649>
- Baldocchi DD (2008) TURNER REVIEW No. 15. “Breathing” of the terrestrial biosphere: Lessons learned

- 4970 from a global network of carbon dioxide flux measurement systems. *Aust J Bot* 56:1–26.
<https://doi.org/10.1071/BT07151>
- Baldocchi DD, Falge E, Gu L, et al (2001) FLUXNET: A New Tool to Study the Temporal and Spatial Variability of Ecosystem-Scale Carbon Dioxide, Water Vapor, and Energy Flux Densities. *Bull Am Meteorol Soc* 82:2415–2434. [https://doi.org/10.1175/1520-0477\(2001\)082<2415:FANTTS>2.3.CO;2](https://doi.org/10.1175/1520-0477(2001)082<2415:FANTTS>2.3.CO;2)
- 4975 Baldocchi DD, Hicks BB, Meyers TP (1988) Measuring biosphere-atmosphere exchanges of biologically related gases with micrometeorological methods. *Ecology* 69:1331–1340.
<https://doi.org/10.2307/1941631>
- Banerjee T, De Roo F, Mauder M (2017) Connecting the failure of K theory inside and above vegetation canopies and ejection-sweep cycles by a large-eddy simulation. *J Appl Meteorol Climatol* 56:3119–3131. <https://doi.org/10.1175/JAMC-D-16-0363.1>
- 4980 Banerjee T, Katul G, Fontan S, et al (2013) Mean Flow Near Edges and Within Cavities Situated Inside Dense Canopies. *Boundary-Layer Meteorol* 149:19–41. <https://doi.org/10.1007/s10546-013-9826-x>
- Bannister EJ, Cai X, Zhong J, MacKenzie AR (2021) Neighbourhood-scale flow regimes and pollution transport in cities. *Boundary-Layer Meteorol* 179:259–289
- 4985 Bannister EJ, MacKenzie AR, Cai X -M. (2022) Realistic forests and the modeling of forest–atmosphere exchange. *Rev Geophys* 60:1–47. <https://doi.org/10.1029/2021rg000746>
- Barbano F, Brattich E, Di Sabatino S (2021) Characteristic Scales for Turbulent Exchange Processes in a Real Urban Canopy. *Boundary-Layer Meteorol* 178:119–142. <https://doi.org/10.1007/s10546-020-00554-5>
- Barlow JF (2014) Progress in observing and modelling the urban boundary layer. *Urban Clim* 10:216–240.
<https://doi.org/10.1016/j.uclim.2014.03.011>
- 4990 Bash JO, Walker JT, Katul GG, et al (2010) Estimation of in-canopy ammonia sources and sinks in a fertilized zea mays field. *Environ Sci Technol* 44:1683–1689. <https://doi.org/10.1021/es9037269>
- Basu S, Porté-Agel F (2006) Large-eddy simulation of stably stratified atmospheric boundary layer turbulence: A scale-dependent dynamic modeling approach. *J Atmos Sci* 63:2074–2091.
<https://doi.org/10.1175/JAS3734.1>
- 4995 Batchelor GK (1953) *The Theory of Homogeneous Turbulence*. Cambridge University Press, Cambridge, UK
- Batista CE, Ye J, Ribeiro IO, et al (2019) Intermediate-scale horizontal isoprene concentrations in the near-canopy forest atmosphere and implications for emission heterogeneity. *Proc Natl Acad Sci U S A* 116:19318–19323. <https://doi.org/10.1073/pnas.1904154116>
- 5000 Bear J, Bachmat Y (1990) *Introduction to Modeling of Transport Phenomena in Porous Media*. Kluwer Academic Publishers, Dordrecht, The Netherlands
- Belcher SE (2005) Mixing and transport in urban areas. *Phil Trans R Soc A* 363:2947–2968.
<https://doi.org/10.1098/rsta.2005.1673>
- Belcher SE, Harman IN, Finnigan JJ (2012) The Wind in the Willows: Flows in Forest Canopies in Complex Terrain. *Annu Rev Fluid Mech* 44:479–504. <https://doi.org/10.1146/annurev-fluid-120710-101036>
- 5005 Belcher SE, Jerram N, Hunt JCR (2003) Adjustment of a turbulent boundary layer to a canopy of roughness elements. *J Fluid Mech* 488:369–398. <https://doi.org/10.1017/S0022112003005019>
- Belušić D, Mahrt L (2012) Is geometry more universal than physics in atmospheric boundary layer flow? *J Geophys Res Atmos* 117:1–10. <https://doi.org/10.1029/2011JD016987>
- 5010 Bergen JD (1975) Air Movement in a Forest Clearing as Indicated by Smoke Drift. *Agric For Meteorol* 15:165–179
- Blocken B (2018) LES over RANS in building simulation for outdoor and indoor applications: A foregone conclusion?
- Blocken B (2014) 50 years of Computational Wind Engineering: Past, present and future. *J Wind Eng Ind Aerodyn* 129:69–102. <https://doi.org/10.1016/j.jweia.2014.03.008>
- 5015 Blunn LP, Coceal O, Nazarian N, et al (2022) Turbulence Characteristics Across a Range of Idealized Urban Canopy Geometries. *Boundary-Layer Meteorol* 182:275–307. <https://doi.org/10.1007/s10546-021-00658-6>
- Bogaert J, Barima Y, Mongo LIW, et al (2011) Forest Fragmentation: Causes, Ecological Impacts and Implications for Landscape Management. In: Li C, Laforteza R, Chen J (eds) *Landscape ecology in forest management and conservation: challenges and solutions for global change*. Springer, Berlin, pp 273–292
- 5020 Böhm M, Finnigan JJ, Raupach MR, Hughes D (2013) Turbulence Structure Within and Above a Canopy of Bluff Elements. *Boundary-Layer Meteorol* 146:393–419. <https://doi.org/10.1007/s10546-012-9770-1>

- 5025 Bohnenstengel SI, Belcher SE, Aiken A, et al (2015) Meteorology, air quality, and health in London: The ClearLo project. *Bull Am Meteorol Soc* 96:779–804. <https://doi.org/10.1175/BAMS-D-12-00245.1>
- Bohrer G, Katul GG, Walko RL, Avissar R (2009) Exploring the effects of microscale structural heterogeneity of forest canopies using large-eddy simulations. *Boundary-Layer Meteorol* 132:351–382. <https://doi.org/10.1007/s10546-009-9404-4>
- 5030 Bohrer G, Wolosin M, Brady R, Avissar R (2007) A virtual canopy generator (V-CaGe) for modelling complex heterogeneous forest canopies at high resolution. In: *Tellus, Series B: Chemical and Physical Meteorology*. Blackwell Munksgaard, pp 566–576
- Bonan GB, Patton EG, Finnigan JJ, et al (2021) Moving beyond the incorrect but useful paradigm: reevaluating big-leaf and multilayer plant canopies to model biosphere-atmosphere fluxes – a review. *Agric For Meteorol* 306:108435. <https://doi.org/10.1016/j.agrformet.2021.108435>
- 5035 Bonan GB, Patton EG, Harman IN, et al (2018) Modeling canopy-induced turbulence in the Earth system: A unified parameterization of turbulent exchange within plant canopies and the roughness sublayer (CLM-ml v0). *Geosci Model Dev* 11:1467–1496. <https://doi.org/10.5194/gmd-11-1467-2018>
- Bonn B, Bourtsoukidis E, Sun TS, et al (2014) The link between atmospheric radicals and newly formed particles at a spruce forest site in Germany. *Atmos Chem Phys* 14:10823–10843. <https://doi.org/10.5194/acp-14-10823-2014>
- 5040 Bou-Zeid E (2014) Challenging the large eddy simulation technique with advanced a posteriori tests. *J Fluid Mech* 764:1–4. <https://doi.org/10.1017/jfm.2014.616>
- Bou-Zeid E, Anderson W, Katul GG, Mahrt L (2020) The Persistent Challenge of Surface Heterogeneity in Boundary-Layer Meteorology: A Review. *Boundary-Layer Meteorol* 177:227–245. <https://doi.org/10.1007/s10546-020-00551-8>
- Boudreault LÉ, Bechmann A, Tarvainen L, et al (2015) A LiDAR method of canopy structure retrieval for wind modeling of heterogeneous forests. *Agric For Meteorol* 201:86–97. <https://doi.org/10.1016/j.agrformet.2014.10.014>
- 5050 Boudreault LÉ, Dupont S, Bechmann A, Dellwik E (2017) How Forest Inhomogeneities Affect the Edge Flow. *Boundary-Layer Meteorol* 162:375–400. <https://doi.org/10.1007/s10546-016-0202-5>
- Boutle IA, Finnenkoetter A, Lock AP, Wells H (2016) The London Model: Forecasting fog at 333 m resolution. *Q J R Meteorol Soc* 142:360–371. <https://doi.org/10.1002/qj.2656>
- Bright VB, Bloss WJ, Cai X (2013) Urban street canyons: Coupling dynamics, chemistry and within-canyon chemical processing of emissions. *Atmos Environ* 68:127–142. <https://doi.org/10.1016/j.atmosenv.2012.10.056>
- 5055 Britter RE, Hanna SR (2003) Flow and dispersion in urban areas. *Annu Rev Fluid Mech* 35:469–496. <https://doi.org/10.1146/annurev.fluid.35.101101.161147>
- Brodribb TJ, Powers J, Cochard H, Choat B (2020) Hanging by a thread? Forests and drought. *Science* (80-) 368:261–266. <https://doi.org/10.1126/science.aat7631>
- 5060 Brüchert F, Gardiner BA (2006) The effect of wind exposure on the tree aerial architecture and biomechanics of Sitka spruce (*Picea sitchensis*, Pinaceae). *Am J Bot* 93:1512–1521. <https://doi.org/10.3732/ajb.93.10.1512>
- Brunet Y (2020) Turbulent Flow in Plant Canopies: Historical Perspective and Overview. *Boundary-Layer Meteorol* 177:315–364. <https://doi.org/10.1007/s10546-020-00560-7>
- 5065 Brunet Y, Irvine MR (2000) The control of coherent eddies in vegetation canopies: Streamwise structure spacing, canopy shear scale and atmospheric stability. *Boundary-Layer Meteorol* 94:139–163. <https://doi.org/10.1023/A:1002406616227>
- Bryan AM, Bertman SB, Carroll MA, et al (2012) In-canopy gas-phase chemistry during CABINEX 2009: Sensitivity of a 1-D canopy model to vertical mixing and isoprene chemistry. *Atmos Chem Phys* 12:8829–8849. <https://doi.org/10.5194/acp-12-8829-2012>
- 5070 Buccolieri R, Sandberg M, Di Sabatino S (2010) City breathability and its link to pollutant concentration distribution within urban-like geometries. *Atmos Environ* 44:1894–1903. <https://doi.org/10.1016/j.atmosenv.2010.02.022>
- 5075 Buccolieri R, Santiago JL, Rivas E, Sanchez B (2018) Review on urban tree modelling in CFD simulations: Aerodynamic, deposition and thermal effects. *Urban For Urban Green* 31:212–220. <https://doi.org/10.1016/j.ufug.2018.03.003>
- Butler TM, Taraborrelli D, Brühl C, et al (2008) Improved simulation of isoprene oxidation chemistry with the ECHAM5/MESy chemistry-climate model: Lessons from the GABRIEL airborne field campaign.

- 5080 Atmos Chem Phys 8:4529–4546. <https://doi.org/10.5194/acp-8-4529-2008>
- Cai X (2012) Effects of differential wall heating in street canyons on dispersion and ventilation characteristics of a passive scalar. *Atmos Environ* 51:268–277. <https://doi.org/10.1016/j.atmosenv.2012.01.010>
- Cai X, Barlow JF, Belcher SE (2008) Dispersion and transfer of passive scalars in and above street canyons—Large-eddy simulations. *Atmos Environ* 42:5885–5895. <https://doi.org/10.1016/j.atmosenv.2008.03.040>
- 5085 Calders K, Adams J, Armston J, et al (2020) Terrestrial laser scanning in forest ecology: Expanding the horizon. *Remote Sens Environ* 251:112102. <https://doi.org/10.1016/j.rse.2020.112102>
- Calders K, Schenkels T, Bartholomeus H, et al (2015) Monitoring spring phenology with high temporal resolution terrestrial LiDAR measurements. *Agric For Meteorol* 203:158–168. <https://doi.org/10.1016/j.agrformet.2015.01.009>
- 5090 Calfapietra C, Ainsworth EA, Beier C, et al (2010) Challenges in elevated CO₂ experiments on forests. *Trends Plant Sci* 15:5–10. <https://doi.org/10.1016/j.tplants.2009.11.001>
- Campbell GS, Norman JM (1998) *An Introduction to Environmental Biophysics*, Second. Springer-Verlag, New York
- Carpentieri M, Robins AG (2015) Influence of urban morphology on air flow over building arrays. *J Wind Eng Ind Aerodyn* 145:61–74. <https://doi.org/10.1016/j.jweia.2015.06.001>
- 5095 Carpentieri M, Salizzoni P, Robins AG, Soulhac L (2012) Evaluation of a neighbourhood scale, street network dispersion model through comparison with wind tunnel data. *Environ Model Softw* 37:110–124. <https://doi.org/10.1016/j.envsoft.2012.03.009>
- Cassiani M, Katul GG, Albertson JD (2008) The Effects of Canopy Leaf Area Index on Airflow Across Forest Edges: Large-eddy Simulation and Analytical Results. 126:433–460. <https://doi.org/10.1007/s10546-007-9242-1>
- 5100 Castro IP (2017) Are Urban-Canopy Velocity Profiles Exponential? *Boundary-Layer Meteorol* 164:337–351. <https://doi.org/10.1007/s10546-017-0258-x>
- Castro IP, Cheng H, Reynolds R (2006) Turbulence over urban-type roughness: Deductions from wind-tunnel measurements. *Boundary-Layer Meteorol* 118:109–131. <https://doi.org/10.1007/s10546-005-5747-7>
- 5105 Cava D, Katul GG (2008) Spectral short-circuiting and wake production within the canopy trunk space of an alpine hardwood forest. *Boundary-Layer Meteorol* 126:415–431. <https://doi.org/10.1007/s10546-007-9246-x>
- Cava D, Katul GG, Scrimieri A, et al (2006) Buoyancy and the sensible heat flux budget within dense canopies. *Boundary-Layer Meteorol* 118:217–240. <https://doi.org/10.1007/s10546-005-4736-1>
- 5110 Cava D, Mortarini L, Giostra U, et al (2019) Submeso Motions and Intermittent Turbulence Across a Nocturnal Low-Level Jet: A Self-Organized Criticality Analogy. *Boundary-Layer Meteorol* 172:17–43. <https://doi.org/10.1007/s10546-019-00441-8>
- Cescatti A, Marcolla B (2004) Drag coefficient and turbulence intensity in conifer canopies. *Agric For Meteorol* 121:197–206. <https://doi.org/10.1016/j.agrformet.2003.08.028>
- 5115 Chaudhari A, Conan B, Aubrun S, Hellsten A (2016) Numerical study of how stable stratification affects turbulence instabilities above a forest cover: Application to wind energy. *J Phys Conf Ser* 753:. <https://doi.org/10.1088/1742-6596/753/3/032037>
- Chen B, Chamecki M, Katul GG (2019a) Effects of topography on in-canopy transport of gases emitted within dense forests. *Q J R Meteorol Soc* 145:2101–2114. <https://doi.org/10.1002/qj.3546>
- 5120 Chen B, Chamecki M, Katul GG (2020) Effects of Gentle Topography on Forest-Atmosphere Gas Exchanges and Implications for Eddy-Covariance Measurements. *J Geophys Res Atmos* 125:1–15. <https://doi.org/10.1029/2020JD032581>
- Chen D, Hu F, Xu J, Liu L (2019b) Long-range correlation analysis among non-stationary passive scalar series in the turbulent boundary layer. *Phys A Stat Mech its Appl* 517:290–296. <https://doi.org/10.1016/j.physa.2018.09.094>
- 5125 Chen L, Liu C, Zhang L, et al (2017) Variation in Tree Species Ability to Capture and Retain Airborne Fine Particulate Matter (PM_{2.5}). *Sci Rep* 7:1–11. <https://doi.org/10.1038/s41598-017-03360-1>
- Chen Y, Ryder J, Bastrikov V, et al (2016) Evaluating the performance of land surface model ORCHIDEE-CAN v1.0 on water and energy flux estimation with a single-and multi-layer energy budget scheme. *Geosci Model Dev* 9:2951–2972. <https://doi.org/10.5194/gmd-9-2951-2016>
- 5130 Cheng H, Castro IP (2002) Near wall flow over urban-like roughness. *Boundary-Layer Meteorol* 104:229–259
- Cheng H, Hayden P, Robins AG, Castro IP (2007) Flow over cube arrays of different packing densities. *J Wind Eng Ind Aerodyn* 95:715–740. <https://doi.org/10.1016/j.jweia.2007.01.004>

- 5135 Chester S, Meneveau C (2007) Renormalized numerical simulation of flow over planar and non-planar fractal trees. *Environ Fluid Mech* 7:289–301. <https://doi.org/10.1007/s10652-007-9026-7>
- Chester S, Meneveau C, Parlange MB (2007) Modeling turbulent flow over fractal trees with renormalized numerical simulation. *J Comput Phys* 225:427–448. <https://doi.org/10.1016/j.jcp.2006.12.009>
- Chiesa M, Bignotti L, Finco A, et al (2019) Size-resolved aerosol fluxes above a broadleaved deciduous forest. *Agric For Meteorol* 279:107757. <https://doi.org/10.1016/j.agrformet.2019.107757>
- 5140 Christen A (2005) *Atmospheric Turbulence and Surface Energy Exchange in Urban Environments*. University of Basel
- Cionco RM (1965) A Mathematical Model for Air Flow in a Vegetative Canopy. *J. Appl. Meteorol.* 4:517–522
- 5145 Cionco RM (1978) Analysis of canopy index values for various canopy densities. *Boundary-Layer Meteorol* 15:81–93. <https://doi.org/10.1007/BF00165507>
- Coceal O, Belcher SE (2004) A canopy model of mean winds through urban areas. *Q J R Meteorol Soc* 130:1349–1372. <https://doi.org/10.1256/qj.03.40>
- Coceal O, Belcher SE (2005) Mean winds through an inhomogeneous urban canopy. *Boundary-Layer Meteorol* 115:47–68. <https://doi.org/10.1007/s10546-004-1591-4>
- 5150 Coceal O, Dobre A, Thomas TG (2007) Unsteady dynamics and organized structures from DNS over an idealized building canopy. *Int J Climatol* 27:1943–1953. <https://doi.org/10.1002/joc.1549>
- Coceal O, Thomas TG, Castro IP, Belcher SE (2006) Mean flow and turbulence statistics over groups of urban-like cubical obstacles. *Boundary-Layer Meteorol* 121:491–519. <https://doi.org/10.1007/s10546-006-9076-2>
- 5155 Coleman GN, Sandberg RD (2010) *A primer on direct numerical simulation of turbulence - methods, procedures and guidelines*. Southampton, UK
- Cook BD, Davis KJ, Wang W, et al (2004) Carbon exchange and venting anomalies in an upland deciduous forest in northern Wisconsin, USA. *Agric For Meteorol* 126:271–295. <https://doi.org/10.1016/j.agrformet.2004.06.008>
- 5160 Corrsin S (1975) Limitations of gradient transport models in random walks and in turbulence. *Adv Geophys* 18:25–60. [https://doi.org/10.1016/S0065-2687\(08\)60451-3](https://doi.org/10.1016/S0065-2687(08)60451-3)
- Crandall SG, Gilbert GS (2017) Meteorological factors associated with abundance of airborne fungal spores over natural vegetation. *Atmos Environ* 162:87–99. <https://doi.org/10.1016/j.atmosenv.2017.05.018>
- 5165 Crowley LM, Sadler JP, Pritchard J, Hayward SAL (2021) Elevated co2 impacts on plant–pollinator interactions: A systematic review and free air carbon enrichment field study. *Insects* 12:.. <https://doi.org/10.3390/insects12060512>
- Cucchi V, Meredieu C, Stokes A, et al (2004) Root anchorage of inner and edge trees in stands of Maritime pine (*Pinus pinaster*Ait.) growing in different podzolic soil conditions. *Trees - Struct Funct* 18:460–466. <https://doi.org/10.1007/s00468-004-0330-2>
- 5170 Cui PY, Li Z, Tao WQ (2016) Wind-tunnel measurements for thermal effects on the air flow and pollutant dispersion through different scale urban areas. *Build Environ* 97:137–151. <https://doi.org/10.1016/j.buildenv.2015.12.010>
- Cui Z, Cai X, Baker CJ (2004) Large-eddy simulation of turbulent flow in a street canyon. *Q J R Meteorol Soc* 130:1373–1394. <https://doi.org/10.1256/qj.02.150>
- 5175 Dai Y, Cai X, Zhong J, MacKenzie AR (2021) Modelling chemistry and transport in urban street canyons: Comparing offline multi-box models with large-eddy simulation. *Atmos Environ* 264:118709. <https://doi.org/10.1016/j.atmosenv.2021.118709>
- Danckwerts P V. (1951) Significance of Liquid-Film Coefficients in Gas Absorption. *Ind Eng Chem* 43:1460–1467. <https://doi.org/10.1021/ie50498a055>
- 5180 Davidson MJ, Mylne KR, Jones CD, et al (1995) Plume dispersion through large groups of obstacles-A field investigation. *Atmos Environ* 29:3245–3256. [https://doi.org/10.1016/1352-2310\(95\)00254-V](https://doi.org/10.1016/1352-2310(95)00254-V)
- Davidson MJ, Snyder WH, Lawson RE, Hunt JCR (1996) Wind tunnel simulations of plume dispersion through groups of obstacles. *Atmos Environ* 30:3715–3731. [https://doi.org/10.1016/1352-2310\(96\)00103-3](https://doi.org/10.1016/1352-2310(96)00103-3)
- 5185 De Langre E (2019) Plant vibrations at all scales: A review. *J Exp Bot* 70:3521–3531. <https://doi.org/10.1093/jxb/erz209>
- De Langre E (2008) Effects of Wind on Plants. *Annu Rev Fluid Mech* 40:141–168. <https://doi.org/10.1146/annurev.fluid.40.111406.102135>

- 5190 Deardorff JW (1970) A numerical study of three-dimensional turbulent channel flow at large Reynolds numbers. *J Fluid Mech* 41:453–480. <https://doi.org/10.1017/S0022112070000691>
- DEFRA (2019) Air Pollution in the UK 2018
- DEFRA (2022) Automatic Urban and Rural Network (AURN). In: *Air Inf. Resour.* <https://uk-air.defra.gov.uk/networks/network-info?view=aurun>. Accessed 5 May 2022
- 5195 Dellwik E, Bingöl F, Mann J (2014) Flow distortion at a dense forest edge. *Q J R Meteorol Soc* 140:676–686. <https://doi.org/10.1002/qj.2155>
- Dellwik E, Mann J, Larsen KS (2010) Flow tilt angles near forest edges -Part 1: Sonic anemometry. *Biogeosciences* 7:1745–1757. <https://doi.org/10.5194/bg-7-1745-2010>
- Detto M, Katul GG, Siqueira M, et al (2008) The structure of turbulence near a tall forest edge: The backward-facing step flow analogy revisited. *Ecol Appl* 18:1420–1435. <https://doi.org/10.1890/06-0920.1>
- 5200 Di Sabatino S, Solazzo E, Paradisi P, Britter R (2008) A simple model for spatially-averaged wind profiles within and above an urban canopy. *Boundary-Layer Meteorol* 127:131–151. <https://doi.org/10.1007/s10546-007-9250-1>
- 5205 Dickson RE, Lewin KF, Isebrands JG, et al (2000) Forest Atmosphere Carbon Transfer and Storage (FACTS-II) The Aspen Free-air CO₂ and O₃ Enrichment (FACE) Project : An Overview
- Drake JE, Macdonald CA, Tjoelker MG, et al (2016) Short-term carbon cycling responses of a mature eucalypt woodland to gradual stepwise enrichment of atmospheric CO₂ concentration. *Glob Chang Biol* 22:380–390. <https://doi.org/10.1111/gcb.13109>
- 5210 Düben PD, Dolapchiev SI (2015) Rounding errors may be beneficial for simulations of atmospheric flow: results from the forced 1D Burgers equation. *Theor Comput Fluid Dyn* 29:311–328. <https://doi.org/10.1007/s00162-015-0355-8>
- Düben PD, Joven J, Lingamneni A, et al (2014) On the use of inexact, pruned hardware in atmospheric modelling. *Philos Trans R Soc A Math Phys Eng Sci* 372:. <https://doi.org/10.1098/rsta.2013.0276>
- 5215 Dupont S, Bonnefond JM, Irvine MR, et al (2011) Long-distance edge effects in a pine forest with a deep and sparse trunk space: In situ and numerical experiments. *Agric For Meteorol* 151:328–344. <https://doi.org/10.1016/j.agrformet.2010.11.007>
- Dupont S, Brunet Y (2008a) Influence of foliar density profile on canopy flow: A large-eddy simulation study. *Agric For Meteorol* 148:976–990. <https://doi.org/10.1016/j.agrformet.2008.01.014>
- 5220 Dupont S, Brunet Y (2008b) Edge flow and canopy structure: A large-eddy simulation study. *Boundary-Layer Meteorol* 126:51–71. <https://doi.org/10.1007/s10546-007-9216-3>
- Dupont S, Brunet Y (2009) Coherent structures in canopy edge flow: A large-eddy simulation study. *Tech Reports* 630:93–128. <https://doi.org/10.1017/S0022112009006739>
- Dupont S, Brunet Y (2008c) Impact of forest edge shape on tree stability: A large-eddy simulation study. *Forestry* 81:299–315. <https://doi.org/10.1093/forestry/cpn006>
- 5225 Dupont S, Défossez P, Bonnefond JM, et al (2018) How stand tree motion impacts wind dynamics during windstorms. *Agric For Meteorol* 262:42–58. <https://doi.org/10.1016/j.agrformet.2018.06.022>
- Dupont S, Gosselin FP, Py C, et al (2010) Modelling waving crops using large-eddy simulation: Comparison with experiments and a linear stability analysis. *J Fluid Mech* 652:5–44. <https://doi.org/10.1017/S0022112010000686>
- 5230 Dupont S, Patton EG (2012) Influence of stability and seasonal canopy changes on micrometeorology within and above an orchard canopy: The CHATS experiment. *Agric For Meteorol* 157:11–29. <https://doi.org/10.1016/j.agrformet.2012.01.011>
- Dwyer MJ, Patton EG, Shaw RH (1997) Turbulent kinetic energy budgets from a large-eddy simulation of airflow above and within a forest canopy. *Boundary-Layer Meteorol* 84:23–43. <https://doi.org/10.1023/A:1000301303543>
- 5235 Edburg SL, Stock D, Lamb BK, Patton EG (2012) The Effect of the Vertical Source Distribution on Scalar Statistics within and above a Forest Canopy. *Boundary-Layer Meteorol* 142:365–382. <https://doi.org/10.1007/s10546-011-9686-1>
- 5240 Ellsworth DS, Anderson IC, Crous KY, et al (2017) Elevated CO₂ does not increase eucalypt forest productivity on a low-phosphorus soil. *Nat Clim Chang* 7:279–282. <https://doi.org/10.1038/nclimate3235>
- Fahrig L (2003) Effects of Habitat Fragmentation on Biodiversity. *Annu Rev Ecol Evol Syst* 34:487–515. <https://doi.org/10.1146/annurev.ecolsys.34.011802.132419>

- 5245 Farmer DK, Cohen RC (2008) Observations of HNO₃, ΣaN, ΣPN and NO₂ fluxes: Evidence for rapid HO_x chemistry within a pine forest canopy. *Atmos Chem Phys* 8:3899–3917. <https://doi.org/10.5194/acp-8-3899-2008>
- Feigenwinter C, Bernhofer C, Eichelmann U, et al (2008) Comparison of horizontal and vertical advective CO₂ fluxes at three forest sites. *Agric For Meteorol* 148:12–24. <https://doi.org/10.1016/j.agrformet.2007.08.013>
- 5250 Finnigan JJ (2008) An introduction to flux measurements in difficult conditions. *Ecol Appl* 18:1340–1350. <https://doi.org/10.1890/07-2105.1>
- Finnigan JJ (2000) Turbulence in Plant Canopies. *Annu Rev Fluid Mech* 32:519–571
- Finnigan JJ (1985) Turbulent transport in flexible plant canopies. In: Hicks BB, Hutchinson BA (eds) *The Forest-Atmosphere Interaction*. Reidel, Dordrecht, pp 443–480
- 5255 Finnigan JJ (1979a) Turbulence in Waving Wheat: I Mean Statistics and Honami
- Finnigan JJ (1979b) Turbulence in waving wheat: II. Structure of Momentum Transfer. *Boundary-Layer Meteorol* 16:213–236. <https://doi.org/10.1007/bf02350512>
- Finnigan JJ, Ayotte K, Harman IN, et al (2020) Boundary-Layer Flow Over Complex Topography. *Boundary-Layer Meteorol* 177:247–313. <https://doi.org/10.1007/s10546-020-00564-3>
- 5260 Finnigan JJ, Belcher SE (2004) Flow over a hill covered with a plant canopy. *Q J R Meteorol Soc* 130:1–29. <https://doi.org/10.1256/qj.02.177>
- Finnigan JJ, Bradley EF (1983) The turbulent kinetic energy budget behind a porous barrier: An analysis in streamline co-ordinates. *J Wind Eng Ind Aerodyn* 15:157–168. [https://doi.org/10.1016/0167-6105\(83\)90186-1](https://doi.org/10.1016/0167-6105(83)90186-1)
- 5265 Finnigan JJ, Brunet Y (1995) Turbulent airflow in forests on flat and hilly terrain. In: Coutts MP, Grace J (eds) *Wind and Trees*. Cambridge University Press, Cambridge, UK, pp 3–40
- Finnigan JJ, Clement R, Malhi Y, et al (2003) Techniques Part I: Averaging and Coordinate Rotation. *Boundary-Layer Meteorol* 107:1–48
- 5270 Finnigan JJ, Harman I, Ross A, Belcher S (2015) First-order turbulence closure for modelling complex canopy flows. *Q J R Meteorol Soc* 141:2907–2916. <https://doi.org/10.1002/qj.2577>
- Finnigan JJ, Shaw RH (2008) Double-averaging methodology and its application to turbulent flow in and above vegetation canopies. *Acta Geophys* 56:534–561. <https://doi.org/10.2478/s11600-008-0034-x>
- Finnigan JJ, Shaw RH, Patton EG (2009) Turbulence structure above a vegetation canopy. *J Fluid Mech* 637:387–424. <https://doi.org/10.1017/S0022112009990589>
- 5275 Fisher RA, Koven CD (2020) Perspectives on the Future of Land Surface Models and the Challenges of Representing Complex Terrestrial Systems. *J Adv Model Earth Syst* 12:. <https://doi.org/10.1029/2018MS001453>
- Fleischbein K, Wilcke W, Goller R, et al (2005) Rainfall interception in a lower montane forest in Ecuador: Effects of canopy properties. *Hydrol Process* 19:1355–1371. <https://doi.org/10.1002/hyp.5562>
- 5280 Foken T (2008) *Micrometeorology*. Springer-Verlag, Berlin Heidelberg
- Foken T (2006) 50 years of the Monin-Obukhov similarity theory. *Boundary-Layer Meteorol* 119:431–447. <https://doi.org/10.1007/s10546-006-9048-6>
- Foken T, Aubinet M, Finnigan JJ, et al (2011) Results of a panel discussion about the energy balance closure correction for trace gases. In: *Bulletin of the American Meteorological Society*
- 5285 Forestry Commission (2021) *Woodland Carbon Code*. Bristol, UK
- Forkel R, Guenther AB, Ashworth K, et al (2015) Review and Integration of Biosphere-Atmosphere Modelling of Reactive Trace Gases and Volatile Aerosols. *Rev Integr Biosph Model React Trace Gases Volatile Aerosols* 169–179. <https://doi.org/10.1007/978-94-017-7285-3>
- 5290 Fowler D, Pilegaard K, Sutton MA, et al (2009) Atmospheric composition change: Ecosystems-Atmosphere interactions. *Atmos Environ* 43:5193–5267. <https://doi.org/10.1016/j.atmosenv.2009.07.068>
- Fox J (1977) Alternation and Coexistence of Tree Species. *Am Nat* 111:69–89
- Freire LS, Gerken T, Ruiz-Plancarte J, et al (2017) Turbulent mixing and removal of ozone within an Amazon rainforest canopy. *J Geophys Res* 122:2791–2811. <https://doi.org/10.1002/2016JD026009>
- 5295 Friedlander SK (2000) *Smoke, dust and haze: Fundamentals of aerosol dynamics*
- Friedlingstein P, Jones MW, Sullivan MO, et al (2022) *Global Carbon Budget 2021*. *Earth Syst Sci Data* 14:1917–2005. <https://doi.org/10.5194/essd-2021-386>
- Fuentes JD, Chamecki M, Dos Santos RMN, et al (2016) Linking meteorology, turbulence, and air chemistry in the amazon rain forest. *Bull Am Meteorol Soc* 97:2329–2342. [194](https://doi.org/10.1175/BAMS-D-15-</p>
</div>
<div data-bbox=)

- 5300 00152.1
 Fuentes JD, Lerdaun MT, Atkinson R, et al (2000) Biogenic Hydrocarbons in the Atmospheric Boundary Layer: A Review. *Bull Am Meteorol Soc* 81:1537–1575. [https://doi.org/10.1175/1520-0477\(2000\)081<1537:BHITAB>2.3.CO;2](https://doi.org/10.1175/1520-0477(2000)081<1537:BHITAB>2.3.CO;2)
- 5305 Fuentes JD, Wang D, Bowling DR, et al (2007) Biogenic hydrocarbon chemistry within and above a mixed deciduous forest. *J Atmos Chem* 56:165–185. <https://doi.org/10.1007/s10874-006-9048-4>
- Gadde SN, Stieren A, Stevens RJAM (2021) Large-Eddy Simulations of Stratified Atmospheric Boundary Layers: Comparison of Different Subgrid Models. *Boundary-Layer Meteorol* 178:363–382. <https://doi.org/10.1007/s10546-020-00570-5>
- 5310 Galanti B, Tsinober A (2004) Is turbulence ergodic? *Phys Lett Sect A Gen At Solid State Phys* 330:173–180. <https://doi.org/10.1016/j.physleta.2004.07.009>
- Gao W, Shaw RH, Paw U KT (1989) Observation of Organized Structure in Turbulent Flow within and above a Forest Canopy. In: *Boundary Layer Studies and Applications*. Springer Netherlands, pp 349–377
- Gao Z, Bresson R, Qu Y, et al (2018) High resolution unsteady RANS simulation of wind, thermal effects and pollution dispersion for studying urban renewal scenarios in a neighborhood of Toulouse. *Urban Clim* 23:114–130. <https://doi.org/10.1016/j.uclim.2016.11.002>
- 5315 Garde RJ (2010) *Turbulent Flow*, 3rd edn. New Age Science Ltd., Tunbridge Wells
- Gardiner BA, Berry P, Moulia B (2016) Review: Wind impacts on plant growth, mechanics and damage. *Plant Sci.* 245:94–118
- 5320 Gardner A, Ellsworth DS, Crous KY, et al (2021) Is photosynthetic enhancement sustained through three years of elevated CO₂ exposure in 175-year old *Quercus robur*? *Tree Physiol* tpab090. <https://doi.org/https://doi.org/10.1093/treephys/tpab090>
- Garuma GF (2018) Review of urban surface parameterizations for numerical climate models. *Urban Clim* 24:830–851. <https://doi.org/10.1016/j.uclim.2017.10.006>
- 5325 Gavrillov K, Morvan D, Accary G, et al (2013) Numerical simulation of coherent turbulent structures and of passive scalar dispersion in a canopy sub-layer. *Comput Fluids* 78:54–62. <https://doi.org/10.1016/j.compfluid.2012.08.021>
- Gaylord BP, Denny MW (1997) Flow and flexibility. *J Exp Biol* 200:3141–3164
- Geer AJ (2021) Learning earth system models from observations: Machine learning or data assimilation? *Philos Trans R Soc A Math Phys Eng Sci* 379:. <https://doi.org/10.1098/rsta.2020.0089>
- 5330 Gerken T, Chamecki M, Fuentes JD (2017) Air-Parcel Residence Times Within Forest Canopies. *Boundary-Layer Meteorol* 165:29–54. <https://doi.org/10.1007/s10546-017-0269-7>
- Geurts BJ (2003) *Elements of direct and large eddy simulation*. RT Edwards, Inc
- Ghannam K, Poggi D, Bou-Zeid E, Katul GG (2020) Inverse Cascade Evidenced by Information Entropy of Passive Scalars in Submerged Canopy Flows. *Geophys Res Lett* 47:1–10. <https://doi.org/10.1029/2020GL087486>
- 5335 Giometto MG, Christen A, Egli PE, et al (2017) Effects of trees on mean wind, turbulence and momentum exchange within and above a real urban environment. *Adv Water Resour* 106:154–168. <https://doi.org/10.1016/j.advwatres.2017.06.018>
- 5340 Giometto MG, Christen A, Meneveau C, et al (2016) Spatial Characteristics of Roughness Sublayer Mean Flow and Turbulence Over a Realistic Urban Surface. *Boundary-Layer Meteorol* 160:425–452. <https://doi.org/10.1007/s10546-016-0157-6>
- Gleicher SC, Chamecki M, Isard SA, et al (2014) Interpreting three-dimensional spore concentration measurements and escape fraction in a crop canopy using a coupled Eulerian-Lagrangian stochastic model. *Agric For Meteorol* 194:118–131. <https://doi.org/10.1016/j.agrformet.2014.03.020>
- 5345 Gon Seo Y, Kook Lee W (1988) Single-eddy model for random surface renewal. *Chem Eng Sci* 43:1395–1402. [https://doi.org/10.1016/0009-2509\(88\)85112-1](https://doi.org/10.1016/0009-2509(88)85112-1)
- Goodrick SL, Achtemeier GL, Larkin NK, et al (2013) Modelling smoke transport from wildland fires: A review. *Int J Wildl Fire* 22:83–94. <https://doi.org/10.1071/WF11116>
- Gosselin FP (2019) Mechanics of a plant in fluid flow. *J Exp Bot* 70:3533–3548. <https://doi.org/10.1093/jxb/erz288>
- 5350 Gosselin FP, de Langre E (2009) Destabilising effects of plant flexibility in air and aquatic vegetation canopy flows. *Eur J Mech B/Fluids* 28:271–282. <https://doi.org/10.1016/j.euromechflu.2008.06.003>
- Gosselin FP, De Langre E, MacHado-Almeida BA (2010) Drag reduction of flexible plates by reconfiguration. *J Fluid Mech* 650:319–341. <https://doi.org/10.1017/S0022112009993673>

- 5355 Grant ER, Ross AN, Gardiner BA, Mobbs SD (2015) Field Observations of Canopy Flows over Complex Terrain. *Boundary-Layer Meteorol* 156:231–251. <https://doi.org/10.1007/s10546-015-0015-y>
- Grell GA, Dudhia J, Stauffer DR (1994) A Description of the Fifth-Generation Penn State/NCAR Mesoscale Model (MM5)
- Grimmond CSB, Blackett M, Best MJ, et al (2010) The international urban energy balance models comparison project: First results from phase 1. *J Appl Meteorol Climatol* 49:1268–1292. <https://doi.org/10.1175/2010JAMC2354.1>
- 5360 Grimmond CSB, Blackett M, Best MJ, et al (2011) Initial results from Phase 2 of the international urban energy balance model comparison. *Int J Climatol* 31:244–272. <https://doi.org/10.1002/joc.2227>
- Gromke C (2018) Wind tunnel model of the forest and its Reynolds number sensitivity. *J Wind Eng Ind Aerodyn* 175:53–64. <https://doi.org/10.1016/j.jweia.2018.01.036>
- 5365 Grylls T, Suter I, van Reeuwijk M (2020) Steady-State Large-Eddy Simulations of Convective and Stable Urban Boundary Layers. *Boundary-Layer Meteorol*. <https://doi.org/10.1007/s10546-020-00508-x>
- Gu L, Falge EM, Boden T, et al (2005) Objective threshold determination for nighttime eddy flux filtering. *Agric For Meteorol* 128:179–197. <https://doi.org/10.1016/j.agrformet.2004.11.006>
- 5370 Guenther AB, Jiang X, Heald CL, et al (2012) The model of emissions of gases and aerosols from nature version 2.1 (MEGAN2.1): An extended and updated framework for modeling biogenic emissions. *Geosci Model Dev* 5:1471–1492. <https://doi.org/10.5194/gmd-5-1471-2012>
- Guenther AB, Karl T, Harley P, et al (2006) Edinburgh Research Explorer Estimates of global terrestrial isoprene emissions using MEGAN (Model of Emissions of Gases and Aerosols from Nature) and
- 5375 Physics Estimates of global terrestrial isoprene emissions using MEGAN (Model of Emissions of Gases an. *Atmos Chem Phys* 3181–3210
- Gutiérrez E, Martilli A, Santiago JL, González JE (2015) A Mechanical Drag Coefficient Formulation and Urban Canopy Parameter Assimilation Technique for Complex Urban Environments. *Boundary-Layer Meteorol* 157:333–341. <https://doi.org/10.1007/s10546-015-0051-7>
- 5380 Haddad NM, Brudvig LA, Clobert J, et al (2015) Habitat fragmentation and its lasting impact on Earth’s ecosystems. *Sci Adv* 1:. <https://doi.org/10.1126/sciadv.1500052>
- Haghighi E, Or D (2013) Evaporation from porous surfaces into turbulent airflows: Coupling eddy characteristics with pore scale vapor diffusion. *Water Resour Res* 49:8432–8442. <https://doi.org/10.1002/2012WR013324>
- 5385 Haghighi E, Or D (2015) Thermal signatures of turbulent airflows interacting with evaporating thin porous surfaces. *Int J Heat Mass Transf* 87:429–446. <https://doi.org/10.1016/j.ijheatmasstransfer.2015.04.026>
- Hagishima A, Tanimoto J, Nagayama K, Meno S (2009) Aerodynamic parameters of regular arrays of rectangular blocks with various geometries. *Boundary-Layer Meteorol* 132:315–337. <https://doi.org/10.1007/s10546-009-9403-5>
- 5390 Hakola H, Hellén H, Hemmilä M, et al (2012) In situ measurements of volatile organic compounds in a boreal forest. *Atmos Chem Phys* 12:11665–11678. <https://doi.org/10.5194/acp-12-11665-2012>
- Hamlyn D, Britter R (2005) A numerical study of the flow field and exchange processes within a canopy of urban-type roughness. *Atmos Environ* 39:3243–3254. <https://doi.org/10.1016/j.atmosenv.2005.02.020>
- Hampel FR (1974) The Influence Curve and its Role in Robust Estimation. *J Am Stat Assoc* 69:383–393
- 5395 Hang J, Li Y (2010) Wind conditions in idealized building clusters: Macroscopic simulations using a porous turbulence model. *Boundary-Layer Meteorol* 136:129–159. <https://doi.org/10.1007/s10546-010-9490-3>
- Hang J, Li Y, Sandberg M, et al (2012) The influence of building height variability on pollutant dispersion and pedestrian ventilation in idealized high-rise urban areas. *Build Environ* 56:346–360. <https://doi.org/10.1016/j.buildenv.2012.03.023>
- 5400 Hari Prasad KBRR, Venkata Srinivas C, Venkateswara Naidu C, et al (2016) Assessment of surface layer parameterizations in ARW using micro-meteorological observations from a tropical station. *Meteorol Appl* 23:191–208. <https://doi.org/10.1002/met.1545>
- Harman IN, Böhm M, Finnigan JJ, Hughes D (2016) Spatial Variability of the Flow and Turbulence Within a Model Canopy. *Boundary-Layer Meteorol* 160:375–396. <https://doi.org/10.1007/s10546-016-0150-0>
- 5405 Harman IN, Finnigan JJ (2007) A simple unified theory for flow in the canopy and roughness sublayer. *Boundary-Layer Meteorol* 123:339–363. <https://doi.org/10.1007/s10546-006-9145-6>
- Harrison RM (2018) Urban atmospheric chemistry: a very special case for study. *npj Clim Atmos Sci* 1:. <https://doi.org/10.1038/s41612-017-0010-8>
- Harrison RM, MacKenzie AR, Xu H, et al (2018) Diesel exhaust nanoparticles and their behaviour in the

- 5410 atmosphere. *Proc R Soc A* 474:20180492. <https://doi.org/10.1098/rspa.2018.0492>
- Hart KM, Curioni G, Blaen P, et al (2020) Characteristics of free air carbon dioxide enrichment of a northern temperate mature forest. *Glob Chang Biol* 26:1023–1037. <https://doi.org/10.1111/gcb.14786>
- Haverd V, Leuning R, Griffith D, et al (2009) The turbulent lagrangian time scale in forest canopies constrained by fluxes, concentrations and source distributions. *Boundary-Layer Meteorol* 130:209–228. <https://doi.org/10.1007/s10546-008-9344-4>
- 5415 Hayek MN, Wehr R, Longo M, et al (2018) A novel correction for biases in forest eddy covariance carbon balance. *Agric For Meteorol* 250–251:90–101. <https://doi.org/10.1016/j.agrformet.2017.12.186>
- Hazeldine A, Kirkpatrick JB (2015) Practical and theoretical implications of a browsing cascade in Tasmanian forest and woodland. *Aust J Bot* 63:435–443. <https://doi.org/10.1071/BT14334>
- 5420 Heinesch B, Yernaux M, Aubinet M (2007) Some methodological questions concerning advection measurements: A case study. *Boundary-Layer Meteorol* 122:457–478. <https://doi.org/10.1007/s10546-006-9102-4>
- Heist DK, Perry SG, Brixey LA (2009) A wind tunnel study of the effect of roadway configurations on the dispersion of traffic-related pollution. *Atmos Environ* 43:5101–5111. <https://doi.org/10.1016/j.atmosenv.2009.06.034>
- 5425 Hendrey GR, Ellsworth DS, Lewin KF, Nagy J (1999) A free-air enrichment system for exposing tall forest vegetation to elevated atmospheric CO₂. *Glob Chang Biol* 5:293–309
- Hicks BB, Baldocchi DD (2020) Measurement of Fluxes Over Land: Capabilities, Origins, and Remaining Challenges. *Boundary-Layer Meteorol* 177:365–394. <https://doi.org/10.1007/s10546-020-00531-y>
- 5430 Higgins CW, Froidevaux M, Simeonov V, et al (2012) The Effect of Scale on the Applicability of Taylor's Frozen Turbulence Hypothesis in the Atmospheric Boundary Layer. *Boundary-Layer Meteorol* 143:379–391. <https://doi.org/10.1007/s10546-012-9701-1>
- Hinds WC (1999) *Aerosol technology: properties, behavior, and measurement of airborne particles*, Second. John Wiley & Sons, Hoboken
- 5435 Hirons AD, Thomas PA (2018) *Applied tree biology*. Wiley Blackwell, Chichester
- Højstrup J (1993) A statistical data screening procedure. *Meas Sci Technol* 4:153–157. <https://doi.org/10.1088/0957-0233/4/2/003>
- Holland JZ (1989) On Pressure-Driven Wind in Deep Forests. *J Appl Meteorol* 28:1349–1355. [https://doi.org/https://doi.org/10.1175/1520-0450\(1989\)028<1349:OPDWID>2.0.CO;2](https://doi.org/https://doi.org/10.1175/1520-0450(1989)028<1349:OPDWID>2.0.CO;2)
- 5440 Holmes NS, Morawska L (2006) A review of dispersion modelling and its application to the dispersion of particles: An overview of different dispersion models available. *Atmos Environ* 40:5902–5928. <https://doi.org/10.1016/j.atmosenv.2006.06.003>
- Hood C, Carruthers D, Seaton M, et al (2014) Urban canopy flow field and advanced street canyon modelling in ADMS-urban. *HARMO 2014 - 16th Int Conf Harmon within Atmos Dispers Model Regul Purp Proc* 366–372
- 5445 Hoosbeek MR (2016) Elevated CO₂ increased phosphorous loss from decomposing litter and soil organic matter at two FACE experiments with trees. *Biogeochemistry* 127:89–97. <https://doi.org/10.1007/s10533-015-0169-1>
- Hourdin F, Mauritsen T, Gettelman A, et al (2017) The art and science of climate model tuning. *Bull Am Meteorol Soc* 98:589–602. <https://doi.org/10.1175/BAMS-D-15-00135.1>
- 5450 Howes FA, Whitaker S (1985) The spatial averaging theorem revisited. *Chem Eng Sci* 40:1387–1392. [https://doi.org/10.1016/0009-2509\(85\)80078-6](https://doi.org/10.1016/0009-2509(85)80078-6)
- Hu T, Yoshie R (2020) Effect of atmospheric stability on air pollutant concentration and its generalization for real and idealized urban block models based on field observation data and wind tunnel experiments. *J Wind Eng Ind Aerodyn* 207:104380. <https://doi.org/10.1016/j.jweia.2020.104380>
- 5455 Hu Z, Yu B, Chen Z, et al (2012) Numerical investigation on the urban heat island in an entire city with an urban porous media model. *Atmos Environ* 47:509–518. <https://doi.org/10.1016/j.atmosenv.2011.09.064>
- Inagaki A, Letzel MO, Raasch S, Kanda M (2006) The impact of the surface heterogeneity on the energy imbalance problem using LES. *J Meteorol Soc Japan* 84:187–198. <https://doi.org/10.2208/prohe.49.343>
- 5460 Inoue E (1955) 'Studies of Phenomena of Waving Plants ('Honami') Caused by Wind. Part 1. Mechanism and Characteristics of Waving Plants Phenomena (in Japanese). *J Agric Meteorol* 11:18–22
- Inoue E (1963) On the Turbulent Structure of Airflow within Crop Canopies. *J Meteorol Soc Japan Ser II* 41:317–326. https://doi.org/10.2151/jmsj1923.41.6_317
- Jacobson MZ (2005) *Fundamentals of Atmospheric Modeling*, Second. Cambridge University Press,

- 5465 Cambridge, UK
- Janhäll S (2015) Review on urban vegetation and particle air pollution - Deposition and dispersion. *Atmos Environ* 105:130–137. <https://doi.org/10.1016/j.atmosenv.2015.01.052>
- Jeanjean APR, Hinchliffe G, McMullan WA, et al (2015) A CFD study on the effectiveness of trees to disperse road traffic emissions at a city scale. *Atmos Environ* 120:1–14. <https://doi.org/10.1016/j.atmosenv.2015.08.003>
- 5470 Jesson M, Sterling M, Bridgeman J (2013) Despiking velocity time-series-Optimisation through the combination of spike detection and replacement methods. *Flow Meas Instrum* 30:45–51. <https://doi.org/10.1016/j.flowmeasinst.2013.01.007>
- Jiménez-Rodríguez CD, Coenders-Gerrits M, Schilperoort B, et al (2021) Vapor plumes in a tropical wet forest: Spotting the invisible evaporation. *Hydrol Earth Syst Sci* 25:619–635. <https://doi.org/10.5194/hess-25-619-2021>
- 5475 Jobst NJ, Zenios SA (2001) The Tail that Wages the Dog: Integrating Credit Risk in Asset Portfolios. *J Risk Financ Iss* 3:31–43
- Juan YH, Yang AS, Wen CY, et al (2017) Optimization procedures for enhancement of city breathability using arcade design in a realistic high-rise urban area. *Build Environ* 121:247–261. <https://doi.org/10.1016/j.buildenv.2017.05.035>
- 5480 Juang JY, Katul GG, Siqueira MB, et al (2008) Investigating a hierarchy of eulerian closure models for scalar transfer inside forested canopies. *Boundary-Layer Meteorol* 128:1–32. <https://doi.org/10.1007/s10546-008-9273-2>
- 5485 Kaimal JC, Finnigan JJ (1994) *Atmospheric boundary layer flows—their structure and measurement*. Oxford University Press, New York
- Kaimal JC, Gaynor JE (1991) Another look at sonic thermometry. *Boundary-Layer Meteorol* 56:401–410. <https://doi.org/10.1007/BF00119215>
- Kanani-Sühring F, Raasch S (2015) Spatial Variability of Scalar Concentrations and Fluxes Downstream of a Clearing-to-Forest Transition: A Large-Eddy Simulation Study. *Boundary-Layer Meteorol* 155:1–27. <https://doi.org/10.1007/s10546-014-9986-3>
- 5490 Kanani-Sühring F, Raasch S (2017) Enhanced Scalar Concentrations and Fluxes in the Lee of Forest Patches: A Large-Eddy Simulation Study. *Boundary-Layer Meteorol* 164:1–17. <https://doi.org/10.1007/s10546-017-0239-0>
- 5495 Kanda M, Inagaki A, Miyamoto T, et al (2013) A New Aerodynamic Parametrization for Real Urban Surfaces. *Boundary-Layer Meteorol* 148:357–377. <https://doi.org/10.1007/s10546-013-9818-x>
- Kang Y (2015) Detection, Classification and Analysis of Events in Turbulence Time Series. *Bull Aust Math Soc* 91:521–522. <https://doi.org/10.1017/S0004972715000106>
- Kang Y, Belušić D, Smith-Miles K (2015) Classes of structures in the stable atmospheric boundary layer. *Q J R Meteorol Soc* 141:2057–2069. <https://doi.org/10.1002/qj.2501>
- 5500 Katul G, Hsieh CI, Oren R, et al (1996) Latent and sensible heat flux predictions from a uniform pine forest using surface renewal and flux variance methods. *Boundary-Layer Meteorol* 80:249–282. <https://doi.org/10.1007/bf00119545>
- Katul G, Liu H (2017) Evaporation Into a Turbulent Atmosphere. *Water* 53:3635–3644. <https://doi.org/10.1002/2016WR020006>.Received
- 5505 Katul GG, Albertson JD (1998) An investigation of higher-order closure models for a forested canopy. *Boundary-Layer Meteorol* 89:47–74. <https://doi.org/10.1023/A:1001509106381>
- Katul GG, Cava D, Siqueira M, Poggi D (2013) Scalar Turbulence within the Canopy Sublayer. *Coherent Flow Struct Earth's Surf* 73–95. <https://doi.org/10.1002/9781118527221.ch6>
- 5510 Katul GG, Finnigan JJ, Poggi D, et al (2006) The influence of hilly terrain on canopy-atmosphere carbon dioxide exchange. *Boundary-Layer Meteorol* 118:189–216. <https://doi.org/10.1007/s10546-005-6436-2>
- Katul GG, Geron CD, Hsieh CI, et al (1998) Active turbulence and scalar transport near the forest-atmosphere interface. *J Appl Meteorol* 37:1533–1546. [https://doi.org/10.1175/1520-0450\(1998\)037<1533:ATASTN>2.0.CO;2](https://doi.org/10.1175/1520-0450(1998)037<1533:ATASTN>2.0.CO;2)
- 5515 Katul GG, Grönholm T, Launiainen S, Vesala T (2011) The effects of the canopy medium on dry deposition velocities of aerosol particles in the canopy sub-layer above forested ecosystems. *Atmos Environ* 45:1203–1212. <https://doi.org/10.1016/j.atmosenv.2010.06.032>
- Katul GG, Hsieh CI, Bowling D, et al (1999) Spatial variability of turbulent fluxes in the roughness sublayer of an even-aged pine forest. *Boundary-Layer Meteorol* 93:1–28.

- 5520 <https://doi.org/10.1023/A:1002079602069>
 Katul GG, Mahrt L, Poggi D, Sanz C (2004) One- and two-equation models for canopy turbulence. *Boundary-Layer Meteorol* 113:81–109. <https://doi.org/10.1023/B:BOUN.0000037333.48760.e5>
- Katul GG, Oren R, Manzoni S, et al (2012) Evapotranspiration: A process driving mass transport and energy exchange in the soil-plant-atmosphere-climate system. *Rev Geophys* 50:.
 5525 <https://doi.org/10.1029/2011RG000366>
- Kelly KE, Whitaker J, Petty A, et al (2017) Ambient and laboratory evaluation of a low-cost particulate matter sensor. *Environ Pollut* 221:491–500. <https://doi.org/10.1016/j.envpol.2016.12.039>
- Kesselmeier J, Staudt M (1999) Biogenic Volatile Organic Compounds (VOC): An Overview on Emission, Physiology and Ecology. *J Atmos Chem* 33:23–88
- 5530 Khan B, Banzhaf S, Chan E, et al (2020) Development of an atmospheric chemistry model coupled to the PALM model system 6.0: Implementation and first applications. *Geosci Model Dev Discuss* 1–34. <https://doi.org/10.5194/gmd-2020-286>
- Killy DK (1962) On the numerical simulation of buoyant convection. *Tellus XIV*:148–172. [https://doi.org/10.1016/0375-9601\(69\)91031-7](https://doi.org/10.1016/0375-9601(69)91031-7)
- 5535 Kim KH, Kabir E, Kabir S (2015) A review on the human health impact of airborne particulate matter. *Environ. Int.* 74:136–143
- Kim S, Park H, Gruszewski HA, et al (2019) Vortex-induced dispersal of a plant pathogen by raindrop impact. *Proc Natl Acad Sci U S A* 116:4917–4922. <https://doi.org/10.1073/pnas.1820318116>
- Kingham S, Longley I, Salmond JA, et al (2013) Variations in exposure to traffic pollution while travelling by different modes in a low density, less congested city. *Environ Pollut* 181:211–218.
 5540 <https://doi.org/10.1016/j.envpol.2013.06.030>
- Kirkil G, Mirocha JD, Bou-Zeid E, et al (2012) Implementation and evaluation of dynamic subfilter-scale stress models for large-eddy simulation using WRF. *Mon Weather Rev* 140:266–284. <https://doi.org/10.1175/MWR-D-11-00037.1>
- 5545 Klaassen W, Van Breugel PB, Moors EJ, Nieveen JP (2002) Increased heat fluxes near a forest edge. *Theor Appl Climatol* 72:231–243. <https://doi.org/10.1007/s00704-002-0682-8>
- Kleine Deters J, Zalakeviciute R, Gonzalez M, Rybarczyk Y (2017) Modeling PM_{2.5} Urban Pollution Using Machine Learning and Selected Meteorological Parameters. *J Electr Comput Eng* 2017:.
<https://doi.org/10.1155/2017/5106045>
- 5550 Koizumi A, Motoyama J ichi, Sawata K, et al (2010) Evaluation of drag coefficients of poplar-tree crowns by a field test method. *J Wood Sci* 56:189–193. <https://doi.org/10.1007/s10086-009-1091-8>
- Kolmogorov AN (1991) The local structure of turbulence in incompressible viscous fluid for very large Reynolds numbers. *Proc R Soc Lond A* 434:9–13. <https://doi.org/10.1098/rspa.1991.0075>
- Kono T, Tamura T, Ashie Y (2010) Numerical investigations of mean winds within canopies of regularly arrayed cubical buildings under neutral stability conditions. *Boundary-Layer Meteorol* 134:131–155. <https://doi.org/10.1007/s10546-009-9434-y>
- 5555 Krayenhoff ES, Santiago JL, Martilli A, et al (2015) Parametrization of Drag and Turbulence for Urban Neighbourhoods with Trees. *Boundary-Layer Meteorol* 156:157–189. <https://doi.org/10.1007/s10546-015-0028-6>
- 5560 Krol MC, Molemaker MJ, Vilà-Guerau de Arellano J (2000) Effects of turbulence and heterogeneous emissions on photochemically active species in the convective boundary layer. *J Geophys Res* 105:6871–6884
- Kruijt B, Malhi Y, Lloyd J, et al (2000) Turbulence statistics above and within two Amazon rain forest canopies. *Boundary-Layer Meteorol* 94:297–331. <https://doi.org/10.1023/A:1002401829007>
- 5565 Kubiske ME, Foss AR, Burton AJ, et al (2015) Supporting 13 Years of Global Change Research : The History , Technology , and Methods of the Aspen FACE Experiment
- Kulmala M, Dal Maso M, Mäkelä JM, et al (2001) On the formation, growth and composition of nucleation mode particles. *Tellus, Ser B Chem Phys Meteorol* 53:479–490. <https://doi.org/10.3402/tellusb.v53i4.16622>
- 5570 Kulmala M, Riipinen I, Sipilä M, et al (2007) Toward direct measurement of atmospheric nucleation. *Science* (80-) 318:89–92. <https://doi.org/10.1126/science.1144124>
- Kumar P, Ketzler M, Vardoulakis S, et al (2011) Dynamics and dispersion modelling of nanoparticles from road traffic in the urban atmospheric environment—A review. *J Aerosol Sci* 42:580–603. <https://doi.org/10.1016/j.jaerosci.2011.06.001>

- 5575 Kumar P, Morawska L, Martani C, et al (2015) The rise of low-cost sensing for managing air pollution in cities. *Environ Int* 75:199–205. <https://doi.org/10.1016/j.envint.2014.11.019>
- Kwak KH, Baik JJ (2014) Diurnal variation of NO_x and ozone exchange between a street canyon and the overlying air. *Atmos Environ* 86:120–128. <https://doi.org/10.1016/j.atmosenv.2013.12.029>
- Kwak KH, Baik JJ, Ryu YH, Lee SH (2015) Urban air quality simulation in a high-rise building area using a
5580 CFD model coupled with mesoscale meteorological and chemistry-transport models. *Atmos Environ* 100:167–177. <https://doi.org/10.1016/j.atmosenv.2014.10.059>
- Lalic B, Mihailovic DT (2004) An empirical relation describing leaf-area density inside the forest for environmental modeling. *J Appl Meteorol* 43:641–645
- Landrigan PJ, Fuller R, Acosta NJR, et al (2018) The Lancet Commission on pollution and health. *Lancet*
5585 391:462–512. [https://doi.org/10.1016/S0140-6736\(17\)32345-0](https://doi.org/10.1016/S0140-6736(17)32345-0)
- Laothawornkitkul J, Taylor JE, Paul ND, Hewitt CN (2009) Biogenic volatile organic compounds in the Earth system: Tansley review. *New Phytol* 183:27–51. <https://doi.org/10.1111/j.1469-8137.2009.02859.x>
- Larcher W (1995) *Physiological Plant Ecology*, Third. Springer-Verlag, Berlin
- Lau GE, Ngan K, Hon KK (2020) Residence times of airborne pollutants in the urban environment. *Urban*
5590 *Clim* 34:100711. <https://doi.org/10.1016/j.uclim.2020.100711>
- Lee X, Black TA (1993) Atmospheric turbulence within and above a Douglas-fir stand. Part I: Statistical properties of the velocity field. *Boundary-Layer Meteorol* 64:149–174. <https://doi.org/10.1007/BF00705666>
- Lefsky MA, Cohen WB, Acker SA, et al (1999) Lidar remote sensing of the canopy structure and biophysical
5595 properties of Douglas-fir western hemlock forests. *Remote Sens Environ* 70:339–361. [https://doi.org/10.1016/S0034-4257\(99\)00052-8](https://doi.org/10.1016/S0034-4257(99)00052-8)
- Legg BJ, Raupach MR, Coppin PA (1986) Experiments on scalar dispersion within a model plant canopy, part III: An elevated line source. *Boundary-Layer Meteorol* 35:277–302. <https://doi.org/10.1007/BF00123645>
- 5600 Lelieveld J, Butler TM, Crowley JN, et al (2008) Atmospheric oxidation capacity sustained by a tropical forest. *Nature* 452:737–740. <https://doi.org/10.1038/nature06870>
- Lemone MA, Angevine WM, Bretherton CS, et al (2019) 100 Years of Progress in Boundary Layer Meteorology. *Meteorol Monogr* 59:9.1-9.85. <https://doi.org/10.1175/AMSMONOGRAPHS-D-18-0013.1>
- 5605 Leonardi S, Castro IP (2010) Channel flow over large cube roughness: A direct numerical simulation study. *J Fluid Mech* 651:519–539. <https://doi.org/10.1017/S002211200999423X>
- Letzel MO, Krane M, Raasch S (2008) High resolution urban large-eddy simulation studies from street canyon to neighbourhood scale. *Atmos Environ* 42:8770–8784. <https://doi.org/10.1016/j.atmosenv.2008.08.001>
- 5610 Letzger P, Lutz T, Krämer E (2018) Detached Eddy Simulations of the local Atmospheric Flow Field within a Forested Wind Energy Test Site located in Complex Terrain. In: *Journal of Physics: Conference Series*. Institute of Physics Publishing
- Leuning R, Zegelin SJ, Jones K, et al (2008) Measurement of horizontal and vertical advection of CO₂ within a forest canopy. *Agric For Meteorol* 148:1777–1797. <https://doi.org/10.1016/j.agrformet.2008.06.006>
- 5615 Levy JI, Hanna SR (2011) Spatial and temporal variability in urban fine particulate matter concentrations. *Environ Pollut* 159:2009–2015. <https://doi.org/10.1016/j.envpol.2010.11.013>
- Leys C, Ley C, Klein O, et al (2013) *Journal of Experimental Social Psychology* Detecting outliers : Do not use standard deviation around the mean, use absolute deviation around the median. *Exp Soc Psychol* 4–6
- Li Q, Bou-Zeid E (2019) Contrasts between momentum and scalar transport over very rough surfaces. *J Fluid*
5620 *Mech* 32–58. <https://doi.org/10.1017/jfm.2019.687>
- Li XX, Britter RE, Norford LK (2015) Transport processes in and above two-dimensional urban street canyons under different stratification conditions: results from numerical simulation. *Environ Fluid Mech* 15:399–417. <https://doi.org/10.1007/s10652-014-9347-2>
- Liang X, Zou T, Guo B, et al (2015) Assessing Beijing’s PM_{2.5} pollution: Severity, weather impact, APEC
5625 and winter heating. *Proc R Soc A Math Phys Eng Sci* 471:. <https://doi.org/10.1098/rspa.2015.0257>
- Liao J, Wang T, Wang X, et al (2014) Impacts of different urban canopy schemes in WRF/Chem on regional climate and air quality in Yangtze River Delta, China. *Atmos Res* 145–146:226–243. <https://doi.org/10.1016/j.atmosres.2014.04.005>
- Lien FS, Yee E (2005) Numerical modelling of the turbulent flow developing within and over a 3-D building

- 5630 array, part III: A distributed drag force approach, its implementation and application. *Boundary-Layer Meteorol* 114:287–313. <https://doi.org/10.1007/s10546-004-1987-1>
- Lien FS, Yee E, Cheng Y (2004) Simulation of mean flow and turbulence over a 2D building array using high-resolution CFD and a distributed drag force approach. *J Wind Eng Ind Aerodyn* 92:117–158. <https://doi.org/10.1016/j.jweia.2003.10.005>
- 5635 Lien FS, Yee E, Wilson JD (2005) Numerical modelling of the turbulent flow developing within and over a 3-D building array, part II: A mathematical foundation for a distributed drag force approach. *Boundary-Layer Meteorol* 114:245–285. <https://doi.org/10.1007/s10546-004-9242-3>
- Lin M, Hang J, Li Y, et al (2014) Quantitative ventilation assessments of idealized urban canopy layers with various urban layouts and the same building packing density. *Build Environ* 79:152–167. <https://doi.org/10.1016/j.buildenv.2014.05.008>
- 5640 Lin M, Katul GG, Khlystov A (2012) A branch scale analytical model for predicting the vegetation collection efficiency of ultrafine particles. *Atmos Environ* 51:293–302. <https://doi.org/10.1016/j.atmosenv.2012.01.004>
- Lin X, Chamecki M, Katul GG, Yu X (2018a) Effects of leaf area index and density on ultrafine particle deposition onto forest canopies: A LES study. *Atmos Environ* 189:153–163. <https://doi.org/10.1016/j.atmosenv.2018.06.048>
- 5645 Lin Y, Zou J, Yang W, Li CQ (2018b) A review of recent advances in research on PM_{2.5} in China. *Int J Environ Res Public Health* 15:. <https://doi.org/10.3390/ijerph15030438>
- Litschike T, Kuttler W (2008) On the reduction of urban particle concentration by vegetation - A review. *Meteorol Zeitschrift* 17:229–240. <https://doi.org/10.1127/0941-2948/2008/0284>
- 5650 Liu Z, Ishihara T, He X, Niu H (2016) LES study on the turbulent flow fields over complex terrain covered by vegetation canopy. *J Wind Eng Ind Aerodyn* 155:60–73. <https://doi.org/10.1016/j.jweia.2016.05.002>
- Lo KW, Ngan K (2015) Characterising the pollutant ventilation characteristics of street canyons using the tracer age and age spectrum. *Atmos Environ* 122:611–621. <https://doi.org/10.1016/j.atmosenv.2015.10.023>
- 5655 Lo KW, Ngan K (2017) Characterizing ventilation and exposure in street canyons using Lagrangian particles. *J Appl Meteorol Climatol* 56:1177–1194. <https://doi.org/10.1175/JAMC-D-16-0168.1>
- Loescher HW, Law BE, Mahrt L, et al (2006) Uncertainties in, and interpretation of, carbon flux estimates using the eddy covariance technique. *J Geophys Res Atmos* 111:D21S90. <https://doi.org/10.1029/2005JD006932>
- 5660 Lorenz EN (1963) Deterministic Nonperiodic Flow. *J Atmos Sci* 20:130–141
- Louka P, Belcher SE, Harrison RM (2000) Coupling between air flow in streets and the well-developed boundary layer aloft. *Atmos Environ* 34:2613–2621. [https://doi.org/10.1016/S1352-2310\(99\)00477-X](https://doi.org/10.1016/S1352-2310(99)00477-X)
- Luyssaert S, Schulze ED, Börner A, et al (2008) Old-growth forests as global carbon sinks. *Nature* 455:213–215. <https://doi.org/10.1038/nature07276>
- 5665 Ma Y, Liu H (2019) An Advanced Multiple-Layer Canopy Model in the WRF Model With Large-Eddy Simulations to Simulate Canopy Flows and Scalar Transport Under Different Stability Conditions. *J Adv Model Earth Syst* 11:2330–2351. <https://doi.org/10.1029/2018MS001347>
- Ma Y, Liu H, Liu Z, et al (2020) Influence of Forest-Edge Flows on Scalar Transport with Different Vertical Distributions of Foliage and Scalar Sources. *Boundary-Layer Meteorol* 174:99–117. <https://doi.org/10.1007/s10546-019-00475-y>
- 5670 Macdonald RW (2000) Modelling the mean velocity profile in the urban canopy layer. *Boundary-Layer Meteorol* 97:25–45. <https://doi.org/10.1023/A:1002785830512>
- MacKenzie AR, Krause S, Hart KM, et al (2021) BIFoR FACE: Water–soil–vegetation–atmosphere data from a temperate deciduous forest catchment, including under elevated CO₂. *Hydrol Process* 35:1–8. <https://doi.org/10.1002/hyp.14096>
- 5675 MacKenzie AR, Langford B, Pugh TAM, et al (2011) The atmospheric chemistry of trace gases and particulate matter emitted by different land uses in Borneo. *Philos Trans R Soc B Biol Sci* 366:3177–3195. <https://doi.org/10.1098/rstb.2011.0053>
- 5680 Magnago LFS, Rocha MF, Meyer L, et al (2015) Microclimatic conditions at forest edges have significant impacts on vegetation structure in large Atlantic forest fragments. *Biodivers Conserv* 24:2305–2318. <https://doi.org/10.1007/s10531-015-0961-1>
- Mahrt L (2014) Stably stratified atmospheric boundary layers. *Annu Rev Fluid Mech* 46:23–45. <https://doi.org/10.1146/annurev-fluid-010313-141354>

- 5685 Mahrt L (2019) Microfronts in the nocturnal boundary layer. *Q J R Meteorol Soc* 145:546–562. <https://doi.org/10.1002/qj.3451>
- Mahrt L (2017a) The near-surface evening transition. *Q J R Meteorol Soc* 143:2940–2948. <https://doi.org/10.1002/qj.3153>
- Mahrt L (1981) The early evening boundary layer transition. *Q J R Meteorol Soc* 107:329–343. <https://doi.org/10.1002/qj.49710745205>
- 5690 Mahrt L (2017b) Lee mixing and nocturnal structure over gentle topography. *J Atmos Sci* 74:1989–1999. <https://doi.org/10.1175/JAS-D-16-0338.1>
- Mahrt L (2000) Surface heterogeneity and vertical structure of the boundary layer. *Boundary-Layer Meteorol* 96:33–62. <https://doi.org/10.1023/A:1002482332477>
- 5695 Mahrt L, Sun J, Blumen W, et al (1998) Nocturnal boundary-layer regimes. *Boundary-Layer Meteorol* 88:255–278. <https://doi.org/10.1023/A:1001171313493>
- Maitani T (1979) An observational study of wind-induced waving of plants. *Boundary-Layer Meteorol* 16:49–65. <https://doi.org/10.1007/BF03335354>
- Makar PA, Staebler RM, Akingunola A, et al (2017) The effects of forest canopy shading and turbulence on boundary layer ozone. *Nat Commun* 8:1–14. <https://doi.org/10.1038/ncomms15243>
- 5700 Margairaz F, Pardyjak ER, Calaf M (2020) Surface Thermal Heterogeneities and the Atmospheric Boundary Layer: The Relevance of Dispersive Fluxes. *Boundary-Layer Meteorol* 175:369–395. <https://doi.org/10.1007/s10546-020-00509-w>
- Martens CS, Shay TJ, Mendlovitz HP, et al (2004) Radon fluxes in tropical forest ecosystems of Brazilian Amazonia: Night-time CO₂ net ecosystem exchange derived from radon and eddy covariance methods. *Glob Chang Biol* 10:618–629. <https://doi.org/10.1111/j.1365-2486.2004.00764.x>
- 5705 Martilli A, Clappier A, Rotach MW (2002) An urban surface exchange parameterisation for mesoscale models. *Boundary-Layer Meteorol* 104:261–304. <https://doi.org/10.1023/A:1016099921195>
- Mason PJ, Thomson DJ (1992) Stochastic backscatter in large-eddy simulations of boundary layers. *J Fluid Mech* 242:51–78. <https://doi.org/10.1017/S0022112092002271>
- 5710 Mason PJ, Thomson DJ (1987) Large-eddy simulations of the neutral-static-stability planetary boundary layer. *Q J R Meteorol Soc* 113:413–443. <https://doi.org/10.1256/qj.03.130>
- Massman WJ, Lee X (2002) Eddy covariance flux corrections and uncertainties in long-term studies of carbon and energy exchanges. *Agric For Meteorol* 113:121–144
- 5715 Mauder M, Foken T, Cuxart J (2020) *Surface-Energy-Balance Closure over Land: A Review*. Springer Netherlands
- Maurer KD, Bohrer G, Kenny WT, Ivanov VY (2015) Large-eddy simulations of surface roughness parameter sensitivity to canopy-structure characteristics. *Biogeosciences* 12:2533–2548. <https://doi.org/10.5194/bg-12-2533-2015>
- 5720 Mavroidis I, Andronopoulos S, Bartzis JG (2012) Computational simulation of the residence of air pollutants in the wake of a 3-dimensional cubical building. The effect of atmospheric stability. *Atmos Environ* 63:189–202. <https://doi.org/10.1016/j.atmosenv.2012.09.032>
- Mayer H (1999) Mayer: Cities. *Atmos Environ* 33:4029–4037
- 5725 McHugh ID, Beringer J, Cunningham SC, et al (2017) Interactions between nocturnal turbulent flux, storage and advection at an “ideal” eucalypt woodland site. *Biogeosciences* 14:3027–3050. <https://doi.org/10.5194/bg-14-3027-2017>
- McLeod AR, Long SP (1999) Free-air Carbon Dioxide Enrichment (FACE) in Global Change Research: A Review. *Adv Ecol Res* 28:1–56. [https://doi.org/10.1016/S0065-2504\(08\)60028-8](https://doi.org/10.1016/S0065-2504(08)60028-8)
- McNaughton KG (1989) Micrometeorology of shelter belts and forest edges. *Philos Trans - R Soc London, B* 324:351–368. <https://doi.org/10.1098/rstb.1989.0052>
- 5730 Met Office (2021) Ground-breaking research in the Amazon announced. In: Press Off. <https://www.metoffice.gov.uk/about-us/press-office/news/weather-and-climate/2021/ground-breaking-research-in-the-amazon-announced>. Accessed 5 May 2022
- Miglietta F, Peressotti A, Vaccari FP, et al (2001) Free-air CO₂ enrichment (FACE) of a poplar plantation: The POPFACE fumigation system. *New Phytol* 150:465–476. <https://doi.org/10.1046/j.1469-8137.2001.00115.x>
- 5735 Miguel AF, Van De Braak NJ, Silva AM, Bot GPA (2001) Wind-induced airflow through permeable materials. Part I: The motion equation. *J Wind Eng Ind Aerodyn* 89:45–57. [https://doi.org/10.1016/S0167-6105\(00\)00027-1](https://doi.org/10.1016/S0167-6105(00)00027-1)

- 5740 Moeng CH, Dudhia J, Klemp J, Sullivan PP (2007) Examining Two-Way Grid Nesting for Large Eddy Simulation of the PBL Using the WRF Model. <https://doi.org/10.1175/MWR3406.1>
- Moltchanov S, Bohbot-Raviv Y, Duman T, Shavit U (2015) Canopy edge flow: A momentum balance analysis. *Water Resour Res* 51:. <https://doi.org/10.1002/2014WR015397>
- Moltchanov S, Bohbot-Raviv Y, Shavit U (2011) Dispersive Stresses at the Canopy Upstream Edge. *Boundary-Layer Meteorol* 139:333–351. <https://doi.org/10.1007/s10546-010-9582-0>
- 5745 Momo Takoudjou S, Ploton P, Sonké B, et al (2018) Using terrestrial laser scanning data to estimate large tropical trees biomass and calibrate allometric models: A comparison with traditional destructive approach. *Methods Ecol Evol* 9:905–916. <https://doi.org/10.1111/2041-210X.12933>
- Moncrieff J, Clement R, Finnigan JJ, Meyers TP (2004) Averaging, Detrending, and Filtering of Eddy Covariance Time Series. In: *Handbook of Micrometeorology*. pp 7–31
- 5750 Monin AS, Obukhov AM (1954) Basic laws of turbulent mixing in the surface layer of the atmosphere. *Akad Nauk SSSR Geofiz Inst Tr* 24:163–187
- Monteith JL, Unsworth MH (2008) *Principles of Environmental Physics*, Fourth. Academic Press, Oxford
- Morse AP, Gardiner BA, Marshall BJ (2002) Mechanics controlling turbulence development across a forest edge. *Boundary-Layer Meteorol* 103:227–251
- 5755 Moser RD, Haering SW, Yalla GR (2021) Statistical Properties of Subgrid-Scale Turbulence Models. *Annu Rev Fluid Mech* 53:255–286. <https://doi.org/10.1146/annurev-fluid-060420-023735>
- Mueller E, Mell W, Simeoni A (2014) Large eddy simulation of forest canopy flow for wildland fire modeling. *Can J For Res* 44:1534–1544. <https://doi.org/10.1139/cjfr-2014-0184>
- 5760 Muller CL, Chapman L, Grimmond CSB, et al (2013a) Toward a standardized metadata protocol for urban meteorological networks. *Bull Am Meteorol Soc* 94:1161–1185. <https://doi.org/10.1175/BAMS-D-12-00096.1>
- Muller CL, Chapman L, Grimmond CSB, et al (2013b) Sensors and the city: A review of urban meteorological networks. *Int J Climatol* 33:1585–1600. <https://doi.org/10.1002/joc.3678>
- 5765 Murena F (2012) Monitoring and modelling carbon monoxide concentrations in a deep street canyon: Application of a two-box model. *Atmos Pollut Res* 3:311–316. <https://doi.org/10.5094/APR.2012.034>
- Murlis J, Willis MA, Cardé RT (2000) Spatial and temporal structures of pheromone plumes in fields and forests. *Physiol Entomol* 25:211–222. <https://doi.org/10.1046/j.1365-3032.2000.00176.x>
- Nakayama H, Takemi T, Nagai H (2011) LES analysis of the aerodynamic surface properties for turbulent flows over building arrays with various geometries. *J Appl Meteorol Climatol* 50:1692–1712. <https://doi.org/10.1175/2011JAMC2567.1>
- 5770 Nebenführ B, Davidson L (2015) Large-Eddy Simulation Study of Thermally Stratified Canopy Flow. *Boundary-Layer Meteorol* 156:253–276. <https://doi.org/10.1007/s10546-015-0025-9>
- Neumann HH, Den Hartog G, Shaw RH (1989) Leaf area measurements based on hemispheric photographs and leaf-litter collection in a deciduous forest during autumn leaf-fall. *Agric For Meteorol* 45:325–345. [https://doi.org/10.1016/0168-1923\(89\)90052-X](https://doi.org/10.1016/0168-1923(89)90052-X)
- 5775 Nguyen DL (2014) A Brief Review of Air Quality Models and Their Applications. *Open J Atmos Clim Chang* 1:60–80
- Niinemets Ü (2010) Mild versus severe stress and BVOCs: thresholds, priming and consequences. *Trends Plant Sci* 15:145–153. <https://doi.org/10.1016/j.tplants.2009.11.008>
- 5780 Nikolova I, Cai X, Alam MS, et al (2018) The influence of particle composition upon the evolution of urban ultrafine diesel particles on the neighbourhood scale. *Atmos Chem Phys* 18:17143–17155. <https://doi.org/10.5194/acp-18-17143-2018>
- Norby RJ, De Kauwe MG, Domingues TF, et al (2016) Model-data synthesis for the next generation of forest free-air CO₂ enrichment (FACE) experiments. *New Phytol* 209:17–28. <https://doi.org/10.1111/nph.13593>
- 5785 Norby RJ, Wullschlegel SD, Hanson PJ, et al (2006) CO₂ Enrichment of a Deciduous Forest: The Oak Ridge FACE Experiment. In: Nösberger J, Long SP, Norby RJ, et al. (eds) *Managed Ecosystems and CO₂. Ecological Studies (Analysis and Synthesis)*. Springer, Berlin, pp 231–251
- 5790 Nordbo A, Järvi L, Haapanala S, et al (2013) Intra-City Variation in Urban Morphology and Turbulence Structure in Helsinki, Finland. *Boundary-Layer Meteorol* 146:469–496. <https://doi.org/10.1007/s10546-012-9773-y>
- Norros V, Rannik Ü, Hussein T, et al (2014) Do small spores disperse further than large spores? *Ecology* 95:1612–1621. <https://doi.org/10.1890/13-0877.1>

- 5795 Nottrott A, Kleissl J, Keeling R (2014) Modeling passive scalar dispersion in the atmospheric boundary layer with WRF large-eddy simulation. *Atmos Environ* 82:172–182.
<https://doi.org/10.1016/j.atmosenv.2013.10.026>
- Obermeier F (2006) Prandtl 's Mixing Length Model - Revisited 2 Basic Equations. *Pamm* 6:577–578.
<https://doi.org/10.1002/pamm.200610>
- 5800 Obukhov AM (1946) ‘Turbulentnost’ v temperaturnoj – neodnorodnoj atmosfere (Turbulence in an Atmosphere with a Non-uniform Temperature)’. *Tr Inst Theor Geofiz AN SSSR* 1:95–115
- Okaze T, Ono A, Mochida A, et al (2015) Evaluation of turbulent length scale within urban canopy layer based on LES data. *J Wind Eng Ind Aerodyn* 144:79–83. <https://doi.org/10.1016/j.jweia.2014.11.016>
- Oke TR (1988a) *Boundary Layer Climates*, Second. Methuen, London
- 5805 Oke TR (1988b) The urban energy balance. *Prog Phys Geogr* 12:471–508.
<https://doi.org/10.1177/030913338801200401>
- Oliphant AJ (2012) Terrestrial Ecosystem-Atmosphere Exchange of CO₂, Water and Energy from FLUXNET; Review and Meta-Analysis of a Global in-situ Observatory. *Geogr Compass* 6:689–705.
<https://doi.org/10.1111/gec3.12009>
- 5810 Orlanski I (1975) A Rational Subdivision of Scales for Atmospheric Processes. *Bull Am Meteorol Soc* 56:527–530. <https://doi.org/10.1175/1520-0477-56.5.527>
- Orrell D, Smith L, Barkmeijer J, Palmer TN (2001) Model error in weather forecasting. *Nonlinear Process Geophys* 8:357–371. <https://doi.org/10.5194/npg-8-357-2001>
- Orszag SA (1970) Analytical theories of turbulence. *J Fluid Mech* 41:363–386.
<https://doi.org/10.1017/S0022112070000642>
- 5815 Pace R, Grote R (2020) Deposition and Resuspension Mechanisms Into and From Tree Canopies: A Study Modeling Particle Removal of Conifers and Broadleaves in Different Cities. *Front For Glob Chang* 3:1–12. <https://doi.org/10.3389/ffgc.2020.00026>
- Palmer H, Gardiner BA, Hislop M, et al (1997) *Forestry Commission Technical Paper 21: Trees for shelter*
- 5820 Palmer T (2015) Build imprecise supercomputers. *Nature* 526:32–33
- Pan Y, Chamecki M, Isard SA (2014a) Large-eddy simulation of turbulence and particle dispersion inside the canopy roughness sublayer. *J Fluid Mech* 753:499–534. <https://doi.org/10.1017/jfm.2014.379>
- Pan Y, Follett E, Chamecki M, Nepf HM (2014b) Strong and weak, unsteady reconfiguration and its impact on turbulence structure within plant canopies. *Phys Fluids* 26:105102. <https://doi.org/10.1063/1.4898395>
- 5825 Patton EG, Finnigan JJ (2012) Canopy Turbulence. In: *Handbook of Environmental Fluid Dynamics, Volume One*. CRC Press, pp 311–328
- Patton EG, Horst TW, Sullivan PP, et al (2011) The canopy horizontal array turbulence study. *Bull Am Meteorol Soc* 92:593–611. <https://doi.org/10.1175/2010BAMS2614.1>
- Patton EG, Katul GG (2009) Turbulent pressure and velocity perturbations induced by gentle hills covered with sparse and dense canopies. *Boundary-Layer Meteorol* 133:189–217.
<https://doi.org/10.1007/s10546-009-9427-x>
- 5830 Patton EG, Sullivan PP, Shaw RH, et al (2016) Atmospheric stability influences on coupled boundary layer and canopy turbulence. *J Atmos Sci* 73:1621–1647. <https://doi.org/10.1175/JAS-D-15-0068.1>
- Paul-Limoges E, Wolf S, Eugster W, et al (2017) Below-canopy contributions to ecosystem CO₂ fluxes in a temperate mixed forest in Switzerland. *Agric For Meteorol* 247:582–596.
<https://doi.org/10.1016/j.agrformet.2017.08.011>
- 5835 Paw U KT, Qiu J, Su, Hong-bing, et al (1995) Surface renewal analysis: a new method to obtain scalar fluxes. *Agric For Meteorol* 74:119–137
- Pearce H, Levine JG, Cai X, Rob Mackenzie A (2021) Introducing the green infrastructure for roadside air quality (Gi4raq) platform: Estimating site-specific changes in the dispersion of vehicular pollution close to source. *Forests* 12:. <https://doi.org/10.3390/f12060769>
- 5840 Peng Z, Sun J (2014) Characteristics of the Drag Coefficient in the Roughness Sublayer over a Complex Urban Surface. *Boundary-Layer Meteorol* 153:569–580. <https://doi.org/10.1007/s10546-014-9949-8>
- Peñuelas J, Staudt M (2010) BVOCs and global change. *Trends Plant Sci* 15:133–144.
<https://doi.org/10.1016/j.tplants.2009.12.005>
- 5845 Petroff A, Mailliat A, Amielh M, Anselmet F (2008) Aerosol dry deposition on vegetative canopies. Part I: Review of present knowledge. *Atmos Environ* 42:3625–3653.
<https://doi.org/10.1016/j.atmosenv.2007.09.043>
- Philips DA, Rossi R, Iaccarino G (2013) Large-eddy simulation of passive scalar dispersion in an urban-like

- 5850 canopy. *J Fluid Mech* 723:404–428. <https://doi.org/10.1017/jfm.2013.135>
- Pierce JR, Leaitch WR, Liggio J, et al (2012) Nucleation and condensational growth to CCN sizes during a sustained pristine biogenic SOA event in a forested mountain valley. *Atmos Chem Phys* 12:3147–3163. <https://doi.org/10.5194/acp-12-3147-2012>
- Piomelli U, Cabot WH, Moin P, Lee S (1991) Subgrid-scale backscatter in turbulent and transitional flows. *Phys Fluids A* 3:1766–1771. <https://doi.org/10.1063/1.857956>
- 5855 Pivato D, Dupont S, Brunet Y (2014) A simple tree swaying model for forest motion in windstorm conditions. *Trees - Struct Funct* 28:281–293. <https://doi.org/10.1007/s00468-013-0948-z>
- Poëtte C, Gardiner BA, Dupont S, et al (2017) The Impact of Landscape Fragmentation on Atmospheric Flow: A Wind-Tunnel Study. *Boundary-Layer Meteorol* 163:393–421. <https://doi.org/10.1007/s10546-017-0238-1>
- 5860 Poggi D, Katul GG (2008a) Micro- and macro-dispersive fluxes in canopy flows. *Acta Geophys* 56:778–799. <https://doi.org/10.2478/s11600-008-0029-7>
- Poggi D, Katul GG (2008b) The effect of canopy roughness density on the constitutive components of the dispersive stresses. *Exp Fluids* 45:111–121. <https://doi.org/10.1007/s00348-008-0467-7>
- 5865 Poggi D, Katul GG, Albertson JD (2004a) A note on the contribution of dispersive fluxes to momentum transfer within canopies. *Boundary-Layer Meteorol* 111:615–621. <https://doi.org/10.1023/B:BOUN.0000016563.76874.47>
- Poggi D, Katul GG, Finnigan JJ, Belcher SE (2008) Analytical models for the mean flow inside dense canopies on gentle hilly terrain. *Q J R Meteorol Soc* 134:1095–1112. <https://doi.org/10.1002/qj.276>
- 5870 Poggi D, Porporato A, Ridolfi L, et al (2004b) The effect of vegetation density on canopy sub-layer turbulence. *Boundary-Layer Meteorol* 111:565–587. <https://doi.org/10.1023/B:BOUN.0000016576.05621.73>
- Pope FD, Gatari M, Ng'ang'a D, et al (2018) Airborne particulate matter monitoring in Kenya using calibrated low-cost sensors. *Atmos Chem Phys* 18:15403–15418. <https://doi.org/10.5194/acp-18-15403-2018>
- 5875 Powers JG, Klemp JB, Skamarock WC, et al (2017) The weather research and forecasting model: Overview, system efforts, and future directions. *Bull Am Meteorol Soc* 98:1717–1737. <https://doi.org/10.1175/BAMS-D-15-00308.1>
- Prandtl L, Tietjens OKG (1957) *Applied hydro-and aeromechanics: based on lectures of L. Prandtl, Volume 2.* Courier Corporation
- 5880 Pryor SC, Barthelmie RJ, Sørensen LL, et al (2008) Upward fluxes of particles over forests: When, where, why? *Tellus, Ser B Chem Phys Meteorol* 60 B:372–380. <https://doi.org/10.1111/j.1600-0889.2008.00341.x>
- Pugh TAM, MacKenzie AR, Langford B, et al (2011) The influence of small-scale variations in isoprene concentrations on atmospheric chemistry over a tropical rainforest. *Atmos Chem Phys* 11:4121–4134. <https://doi.org/10.5194/acp-11-4121-2011>
- 5885 Py C, De Langre E, Moulia B (2006) A frequency lock-in mechanism in the interaction between wind and crop canopies. *J Fluid Mech* 568:425–449. <https://doi.org/10.1017/S0022112006002667>
- Pyle JA, Warwick NJ, Harris NRP, et al (2011) The impact of local surface changes in Borneo on atmospheric composition at wider spatial scales: Coastal processes, land-use change and air quality. *Philos Trans R Soc B Biol Sci* 366:3210–3224. <https://doi.org/10.1098/rstb.2011.0060>
- 5890 Queck R, Bernhofer C, Bienert A, Schlegel F (2016) The TurbEFA Field Experiment—Measuring the Influence of a Forest Clearing on the Turbulent Wind Field. *Boundary-Layer Meteorol* 160:397–423. <https://doi.org/10.1007/s10546-016-0151-z>
- 5895 Queck R, Bienert A, Maas HG, et al (2012) Wind fields in heterogeneous conifer canopies: Parameterisation of momentum absorption using high-resolution 3D vegetation scans. *Eur J For Res* 131:165–176. <https://doi.org/10.1007/s10342-011-0550-0>
- R Core Team (2021) *R: A language and environment for statistical computing*
- Raine JK, Stevenson DC (1977) Wind Protection by Model Fences in a Simulated Atmospheric Boundary Layer. *J Ind Aerodyn* 2:159–180
- 5900 Ramamurthy P, Pardyjak ER (2015) Turbulent Transport of Carbon Dioxide over a Highly Vegetated Suburban Neighbourhood. *Boundary-Layer Meteorol* 157:461–479. <https://doi.org/10.1007/s10546-015-0074-0>
- Ramos FM, Bolzan MJA, Sá LDA, Rosa RR (2004) Atmospheric turbulence within and above an Amazon

- 5905 forest. *Phys D Nonlinear Phenom* 193:278–291. <https://doi.org/10.1016/j.physd.2004.01.026>
- Rap A, Scott CE, Reddington CL, et al (2018) Enhanced global primary production by biogenic aerosol via diffuse radiation fertilization. *Nat Geosci* 11:640–644. <https://doi.org/10.1038/s41561-018-0208-3>
- Raunonen P, Casella E, Calders K, et al (2015) Massive-scale tree modelling from TLS data. *ISPRS Ann Photogramm Remote Sens Spat Inf Sci* 2:189–196. <https://doi.org/10.5194/isprsannals-II-3-W4-189-2015>
- 5910 Raupach MR (1989) Applying Lagrangian fluid mechanics to infer scalar source distributions from concentration profiles in plant canopies. *Agric For Meteorol* 47:85–108. [https://doi.org/10.1016/0168-1923\(89\)90089-0](https://doi.org/10.1016/0168-1923(89)90089-0)
- Raupach MR, Antonia RA, Rajagopalan S (1991) Rough-wall turbulent boundary layers. *Appl Mech Rev* 44:
- 5915 Raupach MR, Bradley EF, Ghadiri H (1987) A wind tunnel investigation into the aerodynamic effect of forest clearings on the nesting of Abbott’s booby on Christmas Island. Canberra, Australia
- Raupach MR, Coppin PA, Legg BJ (1986) Experiments on scalar dispersion within a model plant canopy part I: The turbulence structure. *Boundary-Layer Meteorol* 35:21–52. <https://doi.org/10.1007/BF00117300>
- Raupach MR, Finnigan JJ, Brunet Y (1996) Coherent Eddies and Turbulence in Vegetation Canopies: The Mixing-Layer Analogy. *Boundary-Layer Meteorol 25th Anniv Vol 1970–1995* 351–382. https://doi.org/10.1007/978-94-017-0944-6_15
- 5920 Raupach MR, Shaw RH (1982) Averaging procedures for flow within vegetation canopies. *Boundary-Layer Meteorol* 22:79–90. <https://doi.org/10.1007/BF00128057>
- Raupach MR, Thom AS (1981) Turbulence in and above plant canopies. *Annu Rev fluid Mech Vol 13* 97–129. <https://doi.org/10.1146/annurev.fl.13.010181.000525>
- 5925 Reynolds AM (2012) Incorporating sweeps and ejections into Lagrangian stochastic models of spore trajectories within plant canopy turbulence: Modeled contact distributions are heavy-tailed. *Phytopathology* 102:1026–1033. <https://doi.org/10.1094/PHYTO-01-12-0002>
- Reynolds O (1895) On the dynamical theory of incompressible fluids and the de-termination of the criterion. *Philos Trans R Soc A Math Phys Eng Sci* 10:. <https://doi.org/https://doi.org/10.1098/rsta.1895.0004>
- 5930 Riutta T, Slade EM, Morecroft MD, et al (2014) Living on the edge: Quantifying the structure of a fragmented forest landscape in England. *Landsc Ecol* 29:949–961. <https://doi.org/10.1007/s10980-014-0025-z>
- Rominger JT, Nepf HM (2011) Flow adjustment and interior flow associated with a rectangular porous obstruction. *J Fluid Mech* 680:636–659. <https://doi.org/10.1017/jfm.2011.199>
- 5935 Ross AN (2008) Large-eddy simulations of flow over forested ridges. *Boundary-Layer Meteorol* 128:59–76. <https://doi.org/10.1007/s10546-008-9278-x>
- Ross AN, Harman IN (2015) The Impact of Source Distribution on Scalar Transport over Forested Hills. *Boundary-Layer Meteorol* 156:211–230. <https://doi.org/10.1007/s10546-015-0029-5>
- Ross AN, Vosper SB (2005) Neutral turbulent flow over forested hills. *Q J R Meteorol Soc* 131:1841–1862. <https://doi.org/10.1256/qj.04.129>
- 5940 Rotach MW (1999) On the influence of the urban roughness sublayer on turbulence and dispersion. *Atmos Environ* 33:4001–4008. [https://doi.org/10.1016/S1352-2310\(99\)00141-7](https://doi.org/10.1016/S1352-2310(99)00141-7)
- Roth M (2000) Review of atmospheric turbulence over cities. *Q J R Meteorol Soc* 126:941–990. <https://doi.org/10.1256/smsqj.56408>
- 5945 Rozema W, Bae HJ, Moin P, Verstappen R (2015) Minimum-dissipation models for large-eddy simulation. *Phys Fluids* 27:. <https://doi.org/10.1063/1.4928700>
- Rudnicki M, Mitchell SJ, Novak MD (2004) Wind tunnel measurements of crown streamlining for drag relationships for three conifer species. *Can J For Res* 34:666–676. <https://doi.org/10.1139/x03-233>
- Rummel U (2005) Turbulent exchange of ozone and nitrogen oxides between an amazonian rain forest and the atmosphere. University of Bayreuth
- 5950 Rummel U, Ammann C, Meixner FX (2002) Characterizing turbulent trace gas exchange above a dense tropical rain forest using wavelet and surface renewal analysis. *15th AMS Symp Bound Layers Turbul* 602–605
- Russell ES, Liu H, Gao Z, et al (2016) Turbulence dependence on winds and stability in a weak-wind canopy sublayer over complex terrain. *J Geophys Res* 121:11502–11515. <https://doi.org/10.1002/2016JD025057>
- 5955 Ruth RH, Yoder RA (1953) Reducing wind damage in the forests of the Oregon coast range
- Sabatini FM, Burrascano S, Keeton WS, et al (2018) Where are Europe’s last primary forests? *Divers Distrib* 24:1426–1439. <https://doi.org/10.1111/ddi.12778>
- Salim MH, Schlünzen KH, Grawe D (2015) Including trees in the numerical simulations of the wind flow in

- 5960 urban areas: Should we care? *J Wind Eng Ind Aerodyn* 144:84–95.
<https://doi.org/10.1016/j.jweia.2015.05.004>
- Salim SM, Buccolieri R, Chan A, Di Sabatino S (2011a) Numerical simulation of atmospheric pollutant dispersion in an urban street canyon: Comparison between RANS and LES. *J Wind Eng Ind Aerodyn* 99:103–113. <https://doi.org/10.1016/j.jweia.2010.12.002>
- 5965 Salim SM, Cheah SC, Chan A (2011b) Numerical simulation of dispersion in urban street canyons with avenue-like tree plantings: Comparison between RANS and LES. *Build Environ* 46:1735–1746.
<https://doi.org/10.1016/j.buildenv.2011.01.032>
- Salizzoni P, Marro M, Soulhac L, et al (2011) Turbulent Transfer Between Street Canyons and the Overlying Atmospheric Boundary Layer. *Boundary-Layer Meteorol* 141:393–414. <https://doi.org/10.1007/s10546-011-9641-1>
- 5970 Santiago JL, Martilli A (2010) A Dynamic Urban Canopy Parameterization for Mesoscale Models Based on Computational Fluid Dynamics Reynolds-Averaged Navier-Stokes Microscale Simulations. *Boundary-Layer Meteorol* 137:417–439. <https://doi.org/10.1007/s10546-010-9538-4>
- Schindler D, Fugmann H, Schönborn J, Mayer H (2012) Coherent response of a group of plantation-grown Scots pine trees to wind loading. *Eur J For Res* 131:191–202. <https://doi.org/10.1007/s10342-010-0474-0>
- Schindler D, Schönborn J, Fugmann H, Mayer H (2013) Responses of an individual deciduous broadleaved tree to wind excitation. *Agric For Meteorol* 177:69–82. <https://doi.org/10.1016/j.agrformet.2013.04.001>
- 5980 Schlegel F, Stiller J, Bienert A, et al (2012) Large-Eddy Simulation of Inhomogeneous Canopy Flows Using High Resolution Terrestrial Laser Scanning Data. *Boundary-Layer Meteorol* 142:223–243.
<https://doi.org/10.1007/s10546-011-9678-1>
- Schlegel F, Stiller J, Bienert A, et al (2015) Large-Eddy Simulation Study of the Effects on Flow of a Heterogeneous Forest at Sub-Tree Resolution. *Boundary-Layer Meteorol* 154:27–56.
<https://doi.org/10.1007/s10546-014-9962-y>
- 5985 Schlesinger WH, Bernhardt ES, DeLucia EH, et al (2006) The Duke Forest FACE Experiment: CO₂ Enrichment of a Loblolly Pine Forest. In: Nösberger J, Long SP, Norby RJ, et al. (eds) *Managed Ecosystems and CO₂: Case Studies, Processes, and Perspectives*. Springer-Verlag, Berlin, pp 197–212
- Schmid MF, Lawrence GA, Parlange MB, Giometto MG (2019) Volume Averaging for Urban Canopies. *Boundary-Layer Meteorol* 173:349–372. <https://doi.org/10.1007/s10546-019-00470-3>
- 5990 Schmidt M, Jochheim H, Kersebaum KC, et al (2017) Gradients of microclimate, carbon and nitrogen in transition zones of fragmented landscapes – a review. *Agric. For. Meteorol.* 232:659–671
- Schneider FD, Kükenbrink D, Schaepman ME, et al (2019) Quantifying 3D structure and occlusion in dense tropical and temperate forests using close-range LiDAR. *Agric For Meteorol* 268:249–257.
<https://doi.org/10.1016/j.agrformet.2019.01.033>
- 5995 Scholes RJ (2017) Taking the Mumbo Out of the Jumbo: Progress Towards a Robust Basis for Ecological Scaling. *Ecosystems* 20:4–13. <https://doi.org/10.1007/s10021-016-0047-2>
- Schrötte J, Dörnbrack A (2013) Turbulence structure in a diabatically heated forest canopy composed of fractal Pythagoras trees. *Theor Comput Fluid Dyn* 27:337–359. <https://doi.org/10.1007/s00162-012-0284-8>
- 6000 Schuepp PH (1993) Tansley Review No. 59 Leaf boundary layers. *New Phytol* 125:477–507.
<https://doi.org/10.1111/j.1469-8137.1993.tb03898.x>
- Schymanski SJ, Or D (2016) Wind increases leaf water use efficiency. *Plant Cell Environ* 39:1448–1459.
<https://doi.org/10.1111/pce.12700>
- Seinfeld JH, Pandis SN (2016) *Atmospheric chemistry and physics: from air pollution to climate change*, Third. John Wiley & Sons
- 6005 Selino A, Jones MD (2013) Large and small eddies matter: Animating trees in wind using coarse fluid simulation and synthetic turbulence. *Comput Graph Forum* 32:75–84. <https://doi.org/10.1111/j.1467-8659.2012.03232.x>
- Sellers PJ, Mintz Y, Sud YC, Dalcher A (1986) A Simple Biosphere Model (SiB) for Use within General Circulation Models. *J Atmos Sci* 43:505–531
- 6010 Shao Y, Liu S, Schween JH, Crewell S (2013) Large-Eddy Atmosphere-Land-Surface Modelling over Heterogeneous Surfaces: Model Development and Comparison with Measurements. *Boundary-Layer Meteorol* 148:333–356. <https://doi.org/10.1007/s10546-013-9823-0>
- Sharkey TD, Singaas EL, Vanderveer PJ, Geron CD (1996) Field measurements of isoprene emission from

- 6015 trees in response to temperature and light. *Tree Physiol* 16:649–654.
<https://doi.org/10.1093/treephys/16.7.649>
- Sharma A, García-Mayoral R (2020a) Turbulent flows over dense filament canopies. *J Fluid Mech* 888:.
<https://doi.org/10.1017/jfm.2020.27>
- Sharma A, García-Mayoral R (2020b) Scaling and dynamics of turbulence over sparse canopies. *J Fluid Mech*
 6020 888:.
<https://doi.org/10.1017/jfm.2019.999>
- Shaw RH (1977) Secondary Wind Speed Maxima Inside Plant Canopies. *J Appl Meteorol* 16:514–521
- Shaw RH, Patton EG (2003) Canopy element influences on resolved- and subgrid-scale energy within a large-eddy simulation. In: *Agricultural and Forest Meteorology*. pp 5–17
- Shaw RH, Schumann U (1992) Large-eddy simulation of turbulent flow above and within a forest. *Boundary-Layer Meteorol* 61:47–64. <https://doi.org/10.1007/BF02033994>
- 6025 Shaw RH, Tavangar J (1983) Structure of the Reynolds Stress in the Canopy Layer. *J Clim Appl Meteorol* 22:1922–1931
- Shi Y, Gong W, Duan Q, et al (2019) How parameter specification of an Earth system model of intermediate complexity influences its climate simulations. *Prog Earth Planet Sci* 6:.
<https://doi.org/10.1186/s40645-019-0294-x>
- 6030 Shirzadi M, Tominaga Y, Mirzaei PA (2020) Experimental and steady-RANS CFD modelling of cross-ventilation in moderately-dense urban areas. *Sustain Cities Soc* 52:101849.
<https://doi.org/10.1016/j.scs.2019.101849>
- Shralman BI, Siggia ED (2000) Scalar turbulence. *Nature* 405:639–646. <https://doi.org/10.1038/35015000>
- 6035 Shu Y, Atkinson R (1994) Rate constants for the gas-phase reactions of O₃ with a series of Terpenes and OH radical formation from the O₃ reactions with Sesquiterpenes at 296 ± 2 K. *Int J Chem Kinet* 26:1193–1205. <https://doi.org/10.1002/kin.550261207>
- Silveira C, Ferreira J, Miranda AI (2019) The challenges of air quality modelling when crossing multiple spatial scales. *Air Qual Atmos Heal* 12:1003–1017. <https://doi.org/10.1007/s11869-019-00733-5>
- 6040 Simon E, Lehmann BE, Ammann C, et al (2005) Lagrangian dispersion of 222Rn, H₂O and CO₂ within Amazonian rain forest. *Agric For Meteorol* 132:286–304.
<https://doi.org/10.1016/j.agrformet.2005.08.004>
- Skamarock WC, Klemp JB, Dudhia JB, et al (2021) A Description of the Advanced Research WRF Model Version 4.3
- 6045 Skamarock WC, Klemp JB, Dudhia JB, et al (2008) A description of the Advanced Research WRF Version 3, NCAR Technical Note TN-475+STR
- Smagorinsky J (1963) General Circulation Experiments with the Primitive Equations: 1. The Basic Experiment. *Mon Weather Rev* 91:99–164. <https://doi.org/10.1126/science.12.306.731-a>
- Sogachev A, Leclerc MY, Zhang G, et al (2008) CO₂ fluxes near a forest edge: A numerical study. *Ecol Appl*
 6050 18:1454–1469. <https://doi.org/10.1890/06-1119.1>
- Sogachev A, Panferov O (2006) Modification of two-equation models to account for plant drag. *Boundary-Layer Meteorol* 121:229–266. <https://doi.org/10.1007/s10546-006-9073-5>
- Spatz HC, Theckes B (2013) Oscillation damping in trees. *Plant Sci* 207:66–71.
<https://doi.org/10.1016/j.plantsci.2013.02.015>
- 6055 Speck O (2003) Field measurements of wind speed and reconfiguration in *Arundo donax* (Poaceae) with estimates of drag forces. *Am J Bot* 90:1253–1256. <https://doi.org/10.3732/ajb.90.8.1253>
- Spracklen D V., Bonn B, Carslaw KS (2008) Boreal forests, aerosols and the impacts on clouds and climate. *Philos Trans R Soc A Math Phys Eng Sci* 366:4613–4626. <https://doi.org/10.1098/rsta.2008.0201>
- Spracklen D V., Carslaw KS, Kulmala M, et al (2006) The contribution of boundary layer nucleation events to
 6060 total particle concentrations on regional and global scales. *Atmos Chem Phys* 6:5631–5648.
<https://doi.org/10.5194/acp-6-5631-2006>
- Starkenburg D, Metzger S, Fochesatto GJ, et al (2016) Assessment of despiking methods for turbulence data in micrometeorology. *J Atmos Ocean Technol* 33:2001–2013. <https://doi.org/10.1175/JTECH-D-15-0154.1>
- 6065 Stępańska D, Wolek J (2009) Intradiurnal periodicity of fungal spore concentrations (*Alternaria*, *Botrytis*, *Cladosporium*, *Didymella*, *Ganoderma*) in Cracow, Poland. *Aerobiologia (Bologna)* 25:333–340.
<https://doi.org/10.1007/s10453-009-9137-3>
- Sterk HAM, Steeneveld GJ, Bosveld FC, et al (2016) Clear-sky stable boundary layers with low winds over snow-covered surfaces. Part 2: Process sensitivity. *Q J R Meteorol Soc* 142:821–835.

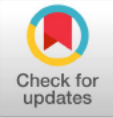
- 6070 <https://doi.org/10.1002/qj.2684>
 Stoy PC, Mauder M, Foken T, et al (2013) A data-driven analysis of energy balance closure across FLUXNET research sites: The role of landscape scale heterogeneity. *Agric For Meteorol* 171–172:137–152. <https://doi.org/10.1016/j.agrformet.2012.11.004>
- Strong C, Fuentes JD, Baldocchi DD (2004) Reactive hydrocarbon flux footprints during canopy senescence. *Agric For Meteorol* 127:159–173. <https://doi.org/10.1016/j.agrformet.2004.07.011>
- 6075 Stull RB (1988) *An Introduction to Boundary Layer Meteorology*. Kluwer Academic Publishers, Dordrecht
- Stull RB (1991) Static stability - an update. *Bull Am Meteorol Soc* 72:1521–1529
- Stull RB (2006) *The Atmospheric Boundary Layer*. In: Wallace JM, Hobbs P V (eds) *Atmospheric science: an introductory survey*, Second. Elsevier, London, pp 375–418
- 6080 Su H, Schmid HP, Grimmond CSB, et al (2004) Spectral Characteristics and Correction of Long-Term Eddy-Covariance Measurements Over Two Mixed Hardwood Forests in Non-Flat Terrain. *Boundary-Layer Meteorol* 110:213–253
- Su HB, Schmid HP, Vogel CS, Curtis PS (2008) Effects of canopy morphology and thermal stability on mean flow and turbulence statistics observed inside a mixed hardwood forest. *Agric For Meteorol* 148:862–882. <https://doi.org/10.1016/j.agrformet.2007.12.002>
- 6085 Su HB, Shaw RH, Pawu KT, et al (1998) Turbulent statistics of neutrally stratified flow within and above a sparse forest from large-eddy simulation and field observations. *Boundary-Layer Meteorol* 88:363–397. <https://doi.org/10.1023/A:1001108411184>
- Sullivan PP, Patton EG (2011) The effect of mesh resolution on convective boundary layer statistics and structures generated by large-eddy simulation. *J Atmos Sci* 68:2395–2415. <https://doi.org/10.1175/JAS-D-10-05010.1>
- 6090 Sun J, Mahrt L, Banta RM, Pichugina YL (2012) Turbulence regimes and turbulence intermittency in the stable boundary layer: During CASES-99. *J Atmos Sci* 69:338–351. <https://doi.org/10.1175/JAS-D-11-082.1>
- 6095 Sun J, Nappo CJ, Mahrt L, et al (2015) Review of wave-turbulence interactions in the stable atmospheric boundary layer. *Rev Geophys* 53:956–993. <https://doi.org/10.1002/2015RG000487>
- Szendrei Z, Rodriguez-Saona C (2010) A meta-analysis of insect pest behavioral manipulation with plant volatiles. *Entomol Exp Appl* 134:201–210. <https://doi.org/10.1111/j.1570-7458.2009.00954.x>
- Tadrist L, Saudreau M, Hémon P, et al (2018) Foliage motion under wind, from leaf flutter to branch buffeting. *J R Soc Interface* 15:. <https://doi.org/10.1098/rsif.2018.0010>
- 6100 Tao T (2008) Why global regularity for Navier-Stokes is hard. In: *Structure and Randomness*. American Mathematical Society, Providence, RI, USA, pp 220–233
- Taubert F, Fischer R, Groeneveld J, et al (2018) Global patterns of tropical forest fragmentation. *Nature* 554:519–522. <https://doi.org/10.1038/nature25508>
- 6105 Taylor GI (1938) The Spectrum of Turbulence. *Philos Trans R Soc A Math Phys Eng Sci* 164:476–490. <https://doi.org/10.2514/8.1235>
- Telewski FW (2009) Wind-induced physiological and developmental responses in trees. In: *Wind and Trees*. Cambridge University Press, pp 237–263
- Telewski FW, Prunyn ML (1998) Thigmomorphogenesis: A dose response to flexing in *Ulmus americana* seedlings. *Tree Physiol* 18:65–68. <https://doi.org/10.1093/treephys/18.1.65>
- 6110 Tenailleau QM, Mauny F, Joly D, et al (2015) Air pollution in moderately polluted urban areas: How does the definition of “neighborhood” impact exposure assessment? *Environ Pollut* 206:437–448. <https://doi.org/10.1016/j.envpol.2015.07.021>
- Thom AS (1971) Momentum absorption by vegetation. *Q J R Meteorol Soc* 097:414–428. <https://doi.org/10.1256/smsqj.41403>
- 6115 Tinya F, Márialigeti S, Király I, et al (2009) The effect of light conditions on herbs, bryophytes and seedlings of temperate mixed forests in Órség, Western Hungary. *Plant Ecol* 204:69–81. <https://doi.org/10.1007/s11258-008-9566-z>
- Tominaga Y, Stathopoulos T (2013) CFD simulation of near-field pollutant dispersion in the urban environment: A review of current modeling techniques. *Atmos Environ* 79:716–730. <https://doi.org/10.1016/j.atmosenv.2013.07.028>
- 6120 Toomey M, Friedl MA, Frohling S, et al (2015) Greenness indices from digital cameras predict the timing and seasonal dynamics of canopy-scale photosynthesis. *Ecol Appl* 25:99–115. <https://doi.org/10.1890/14-0005.1>

- 6125 Toparlar Y, Blocken B, Maiheu B, van Heijst GJF (2017) A review on the CFD analysis of urban microclimate. *Renew. Sustain. Energy Rev.* 80:1613–1640
- Toparlar Y, Blocken B, Vos P, et al (2015) CFD simulation and validation of urban microclimate: A case study for Bergpolder Zuid, Rotterdam. *Build Environ* 83:79–90.
<https://doi.org/10.1016/j.buildenv.2014.08.004>
- 6130 Tóta J, Roy Fitzjarrald D, Da Silva Dias MAF (2012) Amazon rainforest exchange of carbon and subcanopy air flow: Manaus LBA SiteA complex terrain condition. *Sci World J* 2012:.
<https://doi.org/10.1100/2012/165067>
- Trumbore S, Keller M, Wofsy SC, Da Costa JM (1990) Measurements of Soil and Canopy Exchange Rates in the Amazon Rain Forest using ^{222}Rn . *J Geophys Res* 95:16865–16873.
<https://doi.org/https://doi.org/10.1029/JD095iD10p16865>
- 6135 U.S. Department of Agriculture (1982) *Forest stand density guide*
- United Nations (2018) *World Urbanization Prospects*. United Nations, New York
- US EPA (2019) *Air Data: Air Quality Data Collected at Outdoor Monitors Across the US*
- Van de Hoven I (1957) Power Spectrum of Horizontal Wind Speed in the Frequency Range from 0.0007 to 900 Cycles per Hour. *J Meteorol* 14:160–164
- 6140 Van Gardingen P, Grace J (1991) Plants and Wind. *Adv Bot Res* 18:189–253. [https://doi.org/10.1016/S0065-2296\(08\)60023-3](https://doi.org/10.1016/S0065-2296(08)60023-3)
- Van Gorsel E, Harman IN, Finnigan JJ, Leuning R (2011) Decoupling of air flow above and in plant canopies and gravity waves affect micrometeorological estimates of net scalar exchange. *Agric For Meteorol* 151:927–933. <https://doi.org/10.1016/j.agrformet.2011.02.012>
- 6145 Vaughan G, Draude AP, Ricketts HMA, et al (2018) Transport of Canadian forest fire smoke over the UK as observed by lidar. *Atmos Chem Phys* 18:11375–11388. <https://doi.org/10.5194/acp-18-11375-2018>
- Vickers D, Mahrt L (1997) Quality Control and Flux Sampling Problems for Tower and Aircraft Data. *J Atmos Ocean Technol* 14:512–526. [https://doi.org/https://doi.org/10.1175/1520-0426\(1997\)014<0512:QCAFSP>2.0.CO;2](https://doi.org/https://doi.org/10.1175/1520-0426(1997)014<0512:QCAFSP>2.0.CO;2)
- 6150 Villani MG, Schmid HP, Su HB, et al (2003) Turbulence statistics measurements in a northern hardwood forest. *Boundary-Layer Meteorol* 108:343–364. <https://doi.org/10.1023/A:1024118808670>
- Visakorpi K, Gripenberg S, Malhi Y, et al (2018) Small-scale indirect plant responses to insect herbivory could have major impacts on canopy photosynthesis and isoprene emission. *New Phytol* 220:799–810.
<https://doi.org/10.1111/nph.15338>
- 6155 Vita G, Shu Z, Jesson M, et al (2020) On the assessment of pedestrian distress in urban winds. *J Wind Eng Ind Aerodyn* 203:104200. <https://doi.org/10.1016/j.jweia.2020.104200>
- Vogel CS (2009) Leaves in the lowest and highest winds: Temperature, force and shape: Tansley review. *New Phytol* 183:13–26. <https://doi.org/10.1111/j.1469-8137.2009.02854.x>
- 6160 Vogel CS (1989) *Drag and Reconfiguration of Broad Leaves in High Winds*
- Vogel CS (2020) *Life in Moving Fluids: The Physical Biology of Flow-Revised and Expanded Second Edition*. Princeton University Press
- Vogel CS (1968) "Sun Leaves" and "Shade Leaves": Differences in Convective Heat Dissipation Author (s): Steven Vogel Published by: Ecological Society of America Stable URL:
<http://www.jstor.org/stable/1934517>. *Ecology* 49:1203–1204
- 6165 Vollsinger S, Mitchell SJ, Byrne KE, et al (2005) Wind tunnel measurements of crown streamlining and drag relationships for several hardwood species. *Can J For Res* 35:1238–1249. <https://doi.org/10.1139/x05-051>
- Von Arnold K, Nilsson M, Hånell B, et al (2005) Fluxes of CO₂, CH₄ and N₂O from drained organic soils in deciduous forests. *Soil Biol Biochem* 37:1059–1071. <https://doi.org/10.1016/j.soilbio.2004.11.004>
- 6170 von Hippel PT (2005) Mean, median, and skew: Correcting a textbook rule. *J Stat Educ* 13:.
<https://doi.org/10.1080/10691898.2005.11910556>
- Wallace JM, Hobbs P V. (2006) *Atmospheric Science: An Introductory Survey, Second*. Academic Press, Burlington
- 6175 Wang B, Shugart HH, Lerdau MT (2017) An individual-based model of forest volatile organic compound emissions—UVAFME-VOC v1.0. *Ecol Modell* 350:69–78.
<https://doi.org/10.1016/j.ecolmodel.2017.02.006>
- Wang C, Li Q, Wang ZH (2018) Quantifying the impact of urban trees on passive pollutant dispersion using a coupled large-eddy simulation–Lagrangian stochastic model. *Build Environ* 145:33–49.

- 6180 <https://doi.org/10.1016/j.buildenv.2018.09.014>
- Wang D, Momo Takoudjou S, Casella E (2020) LeWoS: A universal leaf-wood classification method to facilitate the 3D modelling of large tropical trees using terrestrial LiDAR. *Methods Ecol Evol* 11:376–389. <https://doi.org/10.1111/2041-210X.13342>
- Wang H, Takle ES, Shen J (2001) Shelterbelts and Windbreaks: Mathematical Modeling and Computer
6185 Simulations of Turbulent Flows. *Annu Rev Fluid Mech* 33:549–586
- Wang L, Li D, Gao Z, et al (2014) Turbulent Transport of Momentum and Scalars Above an Urban Canopy. *Boundary-Layer Meteorol* 150:485–511. <https://doi.org/10.1007/s10546-013-9877-z>
- Wang T, Ding A, Gao J, Wu WS (2006) Strong ozone production in urban plumes from Beijing, China. *Geophys Res Lett* 33:1–5. <https://doi.org/10.1029/2006GL027689>
- 6190 Wang X, Lei H, Han Z, et al (2019) Three-dimensional delayed detached-eddy simulation of wind flow and particle dispersion in the urban environment. *Atmos Environ* 201:173–189. <https://doi.org/10.1016/j.atmosenv.2019.01.004>
- Wang X, Li Y (2016) Predicting urban heat island circulation using CFD. *Build Environ* 99:82–97. <https://doi.org/10.1016/j.buildenv.2016.01.020>
- 6195 Wang X, McNamara KF (2006) Evaluation of CFD simulation using RANS turbulence models for building effects on pollutant dispersion. *Environ Fluid Mech* 6:181–202. <https://doi.org/10.1007/s10652-005-5656-9>
- Watanabe T (2004) Large-eddy simulation of coherent turbulence structures associated with scalar ramps over
6200 plant canopies. *Boundary-Layer Meteorol* 112:307–341. <https://doi.org/10.1023/B:BOUN.0000027912.84492.54>
- Watanabe T, Shimoyama K, Kawashima M, et al (2020) Large-Eddy Simulation of Neutrally-Stratified Turbulent Flow Within and Above Plant Canopy Using the Central-Moments-Based Lattice Boltzmann Method. *Boundary-Layer Meteorol* 176:35–60. <https://doi.org/10.1007/s10546-020-00519-8>
- Way DA, Pearcy RW (2012) Sunflecks in trees and forests: From photosynthetic physiology to global change
6205 biology. *Tree Physiol* 32:1066–1081. <https://doi.org/10.1093/treephys/tps064>
- Webb VA, Rudnicki M (2009) A linear analysis of the interaction between the atmosphere and an underlying compliant plant canopy. *Boundary-Layer Meteorol* 133:93–111. <https://doi.org/10.1007/s10546-009-9417-z>
- Wharton S, Ma S, Baldocchi DD, et al (2017) Influence of regional nighttime atmospheric regimes on canopy
6210 turbulence and gradients at a closed and open forest in mountain-valley terrain. *Agric For Meteorol* 237–238:18–29. <https://doi.org/10.1016/j.agrformet.2017.01.020>
- Whitaker S (1973) The transport equations for multi-phase systems. *Chem Eng Sci* 28:139–147. [https://doi.org/10.1016/0009-2509\(73\)85094-8](https://doi.org/10.1016/0009-2509(73)85094-8)
- Whitmore TC (1989) Canopy Gaps and the Two Major Groups of Forest Trees. *Ecology* 70:536–538
- 6215 Wicker LJ, Skamarock WC (2002) Time-splitting methods for elastic models using forward time schemes. *Mon Weather Rev* 130:2088–2097. [https://doi.org/10.1175/1520-0493\(2002\)130<2088:TSMFEM>2.0.CO;2](https://doi.org/10.1175/1520-0493(2002)130<2088:TSMFEM>2.0.CO;2)
- Wilson K, Goldstein A, Falge E, et al (2002) Energy balance closure at FLUXNET sites. *Agric For Meteorol* 113:223–243. [https://doi.org/10.1016/S0168-1923\(02\)00109-0](https://doi.org/10.1016/S0168-1923(02)00109-0)
- 6220 Wilson NR, Shaw RH (1977) A higher order closure model for canopy flow. *J Appl Meteorol* 16:1197–1205. [https://doi.org/10.1175/1520-0450\(1977\)016<1197:ahocmf>2.0.co;2](https://doi.org/10.1175/1520-0450(1977)016<1197:ahocmf>2.0.co;2)
- Woebbecke DM, Meyer GE, Von Bargen K, Mortensen DA (1995) Color indices for weed identification under various soil, residue, and lighting conditions. *Trans Am Soc Agric Eng* 38:259–269. <https://doi.org/10.13031/2013.27838>
- 6225 Wohlfahrt G, Anfang C, Bahn M, et al (2005) Quantifying nighttime ecosystem respiration of a meadow using eddy covariance, chambers and modelling. *Agric For Meteorol* 128:141–162. <https://doi.org/10.1016/j.agrformet.2004.11.003>
- Wolfe GM, Thornton JA, McKay M, Goldstein A (2011) Forest-atmosphere exchange of ozone: sensitivity to very reactive biogenic VOC emissions and implications for in-canopy photochemistry. *Atmos Chem
6230 Phys* 11:7875–7891. <https://doi.org/10.5194/acp-11-7875-2011>
- Wood CR, Arnold SJ, Balogun AA, et al (2007) Dispersion Experiments in Central London: The 2007 DAPPLE Project. *Bull Am Meteorol Soc* 90:. <https://doi.org/10.1175/2009BAMS2638.I>
- Wood N (2000) Wind flow over complex terrain: A historical perspective and the prospect for large-eddy modelling. *Boundary-Layer Meteorol* 96:11–32. <https://doi.org/10.1023/A:1002017732694>

- 6235 World Health Organization (2016) Ambient air pollution: A global assessment of exposure and the burden of disease
 Wurps H, Steinfeld G, Heinz S (2020) Grid-Resolution Requirements for Large-Eddy Simulations of the Atmospheric Boundary Layer. *Boundary-Layer Meteorol* 175:179–201. <https://doi.org/10.1007/s10546-020-00504-1>
- 6240 Xiao Z, Liang S, Jiang B (2017) Evaluation of four long time-series global leaf area index products. *Agric For Meteorol* 246:218–230. <https://doi.org/10.1016/j.agrformet.2017.06.016>
 Xie ZT (2011) Modelling Street-Scale Flow and Dispersion in Realistic Winds-Towards Coupling with Mesoscale Meteorological Models. *Boundary-Layer Meteorol* 141:53–75. <https://doi.org/10.1007/s10546-011-9629-x>
- 6245 Xie ZT, Castro IP (2009) Large-eddy simulation for flow and dispersion in urban streets. *Atmos Environ* 43:2174–2185. <https://doi.org/10.1016/j.atmosenv.2009.01.016>
 Xie ZT, Fuka V (2018) A Note on Spatial Averaging and Shear Stresses Within Urban Canopies. *Boundary-Layer Meteorol* 167:171–179. <https://doi.org/10.1007/s10546-017-0321-7>
- 6250 Xu L, Pyles RD, Paw U KT, et al (2017) Impact of canopy representations on regional modeling of evapotranspiration using the WRF-ACASA coupled model. *Agric For Meteorol* 247:79–92. <https://doi.org/10.1016/j.agrformet.2017.07.003>
 Xu X, Yi C, Kutter E (2015) Stably stratified canopy flow in complex terrain. *Atmos Chem Phys* 15:7457–7470. <https://doi.org/10.5194/acp-15-7457-2015>
- 6255 Yaglom M (1979) Similarity laws for constant-pressure and pressure-gradient turbulent wall flows. *Annu Rev Fluid Mech* 11:505–540
- Yan C, Huang WX, Miao S, et al (2017) Large-Eddy Simulation of Flow Over a Vegetation-Like Canopy Modelled as Arrays of Bluff-Body Elements. *Boundary-Layer Meteorol* 165:233–249. <https://doi.org/10.1007/s10546-017-0274-x>
- 6260 Yan C, Miao S, Liu Y, Cui G (2020) Multiscale modeling of the atmospheric environment over a forest canopy. *Sci China Earth Sci.* <https://doi.org/10.1007/s11430-019-9525-6>
 Yan G, Hu R, Luo J, et al (2019) Review of indirect optical measurements of leaf area index: Recent advances, challenges, and perspectives. *Agric For Meteorol* 265:390–411. <https://doi.org/10.1016/j.agrformet.2018.11.033>
- 6265 Yang B, Morse AP, Shaw RH, Paw U KT (2006a) Large-eddy simulation of turbulent flow across a forest edge. Part II: Momentum and turbulent kinetic energy budgets. *Boundary-Layer Meteorol* 121:433–457. <https://doi.org/10.1007/s10546-006-9083-3>
 Yang B, Raupach MR, Shaw RH, et al (2006b) Large-eddy simulation of turbulent flow across a forest edge. Part I: Flow statistics. *Boundary-Layer Meteorol* 120:377–412. <https://doi.org/10.1007/s10546-006-9057-5>
- 6270 Yang XIA, Sadique J, Mittal R, Meneveau C (2016) Exponential roughness layer and analytical model for turbulent boundary layer flow over rectangular-prism roughness elements. *J Fluid Mech* 789:127–165. <https://doi.org/10.1017/jfm.2015.687>
 Yim SHL, Fung JCH, Ng EYY (2014) An assessment indicator for air ventilation and pollutant dispersion potential in an urban canopy with complex natural terrain and significant wind variations. *Atmos Environ* 94:297–306. <https://doi.org/10.1016/j.atmosenv.2014.05.044>
- 6275 Yuan C, Ng E, Norford LK (2014) Improving air quality in high-density cities by understanding the relationship between air pollutant dispersion and urban morphologies. *Build Environ* 71:245–258. <https://doi.org/10.1016/j.buildenv.2013.10.008>
- 6280 Yue W, Parlange MB, Meneveau C, et al (2007) Large-eddy simulation of plant canopy flows using plant-scale representation. *Boundary-Layer Meteorol* 124:183–203. <https://doi.org/10.1007/s10546-007-9173-x>
- Zaki SA, Hagishima A, Tanimoto J, Ikegaya N (2011) Aerodynamic Parameters of Urban Building Arrays with Random Geometries. *Boundary-Layer Meteorol* 138:99–120. <https://doi.org/10.1007/s10546-010-9551-7>
- 6285 Zalakeviciute R, López-Villada J, Rybarczyk Y (2018) Contrasted effects of relative humidity and precipitation on urban PM_{2.5} pollution in high elevation urban areas. *Sustain* 10:. <https://doi.org/10.3390/su10062064>
 Zellweger F, De Frenne P, Lenoir J, et al (2020) Forest microclimate dynamics drive plant responses to warming. *Science* (80-) 368:772 LP – 775. <https://doi.org/10.1126/science.aba6880>

- 6290 Zeng P, Takahashi H (2000) A first-order closure model for the wind flow within and above vegetation canopies. *Agric For Meteorol* 103:301–313. [https://doi.org/10.1016/S0168-1923\(00\)00133-7](https://doi.org/10.1016/S0168-1923(00)00133-7)
- Zeri M, Rebmann C, Feigenwinter C, Sedláč P (2010) Analysis of periods with strong and coherent CO₂ advection over a forested hill. *Agric For Meteorol* 150:674–683. <https://doi.org/10.1016/j.agrformet.2009.12.003>
- 6295 Zhao F, Yang X, Schull MA, et al (2011) Measuring effective leaf area index, foliage profile, and stand height in New England forest stands using a full-waveform ground-based lidar. *Remote Sens Environ* 115:2954–2964. <https://doi.org/10.1016/j.rse.2010.08.030>
- Zheng X, Montazeri H, Blocken B (2020) CFD simulations of wind flow and mean surface pressure for buildings with balconies: Comparison of RANS and LES. *Build Environ* 173:106747. <https://doi.org/10.1016/j.buildenv.2020.106747>
- 6300 Zhong J (2015) Modelling Air Pollution Withing a Street Canyon. University of Birmingham
- Zhong J, Cai X, Bloss WJ (2015) Modelling the dispersion and transport of reactive pollutants in a deep urban street canyon: Using large-eddy simulation. *Environ Pollut* 200:42–52. <https://doi.org/10.1016/j.envpol.2015.02.009>
- 6305 Zhong J, Cai X, Bloss WJ (2016) Coupling dynamics and chemistry in the air pollution modelling of street canyons: A review. *Environ Pollut* 214:690–704. <https://doi.org/10.1016/j.envpol.2016.04.052>
- Zhong J, Nikolova I, Cai X, et al (2018) Modelling traffic-induced multicomponent ultrafine particles in urban street canyon compartments: Factors that inhibit mixing. *Environ Pollut* 238:186–195. <https://doi.org/10.1016/j.envpol.2018.03.002>
- 6310 Zhu J, Zhang G, Wang GG, et al (2015) On the size of forest gaps: Can their lower and upper limits be objectively defined? *Agric For Meteorol* 213:64–76. <https://doi.org/10.1016/j.agrformet.2015.06.015>
- Zorzetto E, Peltola O, Grönholm T, Katul GG (2021) Intermittent Surface Renewals and Methane Hotspots in Natural Peatlands. *Boundary-Layer Meteorol* 180:407–433. <https://doi.org/10.1007/s10546-021-00637-x>



Characteristics of free air carbon dioxide enrichment of a northern temperate mature forest

Kris M. Hart¹ | Giulio Curioni^{1,2} | Phillip Blaes^{1,2,3} | Nicholas J. Harper¹ | Peter Miles¹ | Keith F. Lewin⁴ | John Nagy⁴ | Edward J. Bannister^{1,2} | Xiaoming M. Cai^{1,2} | Rick M. Thomas^{1,2} | Stefan Krause^{1,2} | Michael Tausz^{1,5} | A. Robert MacKenzie^{1,2}

¹Birmingham Institute of Forest Research (BIFoR), University of Birmingham, Birmingham, UK

²School of Geography, Earth and Environmental Sciences, University of Birmingham, Birmingham, UK

³Yorkshire Water, Bradford, UK

⁴Brookhaven National Laboratory, Upton, NY, USA

⁵Department of Agriculture, Science and the Environment, School of Medical, Health and Applied Sciences, Central Queensland University, Rockhampton, Qld, Australia

Correspondence

Kris M. Hart and A. Robert MacKenzie, Birmingham Institute of Forest Research (BIFoR), University of Birmingham, Edgbaston, Birmingham B15 2TT, UK. Email: [redacted] and [redacted]

Funding information

JABBS Foundation; University of Birmingham; Natural Environment Research Council, Grant/Award Number: NE/P003486/1 and NE/N020502/1; Brookhaven National Laboratory, Grant/Award Number: DE-SC0012704 and DE-SC0016011; NSF's Macrosystems Biology, Grant/Award Number: EF-1065029 and EF-1702697; United States Geological Survey, Grant/Award Number: G10AP00129 and G16AC00224

Abstract

In 2017, the Birmingham Institute of Forest Research (BIFoR) began to conduct Free Air Carbon Dioxide Enrichment (FACE) within a mature broadleaf deciduous forest situated in the United Kingdom. BIFoR FACE employs large-scale infrastructure, in the form of lattice towers, forming 'arrays' which encircle a forest plot of ~30 m diameter. BIFoR FACE consists of three treatment arrays to elevate local CO₂ concentrations (e[CO₂]) by +150 μmol/mol. In practice, acceptable operational enrichment (ambient [CO₂] + e[CO₂]) is ±20% of the set point 1-min average target. There are a further three arrays that replicate the infrastructure and deliver ambient air as paired controls for the treatment arrays. For the first growing season with e[CO₂] (April to November 2017), [CO₂] measurements in treatment and control arrays show that the target concentration was successfully delivered, that is: +147 ± 21 μmol/mol (mean ± SD) or 98 ± 14% of set point enrichment target. e[CO₂] treatment was accomplished for 97.7% of the scheduled operation time, with the remaining time lost due to engineering faults (0.6% of the time), CO₂ supply issues (0.6%) or adverse weather conditions (1.1%). CO₂ demand in the facility was driven predominantly by wind speed and the formation of the deciduous canopy. Deviations greater than 10% from the ambient baseline CO₂ occurred <1% of the time in control arrays. Incidences of cross-contamination >80 μmol/mol (i.e. >53% of the treatment increment) into control arrays accounted for <0.1% of the enrichment period. The median [CO₂] values in reconstructed three-dimensional [CO₂] fields show enrichment somewhat lower than the target but still well above ambient. The data presented here provide confidence in the facility setup and can be used to guide future next-generation forest FACE facilities built into tall and complex forest stands.

KEYWORDS

deciduous, elevated carbon dioxide, FACE, oak, performance, *Quercus robur*, United Kingdom, Woodland

This is an open access article under the terms of the Creative Commons Attribution License, which permits use, distribution and reproduction in any medium, provided the original work is properly cited.

© 2019 The Authors. *Global Change Biology* published by John Wiley & Sons Ltd




Mass concentration measurements of autumn bioaerosol using low-cost sensors in a mature temperate woodland free-air carbon dioxide enrichment (FACE) experiment: investigating the role of meteorology and carbon dioxide levels

Aileen B. Baird^{1,2}, Edward J. Bannister^{1,2}, A. Robert MacKenzie^{1,2}, and Francis D. Pope^{1,2}

¹School of Geography, Earth and Environmental Sciences, University of Birmingham, Birmingham, B152TT, UK

²Birmingham Institute of Forest Research, University of Birmingham, Birmingham, B15 2TT, UK

Correspondence: Francis D. Pope 

Received: 25 June 2021 Discussion started: 1 July 2021

Revised: 27 April 2022 Accepted: 30 April 2022 Published: 30 May 2022

Abstract. Forest environments contain a wide variety of airborne biological particles (bioaerosols), including pollen, fungal spores, bacteria, viruses, plant detritus, and soil particles. Forest bioaerosol plays a number of important roles related to plant and livestock health, human disease and allergenicity, and forest and wider ecology and are thought to influence biosphere–atmosphere interactions via warm and cold cloud formation. Despite the importance of bioaerosols, there are few measurements of forest aerosol, and there is a lack of understanding of how climate change will affect forest bioaerosol in the future.

We installed low-cost optical particle counters (OPCs) to measure particles in the size range between 1 and 10 μm (PM_{10} – PM_1) for a period of 2 months in autumn 2018 at the Birmingham Institute of Forest Research (BIFoR) free-air carbon dioxide enrichment (FACE) facility. In the paper, we propose that the PM_{10} – PM_1 (particulate matter) metric is a good proxy for bioaerosols because of the bioaerosol representative size range, the location of the study site (a woodland in a rural location), the field measurement taking place during the season of peak fungal activity, and the low hygroscopicity of the particles measured. The BIFoR FACE facility fumigates three 700 m^2 areas of the forest with an additional 150 ppm CO_2 above ambient levels with minimal impacts on other potential environmental drivers such as temperature, humidity, and wind. This experimental set-up enabled us to investigate the effect of environmental variables, including elevated CO_2 ($e\text{CO}_2$), on bioaerosol proxy concentrations

and to evaluate the performance of the low-cost OPCs in a forested environment.

Operating the low-cost OPCs during autumn 2018, we aimed to capture predominantly the fungal bioaerosol season. Across the experimental duration, the OPCs captured both temporal and spatial variation in bioaerosol concentrations. Aerosol concentrations were affected by changing temperatures and wind speeds but, contrary to our initial hypothesis, not by relative humidity. We detected no effect of the $e\text{CO}_2$ treatment on total bioaerosol concentrations, but a potential suppression of high-concentration bioaerosol events was detected under $e\text{CO}_2$. In-canopy atmospheric dispersion modelling indicates that the median spore dispersion distance is sufficiently small that there is little mixing between treatment and control experiments. Our data demonstrate the suitability of low-cost OPCs, interpreted with due caution, for use in forests and so opens the possibility of forest bioaerosol monitoring in a wider range of habitats to a wider range of researchers at a modest cost.

1 Introduction

Aerobiology investigates the production, transport, and removal of airborne biological particles such as bacterial, fungal, and viral microbes; plant pollen; and soil and plant debris. Fungal spores form a large proportion of the bioaerosol population, with ground level concentrations typically of 10 000–50 000 spores m^{-3} (compared with 1000